UNIVERSITY OF SOUTHAMPTON

Wake Generator Control of Flow Distortion Induced Tonal Noise in Fans

Viswanath Kota

A thesis submitted for the degree of Doctor of Philosophy

INSTITUTE OF SOUND AND VIBRATION RESEARCH
FACULTY OF ENGINEERING, SCIENCE AND MATHEMATICS

February 2005

Abstract

UNIVERSITY OF SOUTHAMPTON
INSTITUTE OF SOUND AND VIBRATION RESEARCH

Doctor of Philosophy

WAKE GENERATOR CONTROL OF FLOW DISTORTION INDUCED TONAL NOISE IN FANS

by Viswanath Kota

The predicted increased demand on the operation of aircraft in existing airports or creation of new airports increases the scope for noise pollution. Hence the regulations for new aircraft and engine certification are likely to become more stringent. This is driving the need to explore new methods to control noise. One of the means of generation of tonal noise in aircraft engines is the interaction of fan blades with flow disturbances. This is also the case in non-aviation applications. A novel way to control this noise is to generate further disturbances which interact with the fan to produce anti-noise. Flow disturbances can be created using an array of cylindrical rods protruding into the duct. The variation of the lengths and orientation of these rods results in the production of wakes of varying extent which then interact with the fan blades to produce unsteady blade forces and these radiate noise.

Adaptive control of this form of noise is possible by formulating the acoustic response of the rod obtained through the theoretical relationship between the rod length and the magnitudes of the unsteady blade forces and in turn the magnitudes of the acoustic modes in the duct. Since the control of a single mode could cause the amplitude of the other modes to increase, optimal control of a set of modes is possible by formulating the problem of minimisation of the cost function which is the in-duct sound power level comprising the squares of the modal amplitudes. Convergence of the optimal rod lengths is obtained through the use of the steepest descent algorithm.

Experimental investigations confirm that it is possible to implement the adaptive control of fan tonal noise using wake generators. The concept has been implemented on a test fan rig and an 8-rod controller array using the pressure signals acquired from duct microphones. These signals are phase locked with a

trigger signal consisting of one pulse per fan blade-pass and Fast Fourier Transformed to extract tones which are later decomposed into duct modes and then into modal coupling coefficients. The controller rod response in the form of the modal coupling coefficients is determined experimentally and used in the control algorithm based on steepest gradient descent. Upon running the algorithm at the fan speed corresponding to a blade passing frequency of 262 Hz with one rod made to act as a source and another as a controller, the in-duct noise power in the plane wave mode is reduced from 67 to 42 dB. Far-field sound pressure level reduced from 91 to 87 dB in the 1^{st} harmonic and from 85 to 79 dB in the 2^{nd} harmonic. Control trajectories superposed on error surfaces show that the convergence of the rod lengths is sensitive to the choice of the descent step. Although the controller rod lengths exhibit smooth convergence in the control cases corresponding to the higher fan blade passage frequency of 441 Hz, control doesn't result in significant reduction in the in-duct noise power level at this speed which was around 2 dB. This is due to the difficulty in controllability of multiple cut-on duct modes at this frequency.

Acknowledgements

The research work presented in this thesis was supported financially by the UK Engineering and Physical Sciences Research Council which is gratefully acknowledged. I would also like to thank Rolls Royce plc for making this work possible within the framework of their University Technology Centre established at the ISVR for conducting research on Gas Turbine Engine Noise.

I would like to express my gratitude to Dr. M.C.M. Wright for his support and advice, and to Prof. P.A. Nelson and Dr. P.F. Joseph for sharing their views and experiences.

The experimental work presented in this thesis would have been impossible without the support of the technical staff of ISVR.

Table of Contents

Chapter 1 Introduction: Fan Interaction Noise and its control

1.1. Introduction

Environmental noise is an annoyance to humans. The transportation sector represents one of the major contributors to environmental noise. Vehicles moving along airways, roadways and railways generate considerable noise to pollute the environment. Aircraft noise is particularly bothersome to people living around airports with the frequent landing and taking off of several aircraft at any particular airport. Aviation authorities across the world have adopted regulations for acceptable levels of noise from aircraft and require the airframe and engine manufacturers to pass certification before the operation of any new aircraft commences. These regulations are revised from time to time and the existing fleet of aircraft which do not meet them are phased out. Furthermore, aircraft manufacturers (Airbus 1999) predict that in the future there will be a rise in air traffic due to the increased demand for air travel and freight passage and hence are considering designing newer aircraft with more capacity for freight and passengers. This translates to increased demand on the operation of aircraft in existing airports or creating newer airports. All this means that the scope for noise pollution increases. Consequently the regulations for certification are likely to become more stringent and airframe and engine manufacturers will have to take measures to reduce noise in the newer designs. In order to do this an understanding of the mechanisms of the noise sources is required to either eliminate these sources at the design stage or to investigate methods to control them. Noise from an aircraft arises from the airframe as well as the engine. These days mostly the turbofan variety of engines is used on aircraft for propulsion and the noise spectrum of an engine consists of tones and broadband noise with the contribution of the inlet fan to tonal noise being dominant during take-off and approach.

The need to understand the noise source mechanisms with regard to their controllability also applies to non-aviation situations as in the cooling of electronic systems, HVAC equipment, etc. For instance there is a continuing increase in the heat dissipation from electronic systems due to a rapid rise in

circuit densities. This necessitates an increase in fan speeds and the number of installed fans leading to increased radiated noise which is driving the need to understand all the relevant aero-acoustic processes (Quinlan & Bent 1998).

Section 1.2 outlines a review of the current understanding of the mechanism of interaction tone generation in an engine fan and the methods adopted to reduce noise are discussed in 1.3. Section 1.4 gives an introduction to the method chosen for investigation presented in this thesis. Section 1.5 will give the outline of the thesis.

1.2. Tonal noise sources in an engine fan

A typical turbofan engine consists of a nacelle, surrounding a duct enclosing the fan, compressor and turbine stages terminated by an exhaust jet. The duct from the exit of the fan splits into a core comprising the compressor-turbine stages which then extends into the core jet and the bypass duct extending concentrically along the core duct ends as the bypass jet. An overview of turbomachinery noise sources is given by Groeneweg (1991). Figure 1.1 shows the sources of tonal noise included with the other sources responsible for broadband noise (Greoneweg 1991). Figure 1.2 from the same reference is reproduced here and outlines the processes involved in production of noise. Internal disturbances in flow arise due to presence of support struts or pylons which interact with the rotating blades. Figure 1.3 shows that the contribution of the fan to the total engine noise is dominant during takeoff and landing. Flow entering into the fan could also draw in external disturbances which can interact with the blades. The wakes shed from the rotor can also interact with the stationary stator blades and represent another way in which interaction tones are produced. The disturbances produce unsteady forces on the blades and these unsteady forces then generate noise. The acoustic pressure generated can be expressed as the superposition of spinning modes. The term mode refers to the eigen function and its corresponding mathematical expression. These modes either remain cut-off if their axial wave number is imaginary and decay away exponentially or they remain cut-on and propagate through the duct if that parameter is real. The cut-on modes which reach the duct inlet or exhaust then radiate into the far-field.

Tyler and Sofrin (1961) were the first to explain the mechanism of interaction tone generation. The steady pressure field locked to the rotor blades radiates as noise to the observer only when this pattern moves supersonically with respect to the observer. Consequently in the subsonic case disturbances locked to the rotor are those of the rotor blade order which cannot radiate noise as they can spin only as fast as the rotor. Furthermore, modes of the blade order are not cut-on unless the speed of the rotor is high enough for them to propagate. Hence in the subsonic case it was predicted by Tyler and Sofrin (1961) that since the acoustic modes generated from the subsonic rotor-locked blade-order flow patterns are themselves not cut-on enough to generate tones at blade passing frequency and its harmonics, these should be produced from flow modes of different orders than those of the rotor blades and the acoustic modes should be spinning at a higher or a lower speed than the rotor to generate tones at blade passing frequencies. The modes are generated by the interaction of the multiple modal patterns present in the incoming flow disturbance. The incoming flow disturbance may have several of these modal patterns and these interact with the blades to produce spinning acoustic modes which, depending on their circumferential mode order, spin at either faster or lower speed than the rotor to generate a tone at the blade passing frequency (BPF). The intensities of these modes depend on the magnitudes of the unsteady blade pressures. The situation is different when the flow relative to the blades is supersonic wherein a blade order rotor locked shock pattern rotates and produces multiple pure tones.

Huff (1998) has made a recent review of fan noise prediction, and its status and needs. He states that there are two alternative goals for fan noise prediction. One is to model the effects of changes to geometric features and flow conditions and accurately predict the absolute levels for sound. The other one is to predict the correct trends of the sound as a function of geometry and flow field changes. He goes on to state that neither of these have been fully achieved, although there has been considerable progress. Analytical methods (Sears 1941, Amiet 1974, Graham 1970, Namba 1977, Goldstein and Atassi 1976, Goldstein 1976) were used to predict the blade response by modelling the problem as that of an isolated airfoil or a cascade of airfoils interacting with the flow disturbance represented as 2-D or 3-D gusts and then using radiation/propagation models (Weiner-Hopf and ray tracing and other methods as mentioned in Huff (1998)) to predict the intensities

of the propagating modes and also the far-field directivities. Other researchers (Rangwalla & Rai 1993) have also studied the problem numerically. Another approach to the problem is to use empirical models for the flow disturbances (wakes and vortices) obtained from experimental correlations and then feed them to the analytical or the computational model to predict the noise field (Sutliff 1997). In the CFD-CAA approach RANS or Unsteady Navier-Stokes solvers are used to solve for the mean and unsteady flows and then CAA (FEM or BEM formulation) is used to compute the aeroacoustic response. Huff (1998) mentions there is concern that "real blade" effects, like the distortion of gusts by transonic flows etc., have not been taken into account in the analytical models, and on the computational side time-marching techniques for interaction tone prediction require considerable computational resources.

1.3. Noise control – Active and Passive methods

Noise control can be categorized into active and passive techniques. Under passive control, absorbent acoustic liners are laid along several locations of the engine and these provide an impedance boundary condition to the waves reflecting from the walls and attenuate them. The control of noise through treatment is understood to be effective for high frequency noise as the distance of propagation over the acoustic lining is several wavelengths. Consequently low speed machines which generate relatively low frequencies of noise compared to high-speed machines require longer lengths of ducting. Envia (2002) also mentions that the newer designs of engines tend to have higher bypass ratios with the result that they require lesser nacelle lengths and hence less lengths available for treatment.

Under active control methods a source of noise is identified and is controlled by including secondary noise sources in the system and these secondary noise sources are driven either in an open loop or closed loop to produce the secondary noise field which either cancels or reduces the modes in the primary noise field. Loudspeakers have been used as secondary noise sources. A review of

the work done in this area is contained in Envia (2002). He states that there have been significant noise reduction benefits from the use of active noise control, but the benefits tend to diminish with the increasing number of simultaneously controlled modes. He suggests that this may be due to the multiple modes having a unique phase relationship with each other, and that errors in the measurement of the phase relationship can cause the actuation of the secondary noise sources to produce a noise field that may not exactly match the target field. Furthermore, the power requirements for these secondary noise sources is quite high and this has precluded a cost-effective usage or implementation in real engines so far.

The above means of controlling noise represent techniques to control noise at the propagation level in that the sound field is controlled during the propagation process.

Attempts to control noise at the source have also been summarised in the same reference (Envia 2002). The following is a summary of the methods and the benefits and limitations.

The first of these attempts involves employing a larger rotor stator spacing and a cut-off vane count as done on the Advanced Ducted Propulsor built by Pratt and Whitney (Topol 1993). Acoustic codes were used to optimise the cut-off vane count to reduce the levels of the second and third harmonics of the blade passing frequency (Topol 1993). However a concern realised elsewhere about the increase in rotor stator spacing (Sawyer 2002) is that it increases the size and hence the weight of the engine. The benefit from the increased spacing is that it reduces the amplitudes of the wakes and hence the intensities of the modes produced through interaction. The cut-off vane count causes the modes generated through interaction to be of a higher order such that they remain cut-on only for the higher harmonics.

Another attempt discussed in Envia (2002) concerns the provision of a swept and leant stator. Sweep is the axial distance and lean is the circumferential displacement of the vane leading edge from its nominal position. By providing sweep and lean on the stator blades 3 EPNdB noise reduction was shown to be possible compared to the situation when a radial stator in its nominal position was used. By providing sweep and lean the contribution to the phase of any mode of the interacting disturbance varies with the span and hence lower levels of noise

result from such a design of the stator blading. The limitation of this approach seems to be that it generated more aerodynamic losses than had been anticipated.

The next in the series of methods summarised in Envia (2002) is the trailing edge blowing technique. Flow is supplied through the shaft along a labyrinth of internal passages that start from blade root and terminate at a series of trailing edge ports. Thus the wakes issuing out from the rotor blades are made more uniform so as to cause less unsteady forces on the stator. This technique was originally tried at MIT (Waitz 1996) and was later extended by the researchers at NASA (Sutliff 2002) to conduct a proof-of-concept test to establish the noise reduction benefits. The test conducted at the NASA Active Noise Control Fan facility demonstrated that the far field tone power levels in the first three harmonics were reduced by 5.4, 10.6 and 12.4 dB PWL. The blowing rate of 1.6 - 1.8% (defined as the ratio of flow supplied to the trailing edge to the total fan mass flow) was found to be the optimum.

The last of the methods discussed in the above reference is the scarfed inlet concept which is the provision of a scarfed inlet on the intake to redirect the noise upward. But the scarfed inlet is also thought to cause the production of flow distortions which when ingested could produce noise.

The effect of boundary layer suction on fan noise has been experimentally investigated by Moore (1975). He used a ventilation fan of 1m diameter with suction applied around the circumference of the duct close to the fan inlet. Upon removal of 5% of the main flow reduction of 5 dB in the far field sound power and 15 dB in some of the far field tones was observed. Progressive reduction in the noise was obtained by proportionately varying the amount of flow bled through suction. He mentions that care must be taken in the design of the bleed system so as not to produce any "cut on" residual distortions that could propagate to increase the far field noise.

Ganz *et al.* (1998) offered new insights into broadband noise mechanisms. They focused their study on broadband noise sources by treating them separately as inflow and self noise mechanisms. They used a model scale fan rig with provision to bleed the inlet boundary layer and to vary the tip gap and the loading. Self noise, or the rotor-alone-noise, was parametrically studied by varying the tip gap and loading to observe the variation in broadband noise generated through the tip clearance and rotor exit wake flows. The inflow mechanism in this case was

isolated by completely removing the inlet boundary layer. To study the inflow noise the boundary layer was re-introduced and its effect was studied on the rotor and stator. Of particular interest is the observation that there was a reduction in the broadband noise through boundary layer suction. They were able to qualitatively explain their results by conducting hot-wire measurements of mean flow velocities and turbulent intensities at the rotor exit.

Sawyer and Fleeter (2002) have reported a 10 dB reduction in the rotor-stator interaction tones using active airfoil sources mounted on the stator blades. The active airfoil sources were perforated metal covered cavities in the stators which formed resonators and these were driven by compression drivers. Kousen and Verdon (1994) have used an entirely analytical/computational approach for simulating control of blade-row/wake interaction noise using anti-sound actuators on blade surfaces.

Using a control grid of wake generators Polacsek (1999) was able to reduce rotor-stator interaction modes with the grid mounted upstream of the rotor. An 8 dB reduction in the SPL at the blade passing frequency was achieved by using such a system on the ONERA CERF-rig. Using CFD-CAA approach to simulate the control he has been able to assess the experimental results.

Nuehas *et al.* (2003) have used flow control techniques to reduce blade passage frequency tone levels with steady jets injected into the main flow and cylindrical rods at axial positions downstream of the impeller blades. With cylindrical rods they have been able to report a reduction of 12.6 dB in the BPF tone.

1.4. Flow control

A recent review on flow and noise control (Thomas *et al.* 2002) mentions that there are two critical issues needed to achieve projected noise reduction targets:

> "(1) better understanding and prediction of noise generation and propagation mechanisms for all significant noise sources, and (2) noise reduction concepts that are both technically feasible and economically as well as commercially viable. Apart from the

already existent usage of passive liner treatment for noise reduction many investigators suggest that a combination of passive and active methods should be used for control. Consequent to this it is worthwhile to explore novel means of reducing noise."

As mentioned already before, methods to alter flow non-unformities seem to have an effect in reducing the unsteady forces on the blades which consequently reduces the radiated noise. The trailing edge blowing technique, boundary layer removal and the introduction of rods to generate disturbances fall in this category.

Nelson (2000) theoretically predicted that the tones generated through inlet flow distortions could be used to control a single tone and that optimisation could be done to minimise the total generated sound at higher harmonics of BPF. His prediction follows from an analytical model due to Goldstein (1976), which relates the acoustic response of the fan blades to the intensity of the interacting distorted flow field. Nelson (2000) suggested that distortions could be either introduced as positive or negative defects in the velocity profile of a flow field.

Generation of wakes through the presence of solid bodies in the flow field represents a means of producing defects in the flow field velocity. The concept of noise reduction from this method is illustrated in Figure 1.4. The flow and the acoustic situations inside a duct housing a fan are illustrated separately. The fan encounters a primary disturbance in the flow and generates the primary acoustic field. The acoustic field introduced through the wake generators can be adjusted by varying the lengths of the rods and the azimuthal angle of the array of rods to cancel or reduce the intensity of the total acoustic field in the system. Since a focus on the reduction or cancellation of a single mode may cause generation of, or increase in the intensities of the other modes, the noise power contained in multiple harmonics requires optimisation.

Pitelet (2000) extended the Goldstein (1976) model to a finite-duct case and derived an expression for the acoustic field. He used a single rod to conduct experiments to determine the modal response of the rod and used this response to simulate the minimisation of noise power. His experimental set-up lacked the means of decoupling the secondary acoustic field from the primary acoustic field due to the unavailability of a fan blade passing reference signal.

Though the strategy of flow control as discussed here seems to point to the acoustic benefits involved through its application, there are other applications entailing aerodynamic benefits from its use. In particular flow control technologies using smart materials, vortex generators, etc., have demonstrated benefits like reduction in drag, control of the phenomenon of flow separation etc. For more information one could refer to the review on flow and noise control and the associated references therein (Thomas *et al.* 2002).

1.5. **Outline of the thesis**

The problem of controlling noise using flow distortions generated through introduction of rods in the flow has been taken up further in the present work. The acoustic pressure field expressions have been extended to a semi-infinite ducted case and the derivation of the expression for pressure is given in Chapter 2. The expression for the overall sound power level to be used as a cost function for the optimisation problem along with the numerical simulation of control for a simple case is given in Chapter 3. Simulation of control assuming more general primary flow disturbances is presented in Chapter 4. The implementation of this system was carried out on a model fan and this along with the results is described in Chapter 5. Finally, conclusions and suggestions for further work are made in Chapter 6.

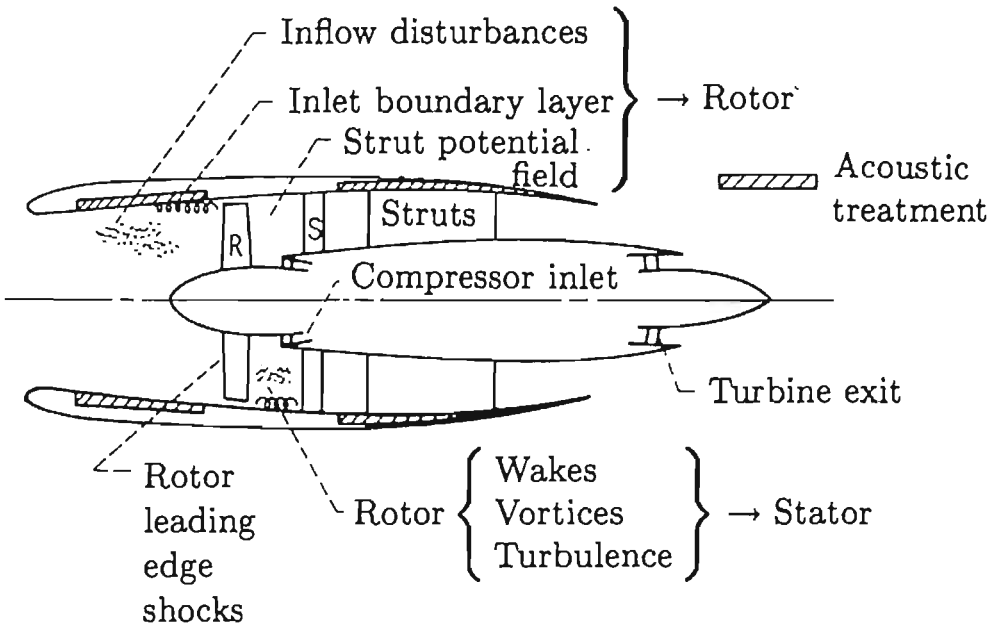

Figure 1.1 Turbofan engine with turbomachinery noise-generating mechanisms. (Groeneweg 1991)

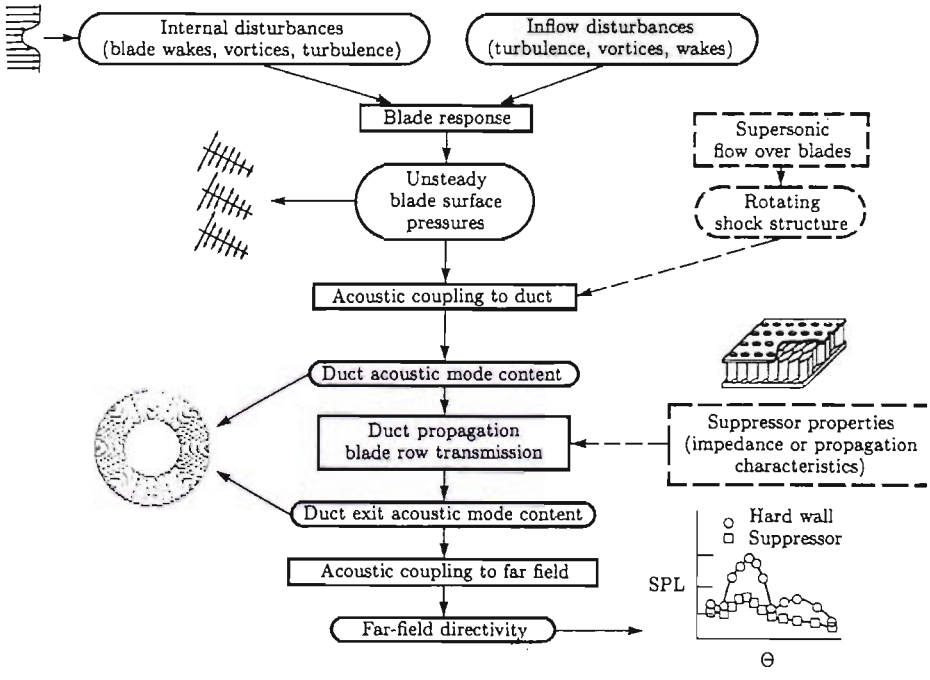

Figure 1.2 Turbomachinery noise generation processes. (Groeneweg 1991)

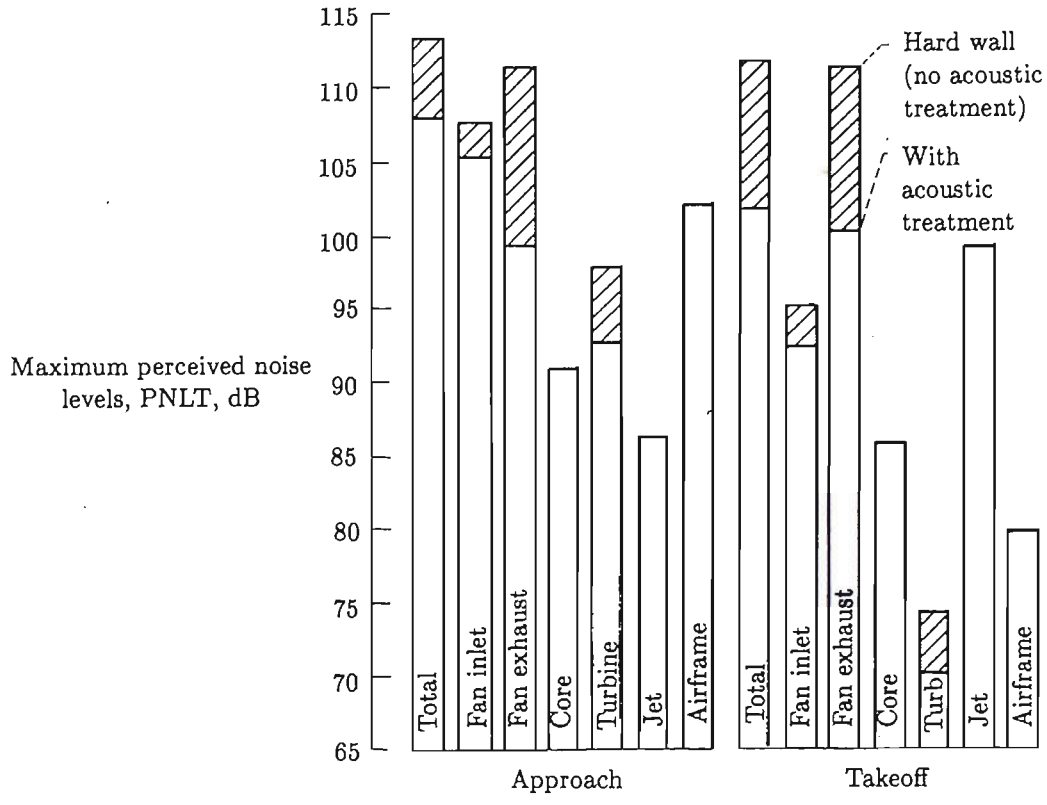

Figure 1.3 Flyover noise levels for a turbofan engine with contribution from each component. (Owens 1979)

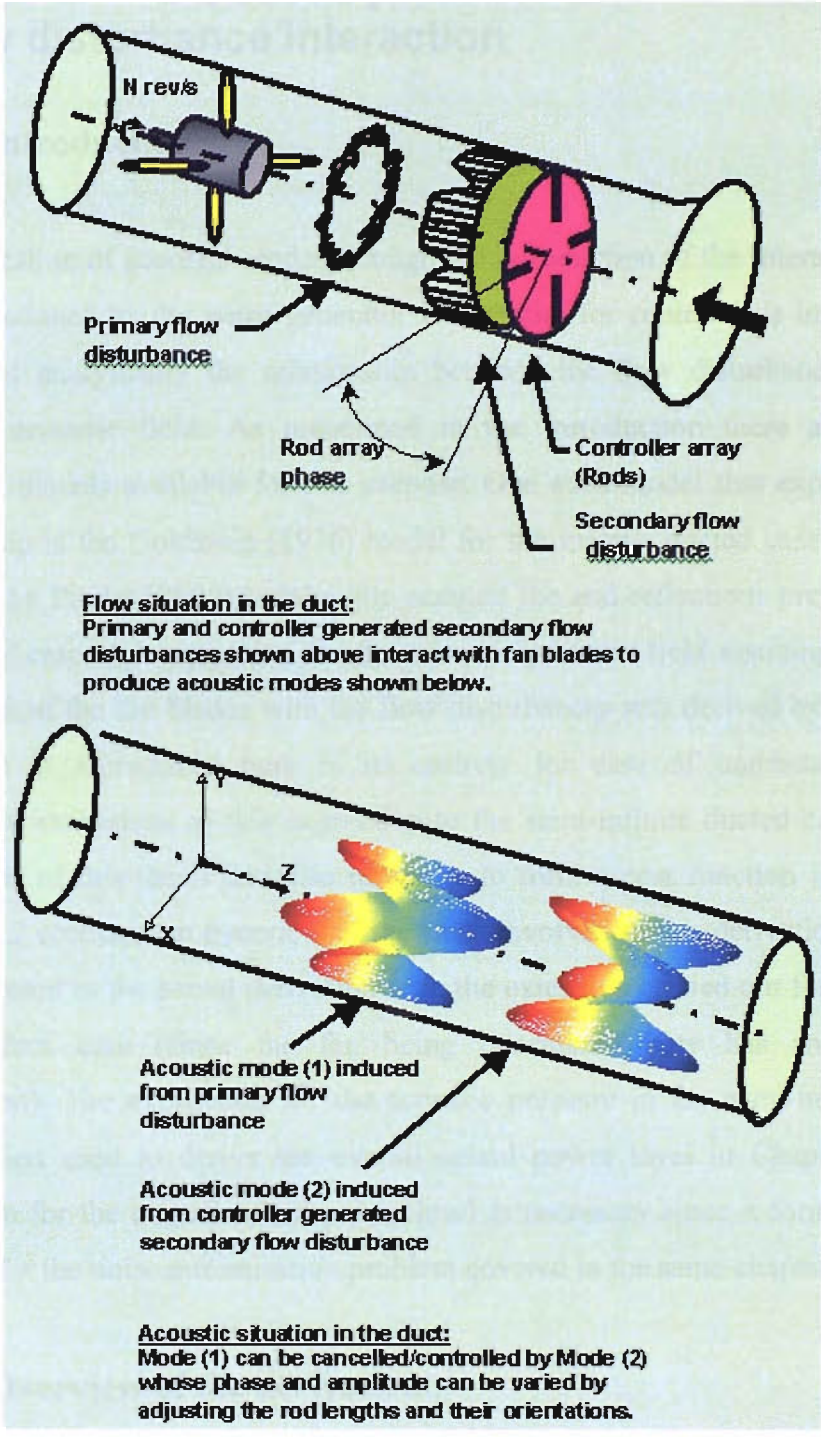

Figure 1.4 Flow and acoustic situations when distortion producing rods are used for control of noise.

Chapter 2 Acoustic pressure field from the fan-flow disturbance interaction

2.1. Introduction

As the creation of acoustic modes through the introduction of the interacting flow modes produced by the wake generator is essential for control it is important to understand analytically the relationship between the flow disturbance and the resulting acoustic field. As mentioned in the introduction there are several analytical models available for this purpose. One such model that expresses this relationship is the Goldstein (1976) model for the infinite ducted case. This was extended by Pitelet (2000) to take into account the end reflections present in the finite duct case. An expression for the acoustic pressure field resulting from the interaction of the fan blades with the flow disturbances was derived by him. This derivation is reproduced here in its entirety for ease of understanding the subsequent extensions of this expression to the semi-infinite ducted case carried out as part of this thesis and also its usage to form a cost function for control. Section 2.2 concerns an overview of the steps involved in this derivation. Section 2.3 is devoted to the actual derivation with the extension carried out for the semi-infinite duct case (since the fan being considered here has an anechoic termination). The expression for the acoustic pressure in the semi-infinite duct case is then used to derive the overall sound power level in Chapter 3. The expression for the overall sound power level is necessary since it forms the cost function for the noise minimisation problem covered in the same chapter.

2.2. Overview of the derivation

The system being considered here is a fan located in a duct with an open inlet and an open exit. There is flow that is ingested into the duct by the rotating fan. The fan interacts with any flow disturbances that are present in the flow and the fluctuating forces on the fan blades cause the acoustic field to radiate and the propagation of this field in the duct has to satisfy the convected wave equation. The radiated acoustic pressure field is obtained by using the Green's function

technique which involves integrating the fluctuating force distribution on the fan blade surface with the Green's function of the convected wave equation. After considering the force response of the blades to the disturbances in the flow field the expression for the acoustic pressure field can finally be related to the disturbance flow field.

The above steps along with the subsequent sections that deal with them are summarised below:

1) The general form of the propagating acoustic field in the duct that satisfies the convected wave equation is covered in Section 2.3.1.
2) The Green's function solution of the above equation for a point monopole source is derived, assuming the presence of reflections from both ends of the duct in which the fan is located. This is covered in Section 2.3.2.
3) The solution in step 2 is extended to the case of the fan for the fluctuating force source on the moving blades. This is covered in Section 2.3.3.
4) The blade force response is expressed in terms of the disturbance flow field. This is covered in Section 2.3.4.
5) A final expression relating the acoustic pressure field to the disturbance flow field is arrived at. This is covered in Section 2.3.5.
6) The fan used for implementing the experiments is provided with an anechoic termination at the exit to reduce reflections from the downstream end. Section 2.3.6 gives the acoustic pressure expression for the fan with the anechoically terminated exit, i.e., the semi-infinite duct case.

   All assumptions involved are stated wherever necessary.

2.3. Derivation of the expression for the acoustic pressure field in a duct with the fan interacting with flow disturbances

2.3.1. Convected wave equation and the general form of its solution

Duct coordinate system:

The duct coordinates are represented by the following vectors, the sense of these is as shown in the schematic of the fan in Figure 2.1; **x** denotes the coordinate of the observer location

$$\mathbf{x} = \begin{cases} (x_1, x_2, x_3) & \text{(Cartesian)} \\ (r, \theta, z),\ z \equiv x_1 & \text{(Cylindrical),} \end{cases}$$

(2.3.1)

and **y** is for the source location in the duct.

$$\mathbf{y} = \begin{cases} (y_1, y_2, y_3) & \text{(Cartesian)} \\ (r_s, \theta_s, z_s),\ z_s \equiv y_1 & \text{(Cylindrical).} \end{cases}$$

(2.3.2)

The variable t is associated with the arrival of the sound wave at the observation point, and τ with the emission of the sound wave. The following sub/superscripts are used:

Axial: Downstream(z^+) and Upstream (z^-)

Rotational: Clockwise (θ^+) and Counter-clockwise (θ^-) as seen from the inlet.

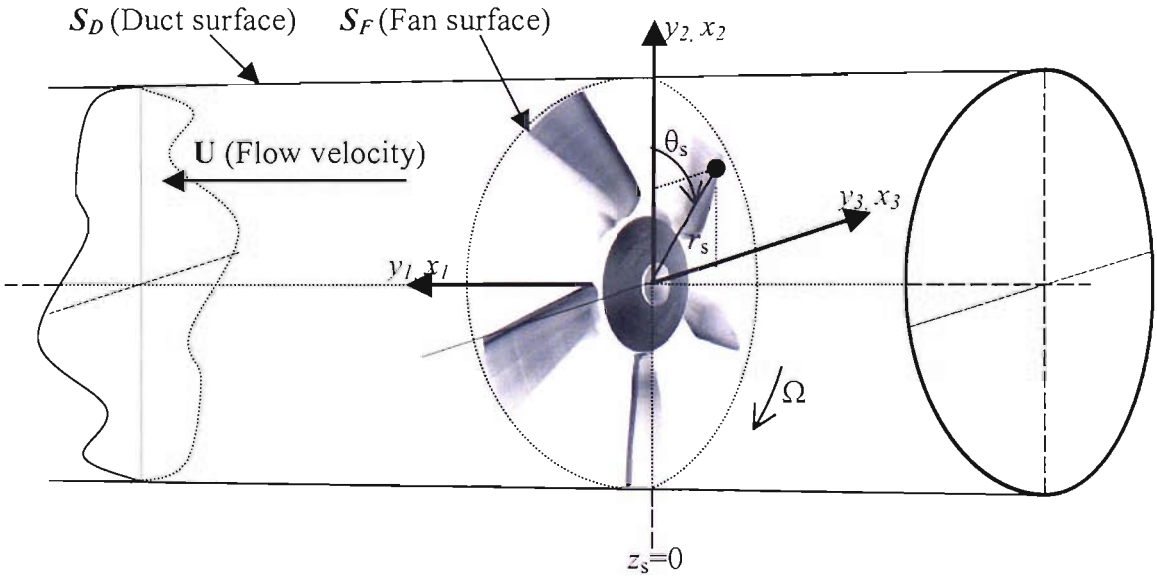

Figure 2.1 Co-ordinate system in the duct.

The acoustic pressure field $p(\mathbf{x},t)$ in a duct of cross sectional area S and radius a with a mean axial flow of $\mathbf{U} = U\,\hat{\boldsymbol{x}}_1$ has to satisfy the convected wave equation, where $\hat{\boldsymbol{x}}_1$ is the unit vector along the x_1- or y_1- direction:

$$\left[\nabla^2 - \frac{1}{c_0^2}\left(\frac{\partial}{\partial t} + \mathbf{U}.\nabla\right)^2\right] p(\mathbf{x},t) = 0\,,$$

(2.3.3)

where c_0 is the speed of sound and the differential operators are

$$\nabla^2 \equiv \frac{\partial^2}{\partial z^2} + \left(\frac{\partial^2}{\partial r^2} + \frac{1}{r}\frac{\partial}{\partial r} + \frac{1}{r^2}\frac{\partial^2}{\partial \theta^2}\right) \equiv \frac{\partial^2}{\partial z^2} + \nabla_\perp^2 \qquad \text{and}$$

$$\nabla \equiv \frac{\partial}{\partial z} + \left(\frac{\partial}{\partial r} + \frac{1}{r}\frac{\partial}{\partial r} + \frac{1}{r}\frac{\partial}{\partial \theta}\right) \equiv \frac{\partial}{\partial z} + \nabla_\perp\,.$$

(2.3.4)

Upon substitution of $p(\mathbf{x},t) = \mathrm{Re}\left\{p(\mathbf{x})\,e^{j\omega t}\right\}$ which is the acoustic pressure for a single frequency ω, Equation (2.3.3) reduces to the following equation (see Appendix 2.1).

$$\left[\nabla^2 + \left(\frac{\omega}{c_0}\right)^2\left(1 - \frac{j}{\omega}\,\mathbf{U}.\nabla\right)^2\right] p(\mathbf{x}) = 0\,.$$

(2.3.5)

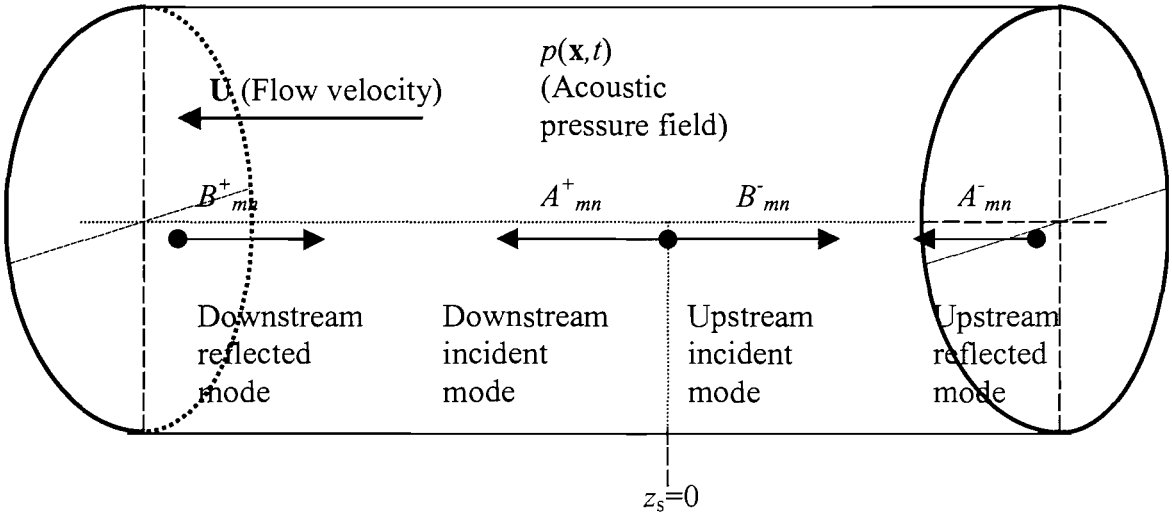

Figure 2.2 Reflected and Incident modes in a cylindrical duct with flow (illustrated for the plane wave mode).

The form of the solution of the above equation is

$$p(r,\theta,z)=\sum_{m=-\infty}^{+\infty}\sum_{n=1}^{+\infty}\left(A_{mn}^{\pm}(\omega)\,e^{-jk_{mn}^{z\pm}z}+B_{mn}^{\pm}(\omega)\,e^{-jk_{mn}^{z\pm}}\right)\Psi_{mn}(r,\theta),$$

(2.3.6)

where A_{mn} and B_{mn} are the unknown amplitudes of the forward (z^+ direction) and backward (z^- direction) propagating mode systems in the duct (illustrated in Figure 2.2 for the plane wave mode), $k_{mn}^{z\pm}$ is the axial wave number, ω is the frequency, $\Psi_{mn}(r,\theta)$ is the duct mode shape, m and n being the circumferential and radial orders of these modes. Upstream of the fan the incident and reflected mode amplitudes are B_{mn}^{-} and A_{mn}^{-}. On the downstream side they are A_{mn}^{+} and B_{mn}^{+}. The wave number $k_{mn}^{z\pm}$ is given by

$$k_{mn}^{z\pm}=\frac{\pm\sqrt{k_0^2-\beta^2\kappa_{mn}^2}-Mk_0}{\beta^2},$$

(2.3.7)

where k_0 is the free-space wave number and is defined as $k_0 = \frac{\omega}{c_0}$, M is the Mach number, β is $\sqrt{(1-M^2)}$, (the derivation of the above expression for $k_{mn}^{z\pm}$ is given in Appendix 2.2), κ_{mn} are the roots of the first derivatives of the Bessel shape function which satisfy the condition that the normal pressure gradient at the duct surface be zero,

$$\left.\frac{\partial p}{\partial r}\right|_{r=a} = 0 .$$

(2.3.8)

The expression for the wave number in Equation (2.3.7) also determines whether a mode is evanescent (cut-off) or propagating (cut-on). If the term $\sqrt{k_0^2 - \beta^2 \kappa_{mn}^2}$ in that equation is imaginary then the mode decays and it propagates otherwise. This is influenced by the Bessel shape function parameter κ_{mn} for any mode. Its value increases as the radial and azimuthal orders of a mode increase and hence the greater possibility of these modes being cut-off. The plane wave mode which has both these orders equal to zero is always cut-on as $\kappa_{mn} = 0$ for this case. The mode shape $\Psi_{mn}(r, \theta)$ is given by the following expression

$$\Psi_{mn}(r,\theta) = \frac{J_m(\kappa_{mn} r)}{N_{mn}} e^{-jm\theta} ,$$

(2.3.9)

where $J_m(\kappa_{mn} r)$ is the Bessel function representing the shape of the duct mode along the radius r, $e^{-jm\theta}$ is the Fourier function used for representing the shape of the duct mode in θ direction, and N_{mn} is a normalisation constant defined as

$$N_{mn}^2 = \int_S J_m^2(\kappa_{mn} r)\, dS ,$$

(2.3.10)

which is obtained from the following orthonormality relationship for $\Psi_{mn}(r, \theta)$.

$$\int_S \Psi_{mn}(r,\theta)\,\Psi_{ql}^{*}(r,\theta)\,\mathrm{d}S = \begin{cases} 0, & (m,n) \neq (q,l) \\ 1, & (m,n) = (q,l) \end{cases}$$

(2.3.11)

Since the solution in Equation (2.3.6) is for a single frequency excitation of the source, the solution of the convected wave equation can be obtained from the inverse Fourier transform of that equation and the resulting expression is

$$p(\mathbf{x},t) = \frac{1}{2\pi}\int_{-\infty}^{+\infty}\sum_{m=-\infty}^{+\infty}\sum_{n=1}^{+\infty}\left(A_{mn}^{\pm}(\omega)\,e^{-jk_{mn}^{z+}z} + B_{mn}^{\pm}(\omega)\,e^{-jk_{mn}^{z-}}\right)e^{j\omega t}\,\Psi_{mn}(r,\theta)\,\mathrm{d}\omega \ .$$

(2.3.12)

2.3.2. Green's function solution of the convected wave equation.

The unknown modal amplitudes A_{mn} and B_{mn} can be obtained for the finite ducted case by deriving the Green's function, $G(\mathbf{x}|\mathbf{y})$, which has to satisfy the following equation:

$$\left[\nabla^2 + k_0^{\,2}\left(1 - \frac{j}{\omega}\,\mathbf{U}.\nabla\right)^2\right]G(\mathbf{x}|\mathbf{y}) = -\delta(\mathbf{x}-\mathbf{y}),$$

(2.3.13)

where k_0 ($=\omega/c_0$) is the free space wave number and $G(\mathbf{x}|\mathbf{y})$ is the resulting acoustic pressure field at the observer location $\mathbf{x}$ due to a point monopole source $-\delta(\mathbf{x}-\mathbf{y})$ of unit strength located at $\mathbf{y}$ as illustrated in Figure 2.3.

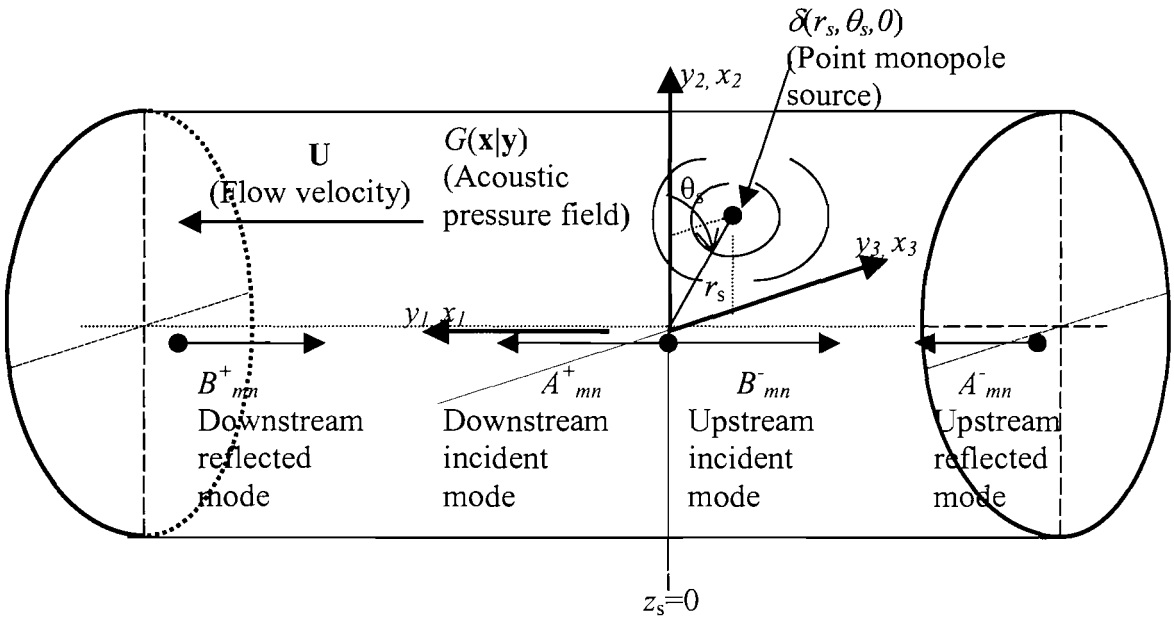

Figure 2.3 The point monopole source and the Green's function solution for the acoustic pressure field in a cylindrical duct with flow (illustrated for the plane wave mode).

The solution to this equation is also expressed in the same form as Equation (2.3.6) as a summation of modes:

$$G(\mathbf{x}|\mathbf{y}) = \sum_{m=-\infty}^{+\infty} \sum_{n=1}^{+\infty} b_{mn}(z)\,\Psi_{mn}(r,\theta),$$

(2.3.14)

where

$$b_{mn}(z) = A^{\pm}_{mn}\, e^{-jk^{\pm}_{mn} z} + B^{\pm}_{mn}\, e^{-jk^{\pm}_{mn} z}.$$

(2.3.15)

The term $b_{mn}(z)$ is the sum of the forward and backward propagating modal amplitudes A_{mn} and B_{mn}. To express it wholly in terms of one of these, the definition of the reflection coefficients $R^{\pm}_{mn}$ given by Morfey (1971) is useful.

These are defined as the ratios of reflected to the incident modal amplitudes, and + and - denote the downstream and upstream values of the reflection coefficients:

$$\begin{cases} R_{mn}^{+} = \dfrac{B_{mn}^{+}}{A_{mn}^{+}} = e^{2j\eta_{mn}^{0+}}, \\ \dfrac{1}{R_{mn}^{-}} = \dfrac{B_{mn}^{-}}{A_{mn}^{-}} = e^{2j\eta_{mn}^{0-}}, \end{cases}$$

(2.3.16)

where $\eta_{mn}^{0\pm}$ is the complex phase of the upstream and downstream reflection coefficients which takes into account the amplitude and phase of the reflection coefficients due to this term being complex valued.

The reflection coefficient at any axial location is a function of the axial coordinate z and is expressed as follows (see Appendix 2.3 for a derivation)

$$\eta_{mn}^{\pm}(z) = \eta_{mn}^{0\pm} + \frac{k_{mn}}{\beta^2} z, \text{ where } k_{mn} = \sqrt{k_0^2 - \beta^2 \kappa_{mn}^2}.$$

(2.3.17)

For the given point monopole source the expression for amplitude term $b_{mn}(z)$ turns out to be

$$b_{mn}^{\pm}(z) = \frac{\Psi_{mn}^{*}(r_s,\theta_s) e^{j(z-z_s)\frac{Mk_0}{\beta^2}}}{k_{mn}\left[\tan\left(\eta_{mn}^{+}(z_s)\right) - \tan\left(\eta_{mn}^{-}(z_s)\right)\right]} \frac{\cos\left(\eta_{mn}^{\pm}(z)\right)}{\cos\left(\eta_{mn}^{\pm}(z_s)\right)}.$$

(2.3.18)

The derivation of this expression is given in Appendix 2.4. Substituting this in the expression for the Green's function (2.3.14) we have

$$G^{\pm}(\mathbf{x}|\mathbf{y}) = \sum_{m=-\infty}^{m=+\infty} \sum_{n=1}^{+\infty} \frac{\Psi_{mn}(r,\theta)\Psi_{mn}^{*}(r_s,\theta_s)}{k_{mn}\left(\tan\left(\eta_{mn}^{+}(z_s)\right) - \tan\left(\eta_{mn}^{-}(z_s)\right)\right)} e^{j(z-z_s)\frac{Mk_0}{\beta^2}} \frac{\cos\left(\eta_{mn}^{\pm}(z)\right)}{\cos\left(\eta_{mn}^{\pm}(z_s)\right)}.$$

(2.3.19)

After performing some trigonometric simplification we have

$$G^{\pm}(\mathbf{x}|\mathbf{y}) = \sum_{m=-\infty}^{m=+\infty} \sum_{n=1}^{+\infty} \frac{\Psi_{mn}(r,\theta)\Psi^{*}_{mn}(r_s,\theta_s)}{k_{mn}\sin(\eta^{0+}_{mn} - \eta^{0-}_{mn})} e^{j(z-z_s)\frac{Mk_0}{\beta^2}} \cos(\eta^{\pm}_{mn}(z))\cos(\eta^{\mp}_{mn}(z_s)).$$

(2.3.20)

2.3.3. Solution of the convected wave equation with the fluctuating force source on the moving blades

We now move onto predicting the pressure field under the influence of a source like the one that the fan experiences by considering the Green's function that has been derived for the point source. The method adopted is the one that is due to Goldstein (1976) for the prediction of the noise generated by axial flow fans in infinite ducts. Here it is extended to the case of a finite duct.

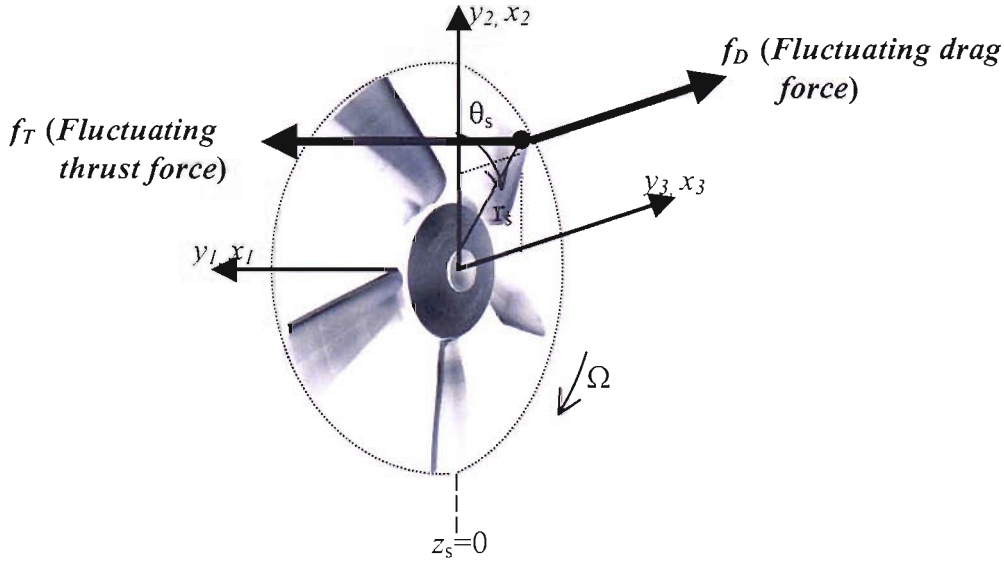

Figure 2.4 Fluctuating forces on the rotor blade surfaces S_f experienced through the interaction of incoming non-uniform flow.

In order to find out the radiated field from the fan source in the duct Goldstein begins his model with Ffowcs Williams and Hawkings (FW-H) equations and neglects the effects of volume quadrupole sources, fluctuating shear

stresses on the duct wall surface S_D and also the volume displacement effect due to the thickness of the blades and considers only the contribution arising from the fluctuating forces exerted on the flow by the rotor blade surfaces S_f shown in Figure 2.4 which act like dipole sources. The volume displacement effect due to thickness of blades causes the production of acoustic modes of fan blade order. For the 9-bladed fan under consideration in this thesis these orders are high enough to be cut-off as seen from the expression in Equation (2.3.7) in Chapter 2. The relative unimportance of volume quadrupole sources is shown by Goldstein in his comparison between the exact and acoustic analogy approaches. Whilst the exact approach uses the linearised continuity and momentum equations to predict the sound pressure field, the Lighthill acoustic analogy approach which forms the basis for the FW-H equations treats certain terms associated with the propagation of the sound as source terms.

The expression for the acoustic pressure $p(\mathbf{x})$ in the presence of the fluctuating forces f on the moving blade surfaces of the fan $S_f(\tau)$ is as follows. The Green's function derived above is used here. The time integral is performed along the time coordinate (τ) during which the source is excited and the surface integral is in the space ($\mathbf{y}$) where the source is located.

$$p(\mathbf{x},t) = \int_{-T}^{T} \int_{S_F(\tau)} \frac{\partial G(\mathbf{x},t|\mathbf{y},\tau)}{\partial y_i} f_i \, \mathrm{d}S(\mathbf{y}) \mathrm{d}\tau \,,$$

(2.3.21)

where $[-T,T]$ is a large but finite time interval, and f_i is the drag or thrust component of the force per unit area produced by blades acting on the fluid. Since the Green's function $G(\mathbf{x}|\mathbf{y})$ derived above has only spatial dependence the corresponding time dependent version $G(\mathbf{x},t|\mathbf{y},\tau)$ is obtained by inverse Fourier transform of $G^{\pm}(\mathbf{x}|\mathbf{y})$ with respect to $(t-\tau)$.

$$G^{\pm}(\mathbf{x},t|\mathbf{y},\tau) = \frac{1}{2\pi} \int_{-\infty}^{+\infty} e^{j\omega(t-\tau)} G^{\pm}(\mathbf{x}|\mathbf{y}) \mathrm{d}\omega \,.$$

(2.3.22)

The force $\mathbf{f}(\tau)$, exerted by the blades on the flow can be resolved into an axial thrust component f_T and a circumferential drag component f_D

$$f_j \frac{\partial}{\partial y_j} = \frac{f_D}{r_s} \frac{\partial}{\partial \theta_s} + f_T \frac{\partial}{\partial z_s}.$$

(2.3.23)

The axial and the circumferential derivatives of the Green's function $G_{mn}^{\pm}(\mathbf{x}|\mathbf{y})$ required in the pressure integral are as follows:

$$\begin{cases} \dfrac{\partial G^{\pm}(\mathbf{x}|\mathbf{y})}{\partial \theta_s} = \displaystyle\sum_{m=-\infty}^{\infty} \sum_{n=1}^{\infty} jm\, G_{mn}^{\pm}(\mathbf{x}|\mathbf{y}), \\ \dfrac{\partial G^{\pm}(\mathbf{x}|\mathbf{y})}{\partial z_s} = \displaystyle\sum_{m=-\infty}^{\infty} \sum_{n=1}^{\infty} j\gamma_{mn}^{\pm}(z_s) G_{mn}^{\pm}(\mathbf{x}|\mathbf{y}). \end{cases}$$

(2.3.24)

where

$$\gamma_{mn}^{\pm}(z_s) = j\frac{k_{mn}}{\beta^2} \tan\left(\eta_{mn}^{\mp}(z_s)\right) - \frac{Mk_0}{\beta^2}.$$

(2.3.25)

The derivation of this is given in Appendix 2.5. The integrand appearing in Equation (2.3.21) which includes the time derivative of the time dependent Green's function $G(x,t|y,\tau)$ is thus

$$\frac{\partial G(\mathbf{x},t|\mathbf{y},\tau)}{\partial y_i} f_i = \frac{j}{2\pi} \sum_{m=-\infty}^{\infty} \sum_{n=1}^{\infty} \int_{-\infty}^{+\infty} e^{j\omega(t-\tau)} \left(m\frac{f_D}{r_s} + \gamma_{mn}^{\pm}(z_s) f_T \right) G_{mn}^{\pm}(\mathbf{x}|\mathbf{y}) \mathrm{d}\omega.$$

(2.3.26)

Substituting this in Equation (2.3.21) the pressure integral becomes

$$p(\mathbf{x},t)=\frac{j}{2\pi}\sum_{m=-\infty}^{\infty}\sum_{n=1}^{\infty}\frac{J_m(\kappa_{mn}r)e^{-jm\theta}}{N_{mn}^2}\int_{-\infty}^{+\infty}\frac{e^{j\left(\frac{Mk_0}{\beta^2}z+\omega t\right)}}{k_{mn}\sin\left(\eta_{mn}^{+0}-\eta_{mn}^{-0}\right)}\cos\left(\eta_{mn}^{\pm}(z)\right)$$
$$\times\int_{-T}^{T}\iint_{S_F(\tau)}J_m(\kappa_{mn}r_s)e^{jm\theta_s}\cos\left(\eta_{mn}^{\mp}(z_s)\right)e^{-j\left(\frac{Mk_0}{\beta^2}z_s+\omega\tau\right)}$$
$$\times\left[\frac{m}{r_s}f_D+\gamma_{mn}^{\pm}(z_s)f_T\right]\ \mathrm{d}S(\mathbf{y})\mathrm{d}\tau\,\mathrm{d}\omega.$$

(2.3.27)

2.3.3.1. Transformation of coordinates of the moving surface

Note that the forces are fluctuating over the moving surface $S_f(\tau)$ and thus have a dependence on $(\mathbf{y},\tau)$. Since the surface is a moving surface its motion can be described using the transformation for a reference frame fixed to the rotor and rotating with it, the coordinates of any point on this surface being described by $\mathbf{y}'=(r_s,\theta_s',z_s)$, where $\theta_s=\theta_s'+\Omega\tau$. This removes the dependence of the surface integral on time τ, to give

$$p(\mathbf{x},t)=\frac{j}{2\pi}\sum_{m=-\infty}^{+\infty}\sum_{n=1}^{+\infty}\frac{J_m(\kappa_{mn}r)e^{-jm\theta}}{N_{mn}^2}\int_{-\infty}^{+\infty}\frac{e^{j\left(\frac{Mk_0}{\beta^2}z+\omega t\right)}}{k_{mn}\sin\left(\eta_{mn}^{+0}-\eta_{mn}^{-0}\right)}\cos\left(\eta_{mn}^{\pm}(z)\right)$$
$$\times\int_{S_F}J_m(\kappa_{mn}r_s)\cos\left(\eta_{mn}^{\mp}(z_s)\right)e^{-j\left(\frac{Mk_0}{\beta^2}z_s-m\theta_s'\right)}$$
$$\times\int_{-T}^{T}e^{-j(\omega-m\Omega)\tau}\left[\frac{m}{r_s}f_D+\gamma_{mn}^{\pm}(z_s)f_T\right]\ \mathrm{d}\tau\,\mathrm{d}S(\mathbf{y}')\,\mathrm{d}\omega.$$

(2.3.28)

2.3.3.2. Projection of source surface (fan blades) onto the fan rotational plane

The surface integral in Equation (2.3.28) is a sum of the integrals on the front and back surfaces of the blades. Goldstein (1976, p. 194) describes a transformation of the surface integral over the front and back surfaces of the blades to an integral over the projected area A of the blades in the rotational plane of the fan. The difference in retarded-time, i.e., the time taken for the sound wave to travel from

the point of emission to the point of observation, between the front and back surfaces of the blades is ignored which is justifiable if the blades are thin. This causes the replacement of z_s in the above equation with the variable $z_s^c(r_s,\theta_s')$, which is the axial co-ordinate of the blade chord measured in the rotating reference frame.

$$p(\mathbf{x},t)=\frac{j}{2\pi}\sum_{m=-\infty}^{+\infty}\sum_{n=1}^{+\infty}\frac{J_m(\kappa_{mn}r)e^{-jm\theta}}{N_{mn}^2}\int_{-\infty}^{+\infty}\frac{e^{j\left(\frac{Mk_0}{\beta^2}z+\omega t\right)}}{k_{mn}\sin\left(\eta_{mn}^{+0}-\eta_{mn}^{-0}\right)}\cos\left(\eta_{mn}^{\pm}(z)\right)$$
$$\times\int_A J_m(\kappa_{mn}r_s)\cos\left(\eta_{mn}^{\mp}(z_s^c)\right)e^{-j\left(\frac{Mk_0}{\beta^2}z_s^c-m\theta_s'\right)}$$
$$\times\int_{-T}^{T}\left[\frac{m}{r_s}\widetilde{f}_D+\gamma_{mn}^{\pm}(z_s^c)\widetilde{f}_T\right]e^{-j(\omega-m\Omega)\tau}\,\mathrm{d}\tau\;r_s\mathrm{d}r_s\mathrm{d}\theta_s'\,\mathrm{d}\omega.$$

(2.3.29)

The force terms averaged over the two sides of the blades are denoted as $\widetilde{f}_D$ and $\widetilde{f}_T$ (with tilde) in Goldstein (1976, p. 195).

2.3.3.3. Periodic blade forces

So far no assumption has been made for the type of fluctuation of the force exerted by the blades on the flow in the above equation. Steady non-uniform inlet velocity profiles present in the flow in the intake of the fan interact with the blades and produce periodic forces which result in the generation of pure tones. These non-uniformities can be generated by obstructions to inflow or by atmospheric disturbances ingested into the intake. The periodic forces $\widetilde{f}_\alpha(\tau)$ generated due to these can be represented in the following Fourier series summation of harmonics F_p^α at p^{th} multiples of the shaft rotating frequency Ω, since each blade experiences every p^{th} cycle of the distortion during a revolution of the fan.

$$\widetilde{f}_\alpha(\tau)=\sum_{p=-\infty}^{+\infty}F_p^\alpha e^{jp\Omega\tau}\qquad\text{for }\alpha=T,D,$$

(2.3.30)

where

$$F_p^{\alpha} = \frac{\Omega}{2\pi} \int_0^{\frac{2\pi}{\Omega}} \widetilde{f}_{\alpha}(\tau)\, e^{-jp\Omega\tau}\, d\tau \qquad \text{for } \alpha = T, D.$$

(2.3.31)

Making the substitution for $\widetilde{f}_{\alpha}(\tau)$ in Equation (2.3.29) we have

$$p(\mathbf{x},t) = \frac{j}{2\pi} \sum_{p=-\infty}^{\infty} \sum_{m=-\infty}^{\infty} \sum_{n=1}^{\infty} \frac{J_m(\kappa_{mn} r) e^{-jm\theta}}{N_{mn}^2} \int_{-\infty}^{+\infty} \frac{e^{j\left(\frac{Mk_0}{\beta^2} z + \omega t\right)}}{k_{mn} \sin\left(\eta_{mn}^{+0} - \eta_{mn}^{-0}\right)} \cos\left(\eta_{mn}^{\pm}(z)\right)$$

$$\times \int_A J_m(\kappa_{mn} r_s) \cos\left(\eta_{mn}^{\mp}\left(z_s^c\right)\right) e^{-j\left(\frac{Mk_0}{\beta^2} z_s^c - m\theta_s'\right)}$$

$$\times \left(\frac{m}{r_s} F_p^D + \gamma_{mn}^{\pm}\left(z_s^c\right) F_p^T \right) \int_{-T}^{T} e^{-j(\omega - (m+p)\Omega)\tau}\, \mathrm{d}\tau\, r_s \mathrm{d}r_s \mathrm{d}\theta_s'\, \mathrm{d}\omega,$$

(2.3.32)

and then substituting for $s = m + p$, and realising that the integral in τ can be expressed in terms of the identity

$$\lim_{T\to\infty} \int_{-T}^{T} e^{-j(\omega - s\Omega)\tau} \mathrm{d}\tau = 2\pi\delta(\omega - s\Omega),$$

(2.3.33)

we have

$$p(\mathbf{x},t) = j \sum_{p=-\infty}^{\infty} \sum_{m=-\infty}^{\infty} \sum_{n=1}^{\infty} \frac{J_m(\kappa_{mn} r) e^{-jm\theta}}{N_{mn}^2} \int_{-\infty}^{+\infty} \frac{e^{j\left(\frac{Mk_0}{\beta^2} z + \omega t\right)}}{k_{mn} \sin\left(\eta_{mn}^{+0} - \eta_{mn}^{-0}\right)} \cos\left(\eta_{mn}^{\pm}(z)\right)$$

$$\times \int_A J_m(\kappa_{mn} r_s) \cos\left(\eta_{mn}^{\mp}\left(z_s^c\right)\right) e^{-j\left(\frac{Mk_0}{\beta^2} z_s^c - m\theta_s'\right)}$$

$$\times \left(\frac{m}{r_s} F_p^D + \gamma_{mn}^{\pm}\left(z_s^c\right) F_p^T \right) \delta(\omega - s\Omega) \quad r_s \mathrm{d}r_s \mathrm{d}\theta_s'\, \mathrm{d}\omega.$$

(2.3.34)

Evaluating the integral in the frequency domain ω, using the sifting property of the delta function, which causes the replacement of ω by $s\Omega$, we have

$$p(\mathbf{x},t) = j\sum_{p=-\infty}^{\infty}\sum_{m=-\infty}^{\infty}\sum_{n=1}^{\infty}\frac{J_m(\kappa_{mn}r)e^{-jm\theta}}{N_{mn}^2}\frac{e^{j\left(\frac{Ms\Omega}{c_0\beta^2}z+s\Omega t\right)}}{k_{mn,s}\sin\left(\eta_{mn,s}^{0+}-\eta_{mn,s}^{0-}\right)}\cos\left(\eta_{mn,s}^{\pm}(z)\right)$$

$$\times\int_A J_m(\kappa_{mn}r_s)\cos\left(\eta_{mn,s}^{\mp}\left(z_s^c\right)\right)e^{-j\left(\frac{Ms\Omega}{c_0\beta^2}z_s^c-m\theta_s'\right)}$$

$$\times\left(\frac{m}{r_s}F_p^D+\gamma_{mn,s}^{\pm}\left(z_s^c\right)F_p^T\right)\quad r_s\mathrm{d}r_s\mathrm{d}\theta_s'.$$

(2.3.35)

Denoting the coupling coefficients $\widetilde{D}_{mn,p}^{\pm}$ and $\widetilde{T}_{mn,p}^{\pm}$ as

$$\widetilde{T}_{mn,p}^{\pm} \equiv \int_A J_m(\kappa_{mn}r_s)\cos\left(\eta_{mn,s}^{\mp}\left(z_s^c\right)\right)e^{-j\left(\frac{Ms\Omega}{c_0\beta^2}z_s^c-m\theta_s'\right)}F_p^T\,\gamma_{mn,s}^{\pm}\left(z_s^c\right)r_s\ \mathrm{d}r_s\ \mathrm{d}\theta_s',$$

$$\widetilde{D}_{mn,p}^{\pm} \equiv \int_A J_m(\kappa_{mn}r_s)\cos\left(\eta_{mn,s}^{\mp}\left(z_s^c\right)\right)e^{-j\left(\frac{Ms\Omega}{c_0\beta^2}z_s^c-m\theta_s'\right)}F_p^D\ \mathrm{d}r_s\ \mathrm{d}\theta_s',$$

(2.3.36)

we have

$$p(\mathbf{x},t) = j\sum_{p=-\infty}^{\infty}\sum_{m=-\infty}^{\infty}\sum_{n=1}^{\infty}\frac{J_m(\kappa_{mn}r)e^{-jm\theta}}{N_{mn}^2\sin\left(\eta_{mn,s}^{0+}-\eta_{mn,s}^{0-}\right)}\frac{e^{j\left(\frac{Ms\Omega}{c_0\beta^2}z+s\Omega t\right)}}{k_{mn,s}}\cos\left(\eta_{mn,s}^{\pm}(z)\right)$$
$$\times\left(m\widetilde{D}_{mn,p}^{\pm}+\widetilde{T}_{mn,p}^{\pm}\right).$$

(2.3.37)

The above equation can be realised as a summation over harmonics of shaft passing order $s\Omega$ in the frequency domain and thus expressed as follows

$$p(\mathbf{x},t) = \sum_{s=-\infty}^{\infty}p_s(\mathbf{x})\,e^{js\Omega t},$$

(2.3.38)

where the acoustic pressure for a given harmonic order s is

$$p_s(\mathbf{x}) = j\sum_{p=-\infty}^{\infty}\sum_{n=1}^{+\infty}\frac{J_m(\kappa_{mn}r)e^{j\left(\frac{Ms\Omega}{c_0\beta^2}z-m\theta\right)}}{N_{mn}^2\sin\left(\eta_{mn,s}^{0+}-\eta_{mn,s}^{0-}\right)k_{mn,s}}\cos\left(\eta_{mn,s}^{\pm}(z)\right)\left(m\widetilde{D}_{mn,p}^{\pm}+\widetilde{T}_{mn,p}^{\pm}\right).$$

(2.3.39)

In the above equation the subscript m, i.e., the circumferential order of the mode at each discrete frequency $s\Omega$ is now evaluated using the relationship $m = s - p$.

2.3.3.4. Equispaced identical fan blades

The forces $\widetilde{f}_\alpha(\tau)$ in Equation (2.3.30) are the net drag and thrust forces per unit area on the fan blade surface. Considering that the force experienced by the first blade (which we shall identify as $s = 0$) at the reference frame location θ_s' and time τ as $f_\alpha^0(r_s,\theta_s',\tau)$, we see that this is the same force that is experienced by the s^{th} blade that is now displaced by $2\pi(s-1)/B$ from the first blade at a prior time $\tau - 2\pi(s-1)/B\Omega$. We thus see that the force on this latter blade at time τ is $f_\alpha^0(r_s,\theta_s' - 2\pi(s-1)/B,\tau + 2\pi(s-1)/B\Omega)$, due to the blades being equally spaced and identical. Expressing the net force $\widetilde{f}_\alpha(\tau)$ in terms of these individual blade forces we have

$$\widetilde{f}_\alpha(\tau) = \sum_{s=1}^{B} f_\alpha^0(r_s,\theta_s' - 2\pi(s-1)/B,\tau + 2\pi(s-1)/B\Omega) \qquad \text{for } \alpha = T, D.$$

(2.3.40)

Substituting this in Equation (2.3.30) we get the p^{th} harmonic of the net periodic force as the following summation

$$F_p^\alpha = \sum_{s=1}^{B} e^{j2\pi p(s-1)/B} F_{\alpha,p}^0(r_s,\theta_s' - 2\pi(s-1)/B) \qquad \text{for } \alpha = T, D,$$

(2.3.41)

where

$$F^0_{\alpha,p} = \frac{\Omega}{2\pi}\int_0^{\frac{2\pi}{\Omega}} f^0_\alpha(r_s,\theta'_s,\tau)e^{-jp\Omega\tau}\,d\tau \qquad \text{for } \alpha = T, D.$$

(2.3.42)

Equation (2.3.41) expresses the net force F^α_p on the rotor related to that on the single (or the first) blade $F^0_{\alpha,p}$.

Substituting the expression (2.3.41) for the thrust component in Equation (2.3.36) we have

$$\begin{aligned}\widetilde{T}^{\pm}_{mn,p} &\equiv \int_A J_m(\kappa_{mn}r_s)\cos\left(\eta^{\mp}_{mn,s}(z^c_s)\right)e^{-j\left(\frac{Ms\Omega}{c_0\beta^2}z^c_s - m\theta'_s\right)}F^T_p\,\gamma^{\pm}_{mn,s}(z^c_s)\,r_s\,\mathrm{d}r_s\,\mathrm{d}\theta'_s \\ &\equiv B\int_{A_0} J_m(\kappa_{mn}r_s)\cos\left(\eta^{\mp}_{mn,s}(z^c_s)\right)e^{-j\left(\frac{Ms\Omega}{c_0\beta^2}z^c_s - m\theta'_s\right)}F^0_{\alpha,p}(r_s,\theta'_s)\,\gamma^{\pm}_{mn,s}(z^c_s)\,r_s\,\mathrm{d}r_s\,\mathrm{d}\theta'_s \\ &\equiv \begin{cases} BT^{\pm}_{mn,p} & \text{for } (m+n) = sB \\ 0 & \text{for } (m+n) \neq sB, \end{cases}\end{aligned}$$

(2.3.43)

where T is the thrust on the single blade. The derivation of the above expression is given in detail in Appendix 2.6. The above result shows that only the harmonics of the BPF, i.e., $B\Omega$ are non-zero. At these harmonics the net thrust or drag forces are obtained by multiplying the same forces on a single blade with a factor equal to the number of blades. Therefore Equation (2.3.38) can be written as

$$p(\mathbf{x},t) = \sum_{sB=-\infty}^{\infty} p_{sB}(\mathbf{x})\,e^{jsB\Omega t},$$

(2.3.44)

where

$$p_{sB}(\mathbf{x}) = jB\sum_{p=-\infty}^{\infty}\sum_{n=1}^{+\infty}\frac{J_m(\kappa_{mn}r)e^{j\left(\frac{MsB\Omega}{c_0\beta^2}z-m\theta\right)}}{N_{mn}^2\sin\left(\eta_{mn,sB}^{0+}-\eta_{mn,sB}^{0-}\right)k_{mn,sB}}\cos\left(\eta_{mn,sB}^{\pm}(z)\right)\left(mD_{mn,p}^{\pm}+T_{mn,p}^{\pm}\right)$$

,

(2.3.45)

where $m = sB - p$ and $k_{mn,sB} = \sqrt{\frac{\Omega^2 s^2 B^2}{c_0^2} - \beta^2\kappa_{mn}^2}$ is evaluated at the discrete frequency $\omega = \Omega sB$. $\widetilde{D}_{mn,p}^{\pm}$ and $\widetilde{T}_{mn,p}^{\pm}$ are replaced by coupling coefficients for single blade $D_{mn,p}^{\pm}$ and $T_{mn,p}^{\pm}$, and the corresponding harmonics for forces F_p^T and F_p^D are replaced by the forces $F_{0,p}^T$ and $F_{0,p}^D$ acting on one blade (Goldstein 1976 p. 197)

$$T_{mn,p}^{\pm} \equiv \int_{A_0} J_m(\kappa_{mn}r_s)\cos\left(\eta_{mn,sB}^{\mp}(z_s^c)\right)e^{-j\left(\frac{MsB\Omega}{c_0\beta^2}z_s^c-m\theta_s'\right)}F_{0,p}^T\,\gamma_{mn,sB}^{\pm}(z_s^c)\,r_s\,\mathrm{d}r_s\,\mathrm{d}\theta_s'$$

$$D_{mn,p}^{\pm} \equiv \int_{A_0} J_m(\kappa_{mn}r_s)\cos\left(\eta_{mn,sB}^{\mp}(z_s^c)\right)e^{-j\left(\frac{MsB\Omega}{c_0\beta^2}z_s^c-m\theta_s'\right)}F_{0,p}^D\,\mathrm{d}r_s\,\mathrm{d}\theta_s'.$$

(2.3.46)

2.3.4. Blade force response

Expressions for drag and thrust forces resulting from the non-uniform component $w(r_s,\theta_s)$ of the inlet flow velocity are derived by Goldstein (1976, p.201). Forces acting on the single blade $F_{0,p}^{\alpha}$ are given by

$$F_{0,p}^T = -\frac{\delta(\theta_s')}{r_s}\pi\, c\,\rho_0\,U_r\,w_p(r_s)\,S_c(\sigma_p,M_r)\sin\chi\sin\mu,$$

$$F_{0,p}^D = -\frac{\delta(\theta_s')}{r_s}\pi\, c\,\rho_0\,U_r\,w_p(r_s)\,S_c(\sigma_p,M_r)\cos\chi\sin\mu,$$

(2.3.47)

where c is the chord length, χ is the blade stagger angle, μ is the angle of attack with which the fluid encounters the blade, U_r is the relative velocity, ρ_0 is the density of the fluid. The above terms are illustrated in Figure 2.5 which is reproduced from Goldstein (1976, p.176).

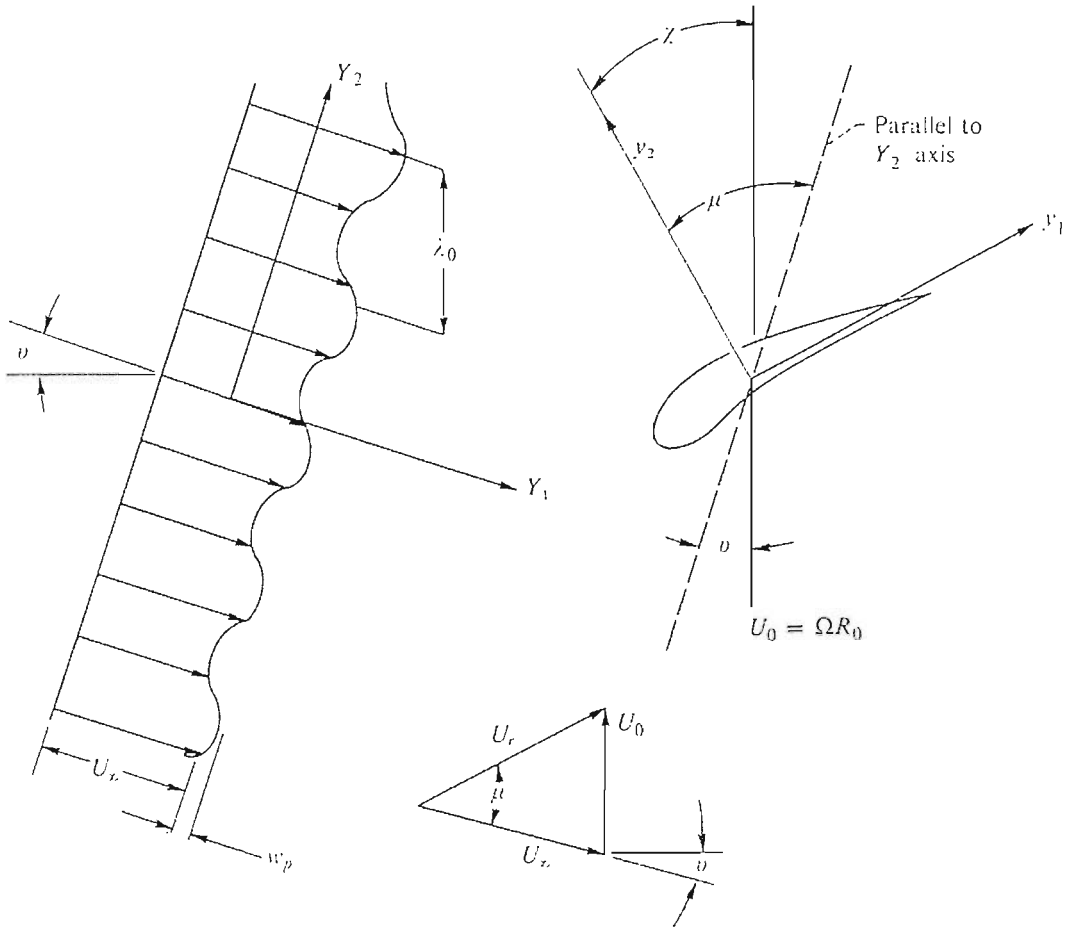

Figure 2.5 Two dimensional model of the fan blade-flow interaction and the associated terms in Equation (2.3.47).

The function S_c is the compressible blade force response function which is also called the Sears function (Goldstein 1976, p.139). The parameters on which this function is shown to depend are σ_p, which is the reduced frequency of the flow gust that the blades receive and, M_r the flow Mach number relative to the blade. The expressions for S_c, σ_p and M_r are given in Appendix 2.7. The forces are assumed to act along the azimuthal centrelines of the blades at θ_s'. The term

$w_p(r_s)$ is the p^{th} Fourier coefficient of the inlet flow velocity distortion $w(r_s,\theta_s)$ and is given by

$$w_p(r_s)=\frac{1}{2\pi}\int_0^{2\pi} e^{-jp\theta_s}\, w(r_s,\theta_s)\,\mathrm{d}\theta_s .$$

(2.3.48)

Substituting (2.3.47) and (2.3.48) in (2.3.46) we have the expression for $D^{\pm}_{mn,p}$ as

$$D^{\pm}_{mn,p} \equiv -\int_{A_0} J_m(\kappa_{mn} r_s)\cos\left(\eta^{\mp}_{mn,sB}(z_s^c)\right) e^{-j\left(\frac{MsB\Omega}{c_0\beta^2} z_s^c - m\theta'_s\right)} \frac{\delta(\theta'_s)}{r_s}\pi\, c\rho_0 U_r$$
$$\times \frac{1}{2\pi}\int_0^{2\pi} e^{-jp\theta_s}\, w(r_s,\theta_s)\,\mathrm{d}\theta_s\; S_c(\sigma_p, M_r)\cos\chi\sin\mu\;\mathrm{d}r_s\;\mathrm{d}\theta'_s .$$

(2.3.49)

The variations of chord length c, stagger angle χ, angle of attack μ and relative velocity U_r along the span are neglected. Taking $\theta'_s = 0$ as the location for the blade identified by $s = 0$, we have

$$D^{\pm}_{mn,p} \equiv -\frac{c}{2}\rho_0 U_r \cos\chi\sin\mu\; S_c(\sigma_p, M_r)\int_{A_0} J_m(\kappa_{mn} r_s)\cos\left(\eta^{\mp}_{mn,sB}(z_s^c)\right)$$
$$\times e^{-j\left(\frac{MsB\Omega}{c_0\beta^2} z_s^c - m\theta'_s\right)} \frac{\delta(\theta'_s)}{r_s}\int_0^{2\pi} e^{-jp\theta_s}\, w(r_s,\theta_s)\,\mathrm{d}\theta_s\;\mathrm{d}r_s\;\mathrm{d}\theta'_s .$$

(2.3.50)

Since an assumption is made that the forces act along the centrelines of the blades, we have the axial coordinate of the chord for the first blade $(\theta'_s = 0)$ as $z_s^c = r_s\theta'_s\cot\chi = 0$. Hence the expression for $D^{\pm}_{mn,p}$ simplifies to

$$D^{\pm}_{mn,p} \equiv -\frac{c}{2}\rho_0 U_r \cos\chi\sin\mu\; S_c(\sigma_p, M_r)$$
$$\times \int_0^a J_m(\kappa_{mn} r_s)\cos\left(\eta^{0\mp}_{mn}\right)\frac{1}{r_s}\int_0^{2\pi} e^{-jp\theta_s}\, w(r_s,\theta_s)\,\mathrm{d}\theta_s\;\mathrm{d}r_s .$$

(2.3.51)

The integral over the duct cross section is expressed as $W^{D}_{mn,p}$ given by

$$W^{D}_{mn,p} = \int_{o}^{a}\int_{0}^{2\pi} e^{-jp\theta_s} J_m(\kappa_{mn} r_s) w(r_s,\theta_s) \frac{1}{r_s} \mathrm{d}\theta_s \, \mathrm{d}r_s \, ,$$

(2.3.52)

and hence

$$D^{\pm}_{mn,p} \equiv -\frac{c}{2} \rho_0 U_r \cos\chi \sin\mu \, S_c(\sigma_p, M_r) \cos(\eta^{0\mp}_{mn}) \, W^{D}_{mn,p} \, .$$

(2.3.53)

Similarly $T^{\pm}_{mn,p}$ is given by

$$T^{\pm}_{mn,p} \equiv -\frac{c}{2} \rho_0 U_r \sin\chi \sin\mu \; S_c(\sigma_p, M_r) \int_{A_0} J_m(\kappa_{mn} r_s) \cos(\eta^{\mp}_{mn,sB}(z^c_s)) e^{-j\left(\frac{MsB\Omega}{c_0\beta^2} z^c_s - m\theta'_s\right)}$$

$$\times \gamma^{\pm}_{mn,sB}(z^c_s) \frac{\delta(\theta'_s)}{r_s} \int_{0}^{2\pi} e^{-jp\theta_s} w(r_s,\theta_s) \, \mathrm{d}\theta_s \, r_s \, \mathrm{d}r_s \, \mathrm{d}\theta'_s .$$

(2.3.54)

Evaluating $\gamma^{\pm}_{mn,sB}(z^c_s)$ at $\theta'_s = 0$, which is $\gamma^{\pm}_{mn} = j\frac{k_{mn}}{\beta^2}\tan(\eta^{\mp 0}_{mn}) - \frac{MsB\Omega}{c_0\beta^2}$, we have

$$T^{\pm}_{mn,p} \equiv -\frac{c}{2} \rho_0 U_r \sin\chi \sin\mu \, S_c(\sigma_p, M_r) \int_{0}^{a}\int_{0}^{2\pi} e^{-jp\theta_s} J_m(\kappa_{mn} r_s) \cos(\eta^{0\mp}_{mn})$$

$$\times \gamma^{\pm}_{mn,sB} \, w(r_s,\theta_s) \, \mathrm{d}\theta_s \, \mathrm{d}r_s ,$$

(2.3.55)

and the surface integral in the thrust expression is given by

$$W^{T}_{mn,p} = \int_{o}^{a}\int_{0}^{2\pi} e^{-jp\theta_s} J_m(\kappa_{mn} r_s) w(r_s, \theta_s)\, \mathrm{d}\theta_s\, \mathrm{d}r_s$$

(2.3.56)

Hence

$$T^{\pm}_{mn,p} \equiv -\frac{c}{2}\rho_0 U_r \sin\chi\ \sin\mu\, S_c(\sigma_p, M_r) \cos(\eta^{0\mp}_{mn}) \gamma^{\pm}_{mn,sB}\, W^{T}_{mn,p}$$

(2.3.57)

Goldstein (1976, p. 202) defines the thrust and drag coupling coefficients as follows:

$$\hat{T}_{mn,p} \equiv -\frac{c}{2}\rho_0 U_r \sin\chi\ \sin\mu\, S_c(\sigma_p, M_r) W^{T}_{mn,p},$$
$$\hat{D}_{mn,p} \equiv -\frac{c}{2}\rho_0 U_r \cos\chi\ \sin\mu\, S_c(\sigma_p, M_r) W^{D}_{mn,p}.$$

(2.3.58)

The coupling coefficients derived here, i.e., $T^{\pm}_{mn,p}$ and $D^{\pm}_{mn,p}$ can be related to the above using the following expressions.

$$T^{\pm}_{mn,p} = \hat{T}_{mn,p} \cos(\eta^{0\mp}_{mn}) \gamma^{\pm}_{mn,sB}$$
$$D^{\pm}_{mn,p} = \hat{D}_{mn,p} \cos(\eta^{0\mp}_{mn})$$

(2.3.59)

2.3.5. Final expression for the acoustic pressure in terms of the flow disturbance

Finally the expression for the acoustic pressure can be given in terms of $\hat{T}_{mn,p}$ and $\hat{D}_{mn,p}$ as follows:

$$p_{sB}(\mathbf{x}) = jB\sum_{p=-\infty}^{\infty}\sum_{n=1}^{\infty}\frac{J_m(\kappa_{mn}r)e^{j\left(\frac{MsB\Omega}{c_0\beta^2}z-m\theta\right)}}{N_{mn}^2\ k_{mn,sB}} \times\cos\left(\eta_{mn,sB}^{\pm}(z)\right)\frac{\cos\left(\eta_{mn}^{0\mp}\right)}{\sin\left(\eta_{mn}^{0+}-\eta_{mn}^{0-}\right)}\left(m\hat{D}_{mn,p}+\gamma_{mn,sB}^{\pm}\hat{T}_{mn,p}\right),$$

(2.3.60)

where $\gamma_{mn}^{\pm} = j\frac{k_{mn}}{\beta^2}\tan\left(\eta_{mn}^{\mp 0}\right)-\frac{MsB\Omega}{c_0\beta^2}$ and $m = sB - p$. Since finiteness of the duct was assumed it is possible to revert back to the infinite duct case considered in Goldstein by setting the reflection coefficients equal to zero, which corresponds to $\eta_{mn}^{0+}\to+j\infty$ and $\eta_{mn}^{0-}\to-j\infty$.

2.3.6. Expression for the acoustic pressure in the semi-infinite duct case

Since the fan system considered for implementation has an anechoic termination at the exit, letting $\eta_{mn}^{0+}\to+j\infty$ to set the downstream reflection to zero yields the acoustic pressure expression for the semi-infinite duct case. The expression for the upstream part is important here since the focus of control is on the inlet side. The expression for the upstream pressure in the finite duct case is

$$p_{sB}(\mathbf{x}) = jB\sum_{p=-\infty}^{\infty}\sum_{n=1}^{\infty}\frac{J_m(\kappa_{mn}r)e^{j\left(\frac{MsB\Omega}{c_0\beta^2}z-m\theta\right)}}{N_{mn}^2\ k_{mn,sB}}\cos\left(\eta_{mn,sB}^{-}(z)\right) \times\frac{\cos\left(\eta_{mn}^{0+}\right)}{\sin\left(\eta_{mn}^{0+}-\eta_{mn}^{0-}\right)}\left(m\hat{D}_{mn,p}+\gamma_{mn,sB}^{-}\hat{T}_{mn,p}\right),$$

(2.3.61)

where $\gamma_{mn}^{-} = j\frac{k_{mn}}{\beta^2}\tan\left(\eta_{mn}^{+0}\right)-\frac{MsB\Omega}{c_0\beta^2}$ and $m = sB - p$. Letting $\eta_{mn}^{0+}\to+j\infty$ in the above expression, the following terms in the above expression simplify to

$$\left.\frac{\cos\left(\eta_{mn}^{0\mp}\right)}{\sin\left(\eta_{mn}^{0+}-\eta_{mn}^{0-}\right)}\right|_{\eta_{mn}^{0+}\to+j\infty} = -je^{-j\eta_{mn}^{0-}};\ \gamma_{mn,sB}^{-} = -\frac{k_{mn,sB}}{\beta^2} - \frac{MsB\Omega}{c_o\beta^2},$$

(2.3.62)

since $\tan\left(\eta_{mn}^{+0}\right)\Big|_{\eta_{mn}^{+0}\to j\infty} = -1/j$. Substituting the above in Equation (2.3.61) leads us to the following expression for the pressure in the upstream side of the fan duct assuming no reflections from the anechoically terminated exit,

$$p_{sB}(x) = B\sum_{p=-\infty}^{\infty}\sum_{n=1}^{\infty}\frac{J_m(\kappa_{mn}r)e^{j\frac{MsB\Omega}{c_o\beta^2}z}e^{-jm\theta}}{N_{mn}^2 k_{mn,sB}}e^{-j\eta_{mn}^{0-}}\cos\left(\eta_{mn,sB}^{-}(z)\right).$$
$$\times\left(m\hat{D}_{mn,p}+\gamma_{mn,sB}^{-}\hat{T}_{mn,p}\right)$$

(2.3.63)

The above equation can be simplified by rewriting $e^{-j\eta_{mn}^{0-}}\cos\left(\eta_{mn,sB}^{-}(z)\right)$ as $e^{-j\eta_{mn}^{0-}}\frac{\left(e^{j\eta_{mn,sB}^{-}(z)}+e^{-j\eta_{mn,sB}^{-}(z)}\right)}{2}$. From the definitions (2.3.7) and (2.3.17) we get (after some algebra)

$$p_{sB}(\mathbf{x}) = \sum_{p=-\infty}^{\infty}\sum_{n=1}^{\infty}\frac{B(m\hat{D}_{mn,p}+\gamma_{mn,sB}^{-}\hat{T}_{mn,p})}{N_{mn}k_{mn,sB}}\frac{J_m(\kappa_{mn}r)e^{-jm\theta}}{N_{mn}}\frac{\left(e^{-jk_{mn}^{z-}z}+e^{-jk_{mn}^{z+}z}e^{-j2\eta_{mn}^{0-}}\right)}{2}$$

.

(2.3.64)

Comparing this with Equation (2.3.6) which is repeated here

$$p(r,\theta,z) = \sum_{m=-\infty}^{+\infty}\sum_{n=1}^{+\infty}\left(A_{mn}(\omega)e^{-jk_{mn}^{z+}z}+B_{mn}(\omega)e^{-jk_{mn}^{z-}}\right)\Psi_{mn}(r,\theta),$$

(2.3.65)

we get the following interpretation for (2.3.64), that the tonal acoustic pressure is the sum of modes of order (m,n). Whereas Equation (2.3.6) was written out as a solution for any single frequency, (2.3.64) tells us that these modes are determined for the any frequency representing either the Blade passing frequency or its

harmonics, $sB\Omega$. Also the circumferential acoustic mode order m is determined using the relationship $m = sB - p$, with p being the circumferential order of flow disturbance interaction with the fan blades. The variation of the acoustic modes in the cross-sectional plane is determined by the shape function term

$$\Psi_{mn}(r,\theta) = \frac{J_m(\kappa_{mn} r) e^{-jm\theta}}{N_{mn}},$$

the axial direction by the term

$$\left(A_{mn}(\omega) e^{-jk_{mn}^{z+} z} + B_{mn}(\omega) e^{-jk_{mn}^{z-}}\right) = \frac{B(m\hat{D}_{mn,p} + \gamma^{-}_{mn,sB}\hat{T}_{mn,p})}{N_{mn} k_{mn,sB}} \times \frac{\left(e^{-jk_{mn}^{z-} z} + e^{-jk_{mn}^{z+} z} e^{-j2\eta_{mn}^{0-}}\right)}{2}$$

which accounts for the amplitudes due to the force fluctuations on B blades i.e,

$$\frac{B(m\hat{D}_{mn,p} + \gamma^{-}_{mn,sB}\hat{T}_{mn,p})}{N_{mn} k_{mn,sB}}$$

and the axial propagation along both directions (z^+ and z^-) with reflections, i.e.,

$$\frac{\left(e^{-jk_{mn}^{z-} z} + e^{-jk_{mn}^{z+} z} e^{-j2\eta_{mn}^{0-}}\right)}{2}$$

which accounts for the sum effect of the propagating and reflected wave train systems.

2.4. Summary

Thus an expression given in Equation (2.3.63) was derived in this Chapter for the acoustic pressure field associated with the interaction of the fan with a flow disturbance. If the profile of the flow disturbance is known then the acoustic pressure field can be estimated from this expression. This equation is used in the control problem formulated in next Chapter which consists of (i) the determination of the acoustic pressure field resulting from the wake generated by the presence of a cylindrical rod in the duct upstream of the fan rotor, and (ii) the problem of optimising the noise power when several such rods are used for control.

Chapter 3 Wake Generator Control

3.1. Introduction

Having developed an expression for the pressure field resulting from the interaction of flow disturbances with the fan blades, we shall now develop the requisite theory for the minimisation of the noise power. Section 3.2 will examine in detail the expressions developed in the previous chapter for the relationship between a flow disturbance and the corresponding acoustic modes that it generates. Section 3.3 will detail the analytical expressions for the flow disturbances (wakes) generated by the control rods. Section 3.4 will look at the problem of cancellation of noise using the expressions developed above by making one of the rods act as a source and another as a controller. The section will in particular look at the effects of translating and rotating the control rod. Section 3.5 will examine the problem of noise optimisation since the presence of the control rod can cause the production of modes other than the mode that is being considered for control. Section 3.6 attempts to solve the problem of noise cancellation outlined in Section 3.4 using an algorithm based on the noise optimisation theory in Section 3.5. The noise cancellation problem thus becomes a test case for the optimisation algorithm which will be used for subsequent optimisation cases in the next chapter.

3.2. Relationship between the interacting flow disturbance and the corresponding acoustic modes

The equations developed in the previous chapter expressing the relationship stated in the heading above are repeated here. Equation (2.3.63) gives the acoustic pressure due to the radiation of the fluctuating forces produced through the interaction of the fan blades with the flow disturbance,

$$p_{sB}(x) = B \sum_{p=-\infty}^{\infty} \sum_{n=1}^{\infty} \frac{J_m(\kappa_{mn} r) e^{j\frac{MsB\Omega}{c_o\beta^2}z} e^{-jm\theta}}{N_{mn}^2 k_{mn,sB}} e^{-j\eta_{mn}^{0-}} \cos\left(\eta_{mn,sB}^{-}(z)\right) \cdot$$
$$\times (m\hat{D}_{mn,p} + \gamma_{mn,sB}^{-} \hat{T}_{mn,p})$$

(3.2.1)

The term in this equation that represents the fluctuating force harmonics is $(m\hat{D}_{mn,p} + \gamma_{mn,sB}^{-} \hat{T}_{mn,p})$. Equations (2.3.53) and (2.3.57) express the relationship between these forces and the flow disturbance harmonics,

$$D_{mn,p}^{\pm} \equiv -\frac{c}{2} \rho_0 U_r \cos\chi \sin\mu \, S_c(\sigma_p, M_r) \cos\left(\eta_{mn}^{0\mp}\right) W_{mn,p}^{D}$$

$$T_{mn,p}^{\pm} \equiv -\frac{c}{2} \rho_0 U_r \sin\chi \sin\mu \, S_c(\sigma_p, M_r) \cos\left(\eta_{mn}^{0\mp}\right) \gamma_{mn,sB}^{\pm} W_{mn,p}^{T}$$

(3.2.2)

Equations (2.3.52) and (2.3.56) obtain these flow disturbance harmonics through a Fourier-Bessel decomposition of the flow disturbance w,

$$W_{mn,p}^{D} = \int_o^a \int_0^{2\pi} e^{-jp\theta_s} J_m(\kappa_{mn} r_s) w(r_s, \theta_s) \frac{1}{r_s} \, d\theta_s \, dr_s$$

$$W_{mn,p}^{T} = \int_o^a \int_0^{2\pi} e^{-jp\theta_s} J_m(\kappa_{mn} r_s) w(r_s, \theta_s) \, d\theta_s \, dr_s$$

(3.2.3)

It is essential to understand the kinematics of the production of an acoustic mode from the interaction of the fan with a flow disturbance. Any velocity disturbance w in a cylindrical cross-section duct can be resolved into weighted Fourier-Bessel shape functions W as indicated in Equation (3.2.3) above. Fan blades are shown on the inner circles in Figure 3.1. A harmonic pattern can be assumed to be generated by the presence of equispaced wake generating rods and these are shown on the outer circle. The pattern of the acoustic mode resulting from the interaction of the fan with the rods is shown on the outside of the outer

circle as a patch. The fan blades rotate at Ω rad/s and the first blade on the fan is marked with a bold dot. The start of the interaction pattern can be thought to be at the instant shown in the same figure when the marked blade coincides with the horizontal rod on the right side of the first of these figures. Thereafter it appears whenever a blade and the rod coincide as the fan rotates past the rods.

In the first example there are 8 blades (sB =8) and 6 rods (p=6) and the pattern has an order of m=2 (since sB-p=2). This pattern rotates in the same direction as that of the fan and it goes through one complete revolution upon completion of a ¼ revolution of the fan which makes the speed of the pattern 4 times that of the fan.

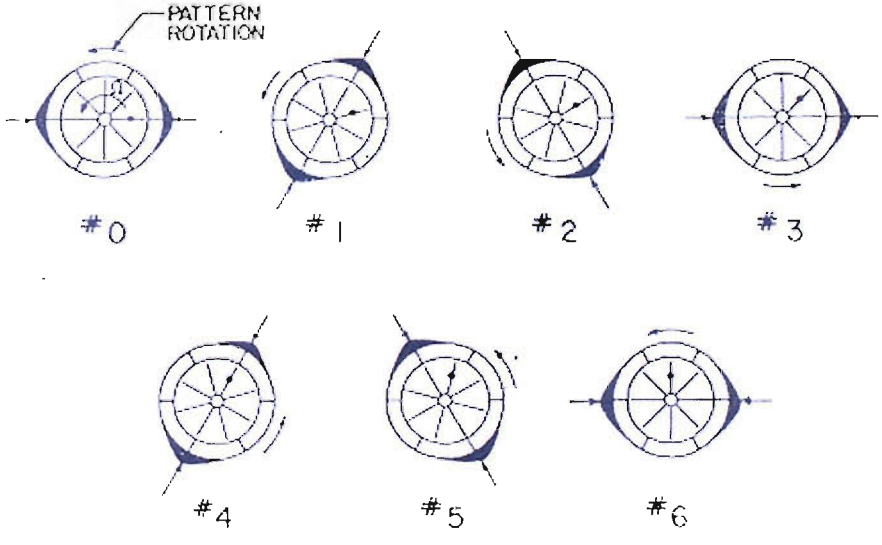

Figure 3.1 Illustration of the production of an acoustic mode pattern from the interaction of fan blades with stationary rods (from Tyler and Sofrin, 1961).

In the second example in Figure 3.2 there are 8 blades (sB =8) and 9 rods (p=9) and the pattern has an order of m=-1 (since sB-p=-1). This pattern rotates in the opposite direction to the fan (hence the negative value for m) and it goes through one complete revolution upon completion of a 1/8th revolution of the fan which makes the speed of the pattern 8 times that of the fan.

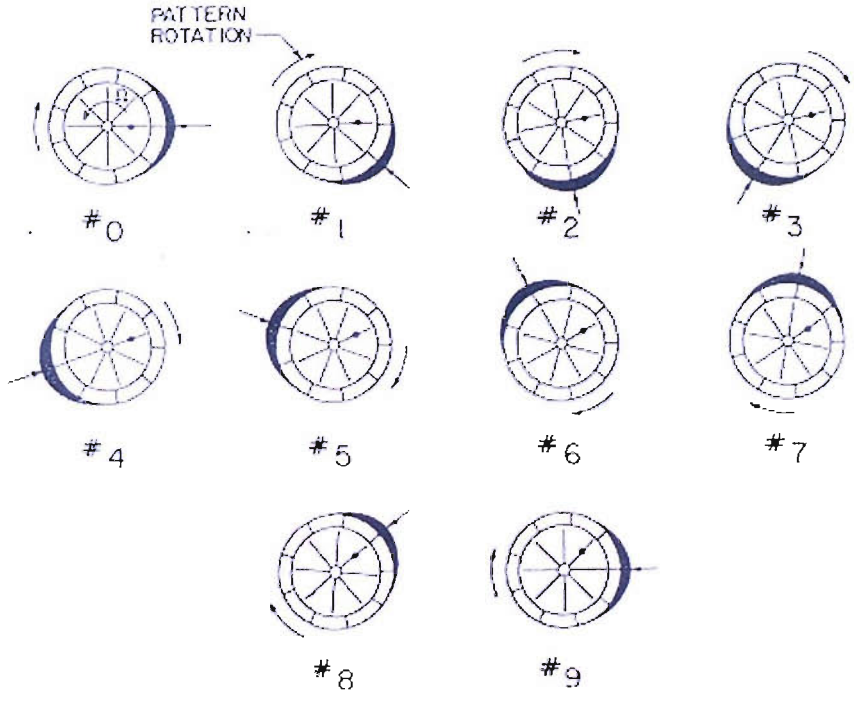

Figure 3.2 Illustration of the production of an acoustic mode pattern from the interaction of fan blades with stationary rods (from Tyler and Sofrin, 1961).

The following table summarises the information described above.

No. of fan blades B	Flow mode order p	Acoustic mode order m $(m=B-p)$	Speed of the fan blades Ω (rad/s)	Speed of the spinning acoustic mode $B\Omega/m$ (rad/s)
8	6	2	Ω	4Ω
8	9	-1	Ω	-8Ω

Table 3.1 Interaction between fan blades and stationary rods.

The relationship employed in the above table is a special case of the general relationship given in the previous chapter which is $(m=sB-p)$ applicable for tones of any harmonic order s. The acoustic modes produced from the interaction do not rotate at the same speed as the fan and some of these modes rotate in the sense opposite to that of the fan.

3.3. Flow disturbance produced by a cylindrical rod and its acoustic response

The flow disturbance that the cylindrical controller rod generates is in the form of a velocity wake distributed over the cross section of the duct and an equation representing the wakes velocity defect distribution is given in terms of the spatial coordinates. The profile is a Gaussian profile for the wake. The original equation as used by Polacsek (1999) is a semi-empirical 2-D model of the turbulent wake behind an infinite cylinder deduced from Abramovich (1963) which is again based on experiments of Schlichting (1960) and also his turbulent wake theory. Schlichting shows that the dimensionless velocity profile distribution of wakes from cylinders obtained from his experiments can be represented by a Gaussian function. The formulae also assume that the Reynolds number is in the range of 10^4-10^5 as the coefficient of drag turns out to be roughly equal to one in this range. The flow situations considered here fall within this range. The equation after the modification for the wake shape at the tip region of the rod given by Pitelet (2000) is as follows:

$$w_q(r,\theta) = U\sqrt{\frac{d}{z_q}}e^{-\frac{\pi}{z_q d}\left(\frac{r(\theta-\theta_q)}{0.8}\right)^2} e^{-\frac{\pi}{z_q d}\left(\frac{a-l-r}{0.8}\right)^2},$$

(3.3.1)

where $w_q(r,\theta)$ is the wake velocity defect distribution generated across the duct cross section at the blades of the fan by a controller rod q of diameter d and length l and located in the duct of radius a at the circumferential and axial coordinates θ_q and z_q respectively, and U is the velocity of the mean flow in the duct. In addition, the presence of the Von karman vortex street downstream of the flow past a cylinder is well known. The potential part of the wake velocity defect from a single rod thus causes each interacting fan blade to experience unsteadiness in the blade loading for every revolution of the fan and hence blade loading harmonics are generated. The emission of the Von karman vortices from the rod adds up to the unsteadiness in the blade loading which will not be periodic with respect to the fan rotation. Polacsek (2003) has observed through his computations that despite

the presence of this phenomenon the blade loading harmonics were dominant compared to other components due to non-periodicity. Substituting the wake profile $w_q(r_s,\theta_s)$ in the integrals in Equation (3.2.3) and defining the coupling coefficient as $C^q_{mn,p} = (m\hat{D}_{mn,p} + \gamma^-_{mn,sB}\hat{T}_{mn,p})$, we see that this term is given by

$$C^q_{mn,p} = -\frac{c}{2}\rho_0 U_r \sin\mu\, S_c(\sigma_p, M_r)$$

$$\times \int_0^a \int_0^{2\pi} e^{-jp\theta_s} J_m(\kappa_{mn} r_s) w_q(r_s,\theta_s)\left(\frac{1}{r_s} m\cos\chi + \gamma^-_{mn,sB}\sin\chi\right) d\theta_s\, dr_s, \quad \textbf{(3.3.2)}$$

where $C^q_{mn,p}$ is the coupling coefficient of the mode *(m,n)* induced by the q^{th} rod. It can be seen through the Fourier-Bessel integral that the complex amplitudes of these coefficients depend on the rod lengths l and their orientation θ_q.

If the response as mentioned above is obtained for a controller at the zero reference of the azimuthal position across the duct cross section then the response of the rod at an angle θ from the reference is given by

$$C^{q(\theta)}_{mn,p} = C^{q(0)}_{mn,p}\, e^{-jp\theta}. \quad \textbf{(3.3.3)}$$

The resolution in Fourier-Bessel space of a flow disturbance generated by positioning a single rod at a reference is explained below.

The real and the imaginary parts of the Fourier-Bessel term appearing in Equation (3.3.2) are shown in Figure 3.3 and Figure 3.4. The shape function has been constructed using $(m,n,p) = (0,0,9)$. The shape function has $2p$ zero crossings in the circumferential direction.

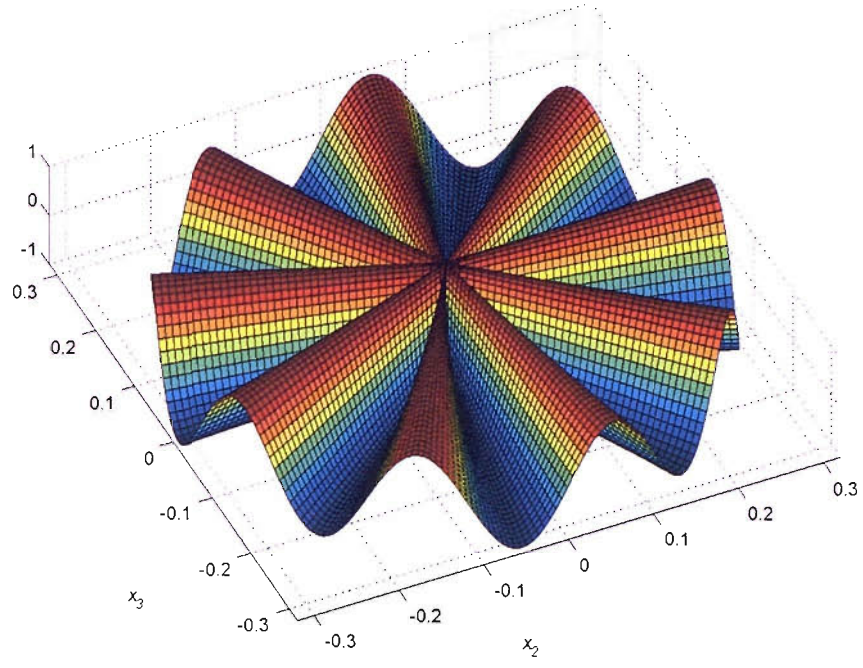

Figure 3.3 Real part of the Fourier-Bessel shape function in Equation (3.3.2).

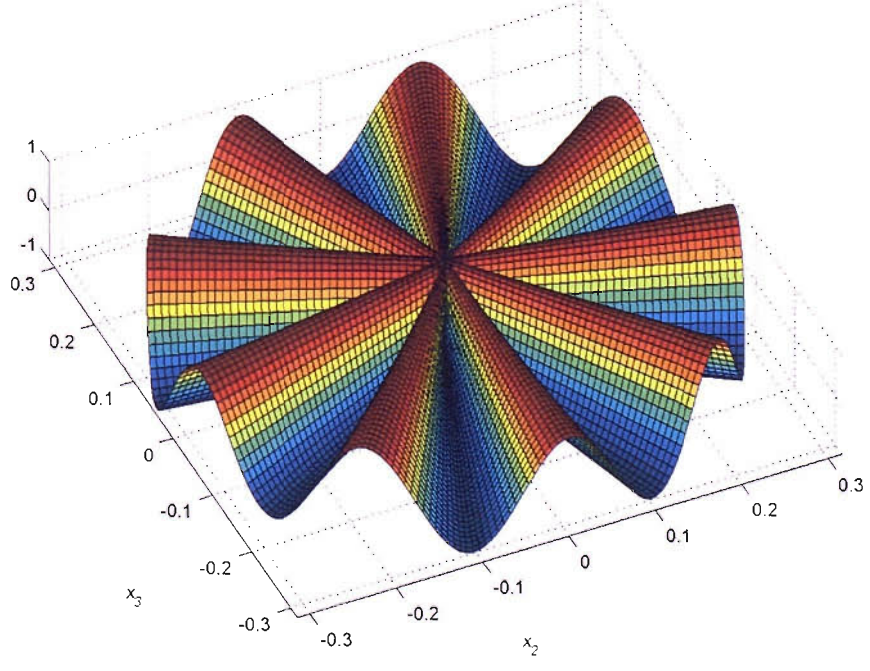

Figure 3.4 Imaginary part of the Fourier-Bessel shape function in Equation (3.3.2).

The projected view of the real part of the shape function as seen from the top is shown in Figure 3.5 which makes the radial nodal lines clearly visible. Each cycle of the Fourier-Bessel shape function has a positive (appearing in red) and negative (appearing in blue) turn across each nodal line in the Figure. As the circumferential order increases the number of these radial nodal lines increases and the additional nodal circles appear for the cases where the radial order $n>0$.

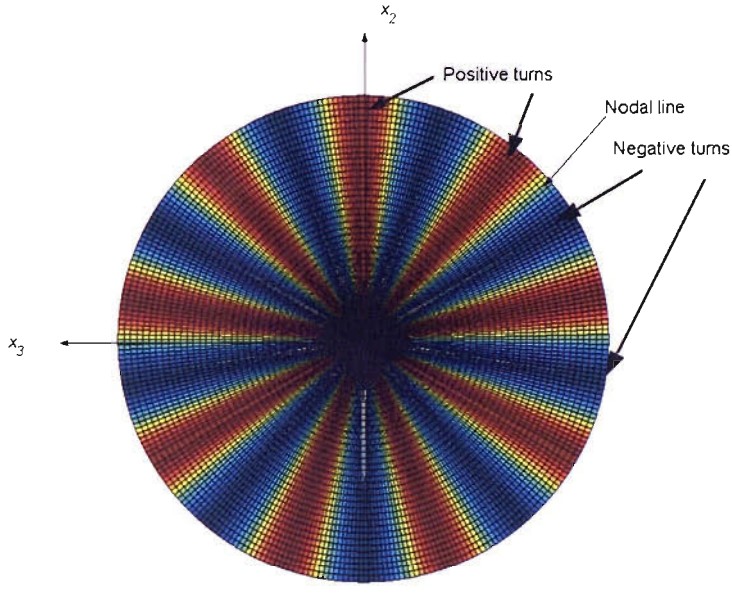

Figure 3.5 Circumferential nodal lines on a Fourier-Bessel shape function.

Using the equations in the previous sections a program was written in MATLAB to estimate the acoustic modal response for a cylindrical rod of length 300mm and diameter 12mm. The rod was assumed to be oriented at a circumferential reference of zero (x_2 axis) and held at an axial distance of 400mm upstream from the fan origin. This causes the wake velocity defect distribution shown in Figure 3.6 to lie between the two adjacent nodal lines in the above Figure 3.5. The defect distribution shown in Figure 3.6 is as seen from the downstream end of the duct, and this is for the situation when the entire length of the rod (300mm) protrudes into the duct. The length was increased incrementally in steps of 10 mm and the coupling coefficient defined as in Equation (3.3.2) was

estimated with the flow wake distribution obtained for each length of the rod. The increase in the length of the rod causes the modal amplitude to register an increase without a change of phase as seen from the integration in Equation (3.3.2) in conjunction with Figure 3.5 and Figure 3.6. This response was evaluated assuming that the fan that interacts with the flow has 9 blades and rotates at 3000 rpm. These parameters correspond to the existing fan on which the control system implementation is carried out. The response was evaluated for all the cut-on modes present in the first three harmonics of the blade passing frequency (BPF =450 Hz). As explained in Chapter 2 the axial wave number k_{mn} has to be real valued for each mode to be cut-on. The other essential parameters for the simulation are as follows: fan blade chord, 130 mm; fan blade stagger angle, 34^0; fan duct diameter, 630 mm; sound speed, 342 m/s and mean flow speed, 30 m/s.

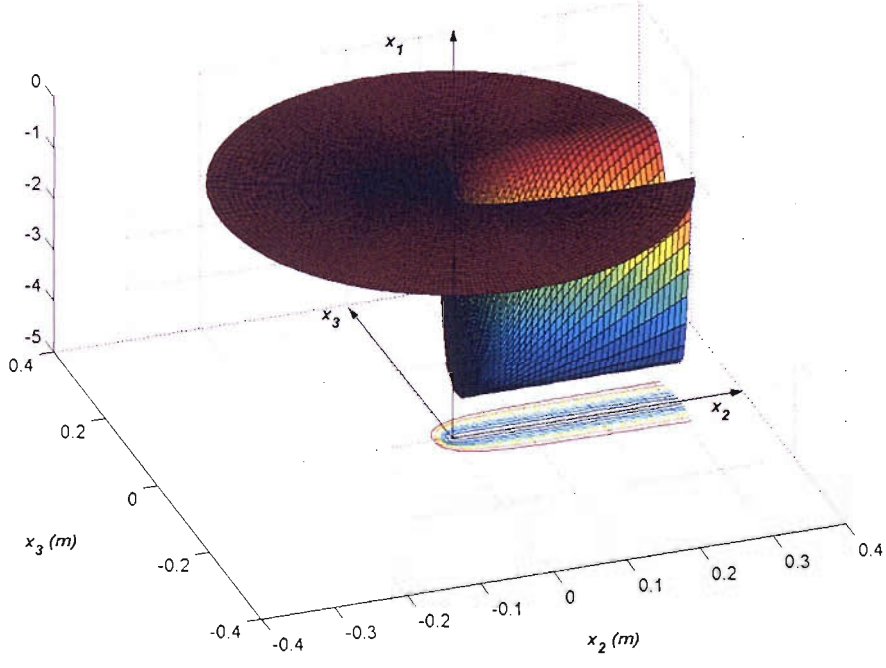

Figure 3.6 Wake velocity defect distribution for a cylindrical rod (300 mm in length, 12 mm in diameter and held at 0^0).

The possible cut-on modes for the speed of fan rotation chosen above are listed in the table below for the first three harmonics.

Harmonic order *s*	Flow mode azimuthal order *p*	Acoustic mode azimuthal order *m (=sB-*	Acoustic mode radial order *n*

		p, where B=9)	
1	10	-1	0
1	9	0	0
1	8	1	0
2	21	-3	0
2	20	-2	0
2	19	-1	0
2	18	0	0
2	17	1	0
2	16	2	0
2	15	3	0
2	18	0	1
3	33	-6	0
3	32	-5	0
3	31	-4	0
3	30	-3	0
3	29	-2	0
3	28	-1	0
3	27	0	0
3	26	1	0
3	25	2	0
3	24	3	0
3	23	4	0
3	22	5	0
3	21	6	0
3	29	-2	1
3	28	-1	1
3	27	0	1
3	26	1	1
3	25	2	1
3	27	0	2

Table 3.2 Cut-on modes in the first three harmonics (BPF = 450 Hz).

The modal response, i.e. the coupling coefficient C_{mn}, is shown plotted against the rod length for only 5 out of the 30 cut-on modes in the first three harmonics in Figure 3.7 for the amplitude and Figure 3.8 for the phase. Each cut-on mode is represented by its circumferential and radial orders (m,n). The order of the harmonic is shown by the term s.

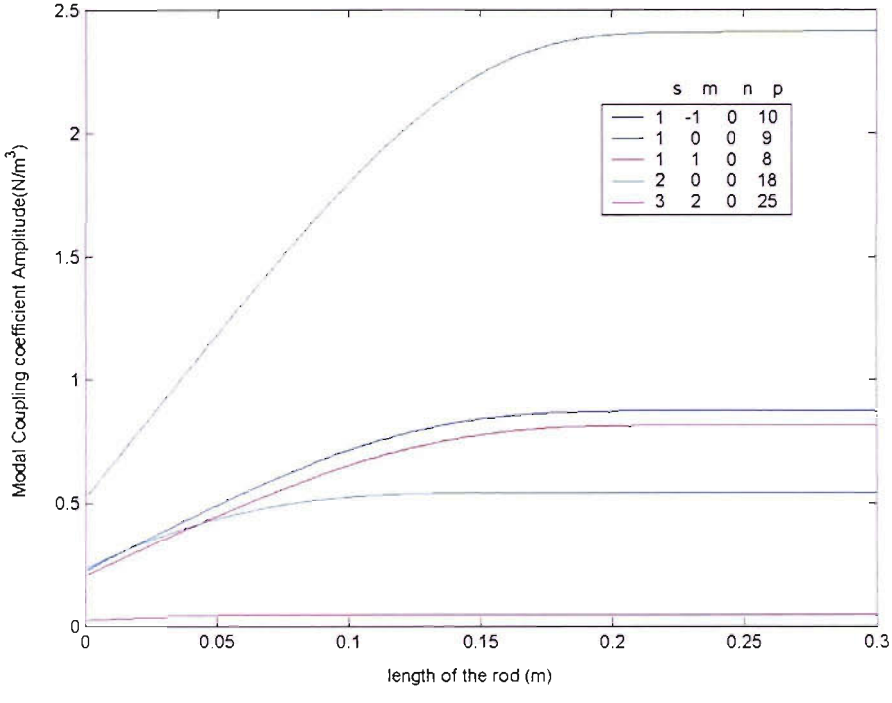

Figure 3.7 Amplitude response of the rod.

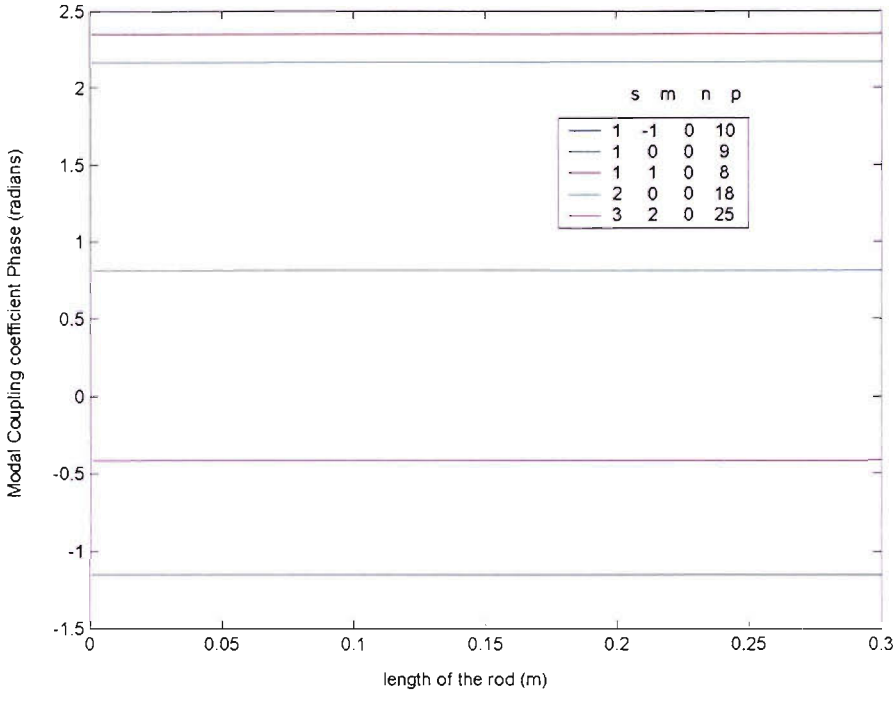

Figure 3.8 Phase response of the rod.

The following observations can be made from the above graphs:

i) The amplitude of the coupling coefficient increases initially with the length because of the integration of the wake profile with the Fourier-Bessel function and as radial nodal lines of these functions converge towards the centre the amplitudes tends to flatten out.

ii) Phase remains flat because the disturbance that is integrated in the equations remains stationary in the circumferential sense.

iii) Multiple modes of varying intensities are generated through the presence of a single rod.

3.4. Cancellation of a mode generated by using a rod as a disturbance source

The rod used to determine the amplitude response is used as a source to generate noise. Considering a single mode of circumferential order *m* for cancellation, the flow mode-acoustic mode relationship tells us that this mode arises out of the flow

disturbance which has a circumferential harmonic of p. The control then requires generating another flow disturbance pattern to cancel out the mode produced by the first rod. This disturbance as seen in Equations (3.3.2) and (3.3.1) produces a corresponding acoustic mode of an intensity adjustable through the variation of its circumferential and radial extent. The effect of rod translation and rod rotation are summarised below and the explanation of the control concept follows later.

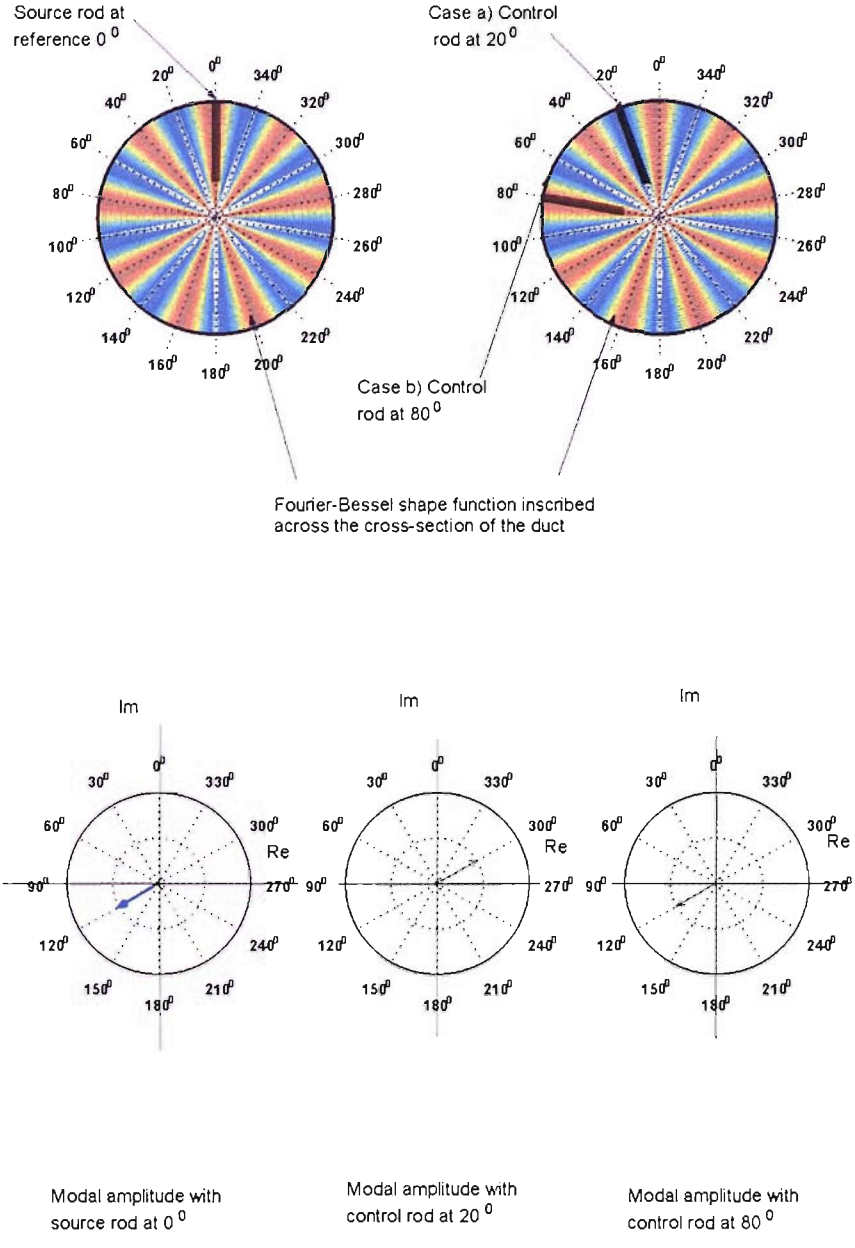

Figure 3.9 Explanation of the cancellation concept using the Fourier-Bessel shape pattern (assuming the various indicated circumferential positions for the control rod).

Effect of rod translation: As seen in the trends of the amplitude response the amplitude rises as the rod length increases and the phase remains constant.

Hence to cancel out the mode produced in the first instance changing the rod length alone will not produce any cancellation as this method will not alter the phase of the mode.

Effect of rod rotation: It is already obvious that holding the length of the rod fixed in a circular duct and rotating it should not cause any alteration of the radial and circumferential extent of the rod's disturbance and hence the amplitude of the mode produced should remain constant. The phase alters by the term $e^{-jp\theta}$ as seen in Equations (3.3.3). The phase change produced in the mode through a rotation of θ in the rod is $p\theta$.

Cancellation of the mode: Let us assume that the mode produced by a source rod mentioned above has an amplitude A and phase of θ_{mI}. To cancel this a mode of the same intensity but of opposite phase has to be induced which means that placement of the control rod should produce a mode that has the phase of $e^{j\theta_{mI}} e^{\pm j\pi}$. This concept is illustrated in Figure 3.9 where the Fourier-Bessel pattern for the plane wave mode (m=0 and p=9) is shown inscribed across the duct cross-section. Considering the plane wave mode for cancellation (m=0), and with a fan of B (=9) blades the flow mode that generates this has a circumferential order of p=9. The Fourier-Bessel pattern for this mode in Figure 3.9 has got 18 radial nodal lines. The source rod is shown placed at the azimuthal reference of 0^0 on the first inscription of the Fourier-Bessel pattern. On the second inscription of this pattern two cases are shown for the control rod, one located at 20^0 and the other at 80^0. When the control rod is placed at 20^0, it can be inferred that the Fourier-Bessel pattern exhibits a turn (hump) that is opposite in sense to that where the source rod is. This is shown in the complex modal amplitudes sketched in bottom half of Figure 3.9 wherein the placement of the control rod at 20^0 is causing the production of the mode in anti-phase with respect to that of the source rod. Hence there are multiple positions where the control rod can be placed to cancel the mode produced in the first place. The placement of the control rod at 80^0 causes the mode generated to be in-phase with respect to that of the source rod. This is also made clear by the term $e^{-jp\theta}$.

Figure 3.10 shows the phase difference induced between the controller and source generated modes for two modes when the source rod is placed along the radial lines shown in Figure 3.9. The two modes are the mode considered for

cancellation (m=0, p=9, B=9) and a different mode (m=-1, p=10, B=9). The orientation of each radial line is denoted as θ.

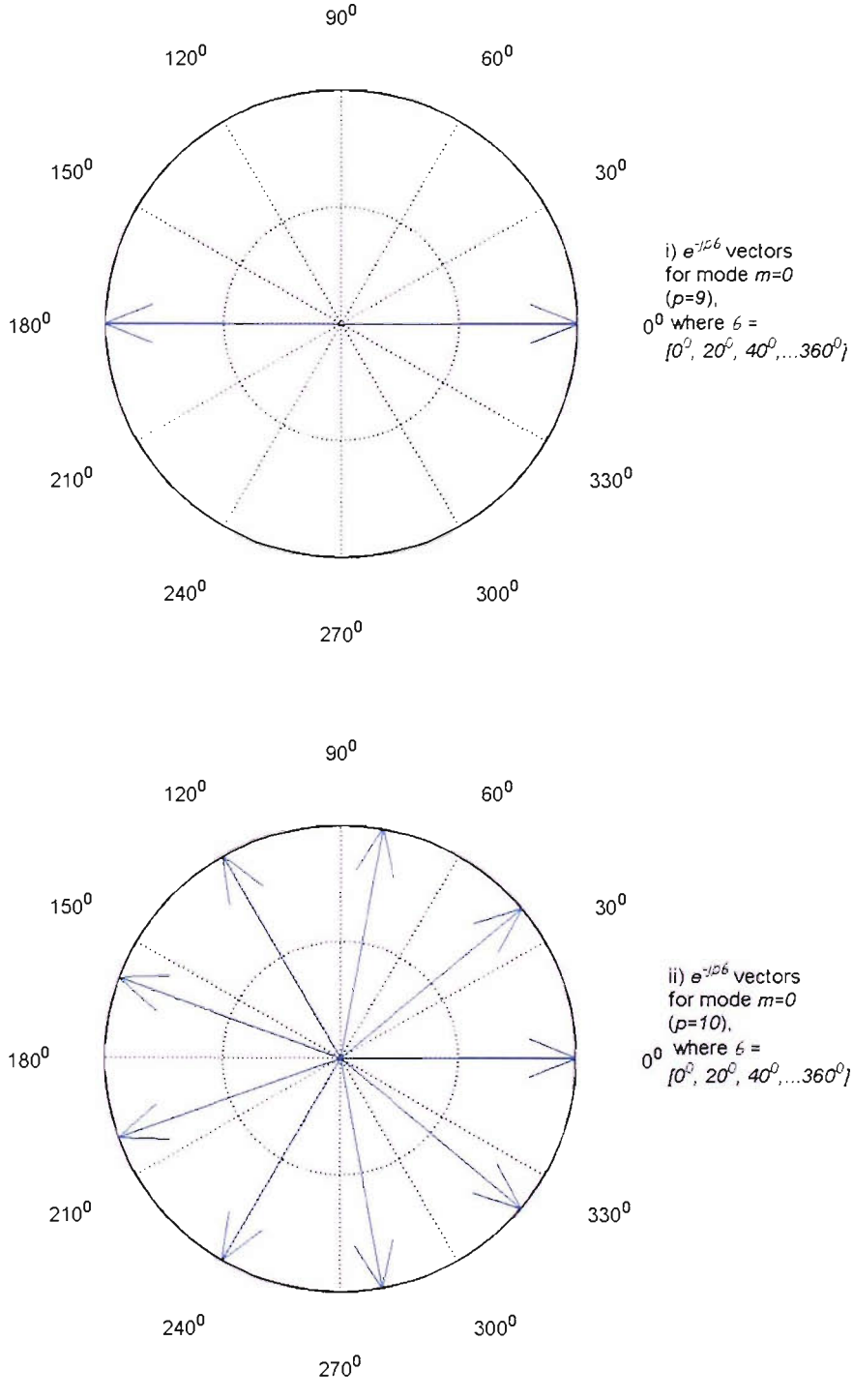

Figure 3.10 Phase difference induced between the controller and source generated modes for two different modes.

The following observations can be made from the information presented in Figure 3.10.

i) For the mode that is cancelled (m=0) the out-of-phase relationship necessary for cancellation, i.e., $e^{-jp\theta} = -1$, holds at exactly half the number of orientations. At the remaining locations it is in-phase, i.e., $e^{-jp\theta} = 1$.

ii) None of the above orientations cause cancellation of the mode *(m=-1)*, i.e., $e^{-jp\theta} \neq -1$. Hence focussing on the cancellation of one mode causes the intensity of the other modes to either increase or decrease but does not necessarily cancel them. This leads us to consider the problem of minimisation of the intensities of multiple modes which is explained in the next section.

3.5. Noise minimisation problem

The problem of the minimisation of the intensities of multiple modes can be considered by forming a cost function to represent the sum of the squared modal amplitudes. The Overall Sound Power level is a quantity that readily represents this summation. An expression has been derived for the transmitted tonal power in the intake duct produced by the fan interaction with the flow disturbance. This expression has been arrived at by using the semi-infinite duct pressure expression developed in Chapter 2 to obtain the sound intensity which when integrated with the normal propagating area gives the power. This derivation is given in Appendix 3.1. Power in any harmonic is given by

$$P_{sB} = B^2(1/\rho_o c_o)\sum_{p=-\infty}^{\infty}\sum_{n=1}^{\infty}\frac{1}{N_{mn}^2 k_{mn,sB}^2}\frac{\alpha_{mn,sB}\beta^4}{(1-\alpha_{mn,sB}^2 M^2)^2}e^{2\phi_{mn,sB}^{0-}}$$
$$\times\left(\frac{e^{2\phi_{mn,sB}^{0-}}}{2}(1+\alpha_{mn,sB}M)^2 - \frac{e^{-2\phi_{mn,sB}^{0-}}}{2}(1-\alpha_{mn,sB}M)^2\right)$$
$$\times\left|(m\hat{D}_{mn,p} + \gamma_{mn,sB}^{-}\hat{T}_{mn,p})\right|^2 .$$

(3.5.1)

All terms are as defined previously, except that the term $\phi_{mn,sB}^{0-}$ represents the imaginary part of the complex valued phase of the upstream modal reflection coefficient $\eta_{mn,sB}^{0-}$ and $\alpha_{mn,sB} = k_{mn,sB}/k_o$.

The above expression for power in a single harmonic, P_{sB} can be considered as

$$P_{sB} = \sum_{mn,p}\varepsilon_{mn}\left|(m\hat{D}_{mn,p} + \gamma_{mn,sB}^{-}\hat{T}_{mn,p})\right|^2 = \sum_{mn,p}\varepsilon_{mn}\left|C_{mn,p}\right|^2 ,$$

(3.5.2)

where ε_{mn} is a mode-specific constant term accounting for all the factors in Equation (3.5.1), other than $\left|(m\hat{D}_{mn,p} + \gamma_{mn,sB}^{-}\hat{T}_{mn,p})\right|^2$.

It should be noted that the expression for power was based on the amplitudes of the incident and reflected modes to estimate the net transmitted tonal power in the duct with a square inlet. If inlet geometry has to be taken into account as in the case of scarfed inlets, then the expression for power can alternatively be based on an appropriate radiation model that accounts for it.

3.5.1.1. Optimisation

Assuming that the action of the controllers can be represented by a control vector **w** representing the controller rod lengths the formulation of the optimisation problem can be phrased as follows: minimise the cost function for error power

$$J = \sum_{sB} P_{sB}(\mathbf{w}),$$

(3.5.3)

subject to the constraint that the control vector $\mathbf{w} > \mathbf{0}$ for all its elements. The above expression expresses the power in the tone as a sum of the squares of the modal coupling coefficient amplitudes and can be considered as the cost function J for the optimisation problem. It should be noted that the expression for the cost function was based on the simple unweighted summation of the individual harmonic powers. Weighting can be introduced in a situation when human response to noise needs to be accounted. The expression for the cost function can include frequency weighting in such a scenario. The modal coupling coefficient for the acoustic field generated in the system due to the disturbance inherent to the system is represented by C_{prim} which is what needs to be controlled. Denoting the same for the controller generated acoustic field as $C_{secondary}$ we see that the total power in the system is obtained from the sum of the squares of the modal coupling coefficient amplitudes in the error acoustic field which is a vector sum of the primary and secondary fields. Also if multiple tones are considered for optimisation the cost function is simply a sum of the tonal powers which in turn is a sum of squares of modal amplitudes in all the cut-on modes in those tones. Since the secondary noise generated by the controllers depends on the lengths of the controller rods we can see that the cost function depends on the rod lengths:

$$\begin{aligned} J &= \sum_{sB} P_{sB} = \sum_{sB} \sum_{mn,p} \varepsilon_{mn,sB} \left(C_{error}^{H} C_{error} \right) \\ &= \sum_{sB} \sum_{mn,p} \varepsilon_{mn,sB} \left(C_{prim} + C_{secondary} \right)^{H} \left(C_{prim} + C_{secondary} \right) \end{aligned}$$

(3.5.4)

where $C_{secondary} = \sum_{w} C_{mn,p,sB}$, which is the sum of the contributions to the coupling coefficient of a mode made by each controller and H (= $*$) denotes the complex conjugate of the modal coupling coefficient which is a scalar quantity.

The optimisation method considered here is based on the gradient based technique. "The use of the negative of the gradient vector as a direction for

minimisation was first made by Cauchy in 1847." (Rao 2000). The steepest descent method will be used for minimisation of the cost function. This technique involves estimating the gradient of the optimisation cost function J with respect to the control vector $\mathbf{w}$ and descending along the gradient $\partial J / \partial \mathbf{w}$ to arrive at the optimum. Differentiating the optimisation cost function J with respect to the control vector of lengths $\mathbf{w}$.

$$\begin{aligned}\frac{\partial J}{\partial \mathbf{w}} &= \sum_{sB}\sum_{mn,p} \varepsilon_{mn,sB}\left(\left(\frac{\partial C_{error}}{\partial \mathbf{w}}\right)^{H} C_{error} + C_{error}^{H}\left(\frac{\partial C_{error}}{\partial \mathbf{w}}\right)\right) \\ &= \sum_{sB}\sum_{mn,p} \varepsilon_{mn,sB} \times 2\,\mathrm{Re}\left(\left(\frac{\partial C_{error}}{\partial \mathbf{w}}\right)^{H} C_{error}\right) \\ &= \sum_{sB}\sum_{mn,p} \varepsilon_{mn,sB} \times 2\,\mathrm{Re}\left(\left(\frac{\partial C_{secondary}}{\partial \mathbf{w}}\right)^{H} C_{error}\right). \qquad \left\{\because \frac{\partial C_{error}}{\partial \mathbf{w}} = \frac{\partial C_{secondary}}{\partial \mathbf{w}}\right\}\end{aligned}$$

(3.5.5)

Hence it turns out that the cost function gradient $\partial J / \partial \mathbf{w}$ is dependent on the modal coupling coefficient gradient $\partial C_{secondary} / \partial \mathbf{w}$. The quantity $C_{secondary}$ was already obtained numerically and presented in Figure 3.7 and Figure 3.8.

Since the coupling coefficient amplitude in Figure 3.7 is not linear with respect to the rod length we have to either linearise or take into account its non-linearity while estimating its gradient. If $C_{secondary}$ is linearised with respect to the control vector length, then $\partial C_{secondary} / \partial \mathbf{w} = \mathbf{g}$. Otherwise, it is the local gradient of the non-linear response function.

The cost function is minimised by iterating the control vector in the direction of the steepest descent and the converged set of control vector lengths $\mathbf{w}$ needs to be obtained,

$$\mathbf{w}(k+1) = \mathbf{w}(k) - \mu \frac{\partial J}{\partial \mathbf{w}},$$

(3.5.6)

with the constraint that $\mathbf{w}>\mathbf{0}$, where μ denotes a convergence coefficient and k is the iteration index. The algorithm requires a value for μ, which represents the length of the step along the gradient to be descended. Using this expression for the update of the control vector in an algorithm coded in MATLAB the noise cancellation problem in the previous section is explained in the next section.

3.6. Numerical simulation of the noise cancellation problem using the steepest descent algorithm

A simple case of optimisation is examined here for the cancellation of a single mode using a single control rod. This is the same mode whose cancellation was discussed in Section 3.4, the only difference being that the fan is assumed to run at a speed of 1800 rpm where only this mode is cut-on for the first harmonic as determined from the axial wave number equation. In order to proceed with the optimisation using the steepest descent algorithm one needs to know the gradient of the cost function as expressed in Equation (3.5.5). This in turn requires the knowledge of C_{error} and $\partial C_{secondary} / \partial \mathbf{w}$. For the initial iteration of the algorithm when the length of the control rod is zero, $C_{error} = C_{prim.}$ This is the noise field generated in the system due to the plane wave mode being considered here. $\partial C_{secondary} / \partial \mathbf{w}$ is the gradient of the modal response of the single control rod. Since the algorithm requires the determination of this gradient for each iteration of the control rod length, a knowledge of the fit of the response would be helpful. Initially a linear fit for the modal response is chosen. The modal response obtained for the plane wave mode ($m=0$) for the single rod along with the linearisation is shown in Figure 3.11. The level of the previously considered plane wave mode for the cancellation problem is also shown as an intercept on this figure. This is obtained by assuming that a source rod is extended fully (300 mm) into the duct. The linearised response, $\partial C_{secondary} / \partial \mathbf{w} = \mathbf{g}$ is utilised in estimating the gradient in Equation (3.5.6). The advantage of linearisation of the response is in the fact that it can make the cost function J a quadratic in terms of the controller length and the optimal control rod length can also be obtained by inversion of a simple linear equation instead of having to use the steepest descent algorithm to obtain this

quantity iteratively. However, attention in this section will be restricted to using the steepest descent algorithm to obtain the optimal control rod length since it was found that the results obtained here are the same as those obtained by using the inversion of the linear equation. For the sake of completeness the method for the inversion of the linear equation is given here for the single control rod and single mode case. The inversion of the linear equations will be attempted for the situation of multiple modes and multiple rods which forms the subject matter of the next chapter. Denoting the control rod length as l_1, the optimal length l_{1opt} can be obtained by setting the gradient of the cost function in Equation (3.5.5) to zero:

$$\frac{\partial J}{\partial l_1} = \varepsilon \times 2\,\mathrm{Re}\left(\left(\frac{\partial C_{secondary}}{\partial l_1} \right)^* C_{error} \right) = 0 .$$

(3.6.1)

Substituting $\partial C_{secondary} / \partial l_1 = g$, $C_{error} = \left(C_{prim} + C_{secondary} \right)$, we find that the optimal rod length satisfies

$$2\,\mathrm{Re}\left(g^* \left(C_{prim} + g l_{1opt} \right) \right) = 0,$$
$$2\,\mathrm{Re}\left(g^* g \right) l_{1opt} = -2\,\mathrm{Re}\left(g^* C_{prim} \right)$$
$$\therefore l_{1opt} = -\mathrm{Re}\left(g^* C_{prim} \right) / \mathrm{Re}\left(g^* g \right)$$

(3.6.2)

Reverting back to the use of the steepest algorithm method, the linearised response was thus input to a program in which the algorithm utilising the steepest descent approach was coded. This algorithm uses the Equations (3.5.5) and (3.5.6) to estimate $\partial J / \partial \mathbf{w}$, the gradient of the cost function and iterate $\mathbf{w}$, the control vector. The constraint $\mathbf{w}>\mathbf{0}$ is ignored initially and is added later to bring out the effect of its imposition. With each iteration k used to update the control vector the final values of the control vector are obtained after having the execution performed for a predetermined number of iterations. This program also needs a value to be set for the gradient step (or the convergence parameter) μ. An input for the circumferential position of the control rod with a zero initial condition length is also given. The circumferential position that is considered is the third of the

positions given in the table in Section 3.4, which is 20^0 (or $2\pi/18$). The program is expected to give the converged rod length for the controller for this case and also the cost function as the algorithm traces out each iteration. Since the linear response was used for $C_{secondary}$ in the algorithm, the cost function J is also estimated using this quantity as expressed in Equation (3.5.4). Note that $C_{secondary}$ can also be estimated for a given control rod length using the exact Fourier-Bessel expansion given Equation (3.3.2) which leads to the exact estimate of J. The difference between the approximated and exact estimates will also be discussed here. The result of running the steepest descent algorithm is shown in Figure 3.12 for the controller rod length and the cost function with these quantities plotted against the iterations. A value of μ=0.3 was chosen for this case. The same results are shown in Figure 3.13 for another value, μ=30. It is well known that the value of μ chosen can influence the convergence: too low a value can lead to slower convergence and too high a value can result in the algorithm becoming unstable and tracing out an oscillatory path (Widrow and Stearns, 1985). Since the cost function J in the above problem comprises of only one mode, the variation of this with respect to the length of the single control rod used here for cancellation is a parabolic characteristic. The convergence is smooth and is either slow or quick as was shown in the illustrations. The next chapter examines multiple mode control with multiple rods and the oscillating or unstable behaviour of the cost function will be illustrated for a few cases there. The value for μ has to be chosen on a trial and error basis. As seen from the illustration in Figure 3.13 the control rod has achieved a length of 0.229m. The reason that this has not matched the length of 0.3m for the source rod is due to linearisation of the response.

It should be noted that in Figure 3.12 , the optimal rod length is reached near an iteration index of about 40 but the cost function continues to reduce up to 100 iterations while the rod length changes slowly. This is due to the flattening of the amplitude response once the rod length starts to exceed 200 mm as seen in Figure 3.11. In practice this reduction of the cost function to 2.5 dB may be unattainable due to factors like unsteadiness in the measurement of the modal coupling coefficient amplitude, and the accuracy of the estimates of the rod length and the modal coupling coefficient amplitude. The effect of measured and simulated unsteadiness in modal coupling coefficient on the convergence of the

algorithm is examined in Chapter 5 where the implementation of the active control system is considered.

Since it was illustrated in the previous section that the circumferential position in which the rod is placed can influence control, the optimisation study was repeated with every phase increment of the control rod. Since there is only one control rod it was phase shifted through 360^0 with an increment of 1^0 and at each increment of the phase the convergence of the control rod was determined, using the linear response as mentioned before. The convergence of the cost function J for some of the phases (1^0, 44^0, 125^0, 193^0, 291^0) of the control rod are displayed in Figure 3.14. For instance, at the control rod location of 1^0 the cost function J is shown to attain a converged minimum of 2.5 dB. The converged minima attained by J for all the 360 increments of phase of the control rod are collectively plotted and compared against the primary power (93.9dB) in the top half of Figure 3.15. This result in Figure 3.15 obtained by using the steepest descent algorithm was found to be the same as that obtained through the optimal rod length inversion discussed in the beginning of this section. In the top half of Figure 3.15 the converged cost function J is estimated using the linear response of the converged rod length. In the bottom half of Figure 3.15 the primary power is compared with the estimate of J obtained using the exact response of the converged rod length evaluated through the Fourier-Bessel expansion. The converged rod length variation with the phase is shown in Figure 3.16. Again, this result in Figure 3.16 obtained by using the steepest descent algorithm was found to be the same as that obtained through the optimal rod length inversion discussed in the beginning of this section. The rod length alternates between positive and negative values as the phase of the control rod is varied. The negative rod lengths arise due to the reason that the algorithm extrapolates the linear response characteristic into the negative controller length space thinking that this would result in the production of the required anti-phase mode. The variations of the converged J in the top and bottom half of Figure 3.15 show that as the phase of the control rod is varied the converged cost function does indeed reduce below the primary power at some phase locations. The reduction in J peaks at certain phase locations as seen in bottom and top halves of that figure. In the top half the peak reduction of J to 2.5dB is attained at 0^0 and later at every 20^0 increment of the phase. In the bottom half the peak reduction of J to 43.08dB is attained first at 20^0

and later at every 40^0 increment of the phase. This difference in the two patterns is explained as follows. Figure 3.14 showed the convergence trajectory for the 1^0 setting of the control rod location, wherein J attained 2.5dB and this value is shown included at a phase of 1^0 in the sinusoidal variation of J in the top half of Figure 3.15. The bottom half of Figure 3.15 shows that at the phase of 1^0, the exact estimate of the converged J is not 2.5 dB, but almost close to the primary power (93.9dB). The reason for this is that the control rod attains a negative value of the converged rod length at the 1^0 setting which is shown in Figure 3.16. At this setting the algorithm sets the rod length to a negative value of -0.229m. The program evaluates the exact estimate of the cost function by setting the rod lengths equal to zero whenever such negative values of rod lengths are attained. In the case of the single control rod problem here this means that when the converged rod length is negative the cost function will be set to the value of the primary power . But the algorithm continues to iterate negative values of the rod length. This behaviour of the algorithm can be explained using the term $e^{-jp\theta}$. In this term p=9 for the plane wave mode m=0 whose cancellation is being examined here and θ is the phase of the control rod. The term $e^{-jp\theta} = -1$ for all peaks mentioned in the bottom half of Figure 3.15, and the control rod produces an anti-phased mode at all these locations, which means there is perfect cancellation here. At the peak reduction locations in the top half of Figure 3.15, the term $e^{-jp\theta}$ alternates between –1 and 1. Cancellation is physically possible when this term equals -1. When the term assumes a value of 1 the control rod produces an in-phase mode with respect to that of the source rod. Cancellation is not physically possible here, as a rod cannot produce only a deficit in the fluid velocity and not an excess. But the algorithm makes this possible by extending the linear response characteristic in Figure 3.11 into the negative length space which reverses the sign of the magnitude of the modal amplitude. This is the reason the estimate of J using the linear response in the top half of Figure 3.15 gives a false indication of noise reduction. In the bottom half the exact response evaluated through the Fourier-Bessel expansion avoids estimating the cost function whenever the rod lengths converge to negative values. The following observations can be made from these illustrations in Figure 3.14, Figure 3.15 and Figure 3.16:

(i) The converged control rod length and cost function (from the linearised response estimates as well as the exact ones) vary sinusoidally illustrating the effect of phase as was explained in Section 3.4.

(ii) Control is not feasible in some sectors where the controller length attains negative values. The program simply sets the value of the exact estimate of the cost function equal to the primary power in such cases. Note that if a controller which exhibits bi-directional action of control, i.e, the one capable of creating both a deficit and excess of the velocity in the mean flow then control is possible even in these unfeasible regions mentioned here since the bi-directional action reverses the sign of the amplitude in the integration involved in the Fourier-Bessel expansions with the controller remains stationary in the spatial sense.

(iii) The maximum reduction obtainable as seen from the exact response based estimate of the cost function in Figure 3.15 is limited by the dotted line. This shows the actual maximum reduction in sound power obtained for the converged rod length of 0.229m against that predicted by the linear response based estimate (dashed line).

The next step is to examine the effect of adding a constraint to keep the rod lengths always positive and also to have the response approximated by a polynomial fit of the response. This is done as follows in a two-step process.

First a constraint is added programatically which zeros out any lengths in the iteration which become negative and the same algorithm is used with the linearised response. The results are shown in Figure 3.17 and Figure 3.18.

Observations:

i) Adding a constraint has eliminated negative lengths.

ii) Response linearisation still affects the error in the residual power (difference between the exact and linearised response based estimates of sound power)

Consequently the response was approximated using an 8^{th} degree polynomial in MATLAB. This approximated response is shown against the exact response in Figure 3.19 and this was fed to the program which was re-run for the above case and the results obtained are shown in Figure 3.20 and Figure 3.21.

Observations:

(i) Better prediction of the reduction in the noise power when compared to the case where linearised responses were used.

(ii) Approximating the response using the polynomial has only yielded a converged length of 0.234m because beyond this length the exact response exhibits a flat amplitude characteristic.

3.7. Summary

Thus the present Chapter has developed the requisite theory for the minimisation of the noise power. The relationship between the flow disturbance and the corresponding acoustic modes that it generates was examined. The controller response was determined using analytical expressions for the flow disturbances generated by the control rods. A simple case of the problem of cancellation of noise was studied by making one of the rods act as a source and another as a controller. It was deduced that cancellation is possible through translations and rotations of the control rod. It was also shown that the presence of the control rod can cause the production of modes other than the mode that is being considered for control and this subsequently led to formulation of the problem of noise optimisation. The simple case attempted for the problem of noise cancellation was repeated using an algorithm based on the noise optimisation theory. The noise cancellation problem thus became a test case for the optimisation algorithm. The simulation of the optimisation problem presented here revealed the importance of the approximation of the controller response and also constraining the control. In particular the polynomial approximation led to less error in the residual power estimates than the linear response, and constraining the algorithm caused the rod lengths to be positive. The next chapter examines the simulation study for the optimisation of noise power with multiple modes with the help of the constrained algorithm using the polynomially fitted response characteristic.

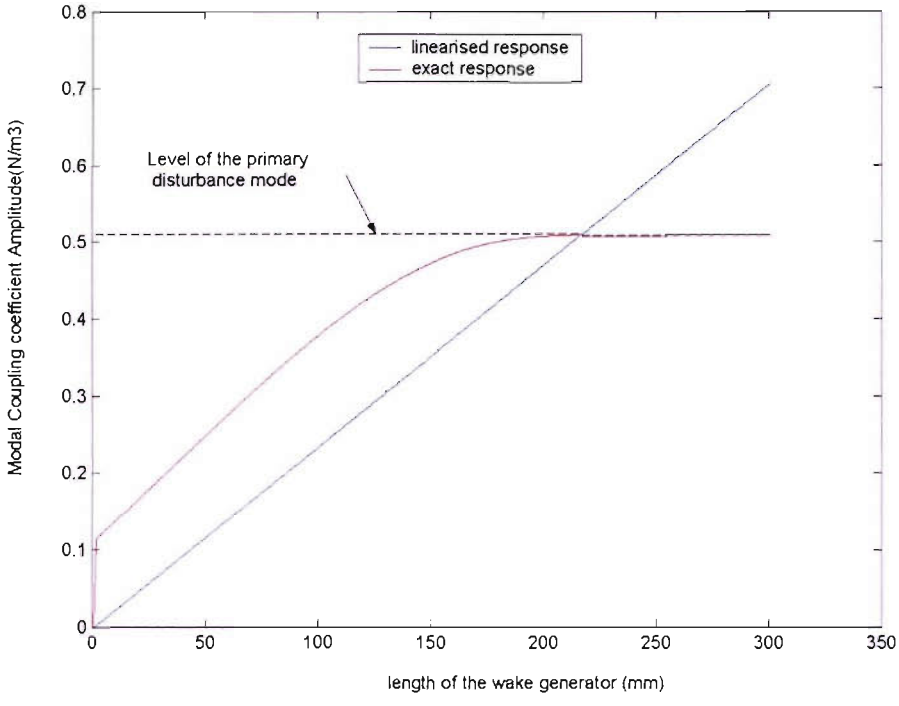

Figure 3.11 Linearised plane wave mode response (Fan speed 1800 rpm, BPF=270 Hz).

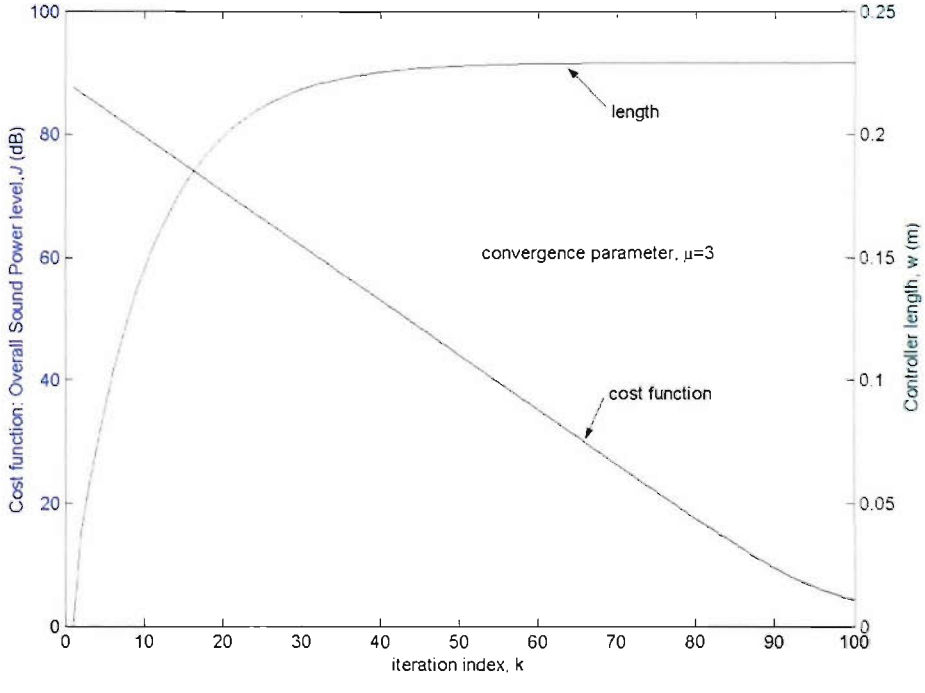

Figure 3.12 Cost function and controller convergence using steepest descent method.

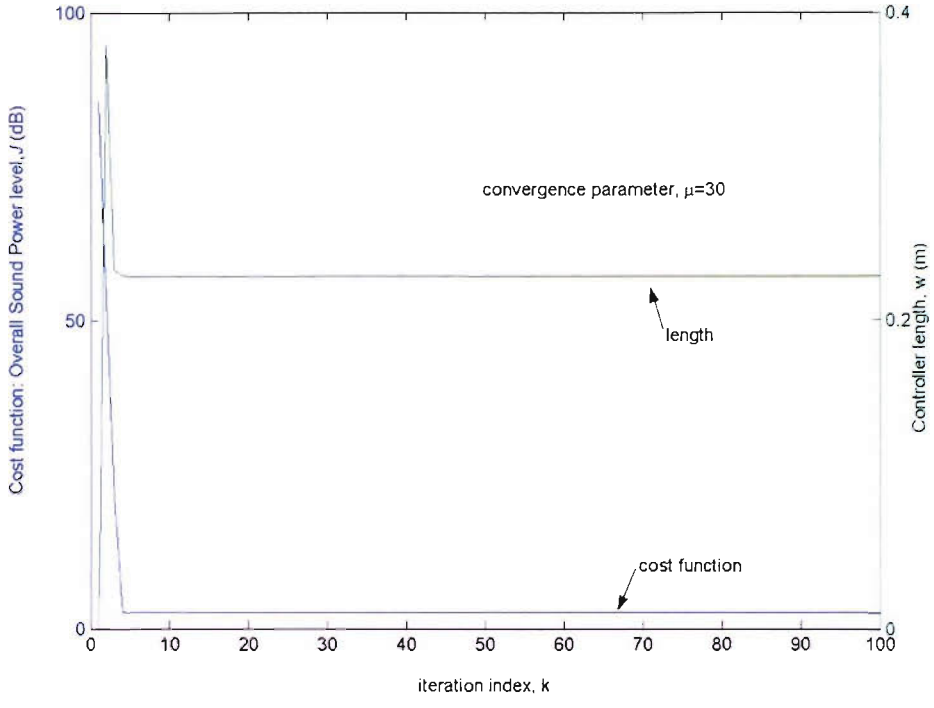

Figure 3.13 Cost function and controller convergence using steepest descent method.

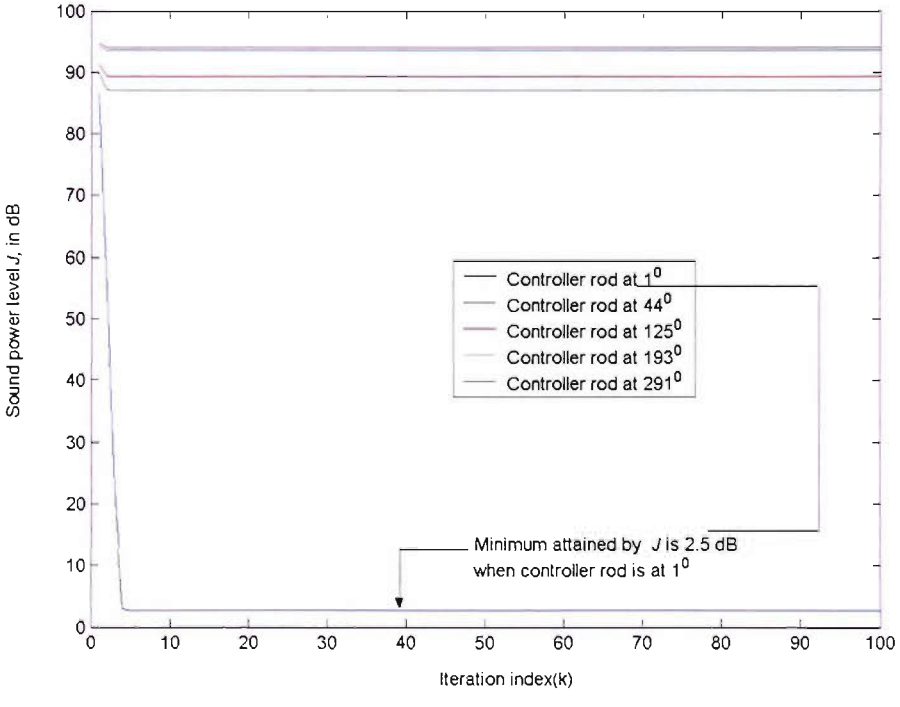

Figure 3.14 Convergence of the cost function with the rotation of the rod (linearised response, unconstrained), Harmonics = 1, Controllers = 1.

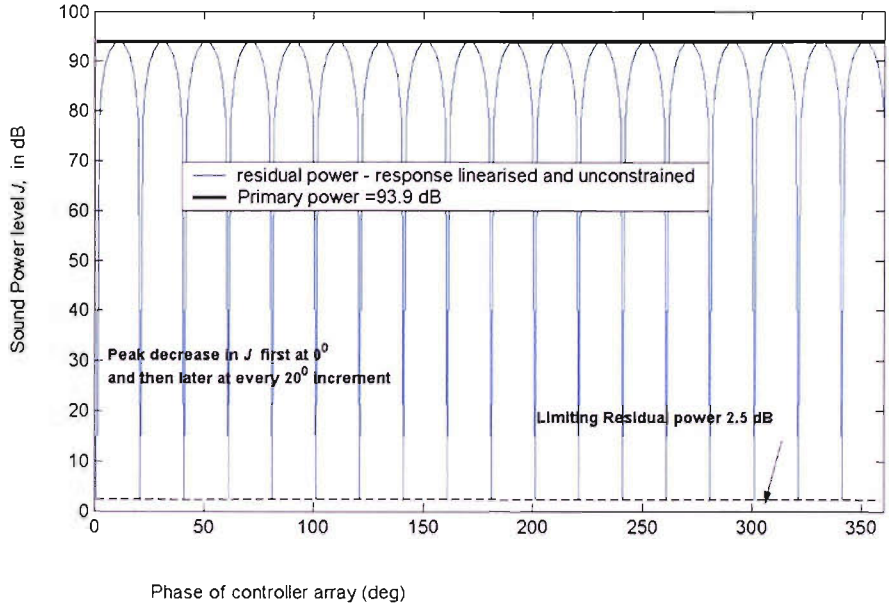

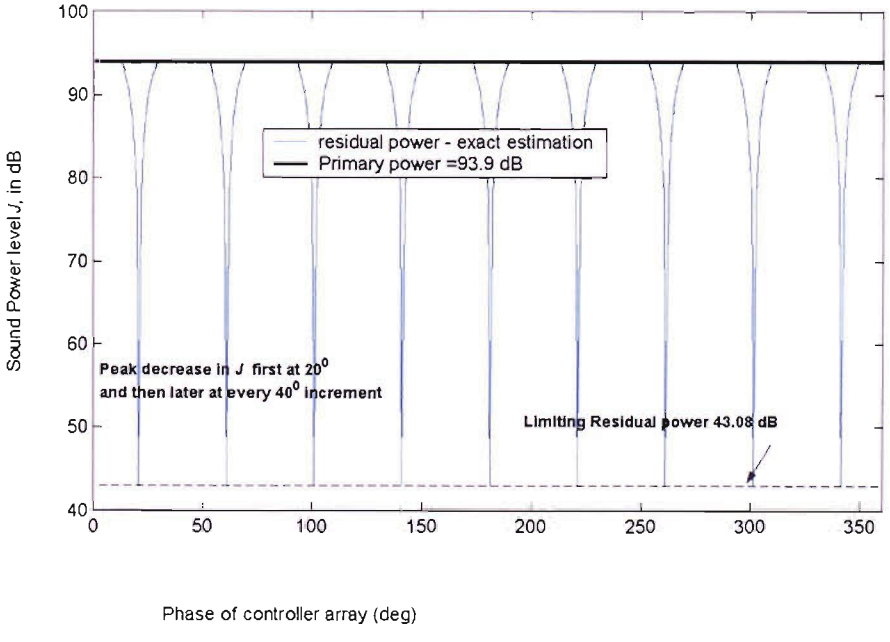

Figure 3.15 Converged cost function variation with rod rotation (linear response and unconstrained run of the algorithm) Harmonics= 1, Controllers= 1.

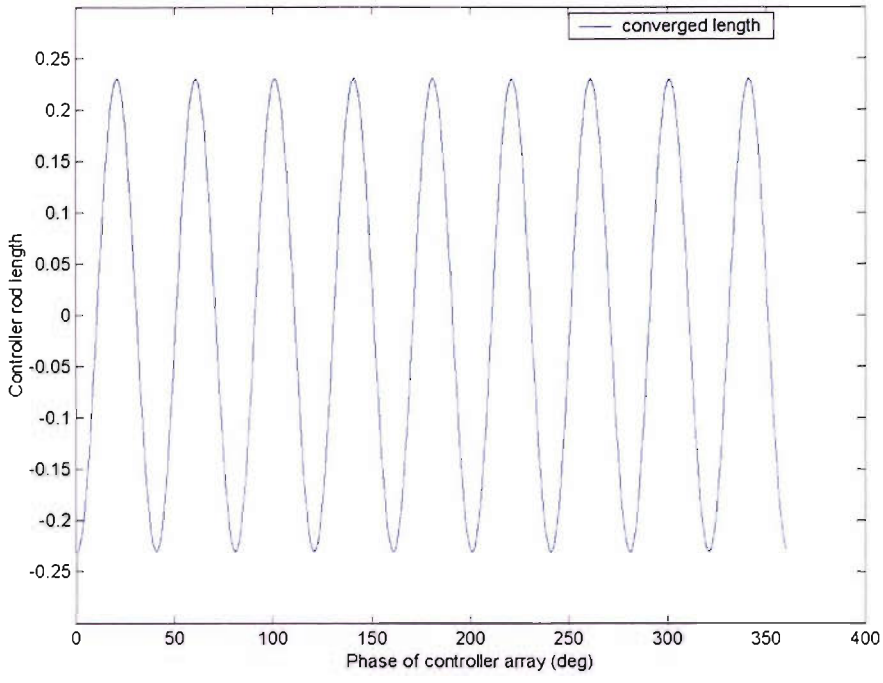

Figure 3.16 Converged rod length variation with rod rotation (linear response and unconstrained run of the algorithm) Harmonics= 1, Controllers= 1.

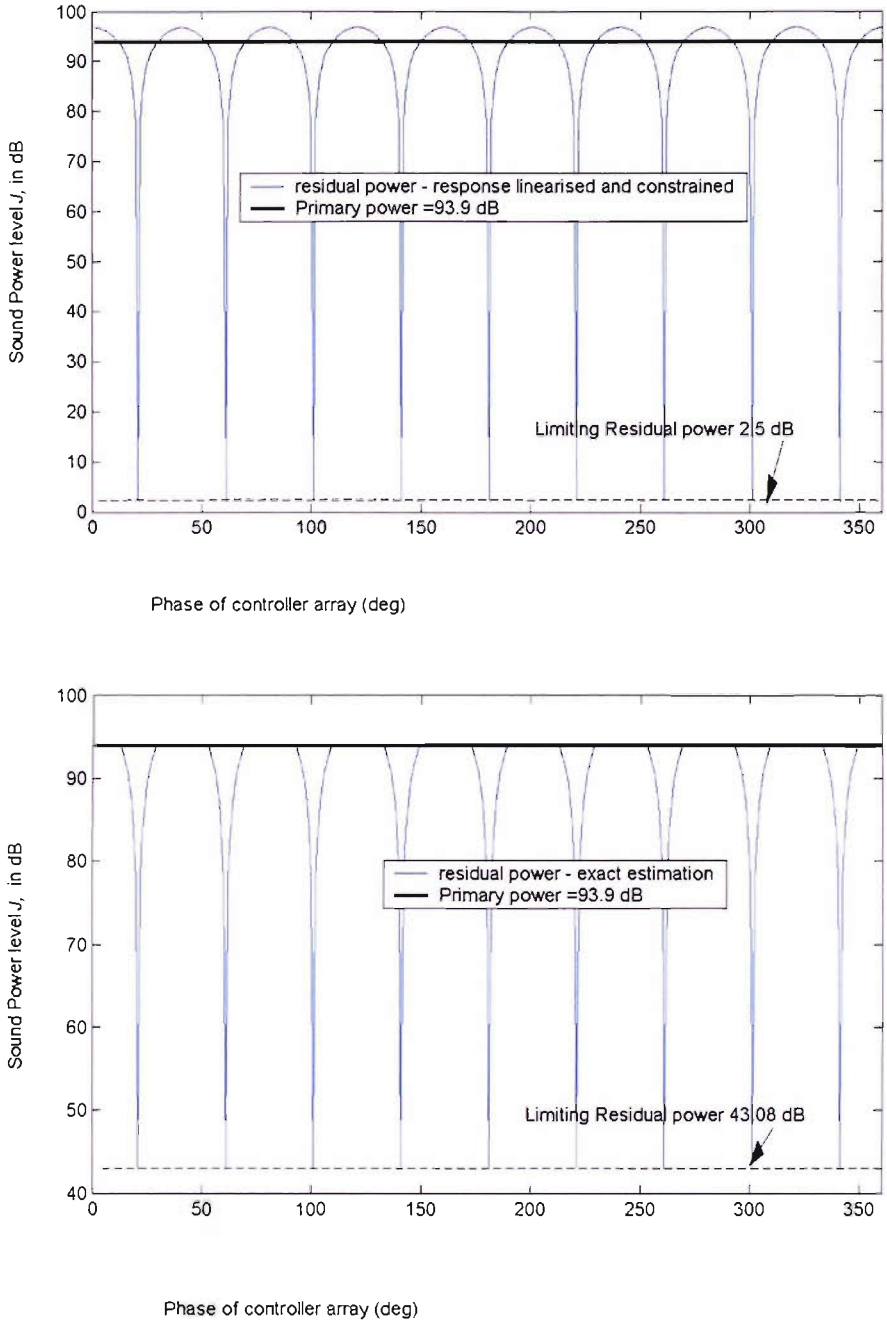

Figure 3.17 Converged cost function variation with rod rotation (linear response and constrained run of the algorithm) Harmonics= 1, Controllers= 1.

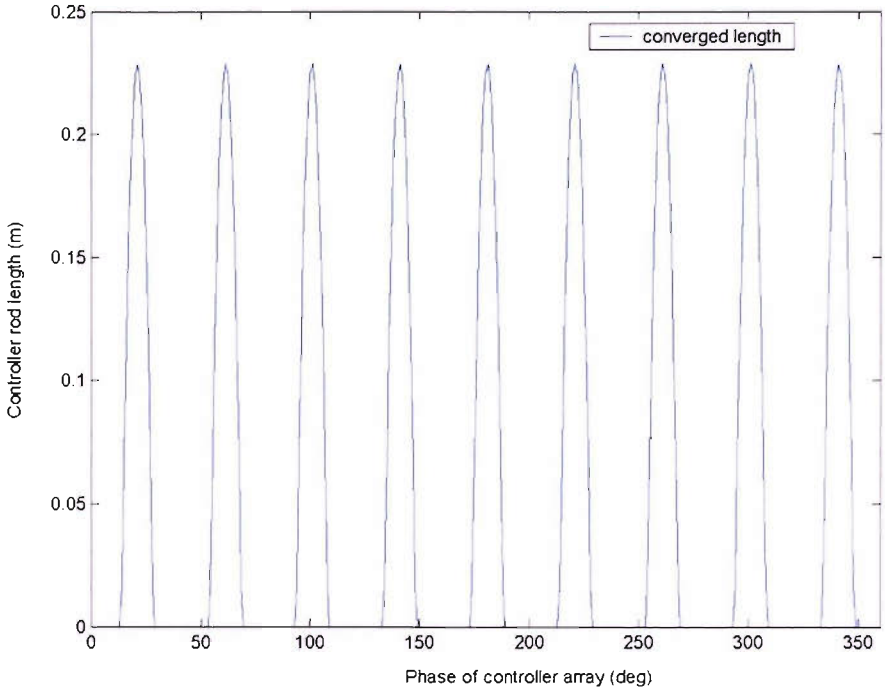

Figure 3.18 Converged rod length variation with rod rotation (linear response and constrained run of the algorithm) Harmonics= 1, Controllers= 1.

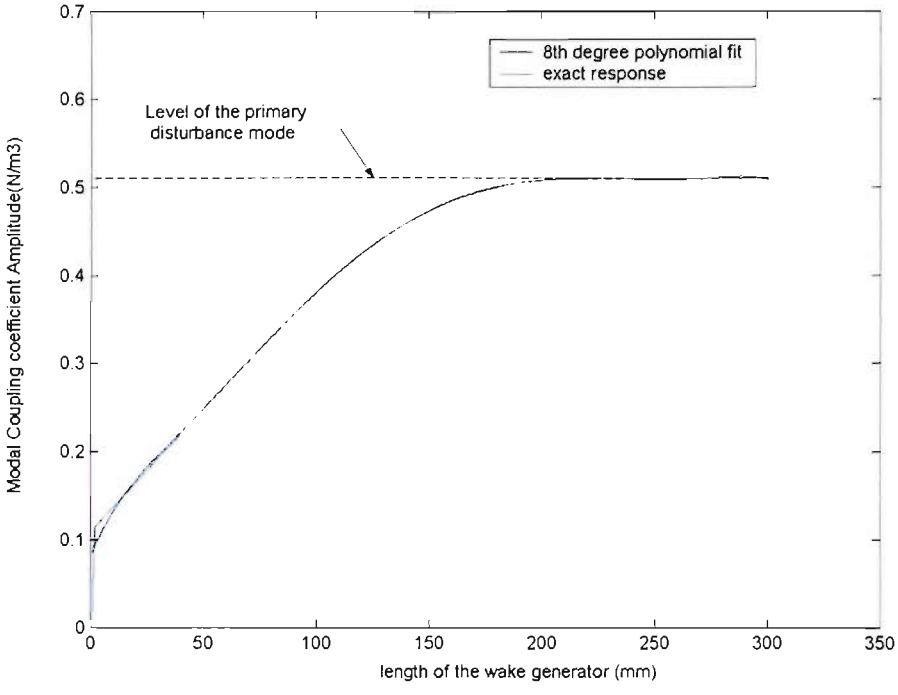

Figure 3.19 Polynomial fitted plane wave mode response (Fan speed 1800 rpm BPF=270 Hz).

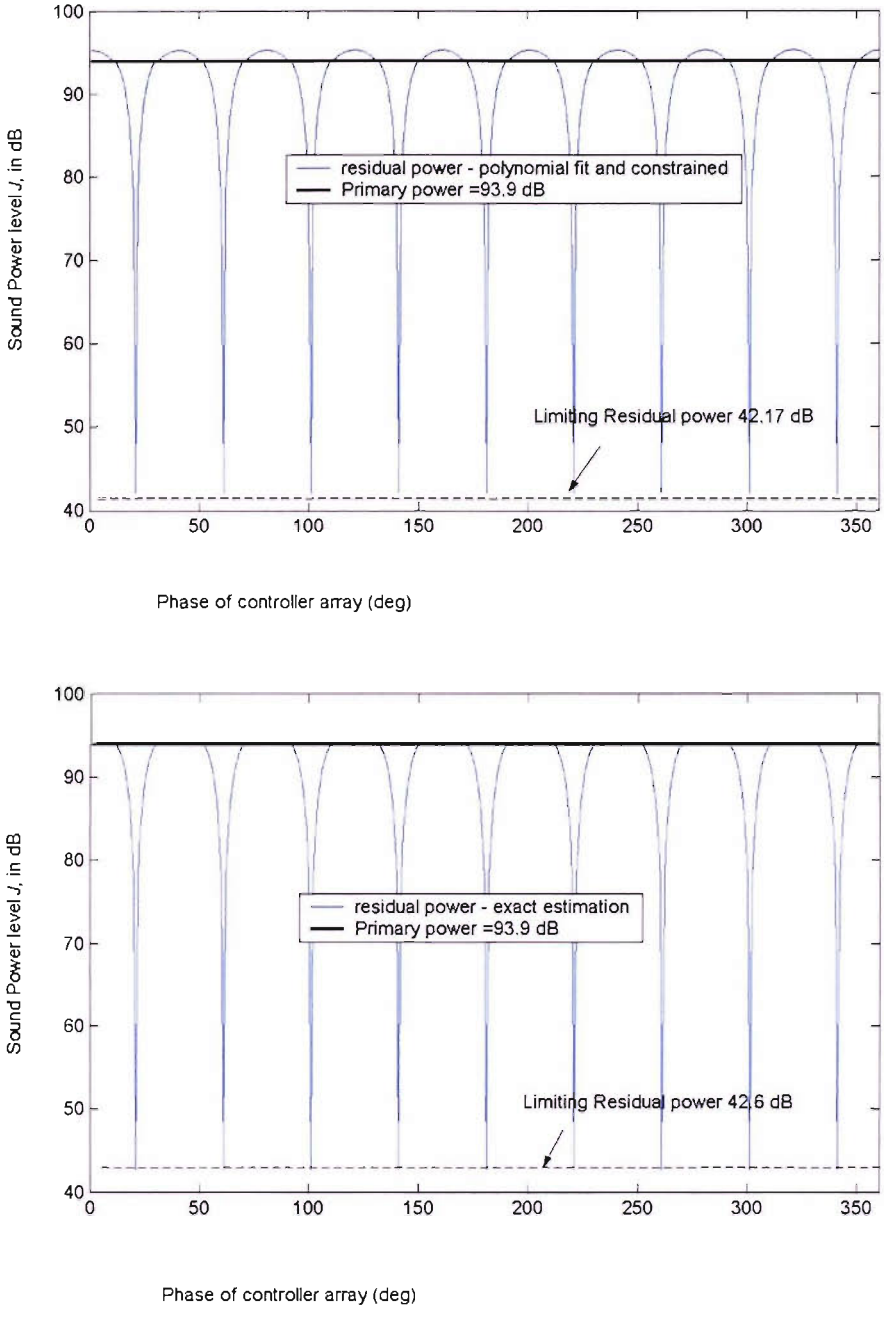

Figure 3.20 Converged cost function variation with rod rotation (polynomially fitted response and constrained run of the algorithm) Harmonics= 1, Controllers= 1.

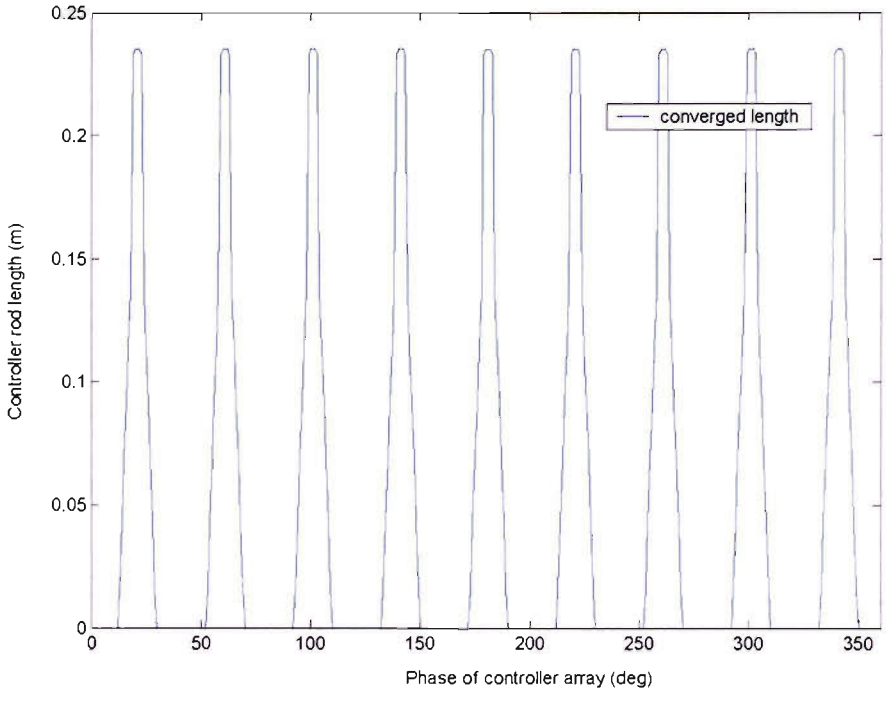

Figure 3.21 Converged rod length variation with rod rotation (polynomially fitted response and constrained run of the algorithm) Harmonics= 1, Controllers= 1.

Chapter 4 Simulation of Noise power minimisation

4.1. Introduction

The previous chapter dealt with the theory of noise optimisation and also with the simulation of a simple case of the cancellation of a single mode. It was pointed out that focussing on the control of a single mode can lead to the alteration in the intensities of the other modes and that the possible increase in the overall sound power evaluated for a set of modes should lead us to consider the optimisation of this quantity, and the present chapter aims to investigate this problem. A primary flow disturbance that is capable of generating multiple modes needs to be considered. Section 4.2 introduces two such disturbances, the first of these being a velocity defect that is harmonic with respect to the circumferential coordinate of the cross sectional plane and the other a random distribution of that quantity in the same plane. The acoustic modal content resulting from the interaction of these with the fan are also presented there. These disturbances are considered for control using equispaced rod arrays in Section 4.3 wherein the simulation problem presented in the previous chapter for the case of a single mode and a single controller is extended to multiple modes and multiple controllers. Section 4.4 considers the problem of cancellation of 3 modes using unequispaced rod arrays. Section 4.5 considers the inclusion of the phase of the array in the control vector.

4.2. Primary flow disturbances and the acoustic modal content from their interaction with the fan

Two flow disturbances were chosen for generating the primary acoustic field. They are (i) crossbar shaped and (ii) the randomly distributed flow disturbances, shown in Figure 4.1 and Figure 4.2. These are in the form of a defect in the velocity superimposed on the mean flow. In Figure 4.1 the crossbar shaped defect has four lobes of the velocity defect of –2 m/s. The random disturbance in Figure 4.2 is a defect in the velocity that was generated through the MATLAB randn() function.

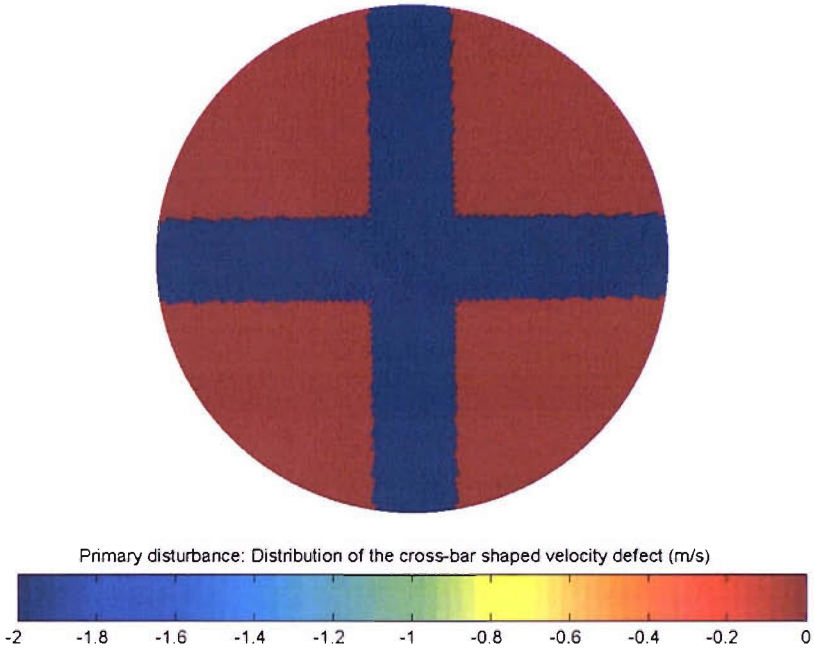

Figure 4.1 Crossbar velocity defect.

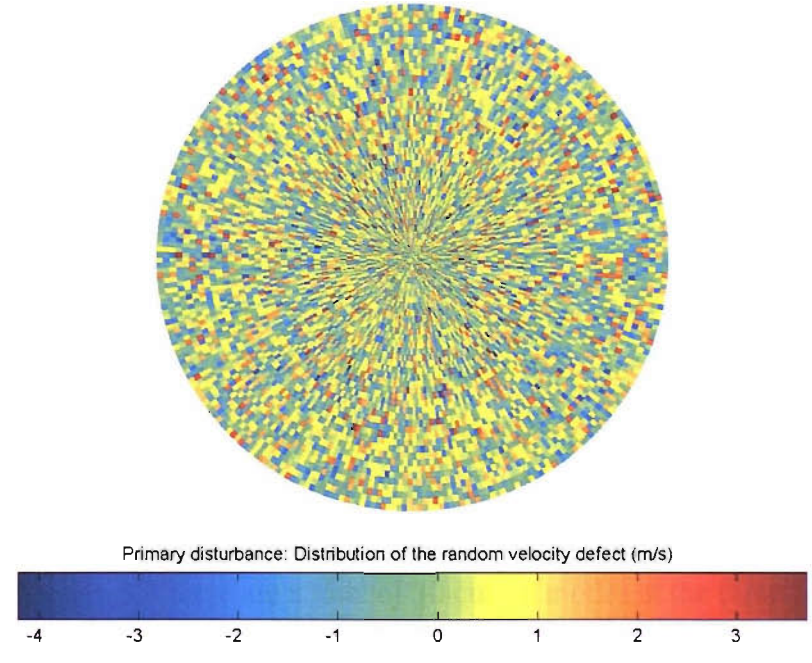

Figure 4.2 Random velocity defect.

Harmonic order (s)	Flow mode azimuthal order (p)	Acoustic mode azimuthal order ($m=sB-p$, $B=9$)	Acoustic mode radial order (n)
1	8	1	0
2	20	-2	0
2	16	2	0
3	32	-5	0
3	28	-1	0
3	24	3	0
3	28	-1	1

Table 4.1 Modes in the crossbar disturbance.

The harmonic-wise distribution of the modal content in the acoustic field generated by these two disturbances is shown in Figure 4.3 and Figure 4.4. This was found by using the acoustic response obtained from Equations (3.2.2) and (3.2.3) of Chapter 3 wherein the drag and the thrust terms $D^{\pm}_{mn,p}$ and $T^{\pm}_{mn,p}$ in Equation (3.2.2) are obtained from a Fourier-Bessel decomposition using Equation (3.2.3) of the two velocity defect profiles $w(r,\theta)$ given in Figure 4.1 and Figure 4.2. The amplitudes of the crossbar disturbance induced acoustic modes are shown in Figure 4.3 for the first three harmonics. They have a relationship with the spatial harmonics of the four-lobed crossbar in Figure 4.1 and only those acoustic modes are present in the system which are excited by the corresponding disturbance flow modes whose azimuthal orders are multiples of 4. As listed in Table 3.2 in Section 3.3 there are a total of 30 cut-on modes at the three harmonics when the fan rotates at 3000 rpm. With the crossbar defect the azimuthal order p of the flow modes can only be multiples of 4, so we have only a few cut-on acoustic modes whose order m bears a relationship with the spatial harmonics of the four-lobed crossbar defect. These modes are listed in Table 4.1 below and they

are the ones that are shown in the modal amplitude distribution in Figure 4.3 which can be referenced by their (m,n) indices.

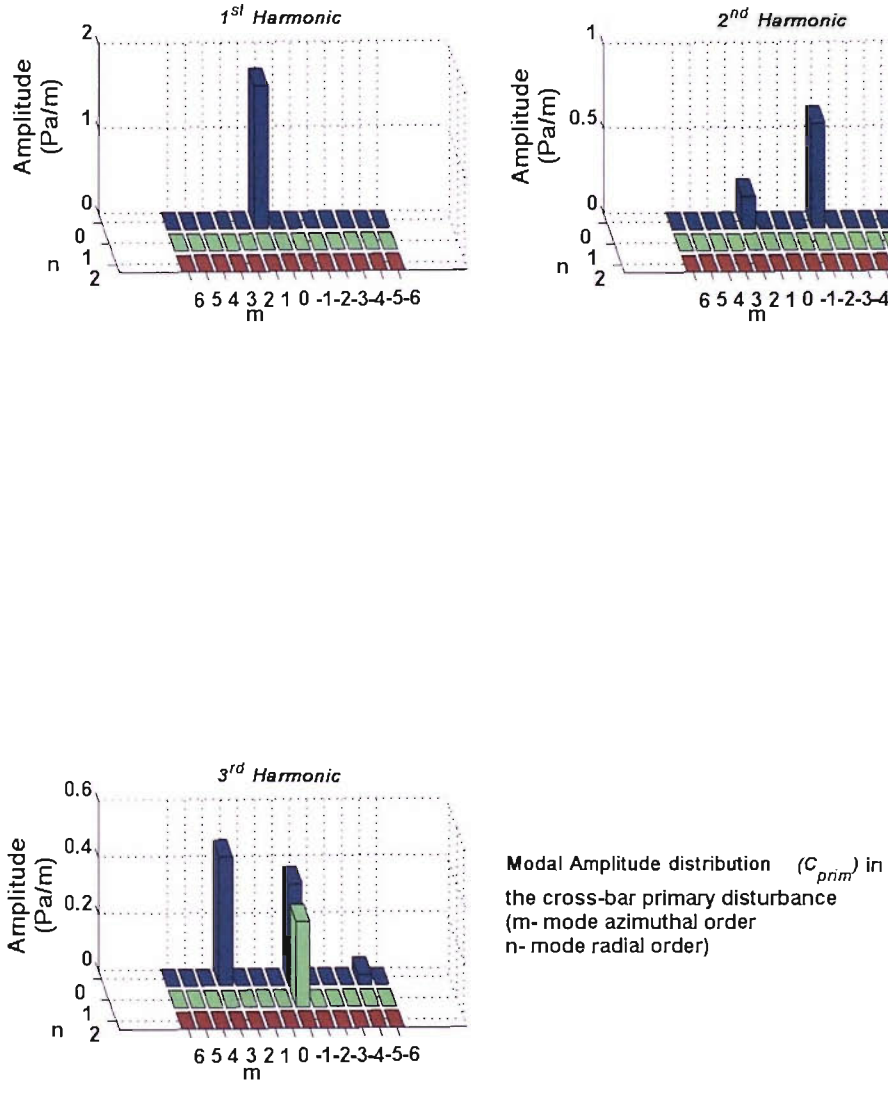

Figure 4.3 Crossbar defect generated modal amplitude distribution.

The random disturbance that was shown in Figure 4.2 induces flow modes of all spatial orders and hence is representative of a more general case of the acoustic modal content which is shown in Figure 4.4.

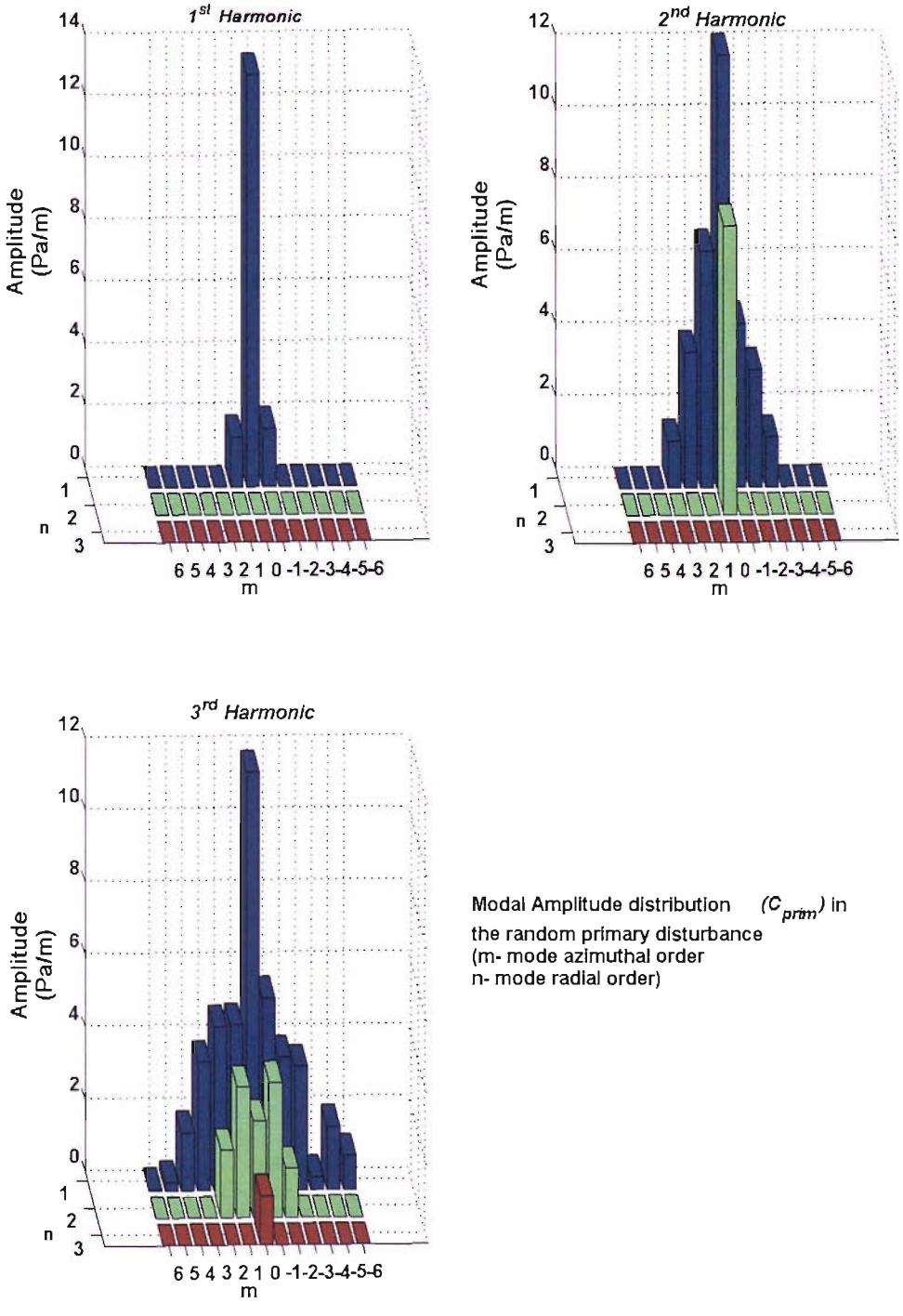

Figure 4.4 Random defect generated modal amplitude distribution.

The modes generated by the two flow disturbances discussed in this section are used as the primary noise field inputs in the optimisation simulations presented in the next section. In particular these inputs for the primary noise field modal amplitudes shown in Figure 4.3 and Figure 4.4 represent the quantity C_{prim} in Equation (3.5.4).

4.3. Control of the two flow disturbances using equispaced rod arrays

4.3.1. Cost functions in a multi-dimensional controller space

Since the problem of optimisation of the cases with multiple modes and multiple controllers is considered in this chapter, this section considers an optimisation case wherein illustration is provided for the error surface of the cost function J representing the total power resulting from the sum of the corresponding primary disturbance and the controller generated noise fields along with the convergence of the algorithm. The controller vector space $\mathbf{w}$ consisting of the rod lengths is gridded and the cost function is evaluated at each point in the gridded vector space. The case taken up here is that where the crossbar type of disturbance is controlled with 4 equispaced rods to optimise the noise power in the first harmonic.

The modal amplitude distribution in the first harmonic for the crossbar case was already shown in Figure 4.3. The modal amplitude distribution resulting from the gridding of the controller vector space of 4 equispaced rods is obtained by summing the responses of the individual rods in that space. The individual rod responses are obtained from the controller rod response which was already illustrated in Figure 3.7 and Figure 3.8 of Chapter 3. The cost function J in the gridded control vector space $\mathbf{w}$ is obtained using Equation (3.5.4). For the sake of illustration only the 2 rod subspace of the 4 equispaced rod array is gridded here. This is followed by running the control algorithm twice which uses a different initial condition of the rod lengths each time it is run.

Figure 4.5 shows the cost function error surface J in decibels of noise power obtained by gridding the 2 rod subspace of a 4 rod controller length vector

space. The space with the first two rods was gridded using the interval [0 0.3] m on each rod's length. The other two rods were maintained at 0.0427 m of length. Relative to the subspace there is a global minimum at the point corresponding to the rod's length vector of $\mathbf{w}=[l_1, l_2, l_3, l_4]=[0, 0.0427, 0.0427, 0.0427, 0.0427]$ m with the cost function at this point being 83.51 dB.

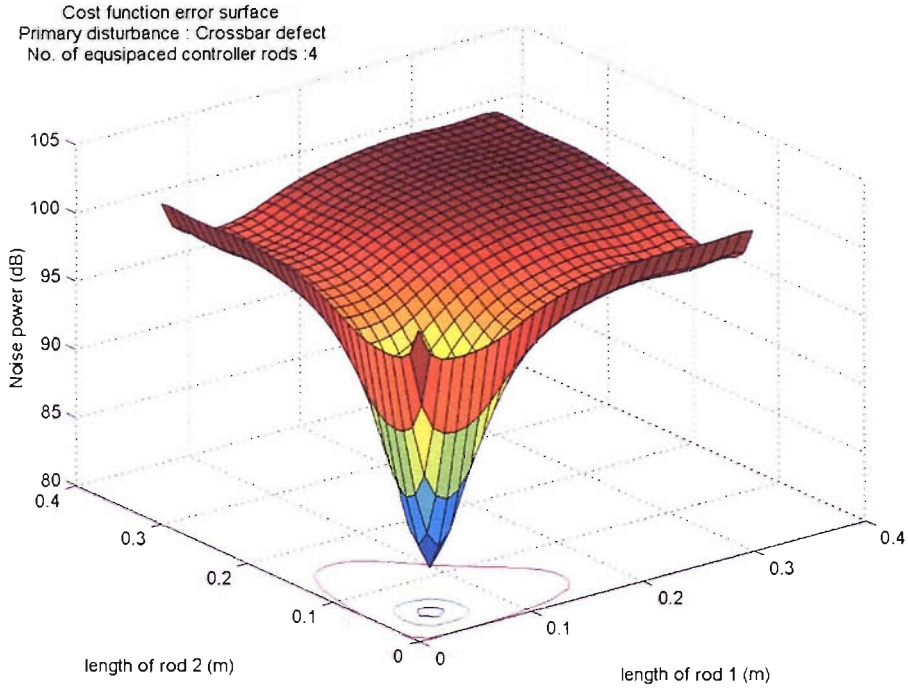

Figure 4.5 Cost function error surface.

The optimisation algorithm was run with a convergence coefficient of μ=.03 and an initial condition for the rod lengths was of $\mathbf{w}=[l_1, l_2, l_3, l_4]=[0, 0, 0.0427, 0.0427]$ m. The algorithm responded by converging to the minimum mentioned above and the trace of the algorithm is shown in Figure 4.6 where in the trace is superposed on the contour plot of the surface shown in Figure 4.5. This trace is marked as T1 on that figure.

Figure 4.6 shows another trace T2 of the algorithm obtained using a convergence coefficient of μ=.0005 and an initial condition for the control rod vector of $\mathbf{w}=[l_1, l_2, l_3, l_4]=[0.2500, 0, 0.0427, 0.0427]$ m. Instead of converging to the global minimum within the subspace the algorithm responded by converging to the local minimum at the point where the control vector corresponds to $\mathbf{w}=[l_1, l_2, l_3, l_4]=[0.2500, 0.0416, 0.0427, 0.0427]$ m and the cost function value of

100.65 dB. This shows that the initial condition selection can affect the optimisation by causing the algorithm to converge to local minima. This is consistent with the behaviour of the gradient-descent class of algorithms in regard to their application in the optimisation of non-linear functions. The cost function is non-linear because of the non-linear acoustic response of the controller rod which was discussed in the previous chapter. The global minimum mentioned above is only relative to the subspace discussed here.

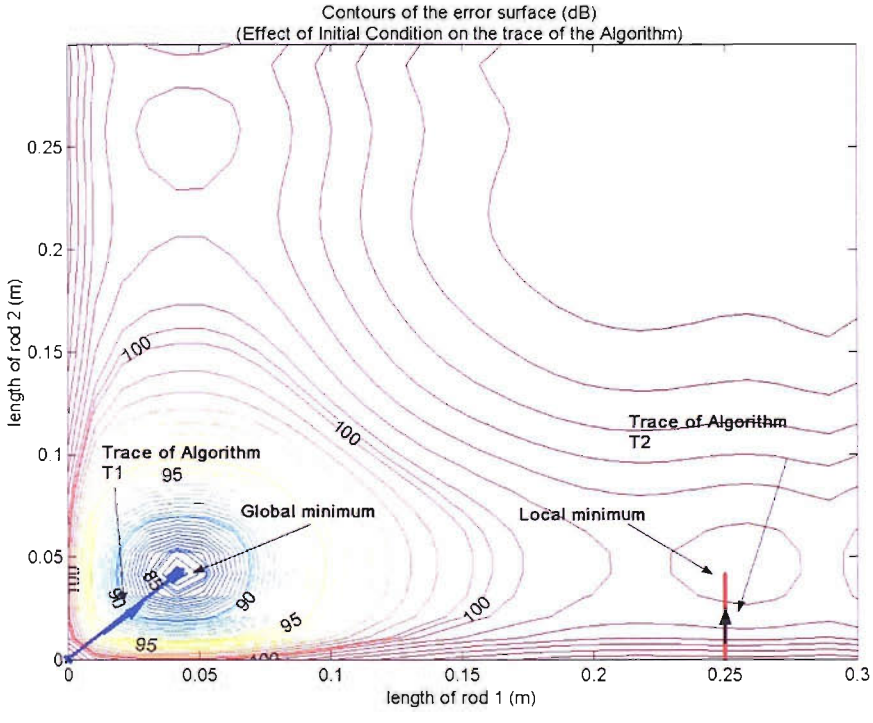

Figure 4.6 Effect of Initial Condition on Convergence.

The above cases were repeated for the random disturbance defect with 5 equispaced controller rods. The gridding was done on the subspace of rods 4 and 5 with the rods 1, 2 and 3 set at [0.2178, 0.0131, 0] m. Figure 4.7 shows the case of the error surface.

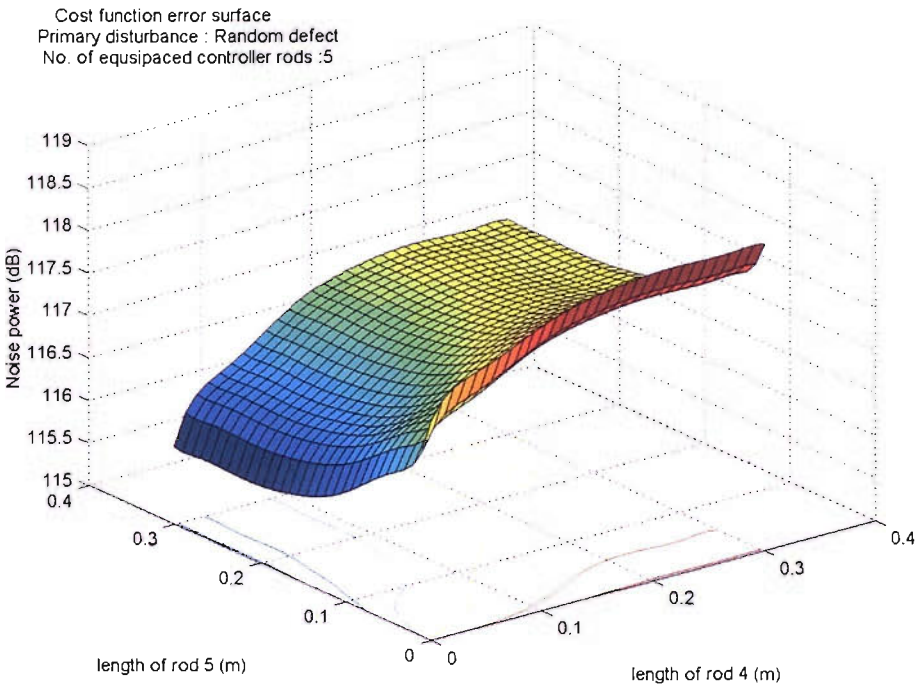

Figure 4.7 Cost function error surface.

Figure 4.8 shows the contours of the above surface with a superposed algorithm trace which starts with the initial condition of $\mathbf{w}=[l_1, l_2, l_3, l_4, l_5]=[0.2178, 0.0131, 0, 0, 0]$ m and a convergence coefficient $\mu = 0.01$. The algorithm traces out its path T1 to the "global" minimum at [0.2178, 0.0131, 0, 0, 0.2170] m with cost function being 115.8 dB. By changing the initial condition to [0.2178, 0.0131, 0, 0.3, 0] m and choosing a convergence coefficient $\mu = .001$ the algorithm traces out the path T2 to the local minimum at [0.2178, 0.0131, 0, 0.3, 0.1418] with cost function being 117.5 dB and this trace is shown in the same figure.

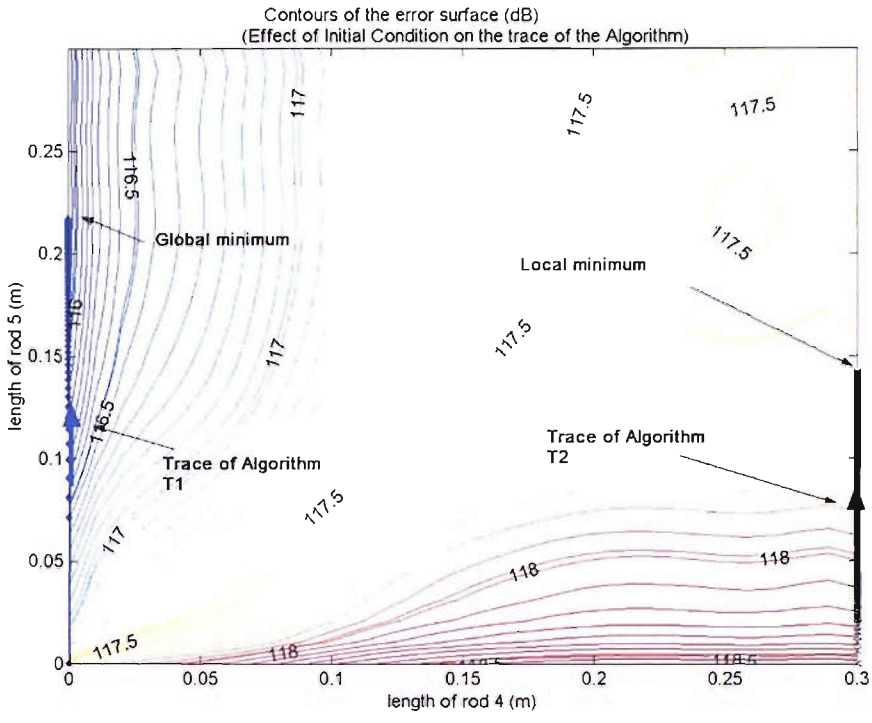

Figure 4.8 Effect of Initial Condition on Convergence (Convergence to local minima)

Having discussed the nature of the cost function and the convergence of the algorithm we now proceed to discuss the optimisation of the crossbar and the random disturbances with equispaced rod arrays in the following two subsections.

4.3.2. Control of the crossbar defect induced acoustic field

In this section the crossbar disturbance is considered for numerically simulating the control using 1, 2, 4 and 8 equispaced rod arrays. This choice of the equispaced rod array limiting it to 8 rods was made initially since the controller array meant for implementing the active control system on the fan rig discussed in Chapter 5 had 8 equispaced rods. The optimisation algorithm written in MATLAB was run for this disturbance by varying the number of harmonics in the cost function J from 1 to 3. As more harmonics are included in the cost function, more modes are present in the system to be controlled. For each case of the controller array, the array is phase shifted through $(2\pi/q)$, where q is the number of controllers since an equispaced rod array exhibits circumferential symmetry. This

means that to test the effect of the rotation of the rod array it would require 360^0 of phase shifting of the array if there is a single rod and 180^0 when there are two equispaced rods. The algorithm was run for each orientation of the rod array and the same quantities that were presented in the last section of Chapter 3 for the simple simulation case, i.e., the vector of converged controller lengths **w**, the minimum of the cost function J are presented for each equispaced rod array case. The case of optimisation with these rod arrays is discussed below for the 1^{st} harmonic modes included in the cost function. As in Chapter 3, in each case the residual power J in the system after convergence is estimated using the approximate and the exact responses of the rods and they are compared with the primary power. Unlike in the illustrations of the last section of Chapter 3 where the exact and linear response estimates were shown separately, these will be shown here superimposed over each other.

Figure 4.9 shows the residual power or the cost function variation with the phase of the array for the single rod array case after convergence. It can be seen that the cost function approaches a minimum at several orientations of the phase of the array when compared with the primary power (shown as straight line). The single rod that is used in this case to control the only mode in the 1^{st} harmonic can be oriented at any of these several locations which is where the controller generated mode is in anti-phase with respect to the primary noise field. The number of these locations also corresponds to the number of peaks or valleys along the circumferential direction on the Fourier-Bessel shape function of the flow mode $(p = 8)$ that induces the corresponding acoustic mode $(m = 1)$. The spacing between these feasible locations also corresponds to the spacing between those peaks or valleys, which is $(2\times360^0/8 = 45^0)$. Any orientation other than these is not optimal. The approximate estimate of the cost function J also tallies with the superimposed exact estimates. The controller length variation with the orientation of the array can also be seen in Figure 4.10. The controller attains positive lengths at the orientations where the cost function is less than the primary power. The last section of Chapter 3 discussed about constraining the algorithm. Due to this the algorithm has responded by turning off the controller at orientations where control is not possible. If a constraint was not used the algorithm would have responded

by setting negative lengths to the controller. This case is similar to the one presented in the last section of Chapter 3.

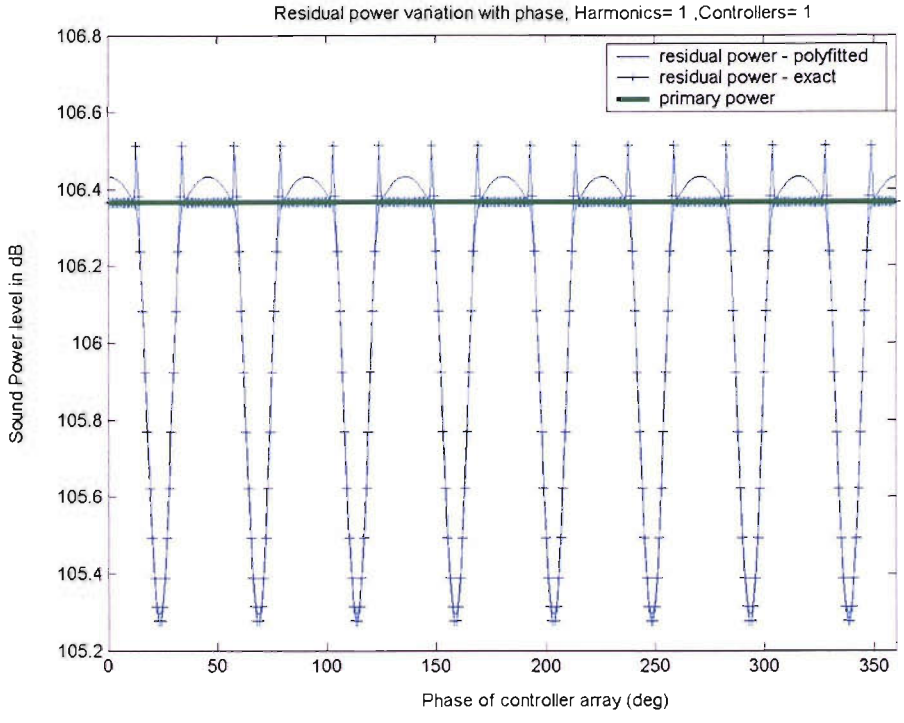

Figure 4.9 Control Cost function variation with phase of rod array.

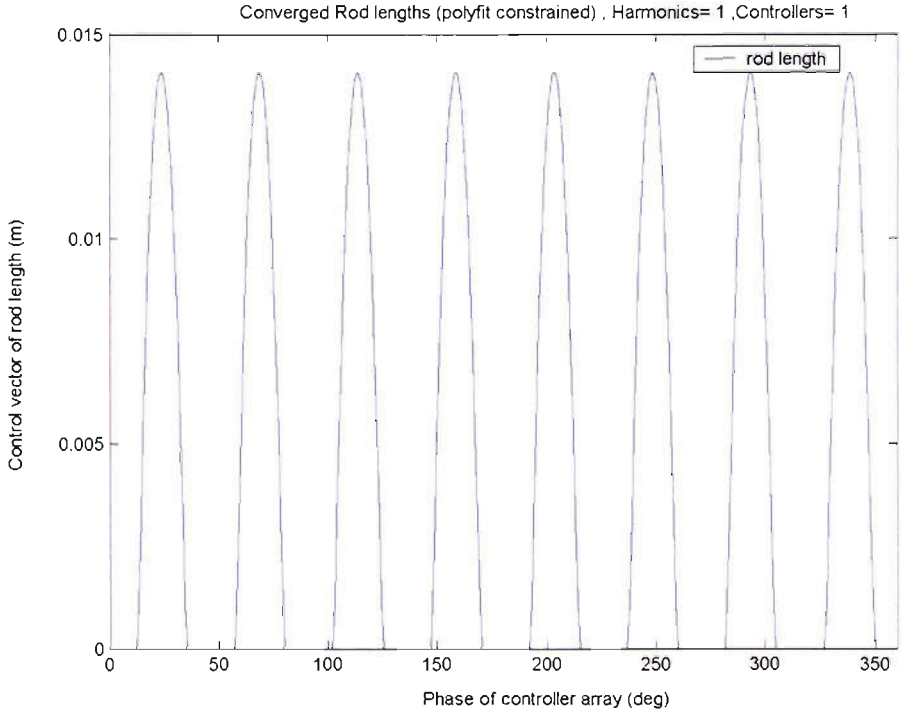

Figure 4.10 Controller length variation with phase of rod array.

Figure 4.11 through Figure 4.13 show the cost function variation with the rotation of the rod array for the 2, 4 and 8-rod array cases. The variation is presented over 180^0 of rotation of the rod array in the 2 rods case, and over 90^0 in the 4 rods and 45^0 in the 8 rods case, due to the effect of circumferential symmetry of the equispaced rods. As in Figure 4.10 the variation of the converged cost function has several dips (best optima) with respect to the phase of the rod array. As the number of controllers increases from 2 through 8 the amount of reduction increases as seen when the dips in the residual power are compared with the primary power in each illustration. Controller lengths are not shown as all the control rods in each case converge to equal lengths and the variation obtained is similar to what was shown in the single rod case in Figure 4.10. The increased reduction is obvious in the case of the crossbar shaped primary disturbance used since it has only one mode (m = 1 and p= 8) in the 1st harmonic and the individual rod positions on the equispaced 8 rod array case form a superset of those of the rest of the cases. And once one rod on the 8-rod array is aligned at an orientation (corresponding to the anti-phase radial line of the Fourier-Bessel shape function for the flow mode) in a way to produce a mode that is in anti-phase with respect to the mode in the primary field the rest of the rod positions can also be seen to be lying on the remaining anti-nodal lines and the effect of increase in the number of rods on the reduction obtained is cumulative. It is instructive to understand this result from the perspective of Equation (3.3.3) which expresses the modal response transposition when a rod is phase shifted. The following should make this clear: $e^{-jp\theta} = e^{-j(8\times q\times 2\pi/8)} = 1 \quad \text{for} q = 0\ldots 7$, which means that all the rods on the 8-rod equispaced array generate a contribution to the mode (of order (m,p)) that is in-phase for the mode that is being controlled in the current case, i.e., m= 1 and p= 8.

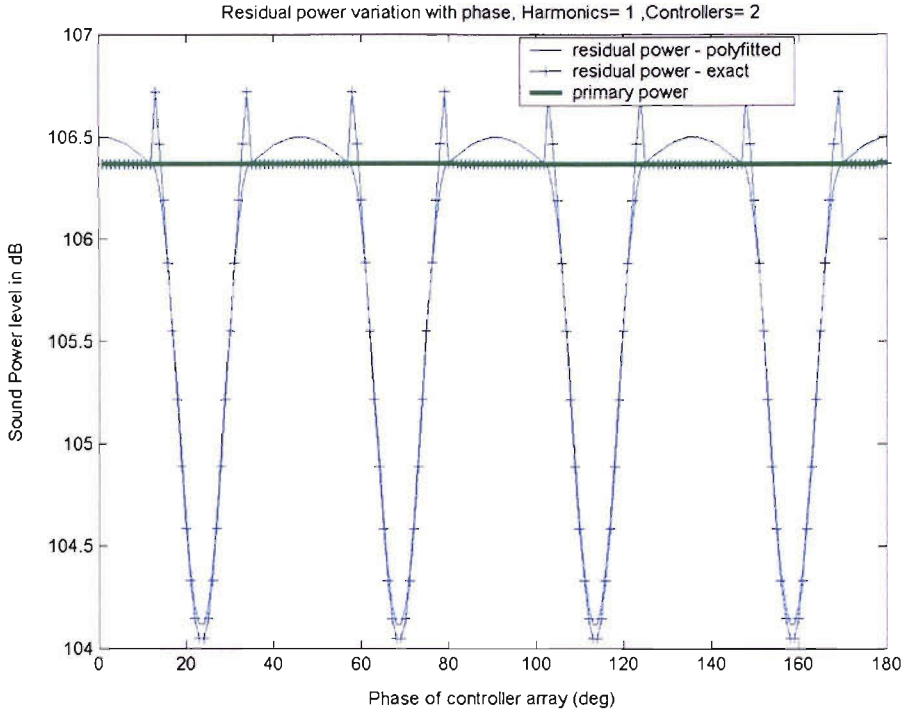

Figure 4.11 Control Cost function variation with phase of rod array.

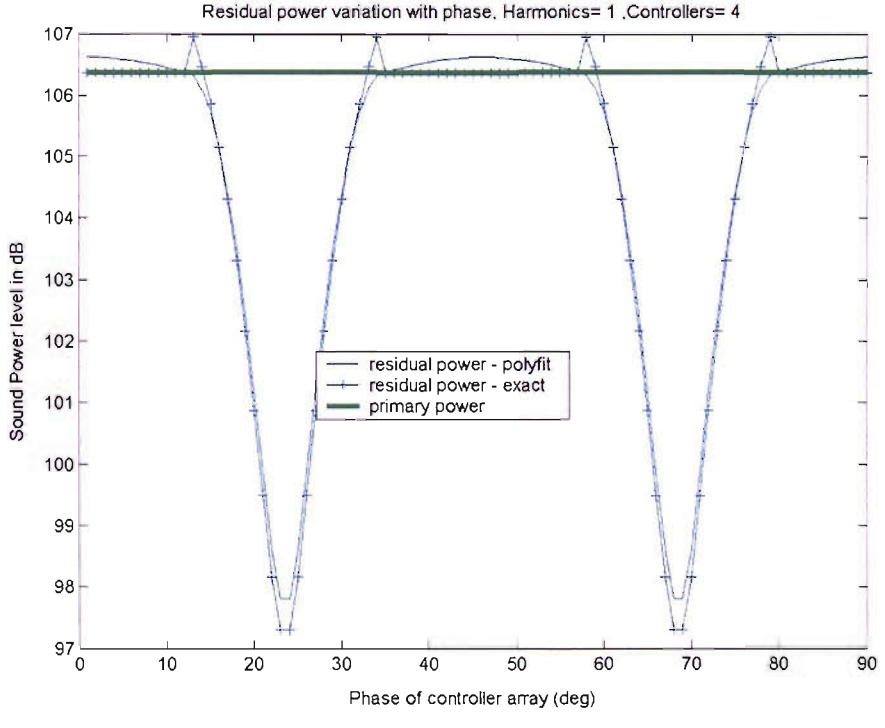

Figure 4.12 Control Cost function variation with phase of rod array.

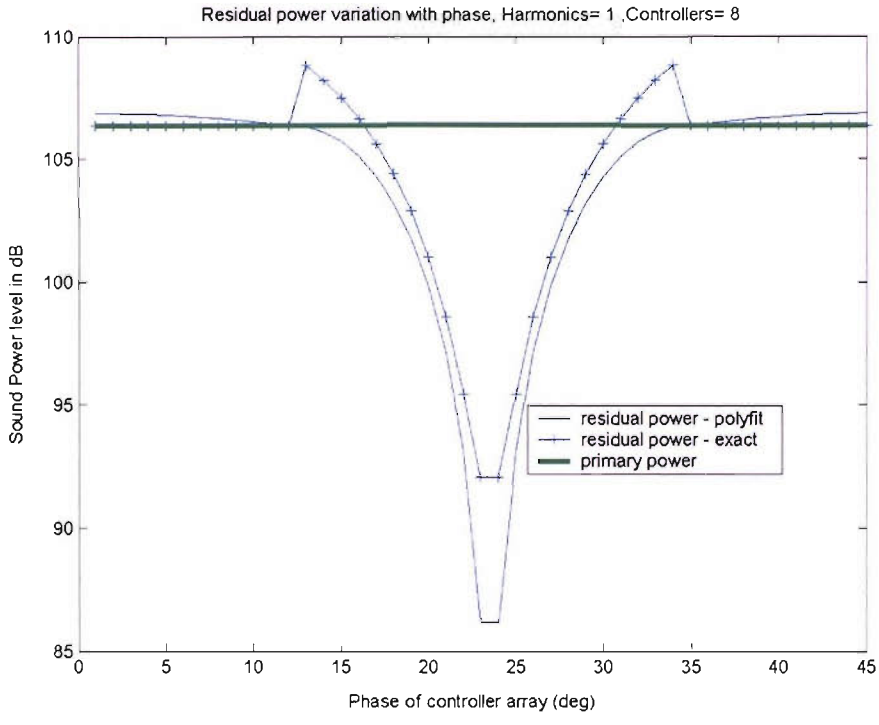

Figure 4.13 Control Cost function variation with phase of rod array.

The controller cost function and length variations are similar to those described above when more harmonics are included in the cost function and hence are not illustrated here.

From the above illustrations it appears that the 8-rod array seemed to have been effective for controlling the crossbar disturbance since the spacing of the rods on the array is perfectly suitable for the order of the mode (m = 1) that is being controlled.

4.3.3. Control of random velocity defect induced acoustic field

Before moving on to discuss the results for the random disturbance case it is instructive to ask ourselves what will happen when modes of different order to be controlled are present in the primary field, which is the case as seen in Figure 4.2 for the random disturbance modal amplitude distribution. Let us assume that there are three modes to be controlled, as in the first harmonic of the random disturbance modal amplitude distribution whose azimuthal orders are m =[-1, 0, 1]. Let us also assume that all 8 controllers are available to control these. Figure

4.14 through Figure 4.17 show the individual phase contribution of each controller on an 8-rod equispaced array for each of the three modes. Figure 4.14 shows the 8-rod array. Figure 4.15 through Figure 4.17 show the contribution to the modal amplitude vector by each controller for the particular mode on the complex plane. The modal phase for the reference controller in each case is assumed to be 0^0 for the sake of simplicity.

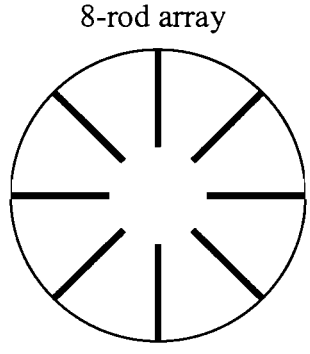

Figure 4.14 The 8–rod array

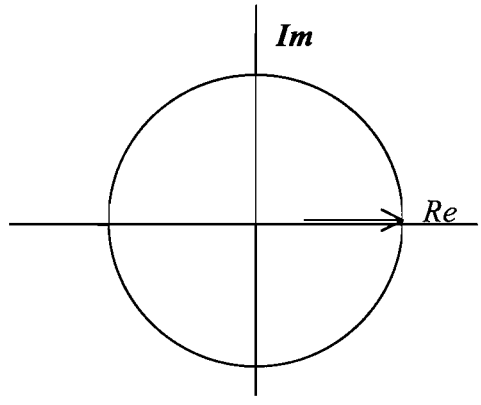

$$e^{-jp\theta} = e^{-j(8\times q\times 2\pi/8)} = 1 \quad \text{for} q = 0\ldots 7$$

Figure 4.15 Phase contribution for mode *m*=1.

From the above expression it is seen that all rods generate an in-phase contribution for mode m=1 (for which p=8).

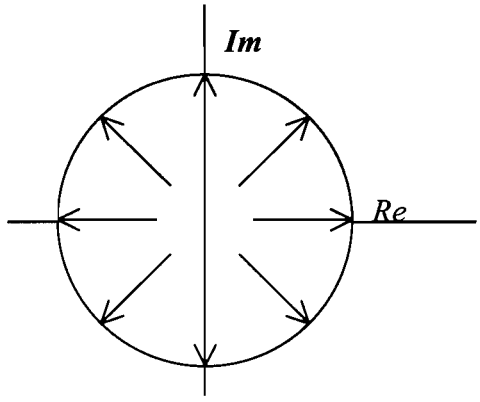

$$e^{-jp\theta} = e^{-j(9\times q\times 2\pi/8)} \quad \text{for} q = 0\ldots 7$$

Figure 4.16 Phase contribution for mode *m*=0.

From the above expression it is seen that half the number of rods generate an out of phase contribution for mode m=0 (for which p=9). For example if we assume that the modal amplitude vector for the first rod (q = 0) is along the real axis of the complex plane then the vector for the fifth rod (q = 4) lies opposite in phase to the that of the first rod. Substituting other values for q we can see that the contribution of rods q = 0-3 are opposite in phase to that of rods q = 4-7.

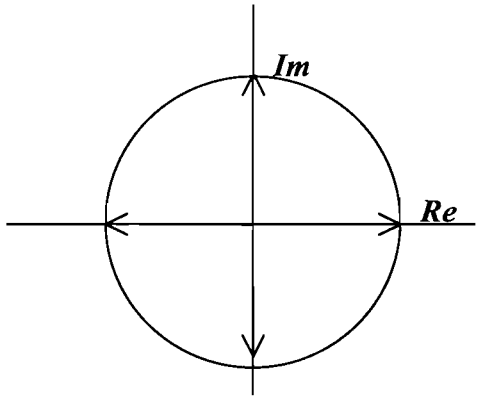

$$e^{-jp\theta} = e^{-j(10\times q\times 2\pi/8)} \quad \text{for} q = 0\ldots 7$$

Figure 4.17 Phase contribution for mode *m*=-1.

From the above expression it is seen that half the number of rods generate an out of phase contribution for mode m=-1 (for which p=10). Substituting q = 0-7 we

can see that the contribution of rods q = 0, 1, 4 and 5 are opposite in phase to that of rods q = 2, 3, 6 and 7.

Considering the problem of having to control three modes simultaneously, we see that the 8 rods produce an in-phase contribution for mode m=1 and if we assume that the three modes in the primary disturbance had some arbitrary phase angles and also assume that all rods on the 8-rod array are used to control the three modes, it would require a simple re-orientation of the controller array to make the rod generated contribution to mode m=1 in Figure 4.15 be out of phase with respect to the corresponding primary disturbance mode. We can also assume that the 8 rods have equal length which means that each rod makes an equal contribution to the anti-phase mode that is being generated. Having adjusted the orientation of the array to control the mode m=1 we see that the equal length 8 rod array will now be unsuitable to control the other two modes m=[0, -1]. This is because half the number of rods on the array generate an anti-phase contribution to other half, which means that the array of 8 rods of equal lengths is self-cancelling as far these two modes are concerned. Let us assume that we set half of the rods on the array to zero lengths and attempt to control the first mode m=1 by way of suitably adjusting the lengths which will not result in a self-cancelling contribution as far as the mode m=0 is concerned since the modal vectors as seen on Figure 4.16 on any consecutive half of the 8 rod array lie on one half-plane. Let us assume now that through readjustment of the lengths of the 4 rods we manage to control both the modes m=1 and m=0. Having done this we can now proceed to look at the control of mode m=-1 using one half of the 8-rod array that was used to control the other two modes. Comparing Figure 4.16 and Figure 4.17 we see that the half of the 8-rod array that was used to control the other two modes can now result in a system wherein one half of the 4 rods produces an out of phase contribution with respect to the other half as far the last mode m=-1 is concerned. Attempting to explain in the above manner the control in case of a system that has an arbitrary number of control rods and modes to be controlled can be quite complex and it should be left to the algorithm to decide the best choice of the rod system for the noise minimization problem.

From the above discussion it should be clear that as more modes are introduced into the control system, using more controllers on the array becomes ineffective. Only a quarter of the controllers on the 8-rod array are effective for

controlling the three modes mentioned above. This should be expected from the simulation results for the random disturbance case. Only two cases are discussed here for the random disturbance, i.e., the single rod and the equispaced 8 rod array cases. The cost function variation is presented for the single rod case in Figure 4.18. The single rod case is illustrated here only to show that the feasible orientations where the controller can be placed for the single rod case follow the same pattern of dips in the variation as was shown in single rod array control of the cross bar defect. But the reduction obtained at each of these locations is not the same since there are three modes being controlled in the 1st harmonic of the random defect unlike, in the crossbar case which had only one mode. Compared to the primary power the dips in the cost function variation had the same depth in the crossbar case as was seen in Figure 4.9, Figure 4.11-Figure 4.13.

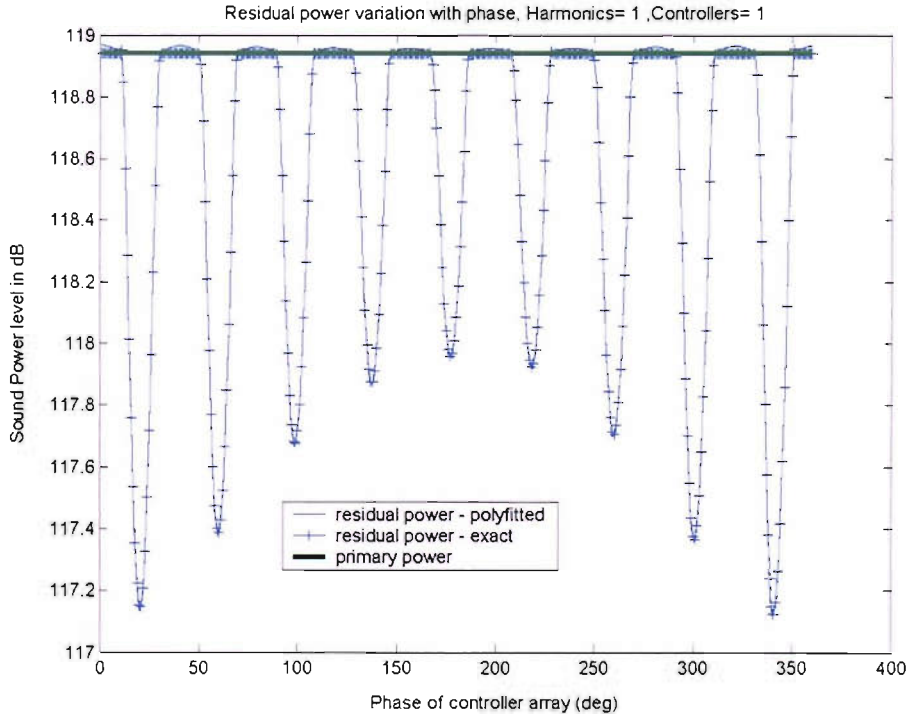

Figure 4.18 Control Cost function variation with phase of rod array.

The cost function variation is presented for the 8 rod case in Figure 4.19. The discrepancy in the exact and approximate estimates of the cost function is due to some of the controllers attaining lengths close to the [0, 0.001] metres length interval range which is where the polynomial fit does not give a good

approximation with the exact response. The 8-rod case assumes significance for illustration here since there are three modes being controlled with 8 rods. As was explained above only quarter the number of controllers, i.e., two controllers, would turn out to be effective for this purpose. The cost function variation shows that the minimum appears when the array is oriented at around 25^0. The variation of the converged controller rod lengths in the 8-rod array are shown against the phase of the rod array in the top half of Figure 4.20 for this case. Around 25^0 for the phase of the 8-rod array Figure 4.19 shows a dip in the variation which means that the power reduction is at its maximum here. Only the variations of four converged controllers (rods 1,2,7 and 8) out of the 8 rods are marked using the symbols '*', 'o', 'x' and '+'. It can seen from these markings that only three controller rods marked (using '*', 'x' and '+') on the illustration converge to positive lengths at 25^0 and they occur one after the other in succession in terms of their order in the controller array. This is made clearer in the bottom half of Figure 4.20 which shows the configuration of the converged rods at the phase of 25^0 of the rod array. All 3 rods are seen to be in the same quadrant. The reason that only 3 out of the 8 rods converged to positive lengths is the same as was explained before regarding effectiveness of an equispaced controller rod array to control multiple modes.

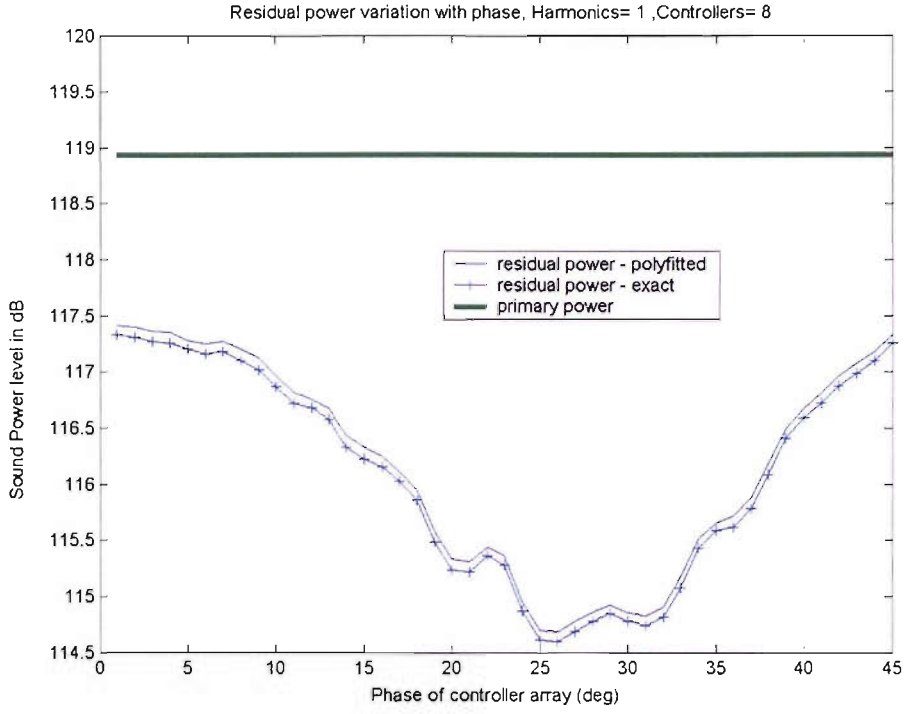

Figure 4.19 Control Cost function variation with phase of rod array.

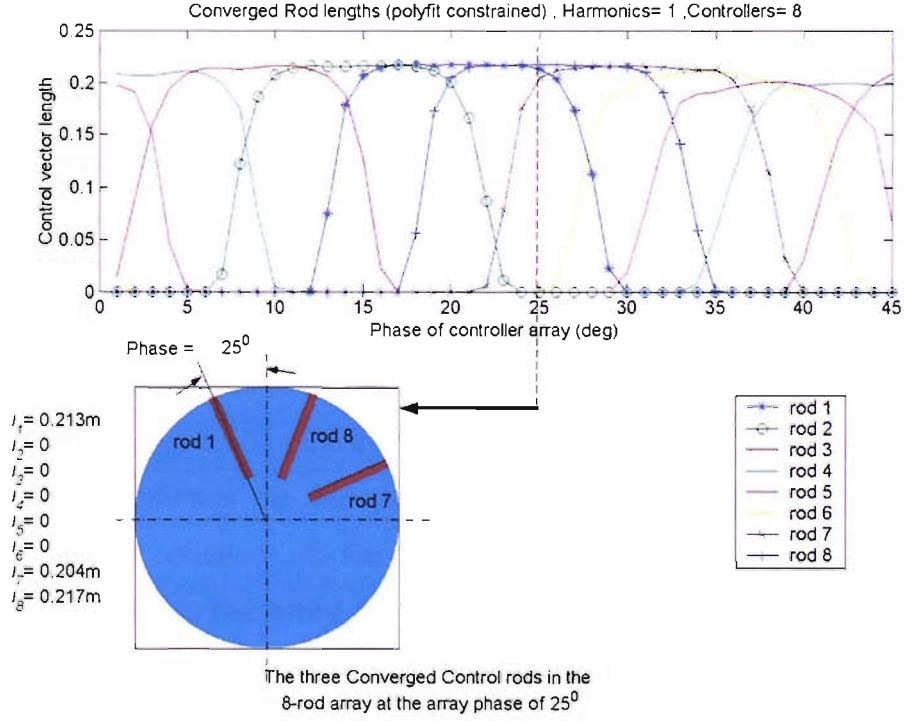

Figure 4.20 Controller length variation with phase of rod array

The number of equispaced rods was stepped from 1 through 20 to control the random disturbance, and the variation of the minimised cost function with the phase of the rod array in each case was determined as was done for the cases described above. The minimum from this phase characteristic was determined and the variation of this minimum is plotted against the number of controllers that were stepped through in Figure 4.21. For example, the effect of an equispaced 8-rod array to control the random disturbance was illustrated in Figure 4.19 for the converged cost function variation with the phase of the rod array. This variation also showed that the best minimisation happens at the phase of 25^0. The cost function attains a value of 114.6 dB at this phase in this variation. Values like these are extracted from each run of the equispaced array with the rods stepped from 1 – 20 and plotted in Figure 4.21 against the number of rods used in each run. The curves shown are for the three harmonics of the blade passing frequency. The primary power without control in each harmonic is also shown in the figure so that the reduction in the power in each control case can be inferred by comparing the variation of the minimised cost function with the primary power. It can be seen that the reduction obtained through control decreases as the number of harmonics being controlled increases. Though there is increased reduction as the rods increase to 20, this is not gradual. In Figure 4.22 - Figure 4.24 the variation given in Figure 4.21 is repeated and also the break-down of the power in the individual harmonics is given. For example in the top half of Figure 4.22 the variation in the minimised cost function with the number of rods is plotted for the control of the first harmonic. In the bottom half the break up of the power in the three individual harmonics is also given. From these three figures, Figure 4.22 - Figure 4.24, it appears that most of the control is happening in the first harmonic. As already mentioned the variation illustrated in Figure 4.21 is that which is obtained after collation of the best minimisations happening at particular orientations of the rod array in each rod array case. These orientations are different for each rod array case. In Chapter 3 while explaining the noise cancellation concept the simulation of the cancellation of the single mode revealed that the cancellation happens when the control rod is placed at orientations along the circumference which have a simple relationship with the nodal line on the Fourier-Bessel function for the corresponding flow mode that excites the acoustic mode. In the present case the best orientations for each rod array case were

examined to see if they have any relationship with the phases of the three modes in the first harmonic. It was found that no such simple relationship exists as was seen to exist in the cancellation of the single mode. This should be expected from the complexity of the problem as was illustrated in the beginning of this section with the case of control of multiple modes with multiple rods. It suggests that it is through running the algorithm that one should determine the positioning of the array in each individual case.

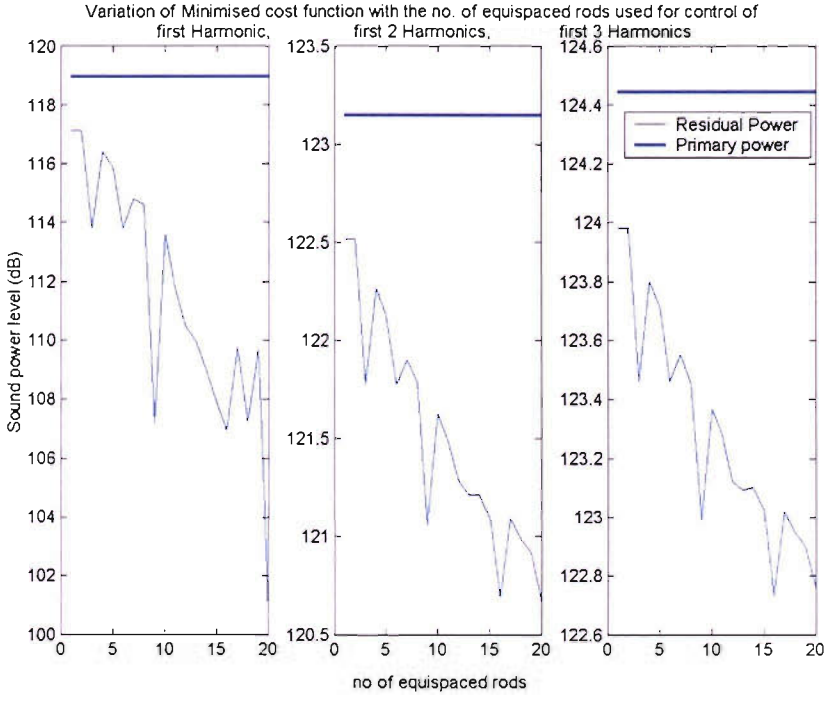

Figure 4.21 Variation of minimised noise power against the number of equispaced controllers for the random disturbance.

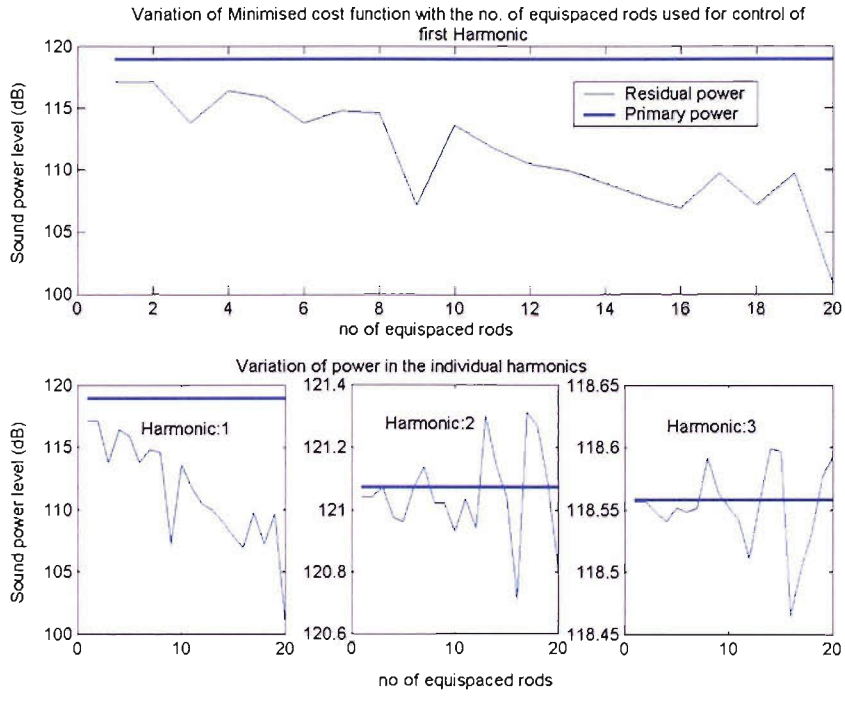

Figure 4.22 Variation of minimised noise power against the number of equispaced rods used to control the 1st harmonic in the random disturbance (with break-down of power in the individual harmonics).

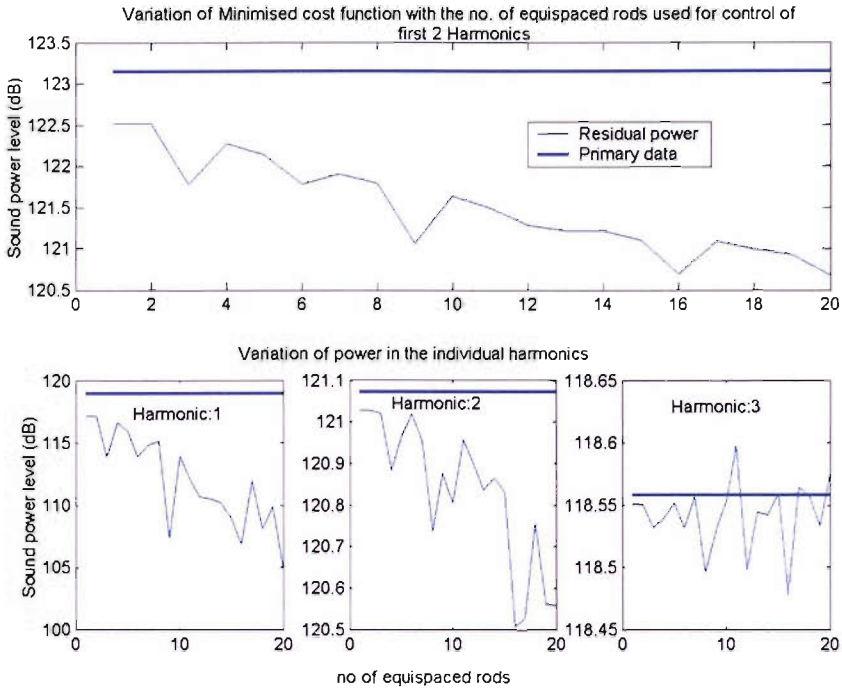

Figure 4.23 Variation of minimised noise power against the number of equispaced rods used to control the first two harmonics in the random disturbance (with break-down of power in the individual harmonics).

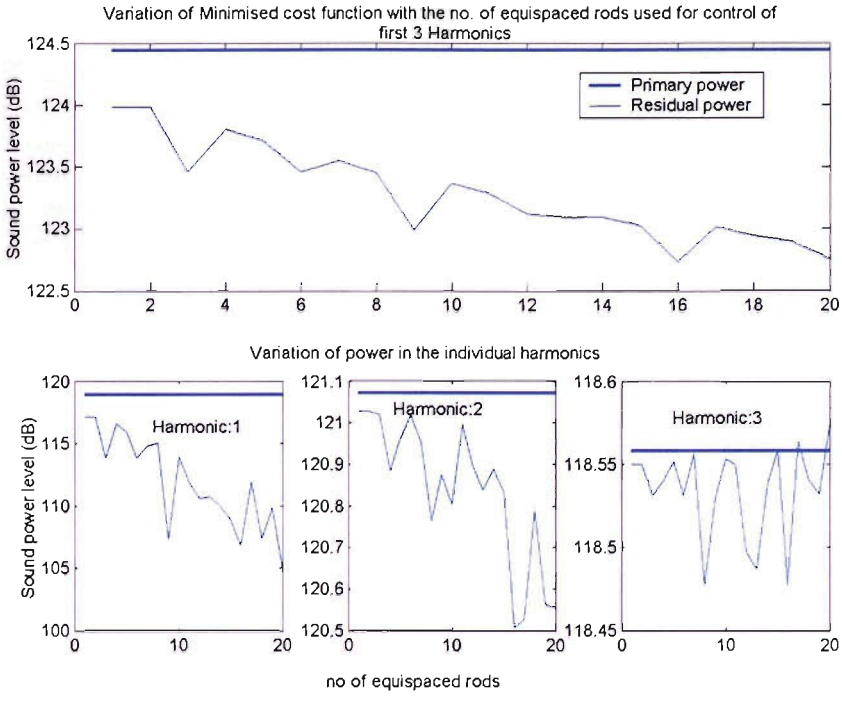

Figure 4.24 Variation of minimised noise power against the number of equispaced rods used to control the first three harmonics in the random disturbance (with break-down of power in the individual harmonics).

For the best orientations discussed previously in the individual cases of control using 1-20 equispaced rod cases, the configuration of the converged rod lengths are shown in Figure 4.25. Similar such configurations were obtained when the subsequent harmonics were also included in the control cost function.

The optimal configurations shown in Figure 4.25 for the equispaced rod cases were analysed to see if they induce similar blade loadings. It was found that they do not induce similar blade loadings since the break-down of power in the individual harmonics in Figure 4.22 - Figure 4.24 show that the residual power resulting from each configuration is different.

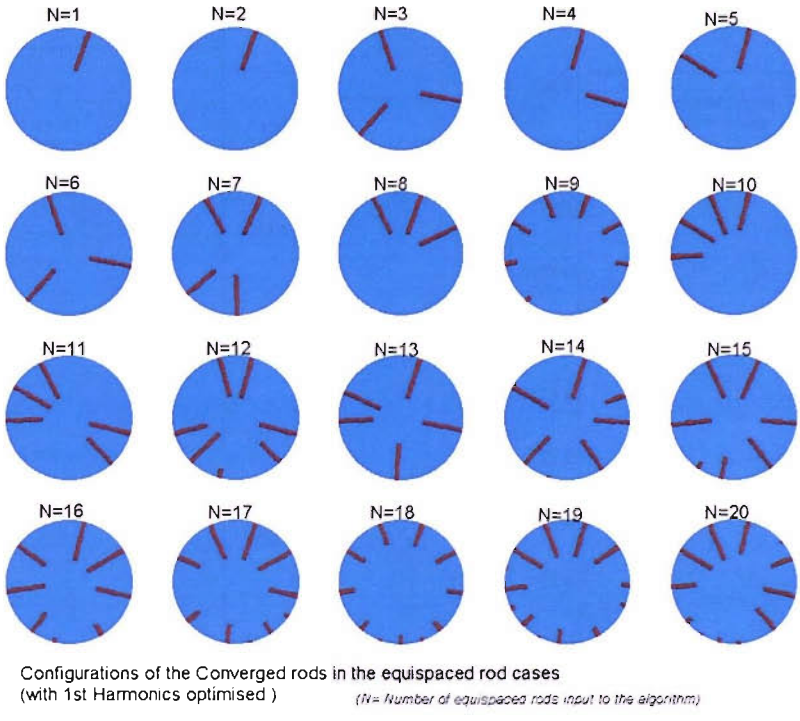

Figure 4.25 Configurations of the Converged rods in the equispaced rod cases (with 1st harmonic optimised)

The optimisation of the random disturbance was also conducted by stepping from 1-20 controllers with the cases of controllers being unequispaced. The variation similar to the one shown in Figure 4.21 was obtained and is plotted in Figure 4.26. The phase variations for the minimised cost function are presented for the optimisation of the disturbance's 1^{st} harmonic with 4 and 10 unequispaced rods in Figure 4.27 and Figure 4.28. These graphs show that the minimisation has a very high phase dependence when unequispaced arrays are used. The 4 unequispaced rod case had the following circumferential locations for the 4 rods: [10^0 35^0 70^0 210^0]. The circumferential locations for the 10 rods case were as follows: [10^0, 39^0, 66^0, 93^0, 129^0, 187^0, 210^0, 299^0, 313^0, 340^0]. Since the rods are unequispaced the phase variation was determined with the controller array rotated through the entire 360^0.

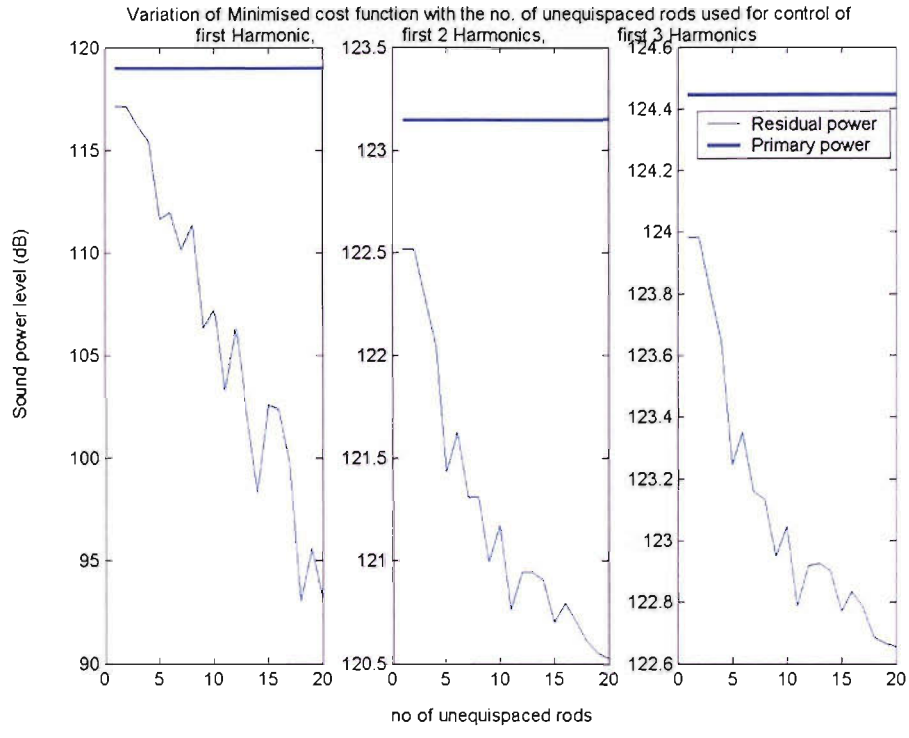

Figure 4.26 Variation of minimised noise power against the number of unequispaced controllers for the random disturbance.

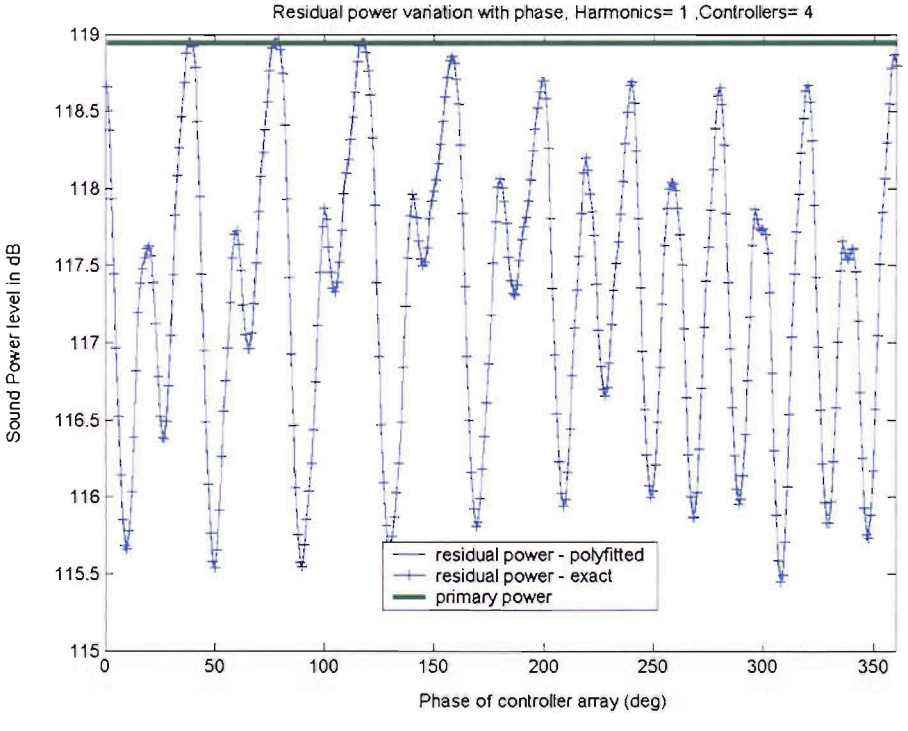

Figure 4.27 Control cost function variation with phase of rod array with 4 unequispaced controllers to control the random disturbance.

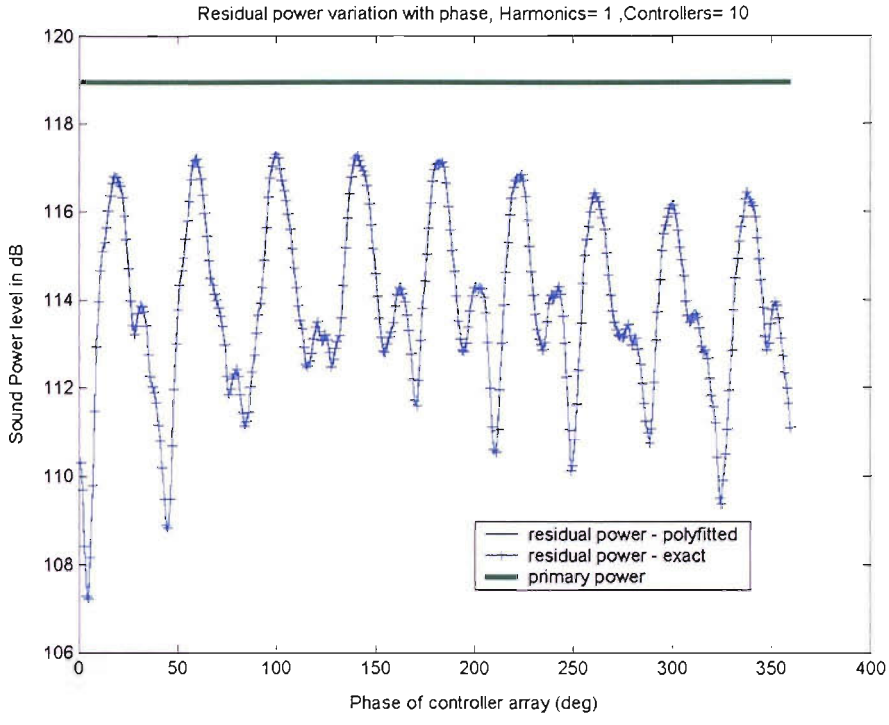

Figure 4.28 Control cost function variation with phase of rod array with 10 unequispaced controllers to control the random disturbance.

4.4. Mode cancellation problem

Cancellation corresponds to complete elimination of the modes under question. As was discussed in the beginning of this chapter, running the steepest descent algorithm would lead the convergence of a non-linear cost function to a local minimum even if there were a global minimum within the system. In the following two subsections two approaches are outlined for the mode cancellation problem. The first one in, Subsection 4.4.1 is based on the method already used here, i.e., the steepest descent approach. This is accompanied by an attempt to solve the same problem using inversion of linear equations for cancellation. The second approach for cancellation is based on a direct method to control flow modes which is discussed in detail in Subsection 4.4.2. A comparison of these should lead us to decide which method is more suitable for cancellation.

4.4.1. N modes vs 2N un-equispaced controllers

In a system of three modes whose amplitudes can be considered as three complex phasors to be cancelled, one would be led to conjecture that the cancellation would require only 6 control rods. As will be shown later, this idea would hold true only if the rod response was linear and the three amplitudes of the modes of the total disturbance (rod generated and the primary disturbance included) were expressed as a system of linear equations in terms of the 6 rod lengths. Before attempting to solve the cancellation problem in terms of the inversion of the linear equations it was decided to try this through the steepest descent approach taking into account the full non-linearity of the response of the control rods. Since an equispaced controller was already used in Section 4.3 to control the first harmonic of the random disturbance (which had only 3 modes in it) and the later use of an un-equispaced rod array also showed the phase of the array influencing the control, it was decided to try different spacings of the 6 rods to see if any of these configurations would result in the noise power reducing below the level that was already achieved for the 6 rod case in Section 4.3. Therefore the same algorithm was used to conduct the optimisation with the cost function formed from the power contained in the three modes of the first harmonic. The phase of the array was still rotated through 360^0 to check if the phase dependency still exists. Five different spacings were tried for a 6-rod array. The various cases with the circumferential positions of these rods are given in the table below.

Array	Angle of rod 1	Angle of rod 2	Angle of rod 3	Angle of rod 4	Angle of rod 5	Angle of rod 6
1	10^0	70^0	120^0	185^0	215^0	315^0
2	0^0	11^0	20^0	45^0	66^0	80^0
3	15^0	35^0	90^0	120^0	185^0	225^0
4	20^0	37^0	88^0	150^0	211^0	287^0
5	25^0	51^0	119^0	145^0	265^0	291^0

Table 4.2 Rod positions for the five different 6-rod arrays

The result of the optimisation for the five different cases is shown in Figure 4.29 with the converged cost function compared with the primary power. The results shows that there is phase dependency in the control.

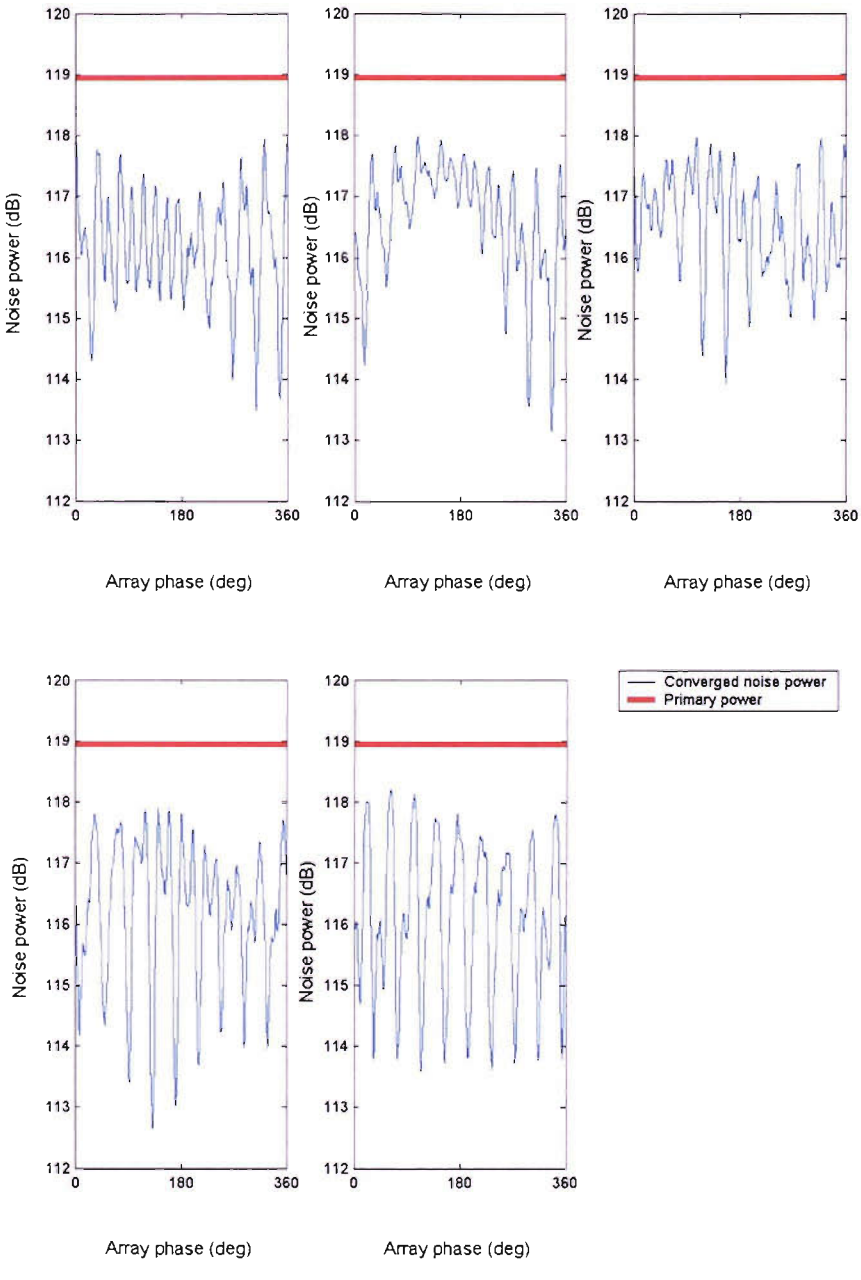

Figure 4.29 Converged cost function vs phase for the five different 6-rod un-equispaced arrays.

The maximum reduction found through running the algorithm only shows that the level ranges from 112-113 dB in the above 5 cases which is not much different from that obtained in the 6 rod equispaced array case as seen in Figure 4.21 which is around 114 dB. Since the cost function formulated is based on the non-linear response of the control rod and the convergence to the minimum using steepest descent method is dependent on the initial condition used for arriving at the global minimum, demonstrating a cancelled system of modes using this method appears to be unrewarding.

One way of doing away with the steepest descent algorithm is to revert back to the use of the linearised response of the control rods. This makes the problem simpler to handle by formulating the total disturbance modal amplitudes in terms of the rod lengths which results in a system of linear equations, whose inversion should give the required lengths for the 6 rods to cancel the 3 modes. The system of equations and the resulting inversion of these to obtain the rod lengths is discussed here. With a linearised response of the rods one can formulate the optimisation cost function as a quadratic in terms of the modal amplitudes. Minimising this function results in the following relationship which is obtained after setting the cost function gradient in Equation (3.5.5) of Chapter 3 to zero. That is

$$\frac{\partial J}{\partial \mathbf{w}} = \sum_{sB} \sum_{mn,p} \varepsilon_{mn,sB} \times 2\,\mathrm{Re}\left(\left(\frac{\partial C_{secondary}}{\partial \mathbf{w}} \right)^{H} C_{error} \right) = 0 \qquad \textbf{(4.4.1)}$$

In all of the simulations discussed in this chapter so far the cost function J utilised a polynomial fit of the rods response which is the quantity $C_{secondary}$. The error resulting in the cost function estimate using the linearised response was already explained in Chapter 3. To formulate the mode cancellation problem the linear fit of the above quantity with respect to the rod length $\mathbf{w}$ is used here. Assume that $C_{secondary}$ depends linearly on rod lengths, i.e., consider that all the rod contributions superpose such that

$$C_{secondary} = g_1 w_1 + g_2 w_2 + \cdots + g_I w_I$$
$$= \mathbf{g}^T \mathbf{w} \quad ,$$

(4.4.2)

where the vectors **g** and **w** are defined by

$$\mathbf{g}^{\mathbf{T}} = [g_1 \quad g_2 \quad \ldots \quad \ldots \quad g_I], \mathbf{w}^{\mathbf{T}} = [w_1 \quad w_2 \quad \ldots \quad \ldots \quad w_I]$$

(4.4.3)

.

Note also that $\frac{\partial C_{secondary}}{\partial w_i} = G_i$ or $\frac{\partial C_{secondary}}{\partial \mathbf{w}} = \mathbf{g}$. At the minimum

$$\frac{\partial J}{\partial \mathbf{w}} = \sum_{sB} \sum_{mn,p} \varepsilon_{mn,sB} \times 2\,\mathrm{Re}\left(\mathbf{g}^* C_{error}\right) = 0 ,$$

(4.4.4)

where $C_{error} = C_{prim} + C_{secondary} = C_{prim} + \mathbf{g}^{\mathbf{T}} \mathbf{w}$. Therefore the condition for the optimum becomes

$$\sum_{sB} \sum_{mn,p} \varepsilon_{mn,sB} \times 2\,\mathrm{Re}\left\{\mathbf{g}^* \left(C_{prim} + \mathbf{g}^{\mathbf{T}} \mathbf{w}_{\mathbf{opt}}\right)\right\} = 0 .$$

(4.4.5)

This equation can be written as

$$\sum_{sB} \sum_{mn,p} \varepsilon_{mn,sB} \times 2\,\mathrm{Re}\left\{\mathbf{g}^* \mathbf{g}^{\mathbf{T}} \mathbf{w}_{\mathbf{opt}}\right\} = -\sum_{sB} \sum_{mn,p} \varepsilon_{mn,sB} \times 2\,\mathrm{Re}\left\{\mathbf{g}^* C_{prim}\right\},$$

(4.4.6)

and therefore

$$\left(\sum_{sB} \sum_{mn,p} \varepsilon_{mn,sB} \times 2\,\mathrm{Re}\left(\mathbf{g}^* \mathbf{g}^{\mathbf{T}}\right)\right) \mathbf{w}_{\mathbf{opt}} = -\sum_{sB} \sum_{mn,p} \varepsilon_{mn,sB} \times 2\,\mathrm{Re}\left(\mathbf{g}^* C_{prim}\right).$$

(4.4.7)

This shows that the optimum control vector $\mathbf{w}_{opt}$ can be determined directly from an inversion of the matrix equation.

The cancellation problem was attempted for the 6 unequispaced rod arrays using the direct inversion approach for determining the controller lengths. Figure 4.30 shows the minimised cost function evaluated after the inversion which is plotted against the phase of the array. All cases show that cancellation is possible using this approach. A check made on the controller lengths showed that for none of the orientations of the array did the control vector have all positive lengths since the formulation of the problem in terms of the linear equations did not employ a constraint. Also the matrix on the left hand side of the Equation (4.4.7), i.e., $\left(\sum_{sB} \sum_{mn,p} \varepsilon_{mn,sB} \times 2\,\mathrm{Re}\left(\mathbf{g}^{*}\mathbf{g}^{\mathrm{T}}\right) \right)$ had the following condition numbers obtained during the inversion of the system of linear equations for the five cases: 19.1, 4814.4, 295.4, 101.4 and 24.3.

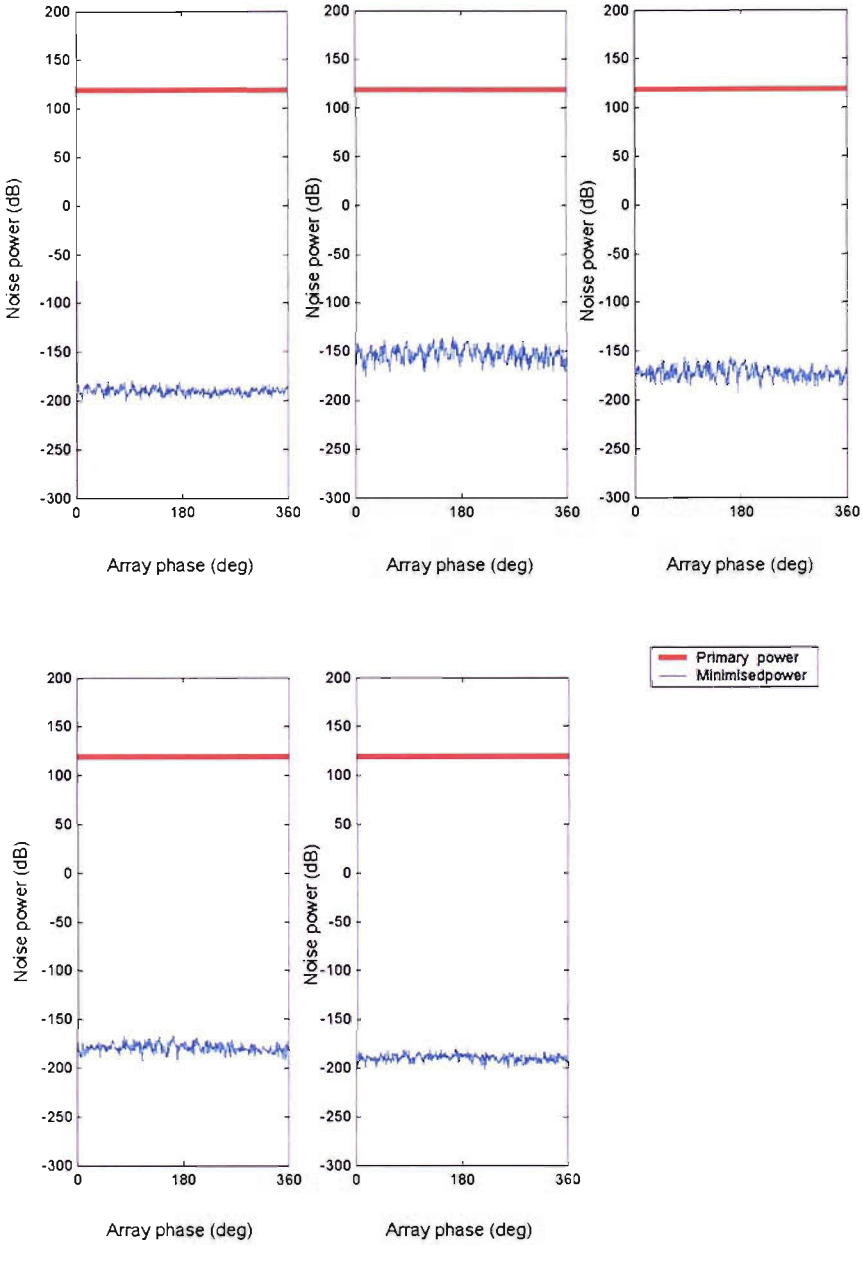

Figure 4.30 Minimised cost function vs phase for the five different 6-rod un-equispaced arrays (Note: Minimised power was obtained using linear response of the rod**).**

4.4.2. Combination of equispaced arrays or the direct control of flow modes

Considering the uncertainty in the possibility of simultaneous cancellation of modes using equispaced or unequispaced arrays, it is worthwhile to take a look at this problem using a different approach. As explained in Chapter 3 we now know that the flow modes of order p induce acoustic modes of order m. If there are three modes m_1, m_2 and m_3, we know that they are induced by flow modes of order p_1, p_2 and p_3 respectively. And a flow disturbance in the duct could have these flow modes in some arbitrary combinations of intensities and phases in the same way as they were assumed for random disturbance modal amplitude distribution. It could be definitively concluded that these three modes could be cancelled using three arrays of equispaced rods. The explanation for this is given as follows: since each acoustic mode is said to be originating from a particular flow mode, we know from Section 3.4 in Chapter 3 that that this mode could be cancelled by placing rods along one of the feasible orientations of the Fourier-Bessel pattern of the inducing flow mode. Since each acoustic mode has a different flow mode inducing it, the only way to prevent the cancellation of one mode affecting the other is to use a different equispaced array of rods for each of the three modes. This way the rods used to cancel one mode will not influence the other mode. For example the cancellation of mode $m=1$ is possible using the 8 rod equispaced rod array with equal lengths for all the rods. Each rod in the array has an in-phase contribution to total modal amplitude as was shown in Figure 4.14 and Figure 4.15. If all the rods were of equal lengths on this array their effect on the other modes will be self-cancelling, as was made evident in the subsequent Figure 4.16 and Figure 4.17. Hence the system of three modes m_1, m_2 and m_3 should have three arrays of p_1, p_2 and p_3 rods to cancel them. These rod arrays should have only equal length rods to generate the corresponding modes. Furthermore, the angular disposition of one of these arrays relative to the other should be such that they produce the same phase difference that exists between the flow modes that are originally present in the system. The three array combination as a whole can be phase shifted to cancel the flow modes originally present in the system, thereby leading to the cancellation of the corresponding acoustic modes.

The theoretical justification for the non-influence of cancelled mode on the other modes is given as follows. Assuming there are p_1 equispaced rods of equal lengths l_1, the coupling coefficient for mode m_2 can be estimated as follows.

$$C_{m_2} = C_{m_2,1} + C_{m_2,2} + C_{m_2,3} + \ldots + C_{m_2,p_n} + \ldots + C_{m_2,p_1}$$
$$= C_{m_2,1}\left[1 + e^{-jp_2\times 1\times(\frac{2\pi}{p_1})\theta} + e^{-jp_2\times 2\times(\frac{2\pi}{p_1})\theta} + \ldots + e^{-jp_2\times n\times(\frac{2\pi}{p_1})\theta} + \ldots + e^{-jp_2\times(p_1-1)\times(\frac{2\pi}{p_1})\theta}\right], \quad \textbf{(4.4.8)}$$

where C_{m_2} is the coupling coefficient of mode m_2 resulting from the p_1 rod array and C_{m_2,p_n} is the contribution of rod p_n in that array. The sum of the complex exponentials equals zero if $p_1 \neq p_2$ and hence the p_1 array cannot contribute to mode m_2.

An attempt is made here to demonstrate the cancellation concept using the 3 modes in the 1st harmonic of the random disturbance. This harmonic in the random disturbance has three modes whose circumferential orders are –1, 0 and 1 respectively and the corresponding flow mode orders inducing them are 10, 9 and 8. The cancellation of these three modes requires three equispaced rod arrays according to the method discussed here. The arrays should have 10, 9 and 8 equispaced rods of equal lengths. The lengths l_1, l_2 and l_3 for these three arrays can be found from the controller response characteristics, which were shown in Figure 3.7. The lengths can be directly read off from the non-linear characteristic of the acoustic modal response. For example the intensity of mode m = -1 in the first harmonic of the random disturbance is given in Figure 4.4. Since 10 rods are required to cancel mode m =-1 without inducing modes m =[0, 1], the length of each rod required should match only 1/10th of the intensity of the mode m = -1 in Figure 4.4. This length needs to be read off from the coupling coefficient characteristic for m=-1 in Figure 3.7 for a value of 1/10th the intensity of mode m =-1. (Note that it is not the exact characteristics shown in Figure 3.7 that are used in the computations mentioned here, rather it is the polynomially fitted characteristics of the variations shown in Figure 3.7 which are used here; an

instance of the polynomial fitting of the response characteristic in Figure 3.7 was already shown in Figure 3.11). Each of these equispaced arrays needs to be oriented relative to the reference on the circumference to make the mode produced by each of the arrays be exactly in anti-phase with respect to the corresponding mode in the primary disturbance as explained in Section 3.4 using the Fourier-Bessel illustrations. Following this method the cost function reduced to 95 dB as opposed to the 6 rod array where the reduction was only to around 112-113 dB. The lengths of the 3 superposed rod arrays were 0.0072, 0.0744 and 0.0090 m respectively. Noise power should have approached zero watts if there was complete cancellation. However a residue still exists in the power after cancellation which is the reason why the residual power is 95 dB. This is because of the approximation of the polynomial fit of the response characteristics for modes in the length range of [0, 1] cm which tends to give large errors. This estimate of 95 dB was obtained using the exact response of the rods as opposed to the 60 dB estimate predicted by the polynomial fit. That this error is justifiable can be seen from Figure 4.31 and Figure 4.32, where the primary disturbance modal amplitudes before cancellation are compared with the residual amplitudes after cancellation estimated using the exact Fourier-Bessel decomposition and the polynomially fitted response. The residual amplitudes estimated using the polynomially fitted response in Figure 4.31 are very small compared to those estimated using the exact method in Figure 4.32. In both cases the residual amplitudes are seen to lie either in phase or out of phase with respect to the primary amplitudes which happens to be the expected consequence of the method adopted here to directly cancel the flow modes inducing the corresponding acoustic modes.

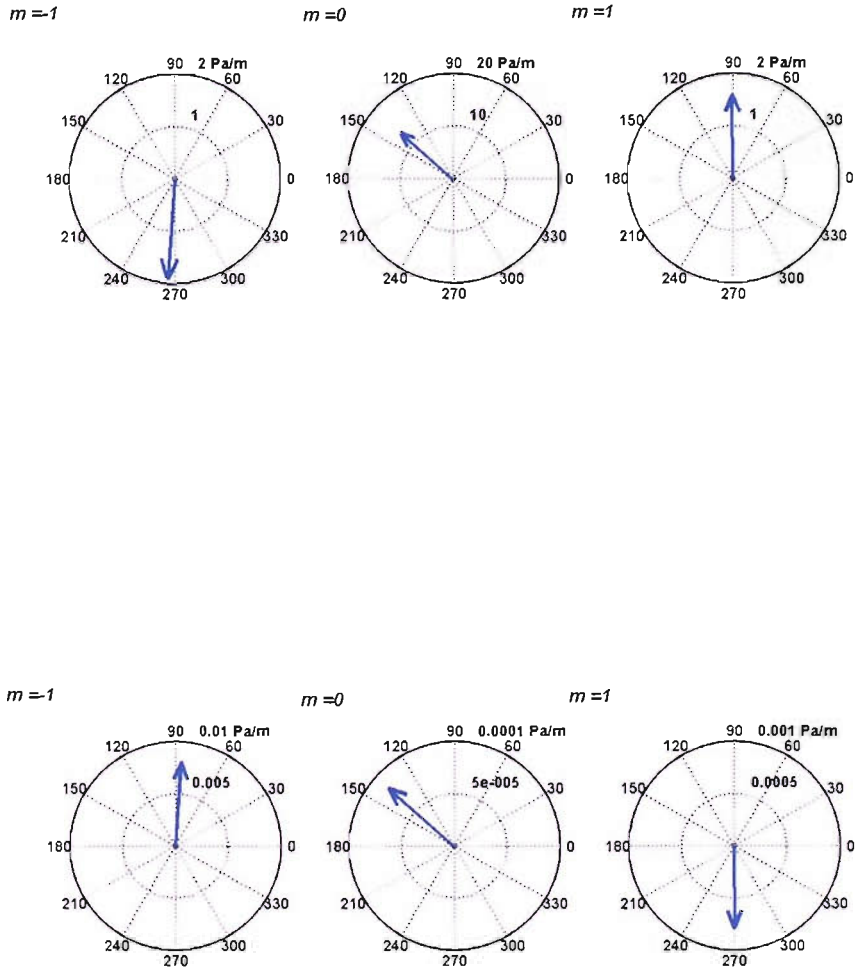

Figure 4.31 Modal amplitudes in the 1st harmonic of the random disturbance before (top row) and after (bottom row) cancellation. (Note: Modal amplitudes were estimated using the polynomially fitted response)

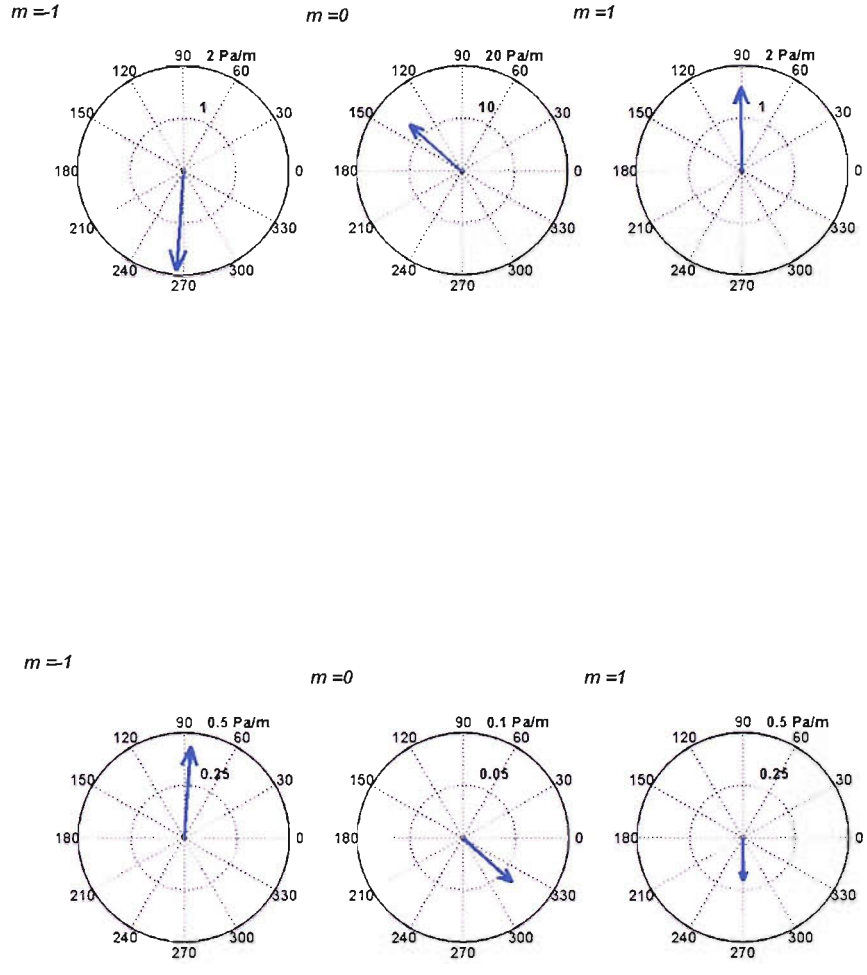

Figure 4.32 Modal amplitudes in the 1st harmonic of the random disturbance before (top row) and after (bottom row) cancellation. (Note: Modal amplitudes were estimated using the exact Fourier-Bessel decomposition)

The 27-rod array was also subjected to the steepest descent algorithm to see if the algorithm actually leads to convergence at the global minimum corresponding to the cancelled modes. The converged minimum from the steepest

descent was only 104.7dB compared to the 95 dB that was obtained from estimating the lengths directly from the response characteristic. A comparison of the direct approach with the 6 unequispaced rod array makes it obvious that the direct approach assures the approach to the global minimum. The approach to the global minimum is not assured in the steepest descent case even with the 27 rod array since it involves converging to a local minimum which may not be the global minimum.

4.5. Inclusion of the rod array phase in the control vector

Since the rotation of the array showed phase dependence in the achievement of the minimum power it was decided to extend the strategy that was discussed so far of altering the rod lengths to include simultaneous rotation of the rod array. The strategy adopted so far does not consider phase of the array as a variable in the optimisation. Since the controllers in the array have fixed angular positions, the angle of each rod can be expressed in terms of that of the first rod and phase of the array can thus be regarded as one of the optimisation variables. This would result in a cost function consisting of $(q+1)$ variables, the extra variable being the phase of the array. The matrix $\partial C_{secondary} / \partial \mathbf{w}$ originally had the gradients of the responses of the individual control rods. Since the coupling coefficient of a rod disposed off by θ radians from the reference differs by a factor of $e^{-jp\theta}$ from that of the rod at the reference, the matrix $\partial C_{secondary} / \partial \mathbf{w}$ will now have an extra column to account for the inclusion of the array phase with each of its elements being $-jpC_{secondary}$, as can be seen from the derivative of the rod response $C_{secondary}$ with respect to the phase angle θ. The simple expression for the derivative is also a consequence of the fact that the phase response doesn't change with length of a rod that is fixed circumferentially. The optimisation should now be expected to cause the objective function to directly approach one of the minima described in the results that were shown in the form of the converged cost function with the phase of the array. Two cases of simulation are repeated here from the

previous cases to test the convergence of the algorithm using simultaneous array rotation and rod translation.

4.5.1. Case 1

The top half of Figure 4.33 shows the variation of the converged cost function with the phase of the array for the optimisation of the 2^{nd} harmonic of the crossbar disturbance with 4 rods. The figure shows that within the phase variation of the converged cost function there is a further minimum with respect to the phase and this is seen to occur at 23^0. The steepest descent algorithm was extended to include the phase in the control vector and the phase was given an initial condition of zero and the convergence coefficient μ was set to .006 for the lengths and angle. The convergence obtained for the cost function is shown in the bottom half of the same figure. The algorithm started with an initial condition of 0 for all lengths and 15^0 for the phase of the array. In Figure 4.34 the length convergence of the 4 rods and the phase of the array are shown along with the configuration of the array of converged rods at the 200^{th} iteration.

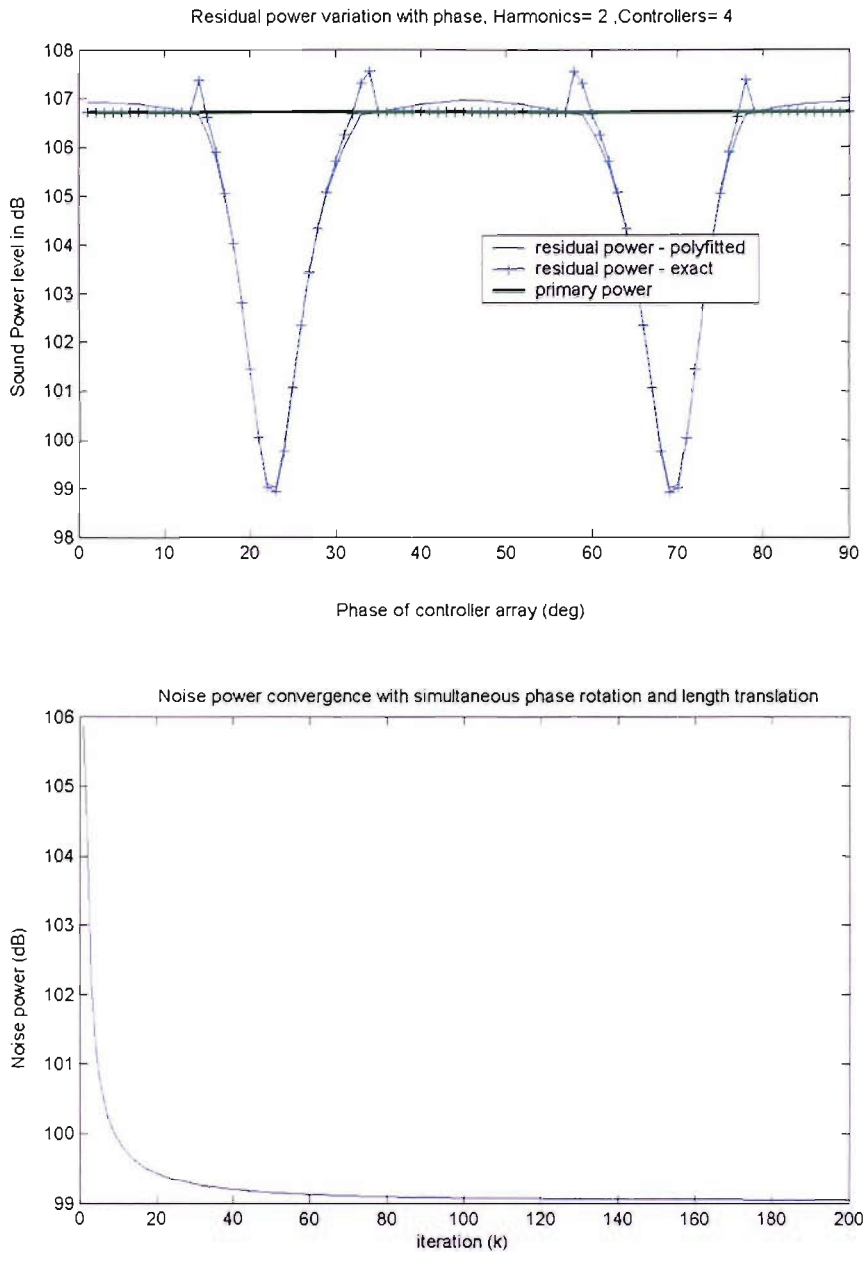

Figure 4.33 Converged cost function variation with the phase of the array and Noise power convergence with simultaneous phase rotation and length translation.

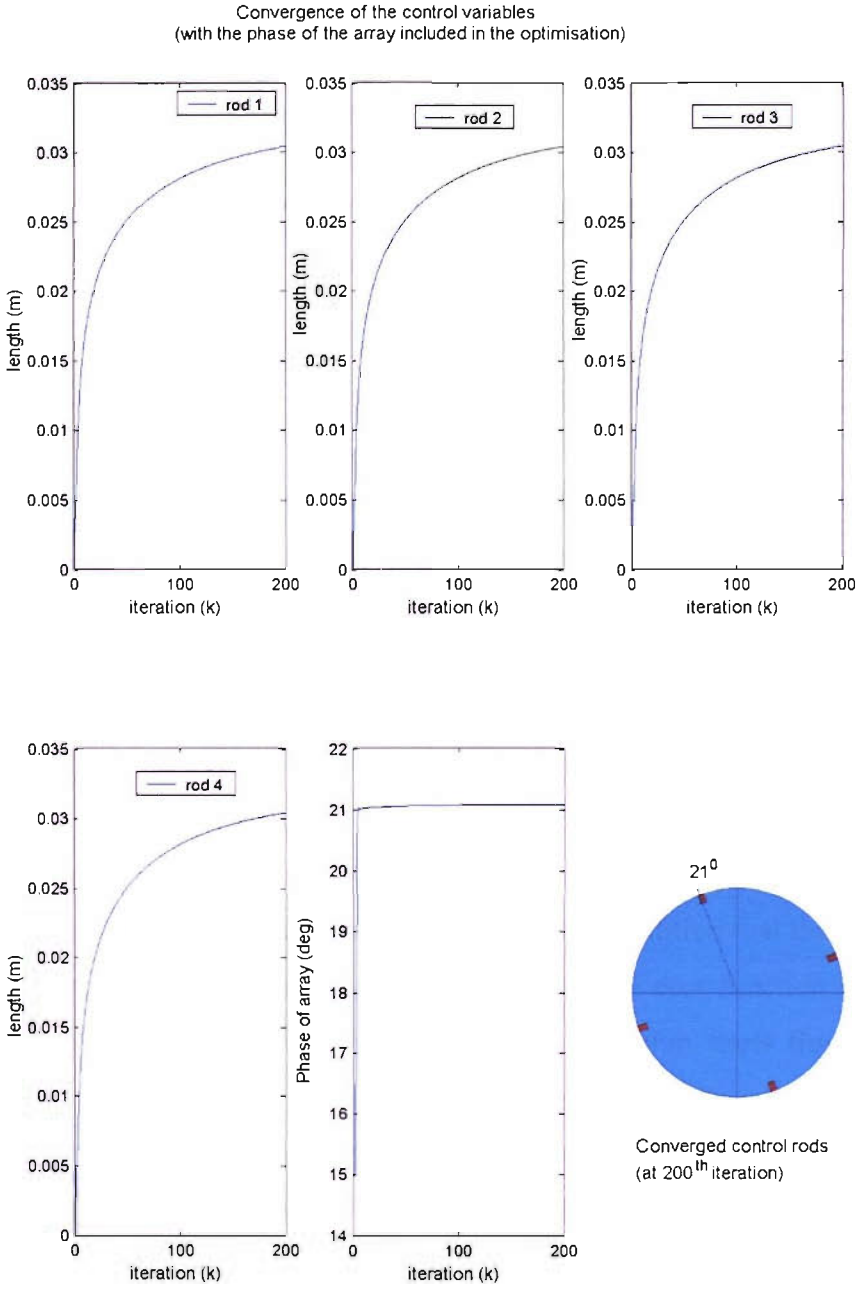

Figure 4.34 Convergence of control variables with simultaneous phase rotation and length translation

The converged lengths and angle are given in the table below for both cases of optimisation with and without the phase of the array included in the control vector. Specifically the case with the phase included in the control vector is compared with the configuration without it being included. We know from the

top half of Figure 4.33 that the best minimisation happens at 23^0 for the case in which the phase is manually varied. There is good agreement between the lengths and the phase from both these methods.

Method	Converged lengths				Array angle
	Rod 1	Rod 2	Rod 3	Rod 4	
Phase included in the algorithm	0.0304	0.0304	0.0304	0.0304	21.08^0
Manual phase variation	0.0334	0.0334	0.0334	0.0334	23^0

Table 4.3 Converged lengths with and without the array phase included in the control vector.

Similar to the error surfaces discussed in the beginning of Section 4.2 an error surface was estimated by gridding in the 2-dimensional subspace consisting of the length of rod 1 ([0, .3] m) and the phase angle θ ($[0^0,60^0]$). The error surface obtained is shown in Figure 4.35. The algorithm was re-run with an initial condition of [0 0.0334 0.0334 0.0334] m for the lengths and 0^0 for the angle, and also a constraint was imposed on rods 2-4 with the condition that they be equal to 0.0334 m in length. The convergence trace T1 of the cost function is plotted in Figure 4.36. The convergence trace shows that algorithm starts from the 0^0 and reaches the first dip/valley in the error surface graph which occurs at 21^0 of the array phase and the length of rod 1 also converges to the value .0291 m which is close to .0304 m given in the above table with the convergence coefficients remaining the same. This shows that for this disturbance the algorithm works when the phase of the array is also included in the control vector.

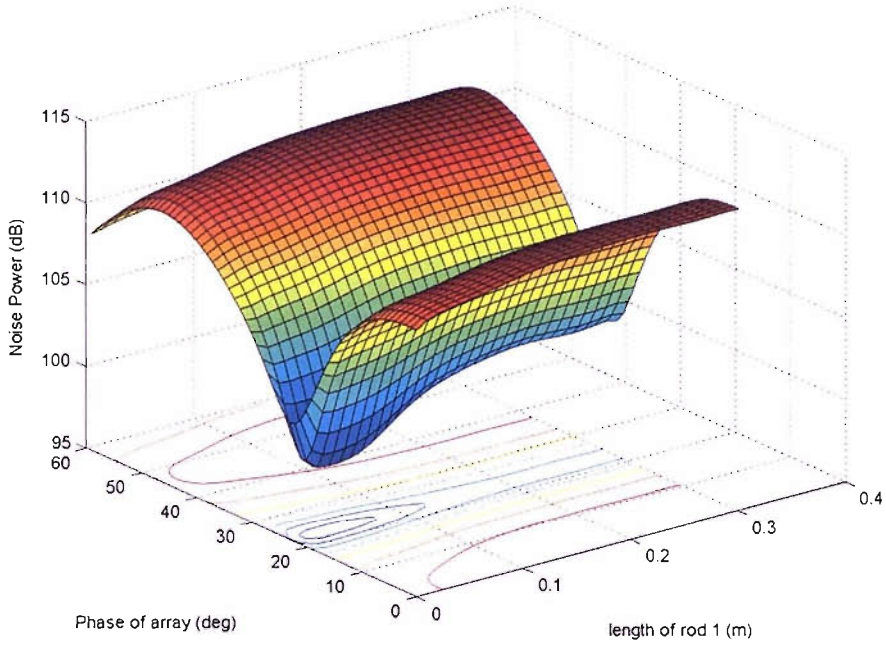

Figure 4.35 Cost function error surface for the crossbar disturbance controlled with 4 rods.

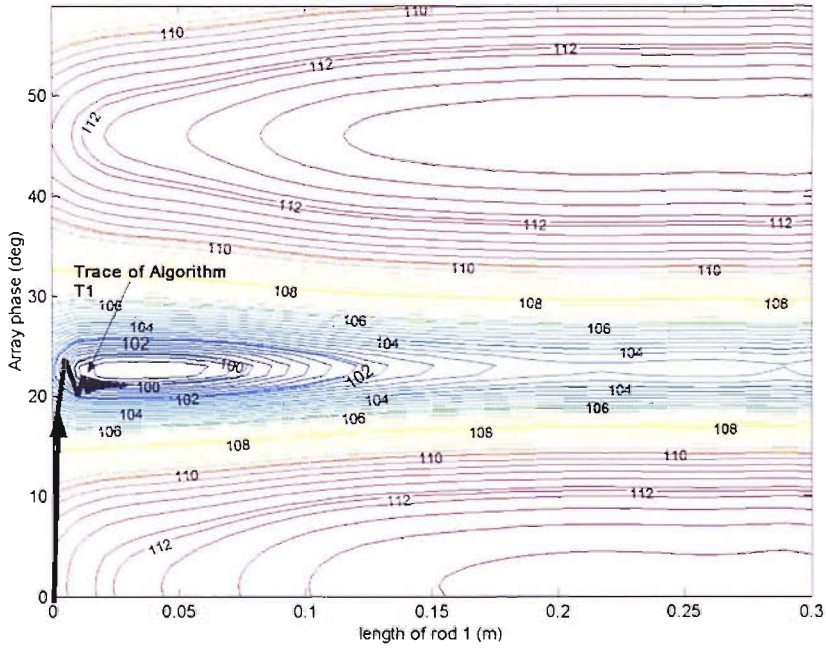

Figure 4.36 Contour plot of the cost function error surface with the superimposed trace of the algorithm.

4.5.2. Case 2

Figure 4.37 is a repeat of Figure 4.19 which shows the variation of the converged cost function with the phase of the array for the optimisation of the 1st harmonic of the random disturbance with 8 rods. The figure shows that within the phase variation of the converged cost function there is a further minimum with respect to the phase which is around 114.5 dB and this is seen to occur at around 25^0. At this phase angle the value of the control vector of rod lengths is [0.2034 0 0 0 0 0.0070 0.2115 0.2170]. The steepest descent algorithm was extended to include the phase in the control vector and the phase was given an initial condition of zero and the algorithm was run with three different convergence coefficients μ, as indicated in Figure 4.38. We see that the convergence with the first trial is noisy and becomes smooth only in the third case where it took around 40,000 iterations to get the pattern of convergence that is shown there. Even with the fine-tuned convergence coefficient in the third case the algorithm does not converge to the value of 114.5 indicated at 25^0 in Figure 4.37. This could probably be due to the algorithm approaching a local minimum. In Figure 4.39 and Figure 4.40 the control variable convergence pattern is shown for the last two cases in Figure 4.38. The oscillatory behaviour of the algorithm is clearly seen in the illustration in Figure 4.39. Figure 4.39 and Figure 4.40 indicate that the algorithm is very sensitive to the convergence coefficient variation.

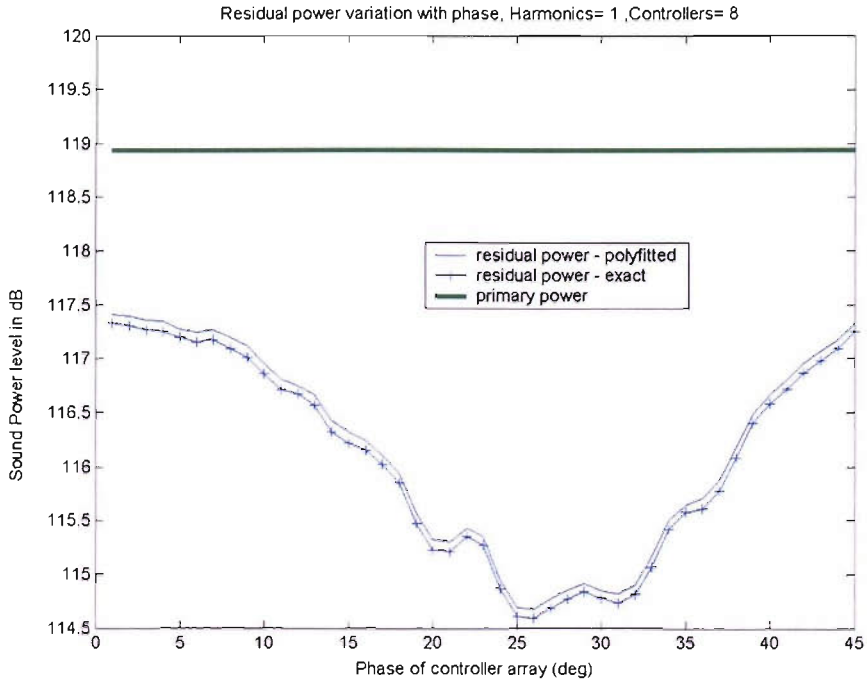

Figure 4.37 Converged cost function variation with the phase of the array.

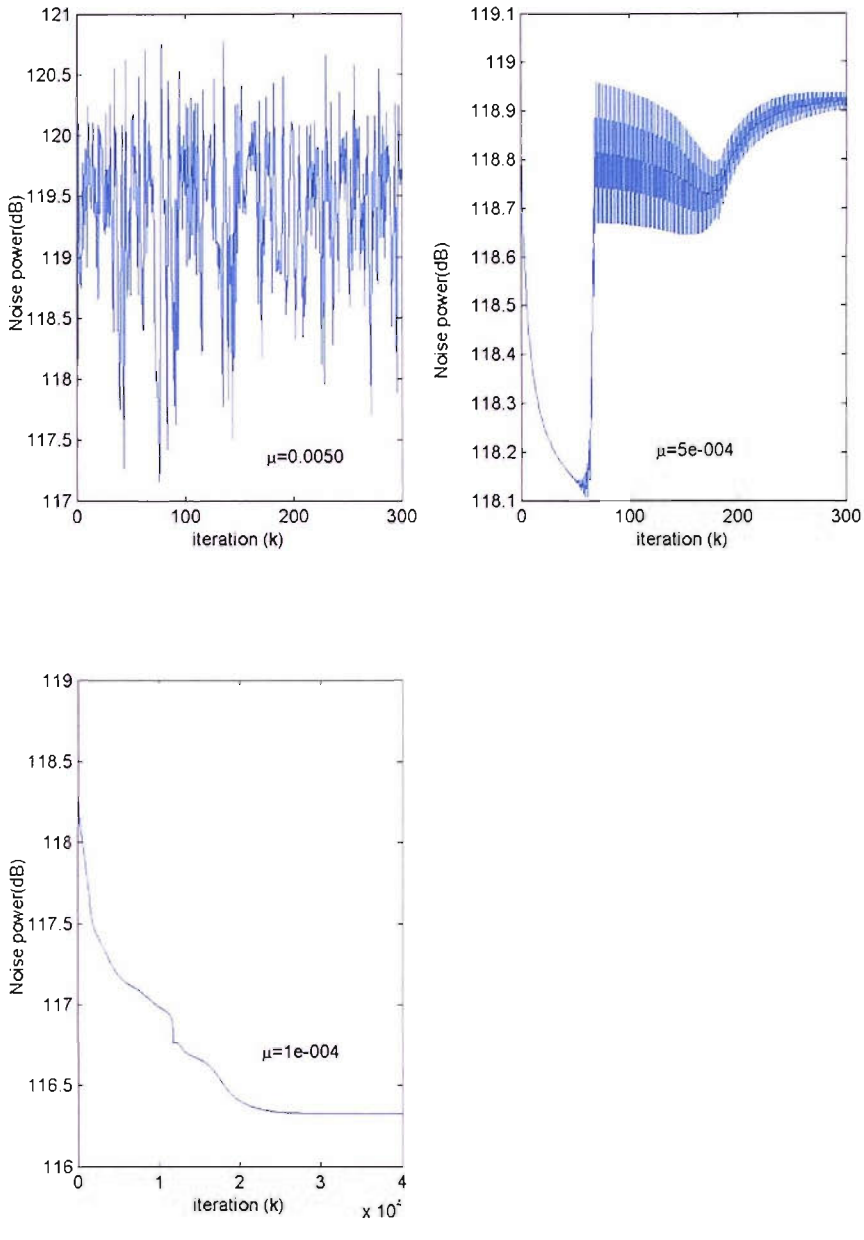

Figure 4.38 Noise power convergence with simultaneous phase rotation and length translation

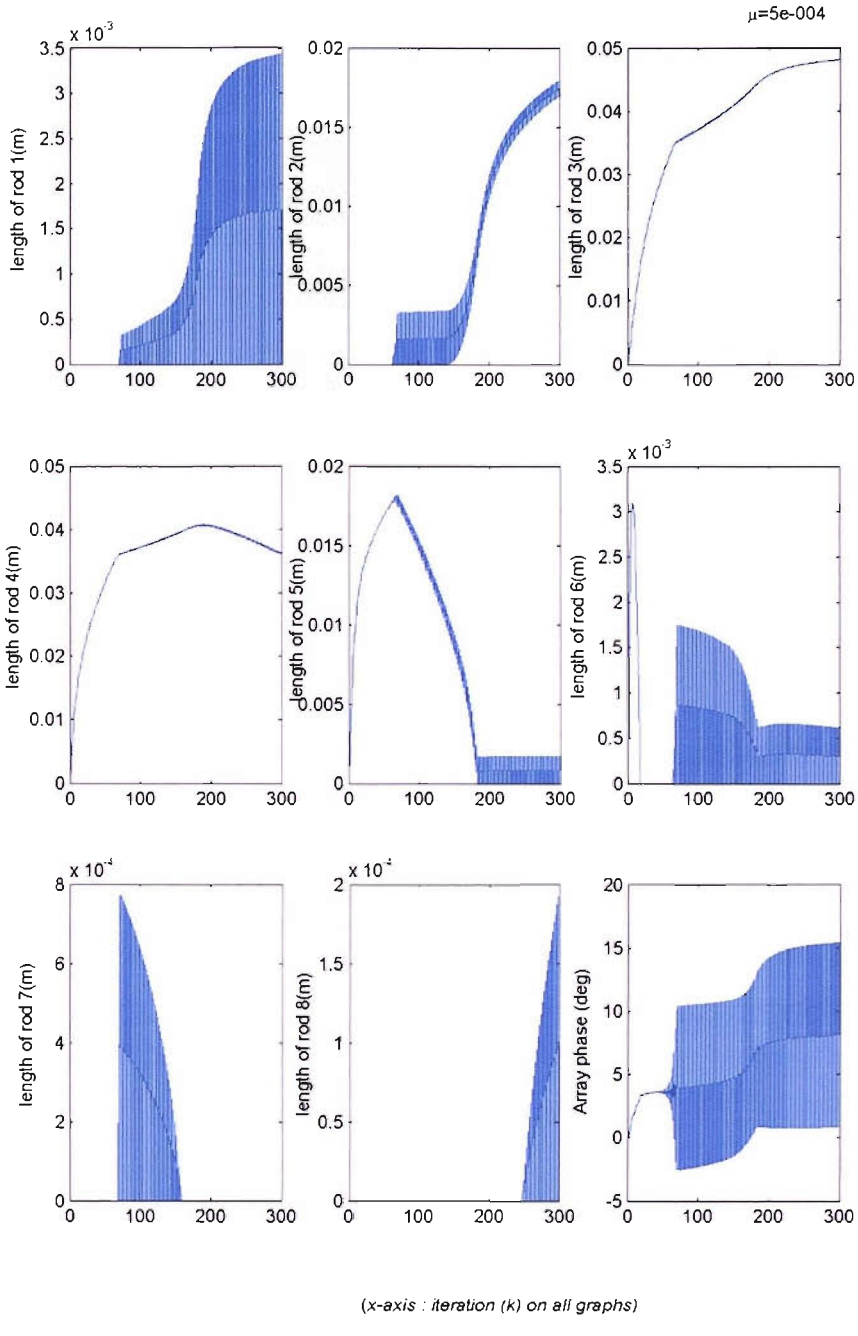

Figure 4.39 Oscillatory behaviour of the algorithm with phase rotation and length translation

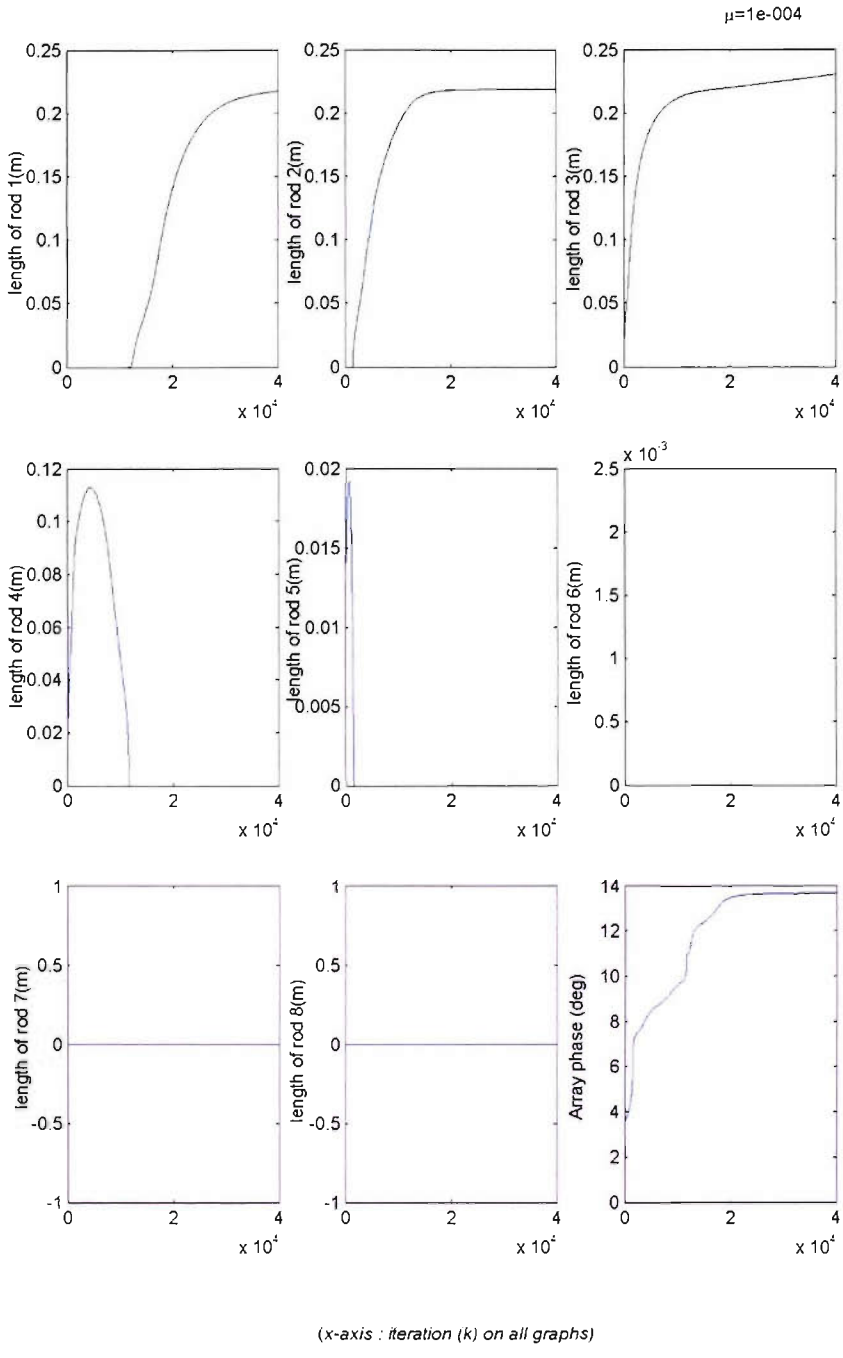

Figure 4.40 Control variable convergence with simultaneous phase rotation and length translation

Error surface was estimated by gridding in the 2 dimensional subspace consisting of the length of rod 8 ([0, .3] m) and the phase angle θ ([0^0, 360^0]). The error surface obtained is shown in Figure 4.41. In Figure 4.42 the same error surface is shown within the phase range of 300-360^0. The algorithm was re-run

with an initial condition of [0.2034 0 0 0 0 0.0070 0.2115 0] m and also a constraint was imposed on rods 1-7 with the condition that they be [0.2034 0 0 0 0 0.0070 0.2115] m in length. This means that only the length of rod 8 and the phase of the array have been included as variables in the control vector. The convergence trace T1 of the cost function superposed on the error surface contour is plotted in Figure 4.43. The error surface on which the trace has been superposed is the same as in Figure 4.42. The convergence trace shows that the algorithm starts from the angle 0 and reaches the dip/valley in the error surface graph in the range of 340-360^0. The length of 0.2170m for rod 8 mentioned while discussing the minimum at 25^0 in Figure 4.37 also occurs in this region. Since the algorithm was given an input of 0^0 for the array phase the array rotated beyond 360^0 and approached the nearest dip in the error surface. Relative to Figure 4.37 the dip in the variation occurs around 25 -30^0 which is offset by 15^0 from the edge of the graph at 45^0. By virtue of the circumferential symmetry of the 8 rod equispaced array that pattern is expected to repeat 8 times in one revolution. This is why the dip in the variation in Figure 4.42 or Figure 4.43 is offset by around 15^0 from the 360^0 limit.

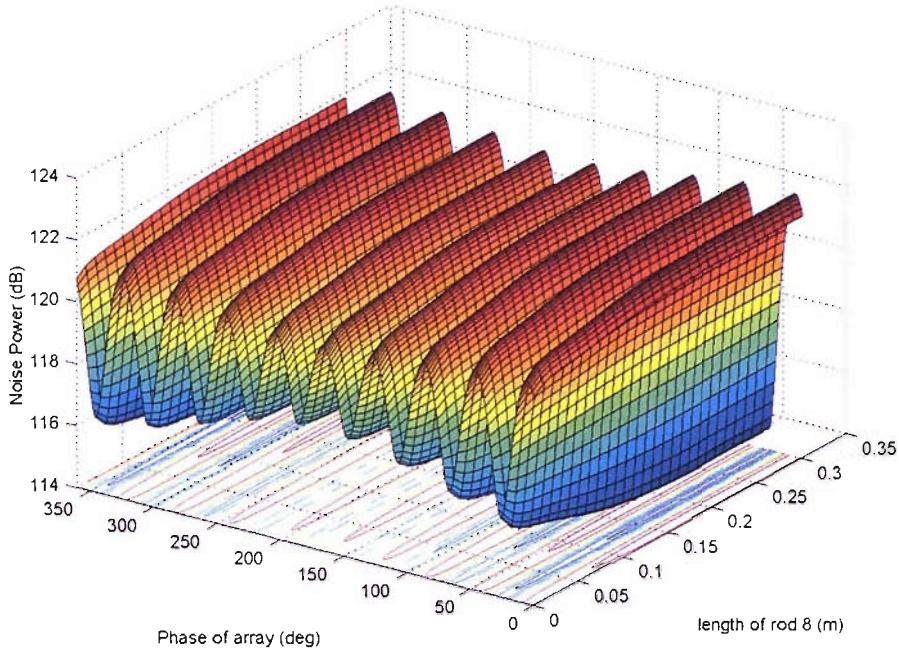

Figure 4.41 Cost function error surface for the random disturbance controlled with 8 rods.

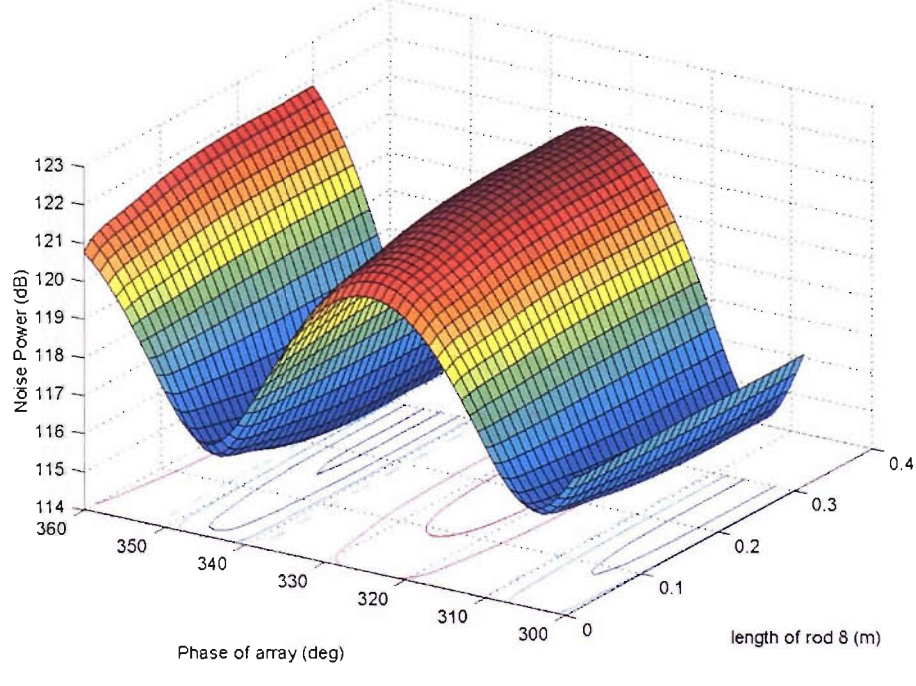

Figure 4.42 Cost function error surface for the random disturbance controlled with 8 rods.

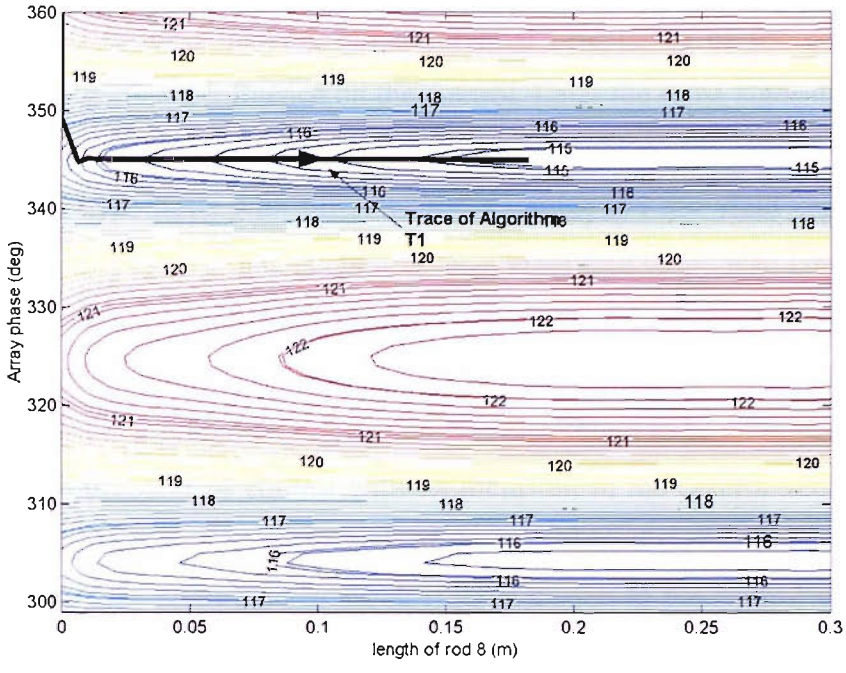

Figure 4.43 Contour plot of the cost function error surface in dB, with the sumperimposed trace of the algorithm.

4.6. Summary

This Chapter focussed on the optimal control of multiple modes using multiple control rods as the previous chapter indicated that focussing the control on a single mode might lead to the increase in the amplitudes of the other modes. Two disturbances were chosen to test the control of multiple modes. One is a spatially harmonic flow disturbance and the other is a randomly distributed flow disturbance. In both situations error surfaces were plotted for selected cases and it was shown that the choice of initial condition could lead the convergence to a local minimum which is a feature of the steepest descent algorithm. While with the spatially harmonic disturbance increasing the number of controllers led to increased reduction in the noise power, the randomly distributed disturbance showed that increasing the number of controllers for the control of multiple modes is not effective. Although increasing the number of equispaced controllers in the random disturbance case showed increased reduction, not all of the controllers used in the array were being utilised by the algorithm. This had later led to the

attempt of controlling this disturbance using un-equispaced rod arrays. Both types of rod arrays showed that the circumferential orientation of the controller rod array has a significant influence on the control. Later the same algorithm was used to test the cancellation problem involving cancelling N modes with 2N controllers. Testing this hypothesis with different rod spacings did not yield cancellation in these cases as we know that steepest descent algorithm could lead convergence to local minimum. An alternative means of cancelling multiple modes with a combination of multiple equispaced rod arrays was found to be promising. Since the rod array circumferential orientation was also found to be an important control variable, the problem of control with its inclusion in the control vector was also attempted for two cases, one in each of the two flow disturbances chosen in this chapter. This was performed to check if its inclusion in the control vector would lead to convergence to that orientation which was found to be the best when it was manually varied. For a control case in the spatially harmonic flow disturbance, the inclusion of the rod array circumferential orientation in the control vector led the convergence of the control algorithm directly to the point which corresponded to best orientation found through manual variation. When the same problem of controlling the array orientation was attempted with a case in the randomly distributed flow disturbance the control showed that it is very sensitive to the choice of the convergence coefficient. The next chapter examines the problem of implementing the control algorithm on a test fan rig for a few cases each representing control of either single or multiple modes with controllers on an 8-rod equispaced array.

Chapter 5 Active control experiments

5.1. Introduction

So far the thesis has dealt with the description of the concept of control in Chapter 1, a model to predict the acoustic field resulting from the fan and flow disturbance interaction in Chapter 2, and the simulation of the controller response and the formulation and solution of the optimisation cases using a cost function and the steepest descent algorithm to iteratively obtain the control vector in Chapter 3 and Chapter 4. This chapter deals with the implementation of the control concept on a model fan rig. Section 5.2 deals with the description of the test facility, the 8-rod controller array and the instrumentation. Section 5.3 deals with the experimental determination of the controller rod response and the implementation of the control algorithm.

5.2. Test Facility Description

Subsection 5.2.1 deals with the general arrangement of the fan rig. Subsection 5.2.2 gives a description of the fan and the optical triggering device used for capturing the blade locked reference signal. While Subsection 5.2.3 describes the controller array, Subsection 5.2.4 deals with the description of the microphone array and Subsection 5.2.5 on the data acquisition system.

5.2.1. General Arrangement

The fan rig facility is situated in a large anechoic chamber in the Doak Laboratory of the ISVR. A schematic of the fan rig in the anechoic chamber with the appropriate dimensions is shown in Figure 5.1. The fan rig consists of a duct housing the 9 bladed fan preceded by an intake nozzle, microphone array rings, a controller rod array ring and followed by a silencer duct. Figure 5.2 shows the photograph of the fan rig in the anechoic chamber.

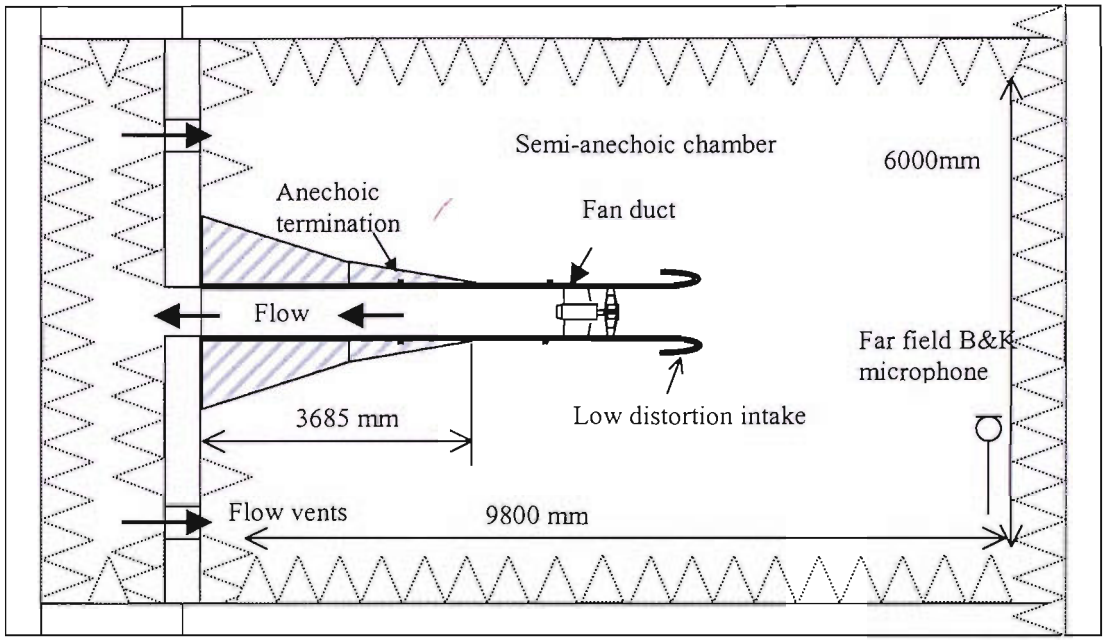

(a) Schematic of the fan rig

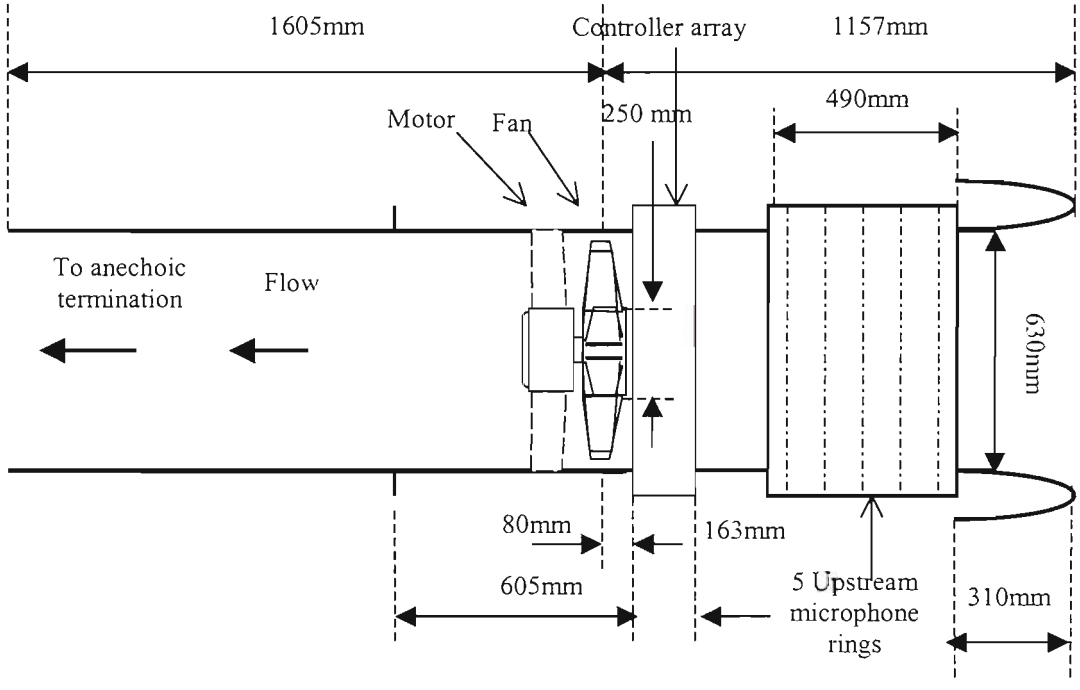

(b) Details of the fan duct

Figure 5.1 Schematic of the fan rig.

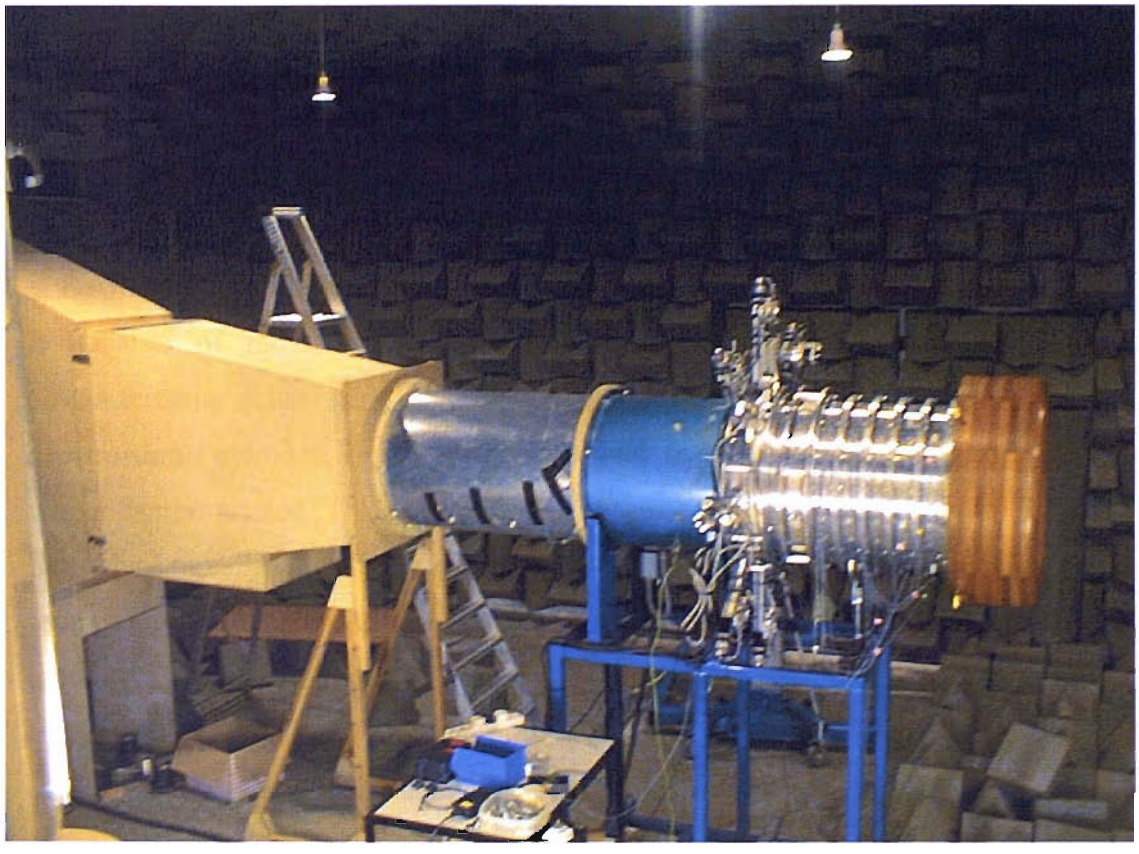

Figure 5.2 Photograph of the fan rig in the anechoic chamber.

5.2.2. Fan and the Optical trigger

The fan diameter was 630 mm with a hub of 250 mm diameter. The fan could be rotated at a maximum speed of 3000rpm. It had 9 blades with variable pitch angle and each blade's chord was 130 mm and the blades were set at a pitch angle of 34^0. The fan motor is driven by an inverter drive whose frequency setting can aid in the adjustment of the speed of the fan. For the experiments discussed here the fan was run only at two speed settings, 1767 and 2934 rpm. On the surface of the duct housing an optical triggering device manufactured by the electronics support group of the ISVR is flush mounted in order to pick up the reflections from a reference fan blade which has its tip covered with a reflecting material. This device issues a single pulse of around 5V for each revolution of the fan. The

reference fan blade will be referred to as the instrumented blade in the rest of the thesis.

5.2.3. Controller Array

The controller rod array is a device manufactured by Time & Precision Industries at Basingstoke, United Kingdom. A picture of this device is shown in Figure 5.3. It consists of radial rods (Electro-thrust cylinders) equally spaced in the circumferential sense on a cylindrical ring. Figure 5.4 shows the picture of an Electro-thrust cylinder. The rods can be made to translate radially and the ring as a whole can be rotated. These motions are possible through stepper motors for the individual radial motions as well as the rotary motion. The radial motion and the rotary motion are constrained to 200 mm of length and 30^0 of rotation respectively. The diameter of these rods is 12mm. The constrainment is also mechanically effected through the presence of limit switches. The stepper motors on the radial rods also have encoders fitted on them to feedback the position information of each rod. Each of these motors is interfaced to the computer through a drive cabinet shown in Figure 5.5 and they can be commanded from the computer's RS232 serial port. The drive cabinet consists of L25i/L50i stepper drives for each stepper motor on the rod array. The motion commands are in the ASCII format of the EASITOOLS language. It should be noted that the 8^{th} rod on this array had a mechanical fault and hence was non-functional throughout the experiments discussed here. A picture of the fan rotor and the rod array inside the duct is shown in Figure 5.6.

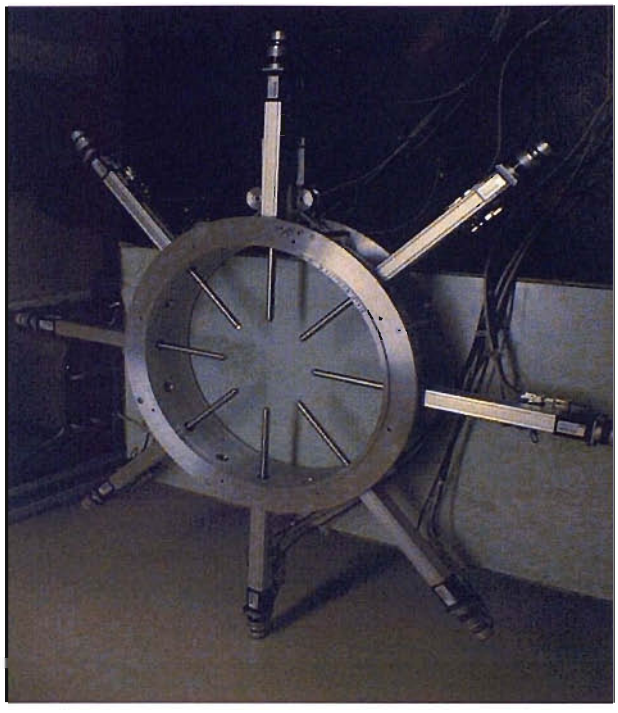

Figure 5.3 Equi-spaced 8-rod array.

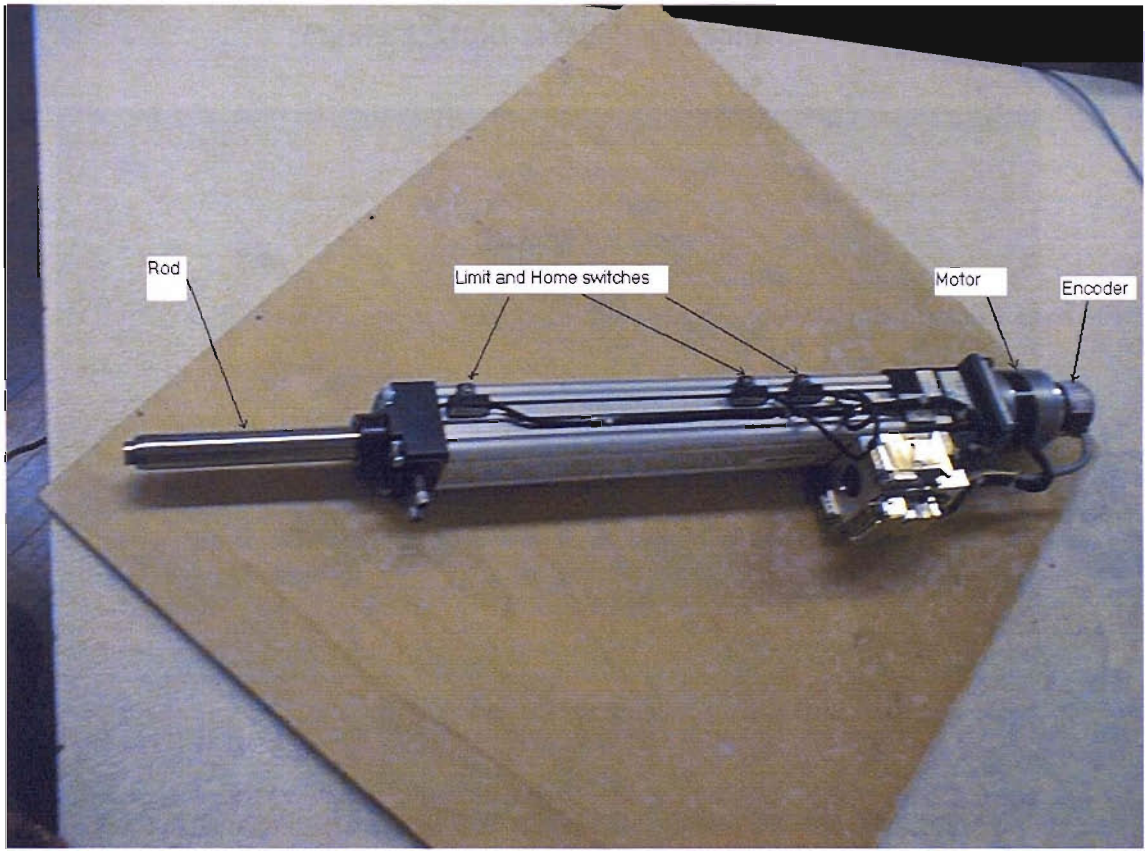

Figure 5.4 Electro-thrust cylinder.

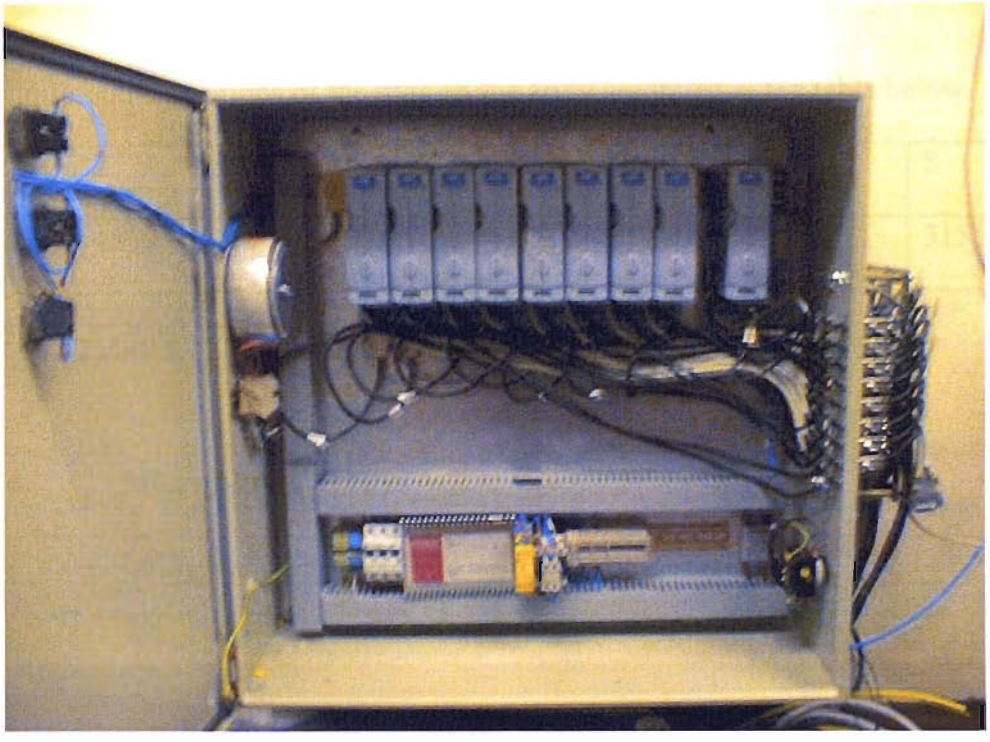

Figure 5.5 Rod-array drive cabinet.

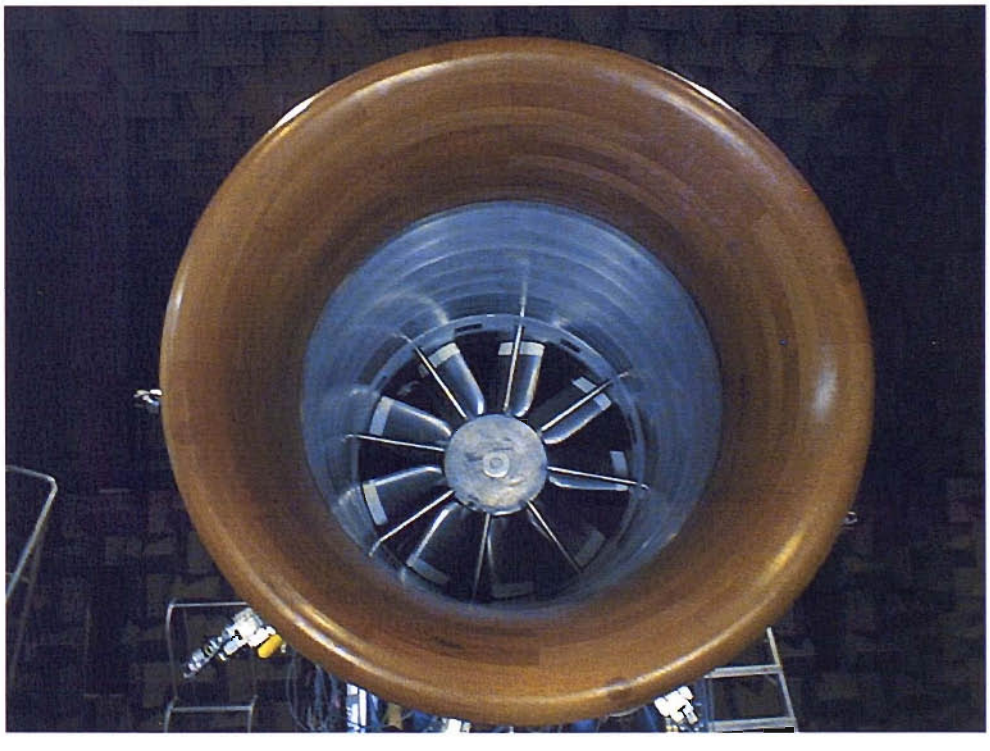

Figure 5.6 Fan rotor and rod array inside the duct.

Circumferential positions of the rods on the array are given in the table below.

Rod 1	2	3	4	5	6	7	8
0	45^0	90^0	135^0	180^0	225^0	270^0	315^0

Table 5.1 Circumferential positions of the rods on the array.

5.2.4. Microphone arrays

Figure 5.7 Electret microphone with the plastic holder.

Microphones were positioned upstream and downstream of the rotor. On the upstream side the microphone array consisted of 5 cylindrical rings with circumferentially spaced flush mountable slots for positioning ¼ inch omni-directional electret microphones from the exterior. A photograph of the electret

microphone with the plastic holder is shown in Figure 5.7. A maximum of up to 24 microphones can be fixed on a single ring making a total of 120 microphones on 5 rings. The five rings are spaced out by 98 cm axially. On the downstream side 4 such microphones were used.

The following tables lists the axial and circumferential positions of the upstream and downstream in-duct microphones used for conducting the experiments. In addition to these a B&K microphone was used in the far-field which was located at approximately 45^0 to the intake axis of the fan.

Upstream set			Downstream set	
Microphone	Circumferential Position	Axial position (m)	Microphone	Axial position (m)
1	285^0	-0.657	1	0.59
2	315^0	-0.853	2	0.88
3	195^0	-0.559	3	1.17
4	90^0	-0.853	4	1.4600
5	165^0	-0.559		
6	270^0	-0.461		
7	135^0	-0.755		
8	105^0	-0.657		
9	255^0	-0.755		
10	210^0	-0.853		
11	330^0	-0.755		
12	45^0	-0.853		
13	165^0	-0.853		
14	270^0	-0.853		

Table 5.2 Microphone positions.

5.2.5. Data Acquisition System

The data acquisition system for acquiring the signals from the microphones and the pulses from the triggering device is a PXI1000B chassis supplied by National

Instruments which has two dynamic signal acquisition cards (NI4472). A photograph of the cards with the chassis is shown in Figure 5.8. Each card has 8 channels which limits the number of microphones to be connected to these to 15 excluding one channel for the trigger signal. This also limits the number of modes into which a tone can be modally decomposed. The microphone cables connect with the analog channels on these cards. The triggering pulse cable is also connected to one of the analog channels on these cards. Data were sampled at 10000Hz. The PXI1000B chassis streams the simultaneously sampled microphone signals into the computer's memory buffers. The computer is interfaced with the PXI1000B chassis through MXI cards and a copper cable. The data can be read off into files or processed online as the data gets streamed in using LABVIEW software.

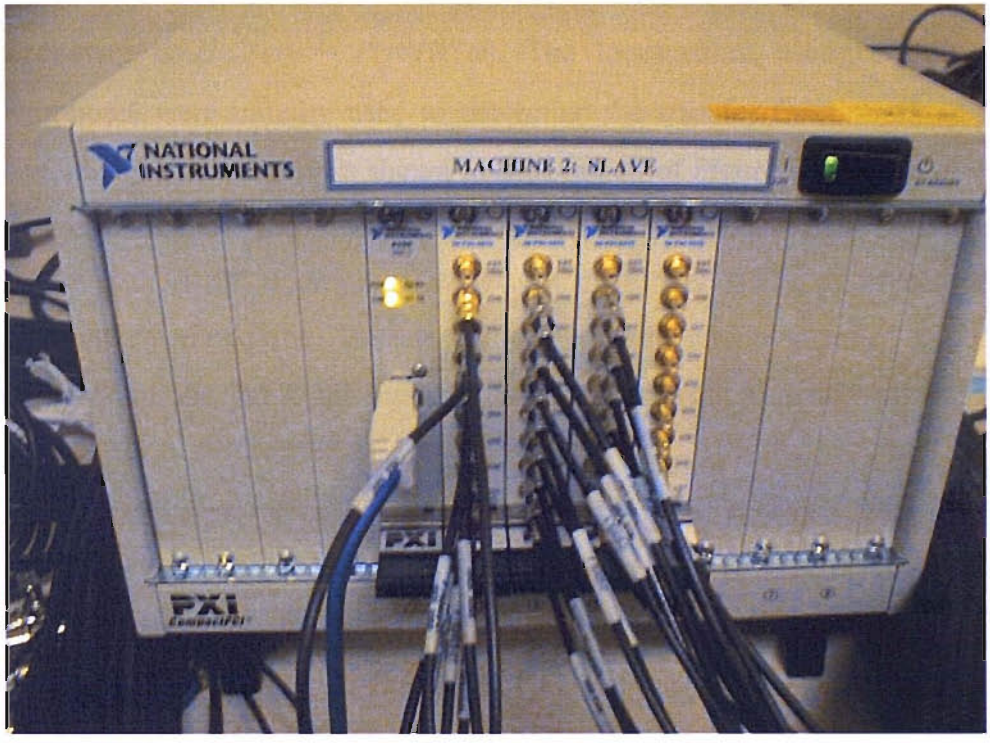

Figure 5.8 PXI1000B chassis with NI4472 data acquisition cards.

5.3. Tests

Since the microphones on the duct are used to sense the acoustic field their calibration is described in Subsection 5.3.1. Subsection 5.3.2 then deals with the control experiments.

5.3.1. Microphone calibration

The calibration procedure is illustrated in Figure 5.9. As mentioned already the microphones were flush mounted into the slots on the rings from the exterior of the rings and the cavity formed between microphone surfaces and the duct interior surface was calibrated to determine its transfer function $H_{cav}(\omega)$ using a calibrating piezoelectric loudspeaker. This procedure is shown in the bottom half of Figure 5.9. The loudspeaker is excited using 10 kHz bandwidth white noise, w, measured in Volts whose Fourier transform is $W(\omega)$. The pressure at the microphone surface, p, is transduced as an electrical signal measured again in Volts with its Fourier transform being $P(\omega)$. Thus the transfer function of the in-duct cavity is $H_{cav}(\omega) = P(\omega)/W(\omega)$. The loudspeaker, along with a B&K microphone, were initially used to determine the transfer function $H_{ref}(\omega)$ of a model cavity surface. This is shown in the top half of Figure 5.9. Again the white noise excitation, w, provided to the loudspeaker is measured in Volts and the pressure at the B&K microphone surface of the model cavity, p_s, is measured in Volts and converted into Pascals using the manufacturer supplied calibration coefficient of the B&K microphone. Thus the transfer function of the model cavity is $H_{ref}(\omega) = P_s(\omega)/W(\omega)$.

Thus the pressures $P_s(\omega)$ on the model surface obtained from the B&K microphone while the loudspeaker was subjected to a 10 kHz bandwidth white noise input were later used to determine the transfer function $H_p(\omega)$ of the in-duct pin-hole cavities and hence the sensitivities of the in-duct microphones. The sensitivity of the microphone is defined as the ratio of the Fourier transform of the microphone surface pressure, p, measured in Volts to the Fourier transform of the in-duct surface pressure, p_s, estimated in Pascals. All transfer functions mentioned above have been determined by forming the cross spectrum of the output signal with respect to the input signal and the auto spectrum of the input signal which were averaged over several blocks of the measured signals. Figure 5.10 and Figure 5.11 illustrate the sensitivity of one of the microphones in the frequency range of 0 to 5 kHz.

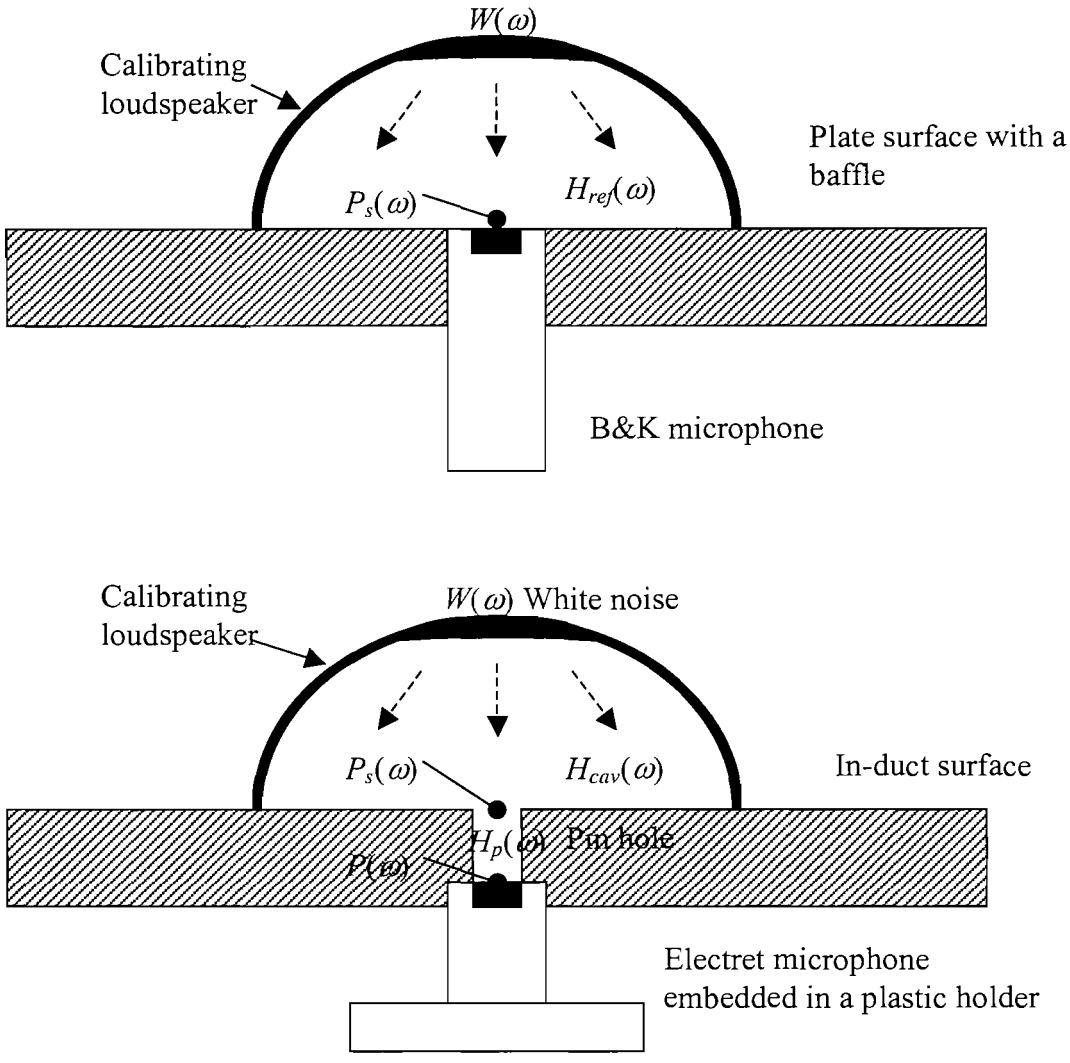

Transfer function of the model cavity : $H_{ref}(\omega) = P_s(\omega)/W(\omega)$

Transfer function of the in-duct cavity : $H_{cav}(\omega) = P(\omega)/W(\omega)$

Transfer function of the pin hole : $H_p(\omega) = H_{cav}(\omega)/H_{ref}(\omega)$

Figure 5.9 Illustration of the microphone calibration procedure.

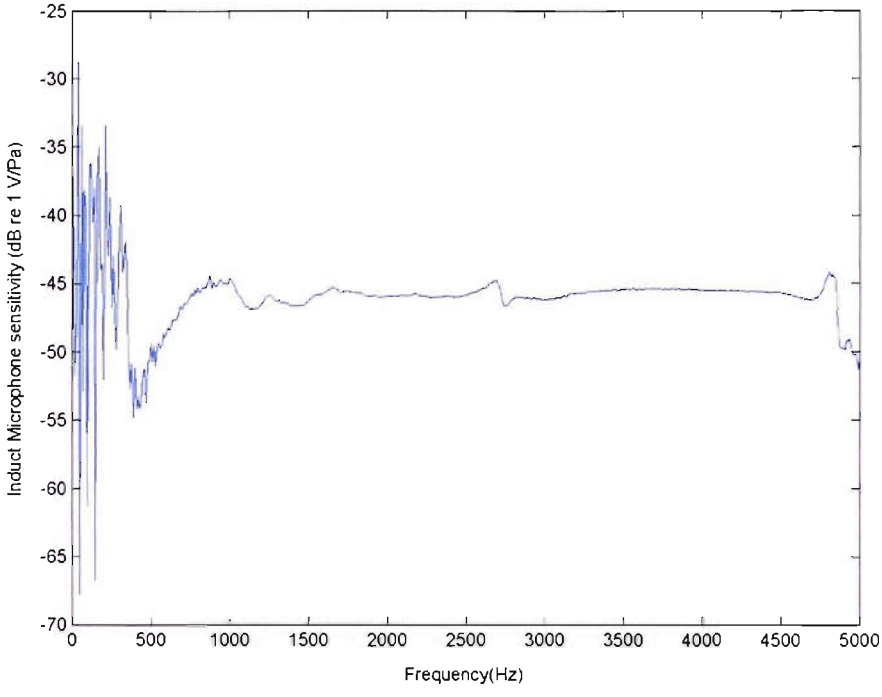

Figure 5.10 Sensitivity of an in-duct microphone (amplitude).

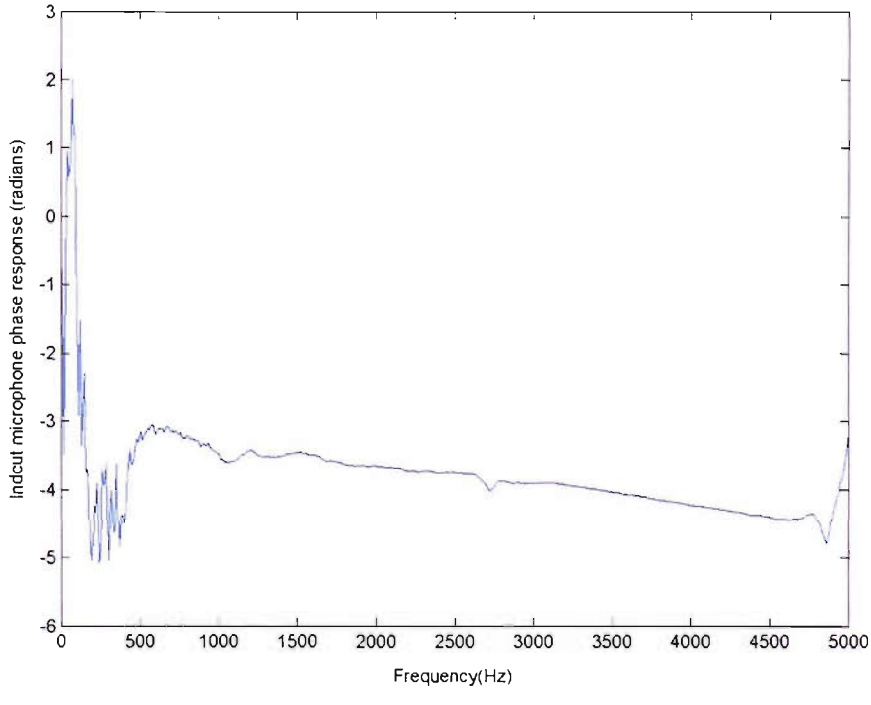

Figure 5.11 Sensitivity of an in-duct microphone (Phase).

5.3.2. Control experiments

Chapter 3 and Chapter 4 dealt with the simulation of the controller response determination and optimisation of control cost function. In Chapter 3 the controller response was determined by feeding the rod's wake profile into expressions which decomposed it into Fourier-Bessel modes and then estimated the fluctuating forces (coupling coefficient) and the resulting acoustic pressure radiated into the duct. This response was later used in the simulation of optimisation presented in Chapter 3 and Chapter 4. In the experimental situation, the propagating acoustic wave can be sensed as a pressure signal by the microphones on the duct surface. Upon fast Fourier transforming the microphone signals one can extract the BPF tone pressures from each microphone and then decompose the vector of BPF pressures into modes which can then be used in the controller response determination and the control algorithm. The variables and the associated processing involved are thoroughly dealt with in Subsection 5.3.2.1. The unsteadiness in the estimates of the quantities mentioned above and the number of averages required are dealt with in Subsection 5.3.2.2. The error in the duct power resulting from the semi-infinite approximation of the analytical model discussed in Chapter 2 is considered in Subsection 5.3.2.3. The experimentally determined acoustic response is discussed in Subsection 5.3.2.4. In Subsections 5.3.2.5, 5.3.2.6 and 5.3.2.7 the theory and results are presented for a few cases in which the implementation of the control algorithm was conducted.

5.3.2.1. Processing

The processing in the experiments consisted mainly of (i) the fast Fourier transformation of the incoming microphone signals, (ii) modal decomposition of the tones from the Fourier transformed pressure signals which are explained below. The estimation of modal coupling coefficients, reflection coefficients and tonal power are also explained.

FFT:

The voltage signals from the microphones are FFT'ed using vector averaging of the FFT estimates over blocks of these signals phase locked with the trigger signal. The trigger signal from the optical trigger registers a peak of around 5 to 6 V for every pass of a blade that has been marked on the fan. Without phase locking the estimate of the phase of the tones can be erroneous as the start of each microphone signal block of arbitrary length can correspond to a different start of the propagating acoustic wave at the source (fan). Each block's length corresponds to a single or multiple revolutions of the fan and the averaging was performed by using a suitable numbers of blocks at the two speeds which were determined from the unsteadiness analysis described later in this section. Only the BPF tone is taken up for the control study. A column vector of the BPF tone's complex amplitude is obtained from the processed signals acquired from the microphone array. Phase locked averaging is explained in Figure 5.12.

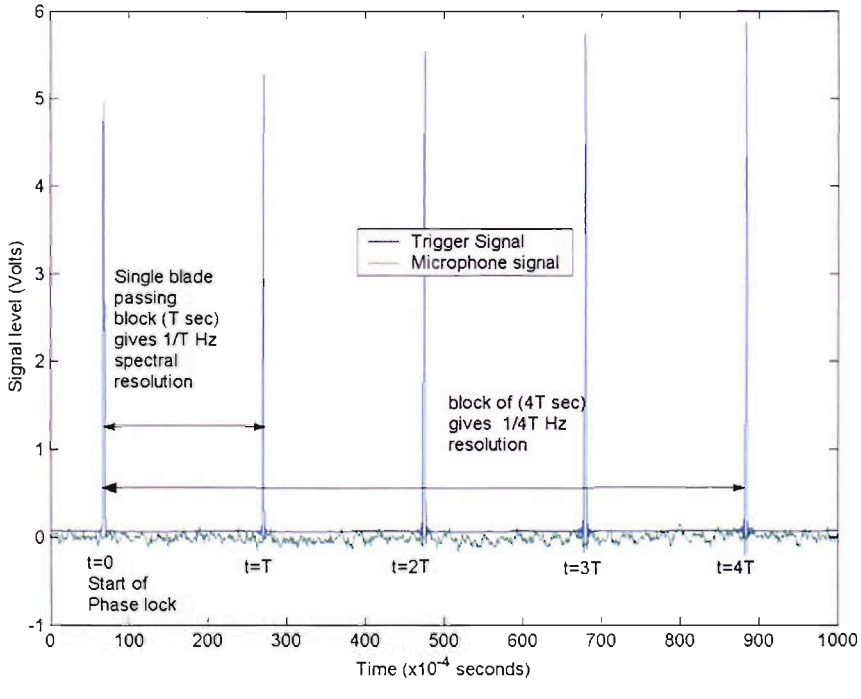

Figure 5.12 Illustration of phase locked averaging.

Modal decomposition:

Since the cost function for the active control algorithm, i.e. the overall sound power level J is expressed as the squared sum of the modal amplitudes in the

tones of the total noise field, these need to be obtained by decomposing the tonal pressures obtained previously from the FFTs into modes. Referring to Equation (2.3.6), and considering only the inlet-radiated noise for control and restricting attention to the M cut-on modes (m,n) in the BPF, the expression for the acoustic pressure at this harmonic then becomes a finite sum over these modes.

$$p_{sB}(\mathbf{x}) = \sum_{(m,n)=(m,n)_1}^{(m,n)_M} \left(A_{mn}^{-} e^{-jk_{mn}^{z+} z} + B_{mn}^{-} e^{-jk_{mn}^{z-} z} \right) \Psi_{mn}(r,\theta).$$

(5.3.1)

The above equation when related to the data obtained from the signals of the microphone array becomes a system of linear equations where the left side is the column vector of the tonal pressures obtained as mentioned in the section on phase locked averaging. The right side involves the unknown cut-on modal amplitudes, i.e., A_{mn} and B_{mn} respectively for the reflected and the incident upstream modes, and terms which have a spatial dependence on the microphone axial and circumferential locations (z and θ). Equations (5.3.2) and (5.3.3) express the system of equations which need to be inverted to get the unknown modal amplitudes.

$$\begin{bmatrix} p_{sB}(x_1) \\ \cdots \\ p_{sB}(x_i) \end{bmatrix}_{i\times 1} =$$

$$\begin{bmatrix} e^{-jk^{z+}_{m_1n_1} z_1} \times \Psi_{m_1n_1}(r_1,\theta_1) & e^{-jk^{z-}_{m_1n_1} z_1} \times \Psi_{m_1n_1}(r_1,\theta_1) & \cdots & \cdots & e^{-jk^{z+}_{m_Mn_M} z_1} \times \Psi_{m_Mn_M}(r_1,\theta_1) & e^{-jk^{z-}_{m_Mn_M} z_1} \times \Psi_{m_Mn_M}(r_1,\theta_1) \\ \cdots & \cdots & \cdots & \cdots & \cdots & \cdots \\ e^{-jk^{z+}_{m_1n_1} z_i} \times \Psi_{m_1n_1}(r_i,\theta_i) & e^{-jk^{z-}_{m_1n_1} z_1} \times \Psi_{m_1n_1}(r_i,\theta_i) & \cdots & \cdots & e^{-jk^{z+}_{m_Mn_M} z_i} \times \Psi_{m_Mn_M}(r_i,\theta_i) & e^{-jk^{z-}_{m_Mn_M} z_i} \times \Psi_{m_Mn_M}(r_i,\theta_i) \end{bmatrix}_{i\times 2M}$$

$$\times \begin{bmatrix} A^-_{m_1n_1} \\ B^-_{m_1n_1} \\ \cdots \\ \cdots \\ A^-_{m_Mn_M} \\ B^-_{m_Mn_M} \end{bmatrix}_{2M\times 1}$$

(5.3.2)

Denoting the column vector of unknown modal amplitudes on the right hand side of the above equation as $\mathbf{a}_{sB}$, we have

$$\mathbf{p}_{sB} = \mathbf{S}_{sB}\mathbf{a}_{sB},$$
$$\mathbf{a}_{sB} = \mathbf{S}^{-1}_{sB}\mathbf{p}_{sB}.$$

(5.3.3)

The inversion depends on how well conditioned the matrix S is, and its condition number was estimated for the experiments described in this section. At the low speed where there is only one cut-on mode, the pseudo-inversion of the above matrix with measurements from 14 microphones gave a condition number of 1.59, and at the high speed where there were three cut-on modes this number was 2.87.

Alternatively one can even extract the modal amplitudes in Equation (5.3.1) by performing a spatial Fourier Transform over the circumferential coordinate if the microphone array had equispaced microphones. Since the array had non-equispaced microphones and it is also necessary to further decompose

these modes into incident and reflected modes, it was decided to use the approach of solving the system of linear equations presented in Equation (5.3.3).

Modal Coupling Coefficient:
Referring to Equation (2.3.63) for the acoustic pressure field in terms of the coupling coefficient and expressing this in terms of the upstream incident modal amplitude B_{mn}, the value of the coupling coefficient $C_{m,pn}$ can be extracted as follows.

$$p_{sB}(x) = B \sum_{p=-\infty}^{\infty} \sum_{n=1}^{\infty} \frac{J_m(\kappa_{mn} r) e^{j\frac{MsB\Omega}{c_o \beta^2} z}}{N_{mn}^2 k_{mn,sB}} e^{-jm\theta} e^{-j\eta_{mn}^{0-}} \cos\left(\eta_{mn,sB}^{-}(z)\right) \times (m\hat{D}_{mn,p} + \gamma_{mn,sB}^{-} \hat{T}_{mn,p})$$
$$= \sum_{p=-\infty}^{\infty} \sum_{n=1}^{\infty} 2B_{mn}^{-} e^{j\left(-\eta_{mn}^{0-} + \frac{MsB\Omega}{c_0 \beta^2} z\right)} \cos\left(\eta_{mn,sB}^{-}(z)\right) \Psi_{mn}(r,\theta),$$

(5.3.4)

$$C_{mn,p} = (m\hat{D}_{mn,p} + \gamma_{mn,sB}^{-} \hat{T}_{mn,p})$$
$$= \left(B_{mn}^{-}\right) / \left(\frac{B}{2N_{mn}\, k_{mn,sB}} \right).$$

(5.3.5)

The contribution of the rod to the acoustic field, i.e., $C_{secondary}$ can be estimated from the relationship which expresses the contribution of the total acoustic field C_{error} as a sum of that of the primary and the secondary fields, C_{prim} and $C_{secondary}$ respectively:

$$C_{error} - C_{prim} = C_{secondary}.$$

(5.3.6)

When using multiple rods or rotating a single rod while implementing the active control system, the theoretical response of the multiple rods or the rotated rod is obtained using the expression $C_{mn,p} \times e^{-jp\theta}$, wherein the response of the reference

rod $C_{mn,p}$ is multiplied by the term $e^{-jp\theta}$ to account for the phase shift involved in the modal response of a rod rotated by angle θ.

Modal Reflection Coefficient:
The reflection coefficients as described in Equation (2.3.16) are repeated here

$$\begin{cases} R^{+}_{mn} = \dfrac{B^{+}_{mn}}{A^{+}_{mn}} = e^{2j\eta^{0+}_{mn}} \\ \dfrac{1}{R^{-}_{mn}} = \dfrac{B^{-}_{mn}}{A^{-}_{mn}} = e^{2j\eta^{0-}_{mn}}. \end{cases}$$

(5.3.7)

Tonal Power:
Power was estimated using the expression (3.5.1) which is repeated here

$$P_{sB} = B^2(1/\rho_o c_o)\sum_{p=-\infty}^{\infty}\sum_{n=1}^{\infty}\frac{1}{N^2_{mn}k^2_{mn,sB}}\frac{\alpha_{mn,sB}\beta^4}{(1-\alpha^2_{mn,sB}M^2)^2}e^{2\phi^{0-}_{mn,sB}} \times\left(\frac{e^{2\phi^{0-}_{mn,sB}}}{2}(1+\alpha_{mn,sB}M)^2-\frac{e^{-2\phi^{0-}_{mn,sB}}}{2}(1-\alpha_{mn,sB}M)^2\right) \times\left|C_{mn,p}\right|^2.$$

(5.3.8)

5.3.2.2. Unsteadiness in the estimates

It is necessary to know the number of averages of the fast Fourier transform estimate to be performed during each data acquisition to obtain steady estimates of the quantities discussed in the previous subsection. A 30 second acquisition on all the microphones (upstream, downstream and far-field) was made and phase locked averaging was performed to get the estimate of the tones on all the microphones. In this time around 1500 blocks of instrumented blade passes exist in the high speed case and 900 for the low speed case. Two types of averaging were performed. The averaging is described in Figure 5.13. The first one is the successive/incremental averaging. Here the number of averages were varied from

1 through 800 (26.77s of the signal) for the low speed case and 1 through 1400 (28s of the signal) for the high speed case. This averaging will determine whether the unsteadiness in the estimates decays and the number of blocks to be used for averaging during the subsequent experiments. The number of instrumented blade passes per block were varied from 1 through 3 for the low speed case and 1 through 5 for the high speed case which improves the resolution from 30 to 10Hz for the low speed and from 50 to 10Hz for the high speed. Figure 5.14 through Figure 5.15 show the effect of incremental averaging for the blade passing frequency tonal estimate in the first in-duct microphone for both the speeds, i.e., over 1 through 800 blocks (26.77s of the signal) for the low speed case and 1 through 1400 (28s of the signal) for the high speed case. It can be seen that increasing the resolution from 30 to 10 Hz in the low speed case and from 50 to 10 Hz in the high speed doesn't have any effect on the estimate.

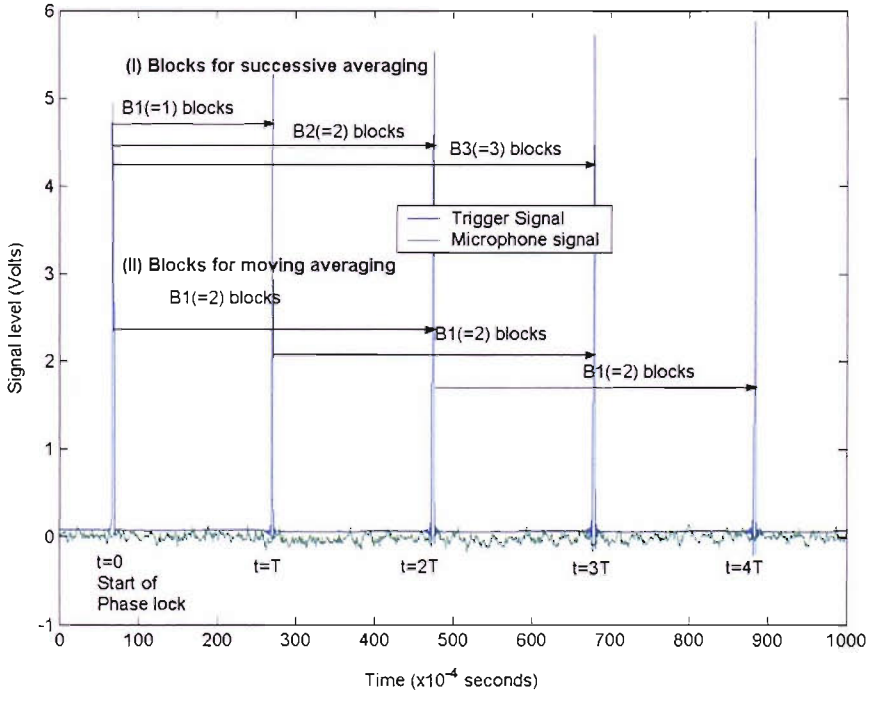

Figure 5.13 Averaging methods for unsteadiness analysis and the determination of number of blocks for phase locked averaging.

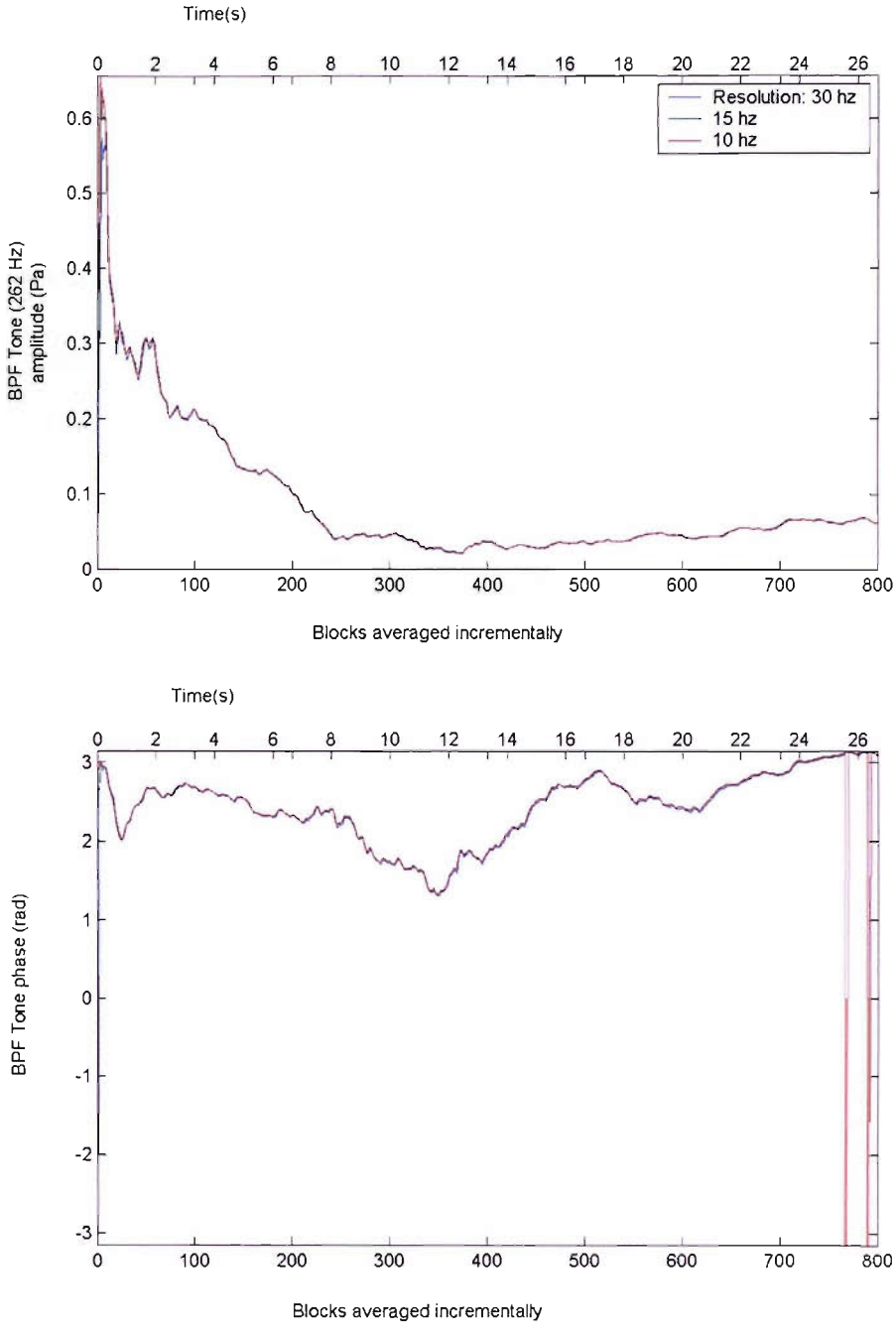

Figure 5.14 Effect of number of blocks of vector averaging on the BPF tone (262 Hz).

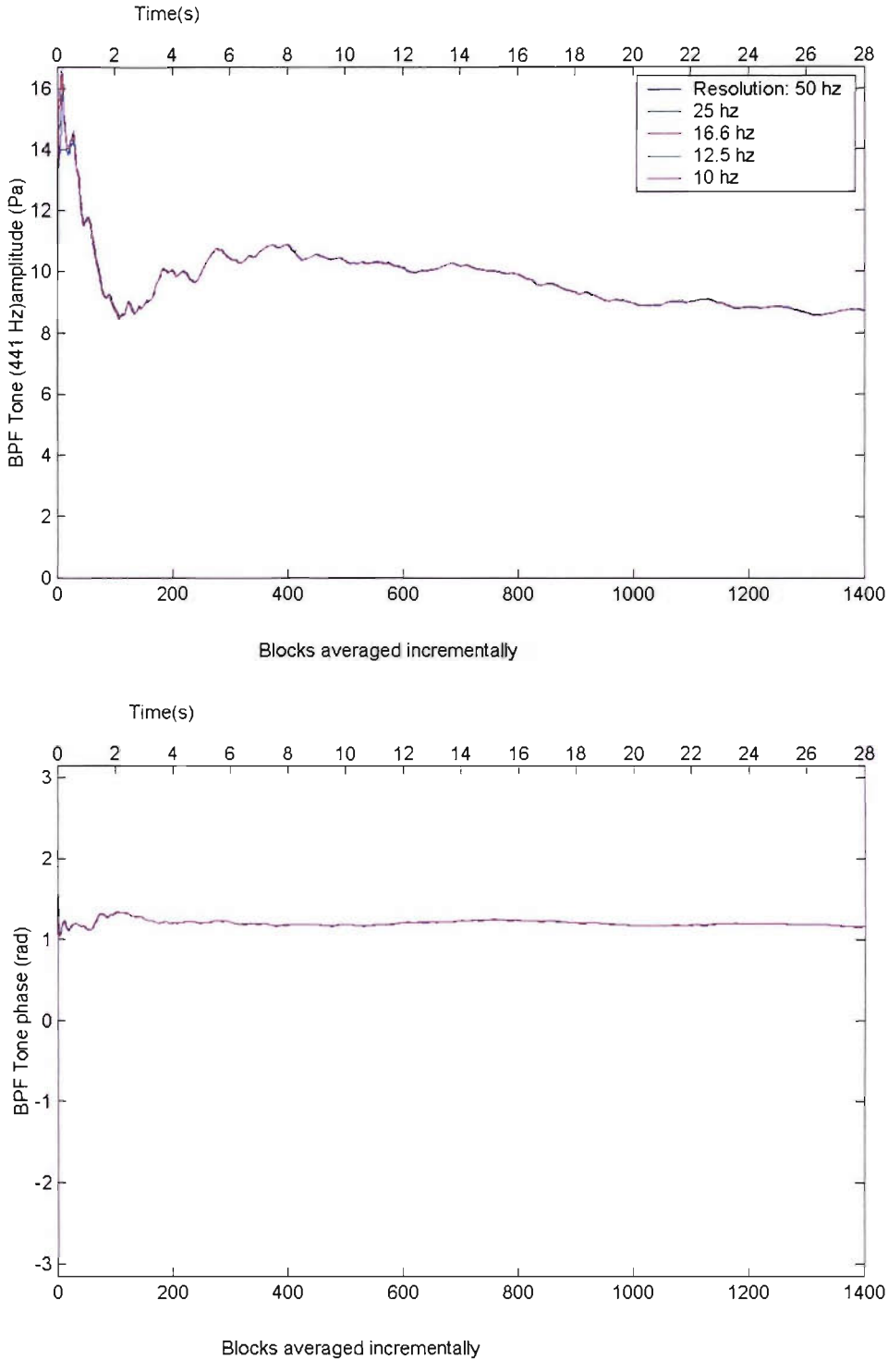

Figure 5.15 Effect of number of blocks of vector averaging on the BPF tone (441 Hz).

The above effect is shown for the case without a rod inside the duct. The 30s data acquisition was also performed for the case of the rod fully inserted into the duct and the above effect of the number of blocks is discussed for the following quantities for the cases with and without the rod insertion in Appendix 5.1.

1) All three harmonic tones on the upstream, downstream and far field for the low speed case and only on the upstream and far-field for the high speed case.
2) In duct upstream incident and reflected modal amplitudes for the low and high speed cases and also downstream incident and reflected modal amplitudes for the low speed case.
3) Coupling coefficients for the low and high speed cases.
4) Reflection coefficients and induct sound power and far field sound pressure levels.

From the above illustrations and the information provided in the Appendix it was decided that the number of blocks appropriate for averaging was 400 for the low speed setting and 600 for the high speed setting with each block representing 3 instrumented blade passes for the low speed case and 5 instrumented blade passes for the high speed case which give a resolution of 10 Hz in both cases.

The second type of averaging shown in Figure 5.13 is the fixed block averaging. After choosing the fixed (400 or 600) number of blocks from the first method of averaging described above a fixed block sliding/moving average over the 30s signal may be performed to describe the residual unsteadiness. 400 fixed blocks were chosen for the low speed case and 600 for the high speed case. Since there were only 800 and 1400 blocks in the first averaging method that was performed before the moving average was performed 400 times for the low speed and 800 times for the high speed case. The moving average variations along with residual unsteadiness in the quantities mentioned above are all given in Appendix 5.1.

In Section 3.6 of Chapter 3 a simple case of simulation of control was performed by holding the source rod at the zero reference and the controller rod at 20^0. Randomness in the primary disturbance coupling coefficient for this case was introduced programmatically by using the MATLAB randn() function. Figure 5.16 illustrates the convergence behaviour with the varying amount of the randomness which is given here in terms of the standard deviation of the modal

coupling coefficient in the primary disturbance (C_{prim}) expressed as a percentage of the mean of the same quantity. As the unsteadiness increases the reduction obtained in noise power decreases.

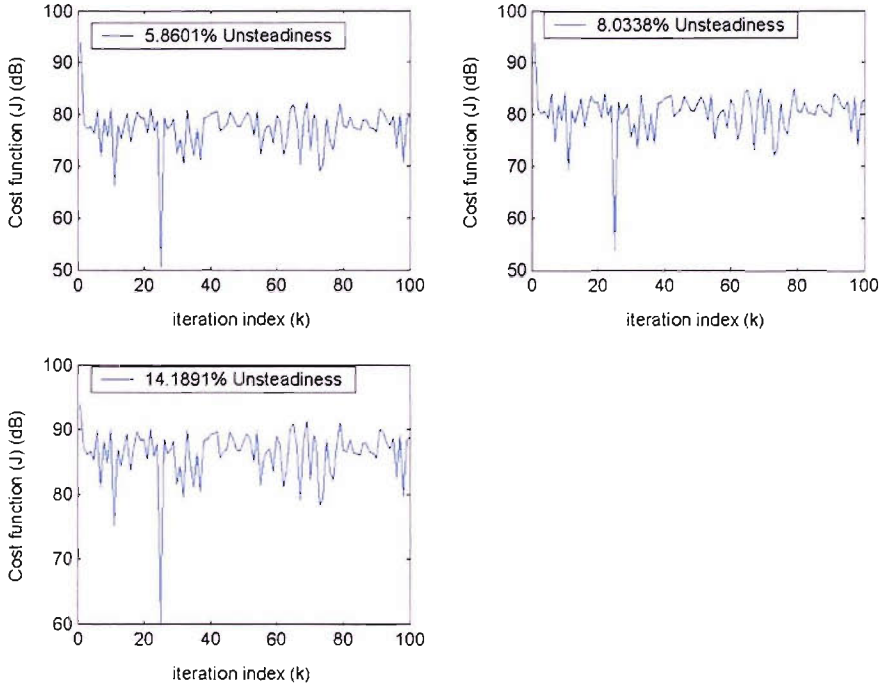

Figure 5.16 Effect of Randomness in primary disturbance coupling coefficient on convergence behaviour.

5.3.2.3. Error in the power through the assumption of semi-infiniteness of the duct

It was assumed in the development of the expression for the acoustic pressure expression in Chapter 2 that the termination at the fan exit is anechoic. The error this assumption would cause in the measured sound power ignoring the downstream reflections forms the subject matter of this subsection. In order to determine this microphone signals were measured using the upstream and downstream microphone arrays while the fan was run at the low speed (262 Hz of BPF) where only the plane wave mode is cut-on. Since both the reflected and incident modal amplitudes are available at the upstream and downstream sections of the fan duct, the estimates of the sound power using the expressions with and without the semi-infiniteness are compared here for the plane wave mode. As

mentioned already the derivation of the expression for the sound power is given in Appendix 3.1. The upstream intensity given in Equation (A.3.1.16) is repeated below. It can be seen that the intensity is dependant on the squared modulus of the pressure for a given mode for which the terms: $\alpha_{mn,sB} = k_{mn,sB}/k_o$, the flow parameters β and M, the reflection coefficient $\eta^{-}_{mn,sB}(z) = \xi^{-}_{mn,sB}(z) + j\phi^{0-}_{mn,sB}$ are constant. The intensity is

$$I_{sB,m,n} = (1/\rho_o c_o)\left(\frac{\begin{array}{l} 2M\alpha^2_{mn,sB}\beta^4 \cosh 2\phi^{0-}_{mn,sB} \\ +\alpha_{mn,sB}\beta^4(1+\alpha^2_{mn,sB}M^2)\sinh 2\phi^{0-}_{mn,sB} \end{array}}{(1-\alpha^2_{mn,sB}M^2)^2(\cosh 2\phi^{0-}_{mn,sB} + \cos 2\xi^{-}_{mn,sB}(z))}\right)\left|p_{sB,m,n}\right|^2.$$

(5.3.9)

The expression for the pressure (2.3.63) using the semi-infinite duct assumption is repeated below:

$$p_{sB}(x) = B\sum_{p=-\infty}^{\infty}\sum_{n=1}^{\infty}\frac{J_m(\kappa_{mn}r)e^{j\frac{MsB\Omega}{c_o\beta^2}z}e^{-jm\theta}}{N^2_{mn}k_{mn,sB}}e^{-j\eta^{0-}_{mn}}\cos\left(\eta^{-}_{mn,sB}(z)\right)\left(m\hat{D}_{mn.p} + \gamma^{-}_{mn,sB}\hat{T}_{mn,p}\right)$$

.

(5.3.10)

Hence the squared modulus of pressure is as follows:

$$\begin{aligned}\left|p_{sB}\right|^2 &= B^2\sum_{p=-\infty}^{\infty}\sum_{n=1}^{\infty}\frac{J^2_m(\kappa_{mn}r)}{N^4_{mn}k^2_{mn,sB}}\left|e^{-j\eta^{0-}_{mn}}\right|^2\left|\left(m\hat{D}_{mn.p} + \gamma^{-}_{mn,sB}\hat{T}_{mn,p}\right)\right|^2\left|\cos\left(\eta^{-}_{mn,sB}(z)\right)\right|^2 \\ &= B^2\sum_{p=-\infty}^{\infty}\sum_{n=1}^{\infty}\frac{J^2_m(\kappa_{mn}r)}{N^4_{mn}k^2_{mn,sB}}e^{2\phi^{0-}_{mn,sB}}\left|\left(m\hat{D}_{mn,p} + \gamma^{-}_{mn,sB}\hat{T}_{mn.p}\right)\right|^2 \\ &\quad\times\frac{(\cosh 2\phi^{0-}_{mn,sB} + \cos 2\xi^{-}_{mn,sB}(z))}{2}.\end{aligned}$$

(5.3.11)

The expression for the pressure (2.3.61) using the finite duct assumption is

$$p_{sB}(\mathbf{x}) = jB\sum_{p=-\infty}^{\infty}\sum_{n=1}^{\infty}\frac{J_m(\kappa_{mn}r)e^{j\left(\frac{MsB\Omega}{c_0\beta^2}z-m\theta\right)}}{N_{mn}^2\ k_{mn,sB}}\cos\left(\eta_{mn,sB}^{-}(z)\right)$$
$$\times\frac{\cos\left(\eta_{mn}^{0+}\right)}{\sin\left(\eta_{mn}^{0+}-\eta_{mn}^{0-}\right)}\left(m\hat{D}_{mn,p}+\gamma_{mn,sB}^{-}\hat{T}_{mn,p}\right)$$

(5.3.12)

Hence the squared modulus of pressure is as follows:

$$\left|p_{sB}\right|^2 = B^2\sum_{p=-\infty}^{\infty}\sum_{n=1}^{\infty}\frac{J_m^2(\kappa_{mn}r)}{N_{mn}^4\ k_{mn,sB}^2}\left|\frac{\cos\left(\eta_{mn}^{0+}\right)}{\sin\left(\eta_{mn}^{0+}-\eta_{mn}^{0-}\right)}\right|^2$$
$$\times\left|\left(m\hat{D}_{mn,p}+\gamma_{mn,sB}^{\pm}\hat{T}_{mn,p}\right)\right|^2\left|\cos\left(\eta_{mn,sB}^{-}(z)\right)\right|^2$$
$$= B^2\sum_{p=-\infty}^{\infty}\sum_{n=1}^{\infty}\frac{J_m^2(\kappa_{mn}r)}{N_{mn}^4\ k_{mn,sB}^2}\left|\frac{\cos\left(\eta_{mn}^{0+}\right)}{\sin\left(\eta_{mn}^{0+}-\eta_{mn}^{0-}\right)}\right|^2$$
$$\times\left|\left(m\hat{D}_{mn,p}+\gamma_{mn,sB}^{\pm}\hat{T}_{mn,p}\right)\right|^2\frac{\left(\cosh 2\phi_{mn,sB}^{0-}+\cos 2\xi_{mn,sB}^{-}(z)\right)}{2}.$$

(5.3.13)

For the plane wave mode situation at the low speed, the ratios of the powers obtained through the two assumptions is a ratio of the intensities which in turn is a ratio of the respective moduli of the squared pressures. This ratio is

$$\frac{\text{Power (semi}-\text{infinite duct assumption)}}{\text{Power (finite duct assumption)}} = \frac{\left|e^{-j\eta_{mn}^{0-}}\right|^2}{\left|\frac{\cos\left(\eta_{mn}^{0+}\right)}{\sin\left(\eta_{mn}^{0+}-\eta_{mn}^{0-}\right)}\right|^2} = \frac{e^{2\phi_{mn,sB}^{0-}}}{\left|\frac{\cos\left(\eta_{mn}^{0+}\right)}{\sin\left(\eta_{mn}^{0+}-\eta_{mn}^{0-}\right)}\right|^2}.$$

.

(5.3.14)

The error can expressed as the logarithm of the above quantity to specify it in decibels. Hence

$$P_{err} = 10\log_{10}\left(\frac{\left|e^{-j\eta_{mn}^{0-}}\right|^2}{\left|\frac{\cos\left(\eta_{mn}^{0+}\right)}{\sin\left(\eta_{mn}^{0+}-\eta_{mn}^{0-}\right)}\right|^2}\right) = 10\log_{10}\left(\frac{e^{2\phi_{mn,sh}^{0-}}}{\left|\frac{\cos\left(\eta_{mn}^{0+}\right)}{\sin\left(\eta_{mn}^{0+}-\eta_{mn}^{0-}\right)}\right|^2}\right).$$

(5.3.15)

It can be seen that the ratio depends on the upstream and downstream reflection coefficients $R_{mn}^{+} = e^{2j\eta_{mn}^{0+}}$ and $1/R_{mn}^{-} = B_{mn}^{-}/A_{mn}^{-} = e^{2j\eta_{mn}^{0-}}$. For the low speed case the reflection coefficients upstream and downstream were found to be 0.367 and .199 in the presence of a controller rod. The ratio of the powers was determined to be –1.2886 dB.

5.3.2.4. Acoustic response of a single control rod

A single cylindrical rod was fixed at the azimuthal zero reference and its length was varied in steps of 10 mm each and the signals from the microphones were captured and processed as described above to obtain the acoustic response in terms of the modal coupling coefficient. The fan was run at the said speeds and the BPF for these speeds corresponds to 262 Hz (low speed setting) and 441 Hz (high speed setting). At the BPF for the low speed, only the plane wave mode (m = 0) is cut-on. At the BPF for the high speed case 3 modes (m=(-1,0,1)) are cut-on in the first harmonic. The acoustic response for all the individual rods in terms of the modal coupling coefficient amplitude and phase is shown in Figure 5.17 and Figure 5.18 for the low speed (plane wave mode, m=0), and Figure 5.19 - Figure 5.24 for the high speed case (all three cut-on modes m=(-1,0,1)). The phase response is nearly flat but exhibits a drift in the lower length range. This could be due to the fan itself inducing a radially varying swirl in the wake generated by the rod which could cause the wake to shift circumferentially as it travels towards the fan. The amplitudes can be seen to be steadily rising.

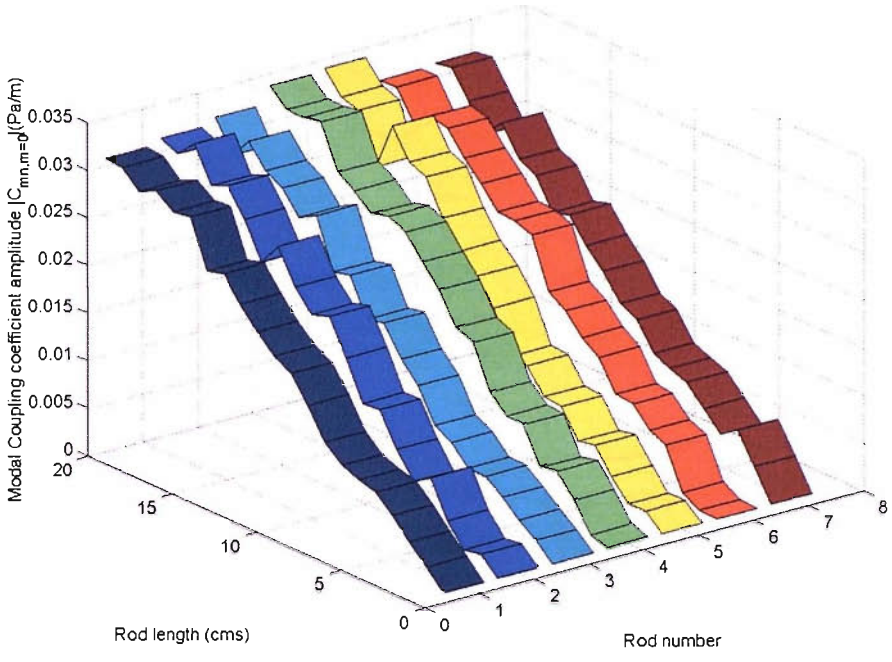

Figure 5.17 Amplitude response (coupling coefficient) of rods on the controller array for the plane wave mode (low speed case, 1st rod at reference 0^0).

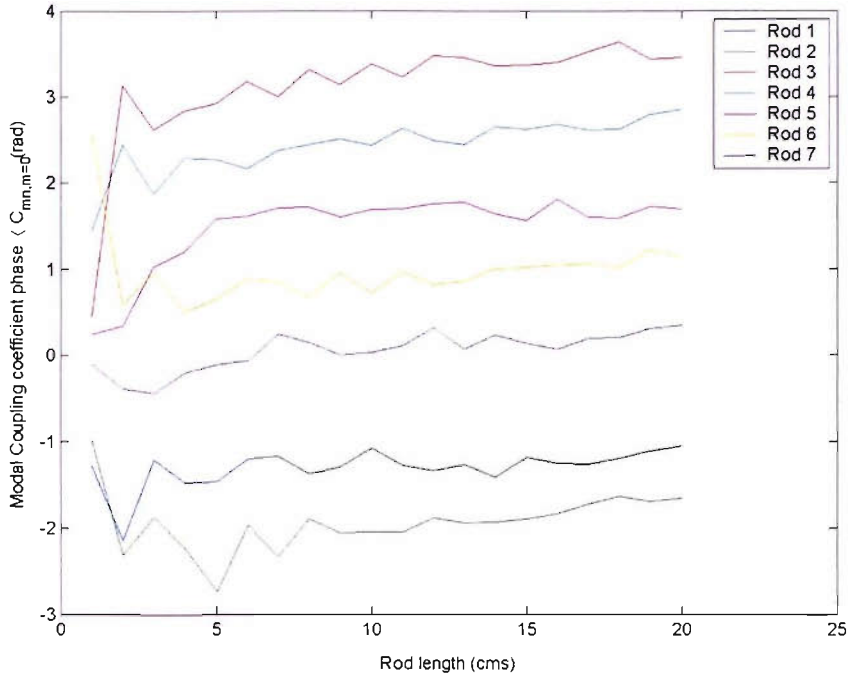

Figure 5.18 Phase response (coupling coefficient) of rods on the controller array for the plane wave mode (low speed case, 1st rod at reference 0^0).

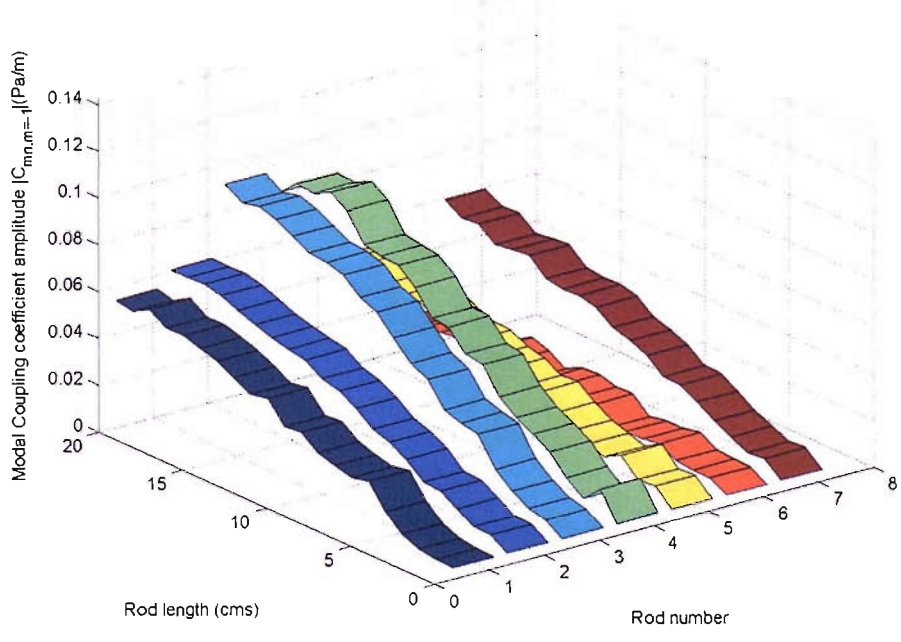

Figure 5.19 Amplitude responses (coupling coefficient) of rods on the controller array for mode *m*=-1 (high speed case, 1st rod at reference 0^0).

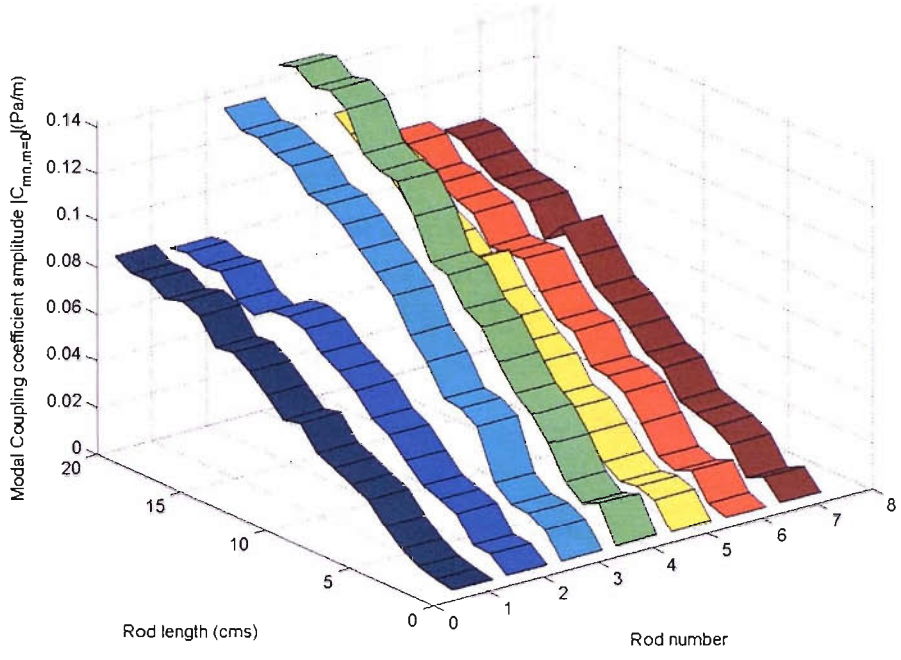

Figure 5.20 Amplitude responses (coupling coefficient) of rods on the controller array for mode m=0 (high speed case, 1st rod at reference 0^0).

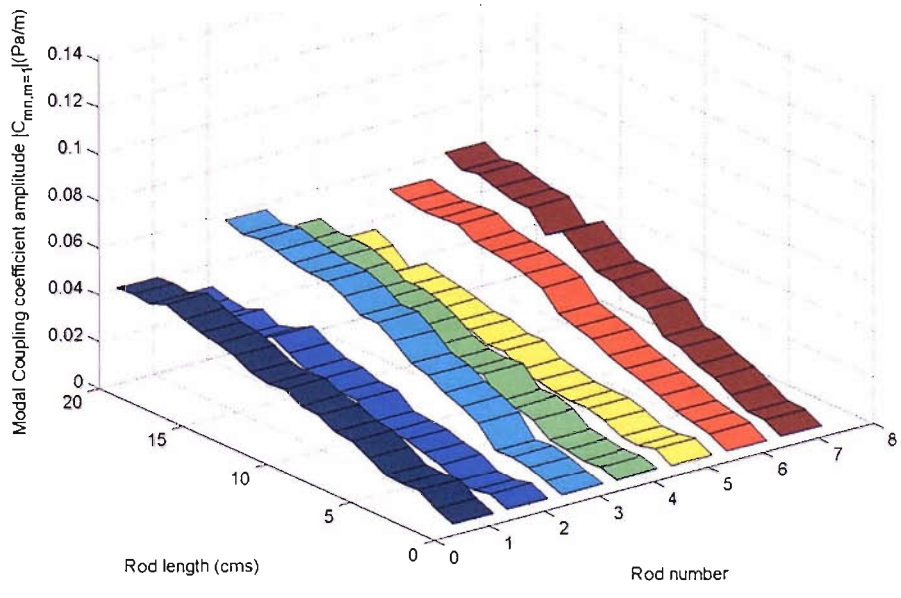

Figure 5.21 Amplitude responses (coupling coefficient) of rods on the controller array for mode m=1 (high speed case, 1st rod at reference 0^0).

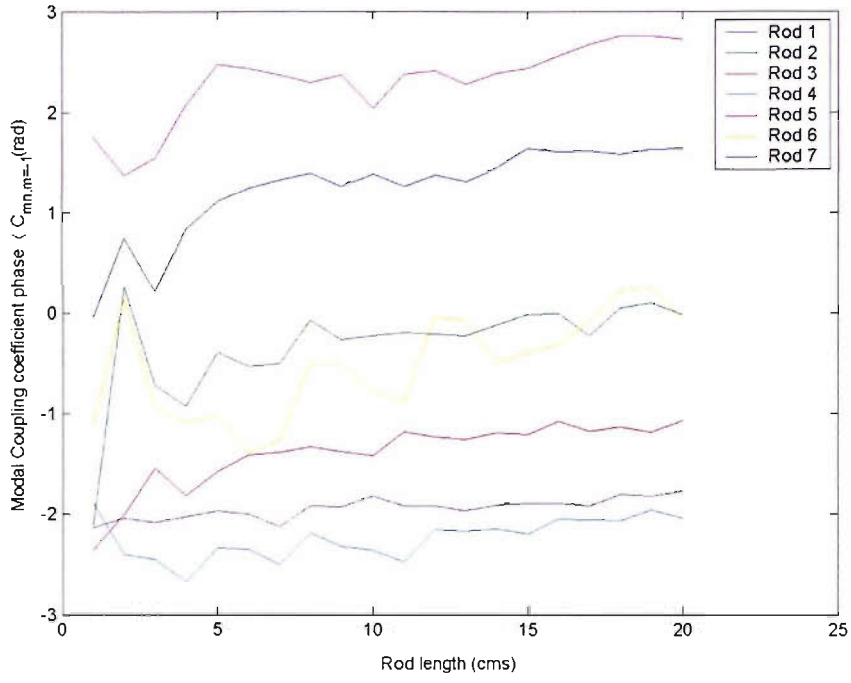

Figure 5.22 Phase responses (coupling coefficient) of rods on the controller array for mode m=-1 (high speed case, 1st rod at reference 0^0).

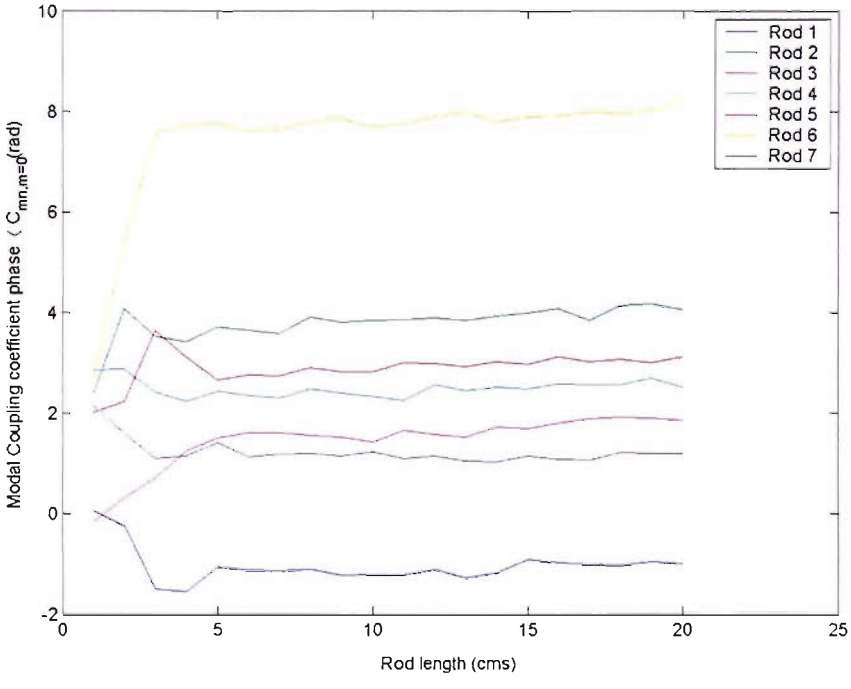

Figure 5.23 Phase responses (coupling coefficient) of rods on the controller array for mode m=0 (high speed case, 1st rod at reference 0^0).

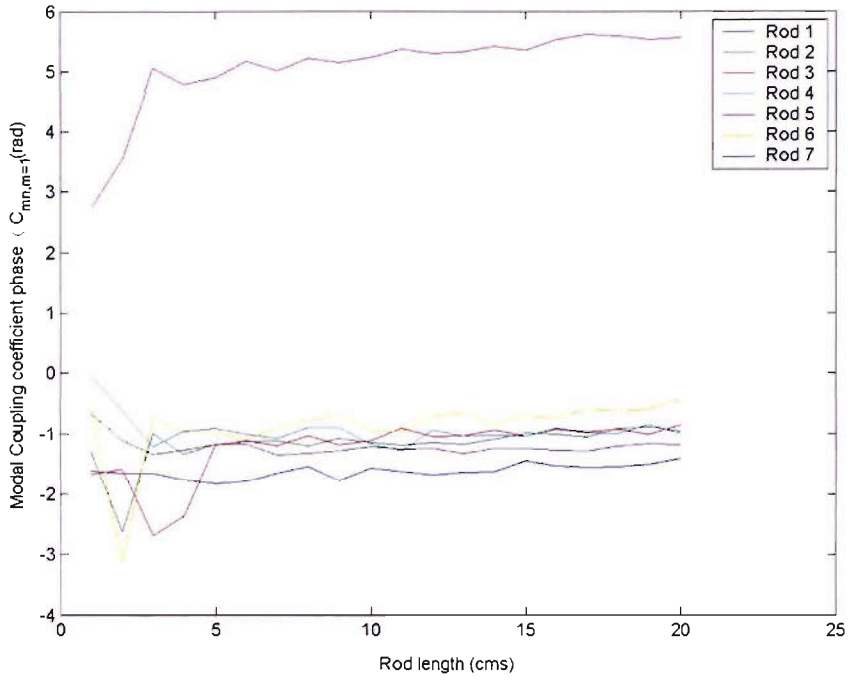

Figure 5.24 Phase responses (coupling coefficient) of rods on the controller array for mode m=1 (high speed case, 1st rod at reference 0^0).

The amplitude responses for the three modes in the high speed case vary across the rods and exhibit a variation with their circumferential orientation. This effect is attributed to the mode scattering effect which is explained in detail in Appendix 5.2. This phenomenon occurs due to the spinning modes' interaction with the rods to scatter off into modes of other circumferential orders.

The graphs in Figure 5.25 and Figure 5.26 show the linearised amplitude and averaged phase responses of the first rod for the plane wave mode at both speeds.

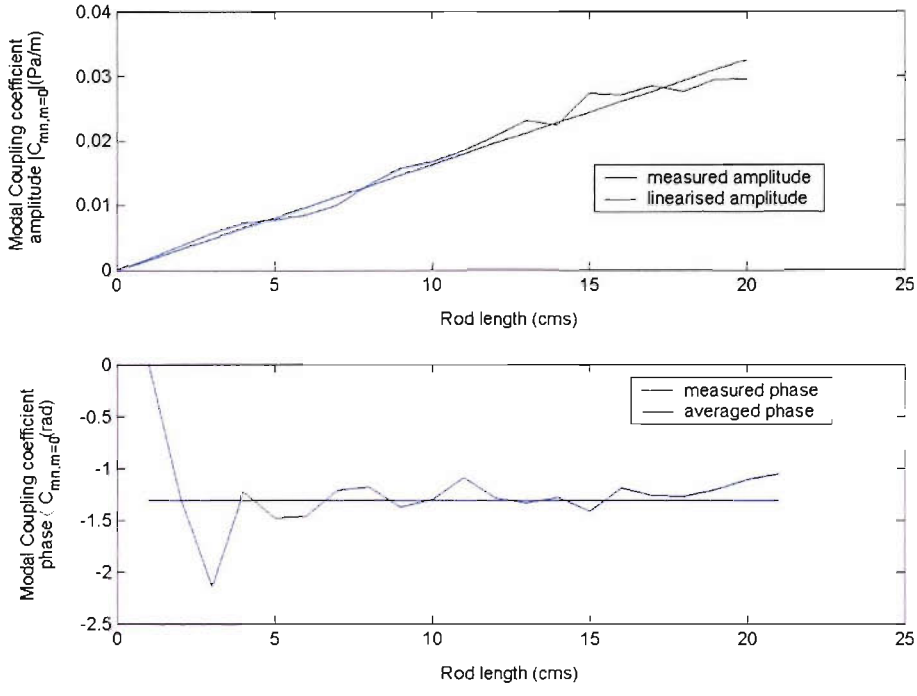

Figure 5.25 Linearised amplitude and averaged phase responses of the first rod for the plane wave mode (low speed).

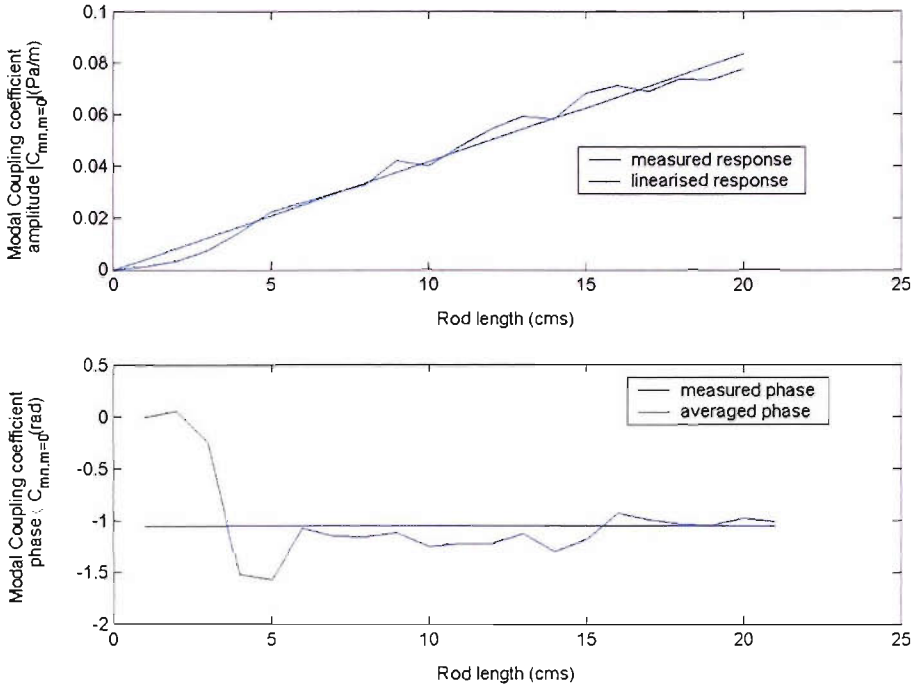

Figure 5.26 Linearised amplitude and averaged phase responses of the first rod for the plane wave mode (high speed).

In addition, we know from the theory that the responses of q rods can be obtained as follows if the response of the first rod is known:

$$C_{mn,p,sB}^{total} = (C_{mn,p,sB}) + (C_{mn,p,sB})e^{-jp\theta_1} + \cdots + (C_{mn,p,sB})e^{-jp\theta_q},$$

(5.3.16)

where $C_{mn,p,sB}^{total}$ is the net coupling coefficient for the mode in question and $(C_{mn,p,sB})$ is the first rod's coupling coefficient for the same mode. The term $e^{-jp\theta_q}$ expresses the phase relationship between the response of rod q and that of rod 1, where θ_q is the angular spacing between the first and the q^{th} rod. To verify if this relationship is true the phase response obtained individually for all the rods described in the figures above can be averaged radially and the averaged phase can be plotted against the rod orientation. This variation of the averaged estimate of the phase response can be compared against the theoretical variation $e^{-jp\theta}$. This variation is given for the low and high speed cases in Figure 5.27. For the

low speed case there is only one mode that is cut-on and at the high speed there are three cut-on modes. It can be seen that there is a fairly good agreement between the theory and the measurements. This provides also a means to verify the modal decomposition, since the program performing the decomposition knows only about the microphone orientations and has no knowledge of the individual positions of the rods.

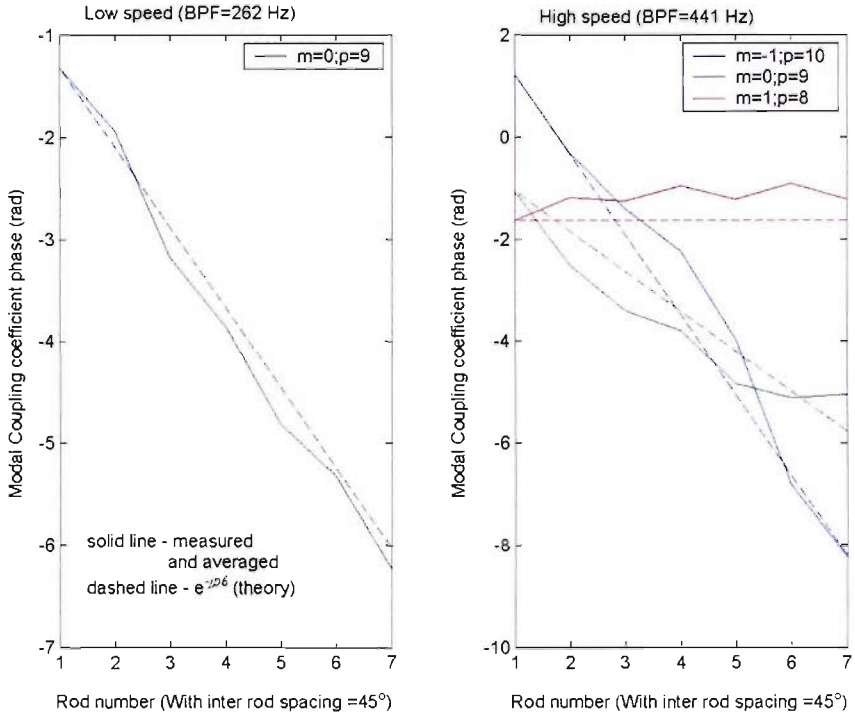

Figure 5.27 Variation of the measured and averaged phase response across the rods in the array as opposed to the theoretical variation.

5.3.2.5. Control Theory and Algorithm for implementation

Only the lengths of the rods in the array are considered the control variables and the control equations used in this context for the algorithm are repeated here. The equation for the cost function, (3.5.4) in terms of the coupling coefficient amplitudes is repeated.

$$J = \sum_{sB} P_{sB} = \sum_{sB} \sum_{mn,p} \varepsilon_{mn,sB} \left(C_{error}^{H} C_{error} \right)$$
$$= \sum_{sB} \sum_{mn,p} \varepsilon_{mn,sB} \left(C_{prim} + C_{secondary} \right)^{H} \left(C_{prim} + C_{secondary} \right)$$

(5.3.17)

where $C_{secondary} = \sum_{w} C_{mn,p,sB}$. The gradient as in Equation (3.5.5) is

$$\frac{\partial J}{\partial \mathbf{w}} = \sum_{sB} \sum_{mn,p} \varepsilon_{mn,sB} \left(\left(\frac{\partial C_{error}}{\partial \mathbf{w}} \right)^{H} C_{error} + C_{error}^{H} \left(\frac{\partial C_{error}}{\partial \mathbf{w}} \right) \right)$$
$$= \sum_{sB} \sum_{mn,p} \varepsilon_{mn,sB} \times 2\,\mathrm{Re} \left(\left(\frac{\partial C_{error}}{\partial \mathbf{w}} \right)^{H} C_{error} \right)$$
$$= \sum_{sB} \sum_{mn,p} \varepsilon_{mn,sB} \times 2\,\mathrm{Re} \left(\left(\frac{\partial C_{secondary}}{\partial \mathbf{w}} \right)^{H} C_{error} \right). \qquad \left\{ \because \frac{\partial C_{error}}{\partial \mathbf{w}} = \frac{\partial C_{secondary}}{\partial \mathbf{w}} \right\}$$

(5.3.18)

The objective function is minimised by iterating the control vector along the steepest descent and the converged set of lengths **w** needs to be obtained. The equation (3.5.6) for iterating the control vector is

$$\mathbf{w}(k+1) = \mathbf{w}(k) - \mu \frac{\partial J}{\partial \mathbf{w}}$$

(5.3.19)

with the constraint that **w**>**0**.

Using the responses of the rod that were obtained previously, active control experiments were performed using the steepest descent algorithm coded in MATLAB and LABVIEW. The LABVIEW code triggers the data acquisition of the signals from the microphones, and the interfaced MATLAB code performs phase locked averaged Fast Fourier Transformations and modal decomposition to finally obtain the estimate of C_{error} and J at each iteration k in the equations above. The linearised amplitude and averaged phase responses obtained previously are then used to obtain the quantity $\partial C_{secondary} / \partial \mathbf{w}$. Following the estimation of both

the quantities, i.e., C_{error} and $\partial C_{secondary}/\partial \mathbf{w}$, the gradient of the cost function $\partial J/\partial \mathbf{w}$ becomes known and the new estimate of the control vector $\mathbf{w}(k+1)$ is iterated from the old estimate of the control vector $\mathbf{w}(k)$. The LABVIEW program then communicates to the controller array through the RS232 port of the PC to make the required move to set the controller rods to the individual lengths in the vector $\mathbf{w}(k+1)$. This above procedure is repeated until convergence is obtained. The constraint that the rod lengths be positive is implemented by setting these to zero whenever they become negative. For all the experiments described the convergence coefficient μ in the initial iteration of the experiment was estimated by equating it to $|\partial J/\partial \mathbf{w}|^{-1}$ in terms of its order of magnitude. Later repetitions of the experiments were performed by fine tuning this estimate. The following assumptions are made in the control algorithm:

1) Gradient linearisation and phase averaging: $\partial C_{secondary}/\partial \mathbf{w}$ is obtained through linearisation and averaging described in Figure 5.25 and Figure 5.26.

2) Phase linearity with rotation: Superposition of the individual responses is done using the relationship obtained and illustrated in Figure 5.27. A diagram illustrating the control system set-up and the steps in the algorithm is shown in Figure 5.28.

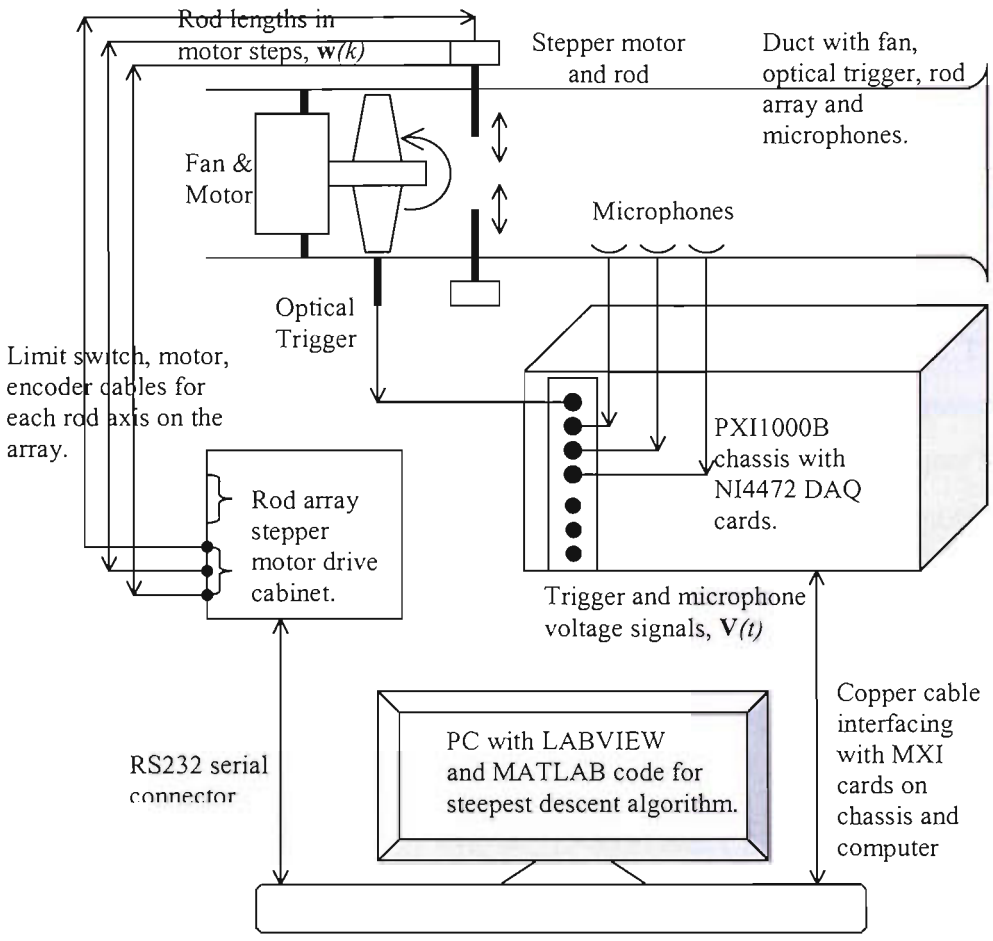

1. Trigger NIDAQ through LABVIEW and acquire the voltage signals $\mathbf{V}(t)$ representing the trigger and microphone signals.
2. Use the phase locked averaging method described in Section 5.3.2.1 to obtain the tonal pressure vector $\boldsymbol{p}_{sB}$ from the voltage signals acquired in the previous step and perform modal decomposition described in the same section to obtain the modal amplitudes and coupling coefficients.
3. Use modal coupling coefficients in step 3 to estimate the cost function J.
4. Estimate the gradient of the cost function $\partial J / \partial \mathbf{w}$ for the chosen number of controller rods using the linearised amplitude response and the radially averaged phase response of the rod.
5. Iterate the control vector $\mathbf{w}$ using the gradient estimated in step 4.
6. Convert the lengths obtained in step 5 into motor steps and send EASITOOL commands through serial RS232 port to cause the rod actuation by the individual stepper motors.
7. Loop through the above steps until convergence of the cost function and controller lengths is obtained.

Figure 5.28 Block diagram of the control system set-up and the control algorithm steps.

5.3.2.6. Active control experiments at low speed

In order to demonstrate the working of the algorithm to control noise using the rod array the list of experiments summarised in the Table 5.3 were performed in the low speed case where there was only one mode cut-on. The first seven experiments are baseline cases where in each case a single rod is inserted fully into the duct and the algorithm is run to see how far the rod is retracted. The later 8 cases deal with the control of the plane wave mode. In these experiments a single rod (rod 1) was used as a source and two other rods (rods 3 and 5) were used as controllers to demonstrate noise control. Under each experiment the number of rods used for the source, and those used as the controllers and the number of iterations (k) taken for convergence, the convergence coefficients (μ) used and the initial conditions used for the controllers are all listed.

Experiment description	BPF of the fan (Hz)	Source rod*	Source rod length (mm)	Controller rods*	Controller rod lengths (Initial condition) (mm)	(k)	(μ)
Retraction of rod 1	262			1	200	36	10^7
Retraction of rod 2	262			2	200	32	10^7
Retraction of rod 3	262			3	200	31	10^7
Retraction of rod 4	262			4	200	30	10^7
Retraction of rod 5	262			5	200	31	10^7
Retraction of rod 6	262			6	200	31	10^7
Retraction of rod 7	262			7	200	32	10^7
Control (Case1)	262	1	200	3 5	[0 0]	33	10^7
(Case2)	262	1	200	3 5	[0 0]	34	10^7
(Case3)	262	1	200	3 5	[200 0]	31	10^7
(Case4)	262	1	200	3 5	[200 0]	31	5×10^6
(Case5)	262	1	200	3 5	[200 0]	36	2.5×10^6
(Case6)	262	1	200	3 5	[0 0]	33	2.5×10^6

(Case7)	262	1	200	3 5	[0 0]	31	2.5×10^6
(Case8)	262	1	200	3 5	[0 0]	31	2.5×10^6

Table 5.3 List of Control experiments conducted at low speed. (*Refer to Table 5.1 for the rod identifications.)

The results for the above experiments are discussed for the baseline cases and then for the control experiments.

5.3.2.6.1. ***Results from the Rod retraction experiments***

The results are shown in Figure 5.29 and Figure 5.30 for the length and in Figure 5.31 and Figure 5.32 the power convergences for all the seven cases.

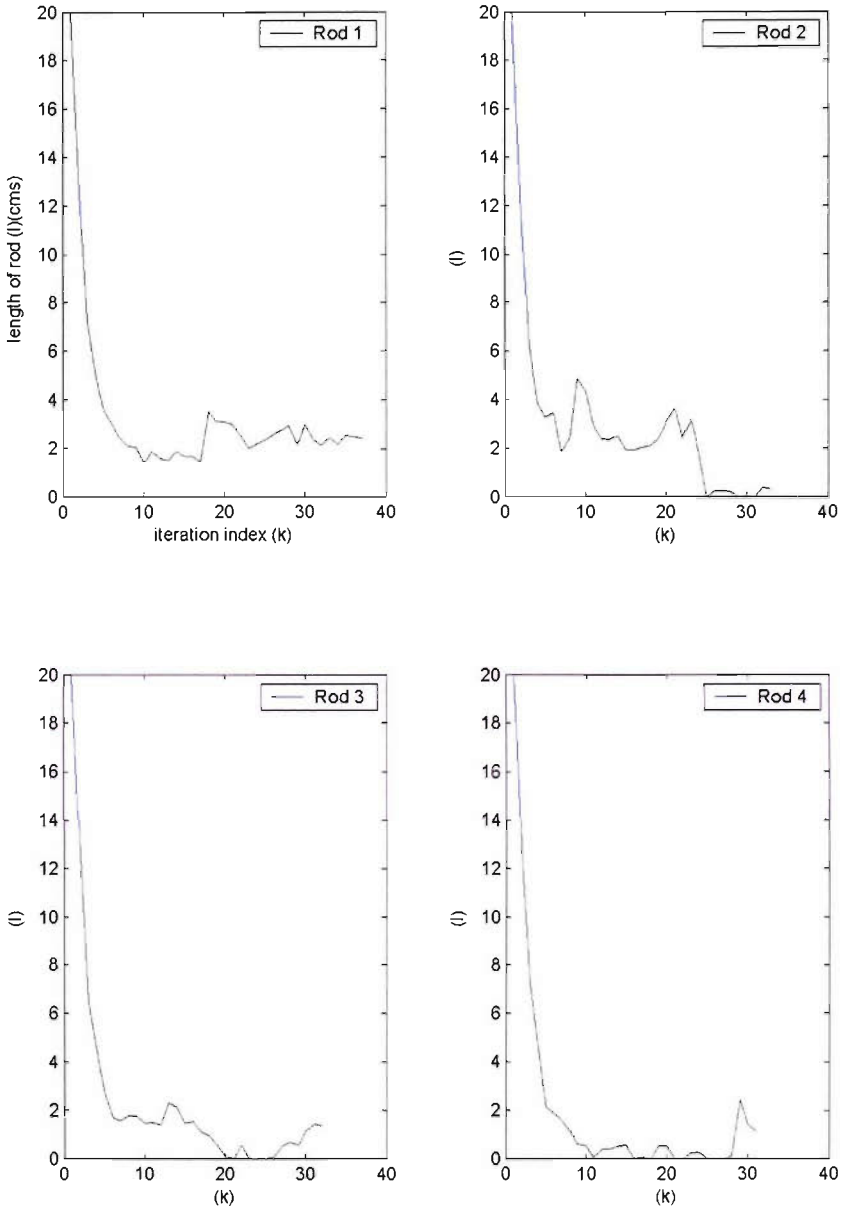

Figure 5.29 Length convergences for the rod retraction cases (1-4) ($\mu = 10^7$, BPF =262 Hz).

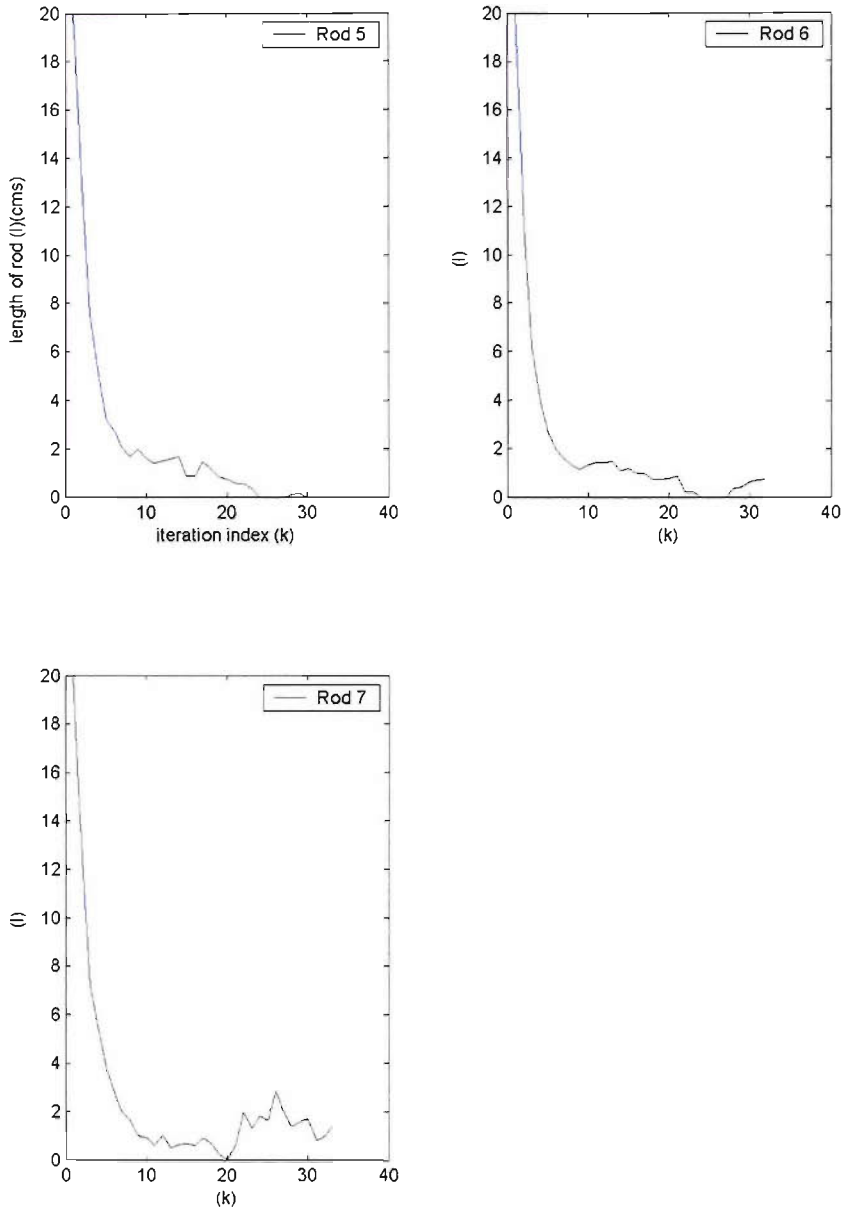

Figure 5.30 Length convergences for the rod retraction cases (5-7) ($\mu = 10^7$, BPF =262 Hz).

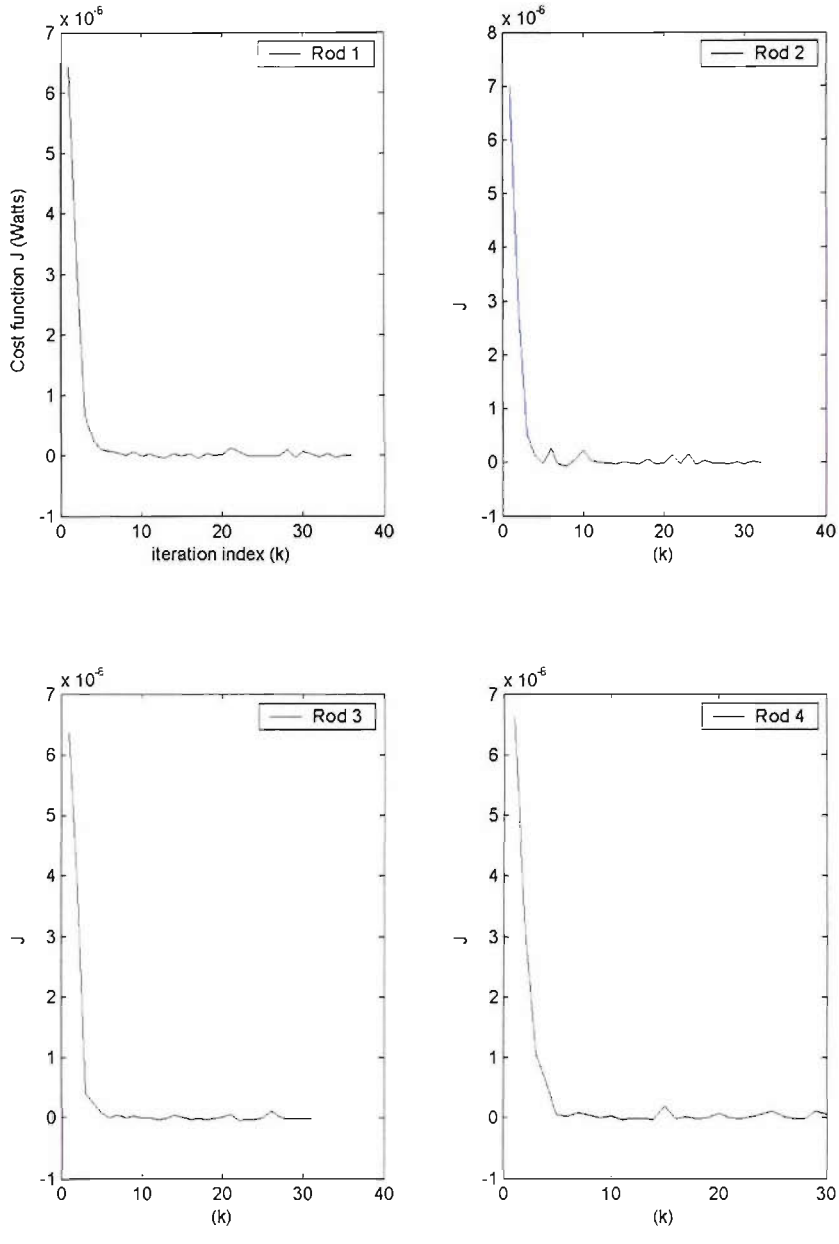

Figure 5.31 Cost function convergences for the rod retraction cases (1-4) (μ = 10^7, BPF =262 Hz).

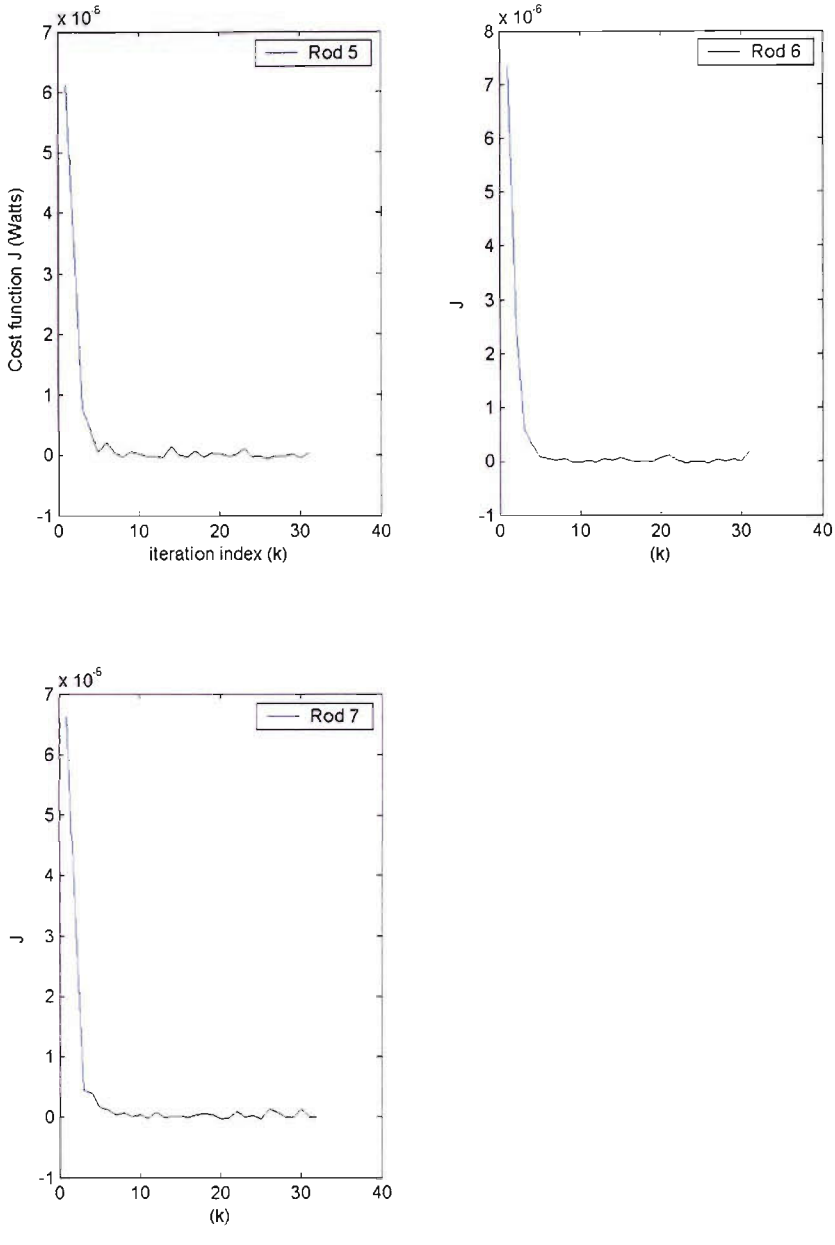

Figure 5.32 Cost function convergences for the rod retraction cases (5-7) (μ = 10^7, BPF =262 Hz).

The lengths of the rods converge starting from 20 cms in each case to about 2-3 cms. This residual length fluctuation is due to the unsteadiness and the low amplitude of the tone in the low speed case. The residual unsteadiness in the estimates after averaging is illustrated in Appendix 5.1 for all the variables. This

was shown to be higher for the low speed without the rod compared to the rest of the cases.

5.3.2.6.2. Results from the Control experiments

All control cases (Cases 1-8) listed in Table 5.3 previously were conducted using rod 1 as the source and rods 3 and 5 as the controllers. Rod 1 was extended into the duct fully (20 cms) to excite the primary disturbance mode.

Before proceeding to perform the control experiments the cost function J was measured at each point in the gridded space of the control vector consisting of controller rods 3 and 5 with the source rod 1 turned on. The length of each controller rod was stepped through 5 cms each time and J was measured at 441 points of the control vector space. The trace of the control algorithm can be superposed on this error surface to visually examine the convergence on this surface. Before describing this surface alternative means of generating this error surface were explored through simulations and then the shape of the simulated surfaces was later compared with the measured surface of J. The simulated error surface is generated in each of the following steps as the assumptions in simulations are relaxed gradually in each step. Each step in the simulation described below involves obtaining J through the coupling coefficient measured for rods 1, 3, and 5.

5.3.2.6.2.1. Step 1

Assumptions

a) The response of rod 1 alone is available which is one of those described in Figure 5.17 and Figure 5.18.

b) Amplitude response of rod 1 is linearised with respect to length, and its gradient $g_{rod1} = \frac{d|C_{rod1}|}{dl_1}$ and the averaged phase response $\overline{\theta_{rod1}}$ obtained as described in Figure 5.25. The phase is assumed to be constant with the

length variation and hence the gradient of the modulus of the amplitude variation with respect to length is considered here.

c) Responses of rods 3 and 5 are obtained via the theoretical phase transposition relationship, $e^{-jp\theta_q}$.

The cost function J can be estimated using Equation (5.3.17).

$$J = \varepsilon \left| C_{prim} + C_{secondary} \right|^2 , \qquad \textbf{(5.3.20)}$$

where the mode constant ε determined from measurements is 0.01. This quantity is evaluated using the expressions given in Equations (3.5.1) and (3.5.2). This quantity is evaluated once the complex valued upstream modal reflection coefficient, R_{mn}^{-}, and its complex phase, η_{mn}^{0-}, are estimated as expressed in Equation (5.3.7). $C_{prim} = C_{rod1}(l_1 = 20\text{cms})$ and since the gradient of the modulus of the amplitude response is known the net secondary coupling coefficient due to the presence of rods 3 and 5 with lengths l_3 and l_5 is evaluated as follows: $C_{secondary} = g_{rod1} \times e^{j\overline{\theta_{rod1}}} \times l_3 \times e^{-jp\pi/2} + g_{rod1} \times e^{j\overline{\theta_{rod1}}} \times l_5 \times e^{-ip\pi}$. The above calculation was performed in the gridded space of [l_3, l_5] and the surface obtained is shown in Figure 5.33. The x-y plane represents the grid of the controller vector space formed by rods 3 and 5 in the presence of the fully inserted rod 1. Hence point (0,0) on this plane corresponds to the situation when only rod 1 is inserted into the duct and rods 3 and 5 are set to zero. Hence the point on the surface corresponding to this (0,0) on the x-y plane represents the duct power when rod 1 is fully inserted into the duct. The rest of the points on this surface show how the power varies as rods 3 and 5 are set to their respective lengths in the grid. We see that the power reduces as the length of rod 5 increases and increases as the length of rod 3 is increased.

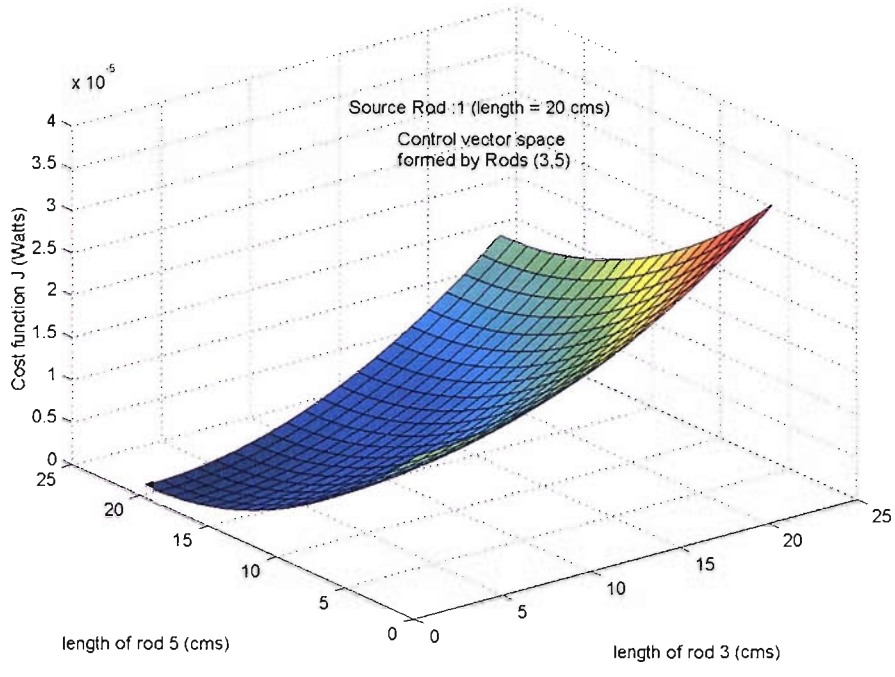

Figure 5.33 Cost function surface plot of *J* using assumptions in Section 5.3.2.6.2.1.

5.3.2.6.2.2. Step 2

Assumptions

a) The response of rod 1 alone is available which is one of those described in Figure 5.17 and Figure 5.18.

b) Actual amplitude and phase response of rod 1, i.e., C_{rod1}, is taken in the following calculation as opposed to the linearised amplitude and averaged phase in the previous step.

c) Responses of rods 3 and 5 are still obtained via the theoretical phase transposition relationship, $e^{-jp\theta_q}$.

Expressing J as the sum of the squares of modal amplitudes as was done before we have

$$J = \varepsilon \left| C_{prim} + C_{secondary} \right|^2 ,$$

(5.3.21)

where $C_{prim} = C_{rod1}(l_1 = 20\text{cms})$,

$C_{secondary} = C_{rod1}(l_1 = l_3) \times e^{-jp(\pi/2)} + C_{rod1}(l_1 = l_5) \times e^{-jp(\pi)}$ and ε =0.01. The above calculation was performed in the same gridded space of [l_3, l_5] and the surface obtained is shown in the Figure 5.34 below.

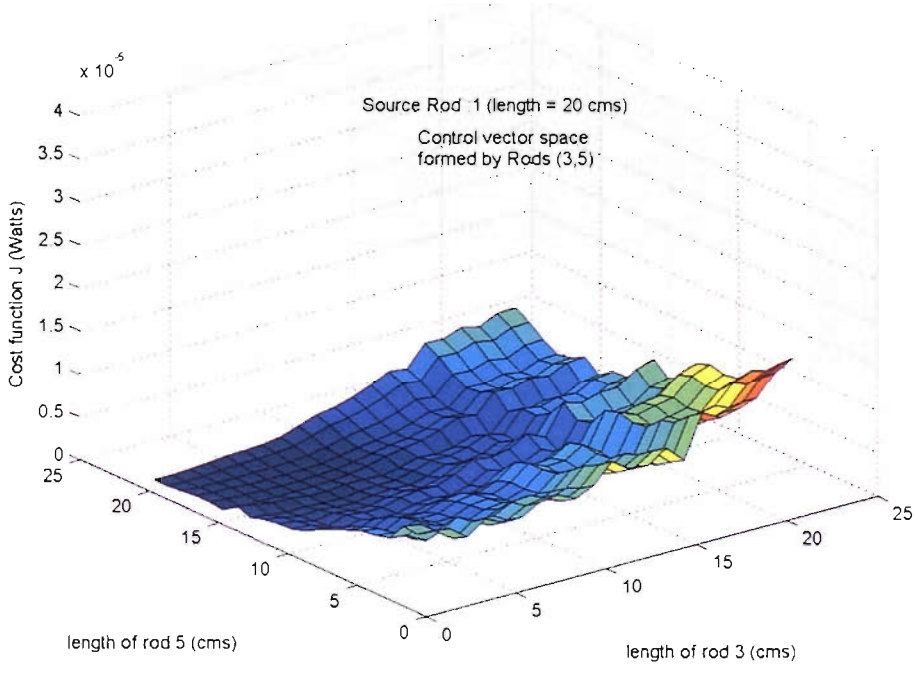

Figure 5.34 Cost function surface plot of *J* using assumptions in Section 5.3.2.6.2.2.

This surface retains the same shape as in the previous illustration in Figure 5.33 except at the edges because of the phase response not being strictly constant with length.

5.3.2.6.2.3. Step 3

Assumptions:

a) Individual responses of rods 1, 3 and 5 are available.

b) Actual amplitude and phase responses of the individual rods are taken. Since individual phase responses are taken into consideration the question of using the phase transposition relationship doesn't arise here.

Expressing J as the sum of the squares of modal amplitudes as was done before we have

$$J = \varepsilon \left| C_{prim} + C_{secondary} \right|^2 \qquad \textbf{(5.3.22)}$$

where $C_{prim} = C_{rod1}(l_1 = 20\text{cms})$, $C_{secondary} = C_{rod3} + C_{rod5}$ and ε =0.01. The above calculation was performed in the same gridded space of $[l_3, l_5]$ and the surface obtained is shown in the Figure 5.35 below.

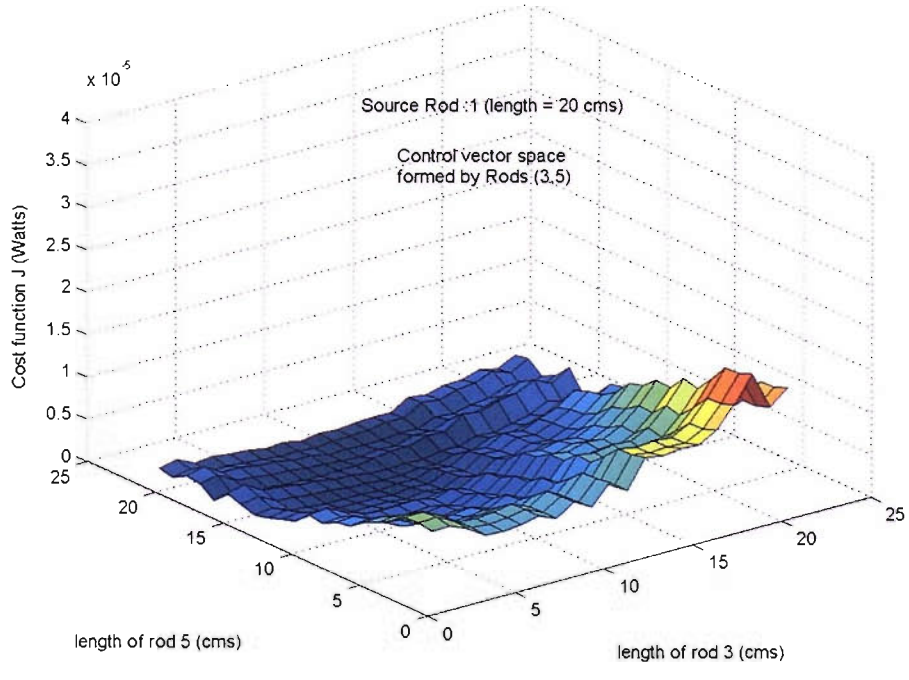

Figure 5.35 Cost function surface plot of J using assumptions in Section 5.3.2.6.2.3.

This surface has also the same shape as the previous ones in Figure 5.33 and Figure 5.34.

5.3.2.6.2.4. Step 4

Direct measurement of *J:*

The measured cost function surface along the previously mentioned control vector space grid of 441 points is shown in Figure 5.36. Unlike in the previous steps, *J* in this illustration accounts for the other factors along with the square of the modal coupling coefficient amplitudes. Though the surfaces in Figure 5.33-Figure 5.36 have the same shape as far as the increase of the lengths of rods 3 and 5 are concerned, the difference in the magnitudes is obvious due to the assumptions involved in Steps 1-3. The surface in Figure 5.33 which was estimated using all the stated assumptions has a peak that is approximately 3 times the magnitude of that in Figure 5.36 which was obtained through measurements. Hence it was decided to use the linearised amplitude and averaged phase responses of the individual rods in the control algorithm.

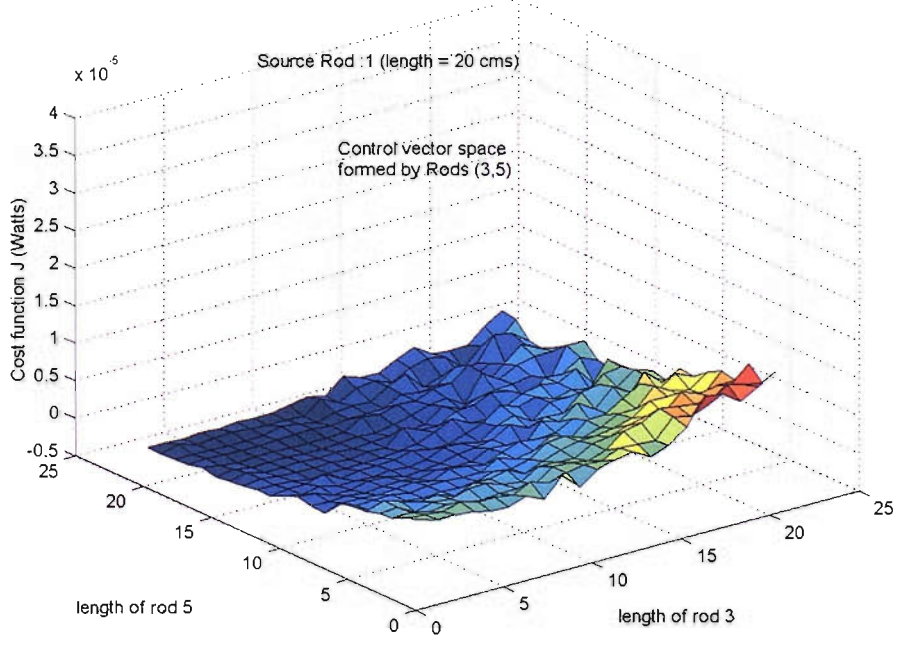

Figure 5.36 Cost function surface plot of *J* obtained through measurement.

Finally the results of the control experiments for cases 1-8 are given below. For the 8 cases the convergence of lengths and in-duct power level variations are given in Figure 5.37-Figure 5.42. In-duct power is plotted in watts

in Figure 5.39-Figure 5.40 and in decibels in Figure 5.41-Figure 5.42 with the points marked appropriately wherever the power is negative. This is because the in the in-duct measurements the first harmonic amplitude for the low speed case without the rod inside the duct was found to be very low due to the phase incoherence of the tone across the individual blade pass segments in the microphone signal. The low amplitude tone combined with the unsteadiness caused the estimate of the reflection coefficient to fluctuate widely. This caused the power to change from positive to negative values due to the reversal of the sign of the transmitted sound intensity. This explanation for the negative power was already given in Appendix 5.1. The in-duct power in the control experiments described in this section reduced from 67 dB to 42 dB. As already mentioned the upstream in-duct power is estimated using Equation (5.3.8) once the modal coupling coefficients and the reflection coefficients are known.

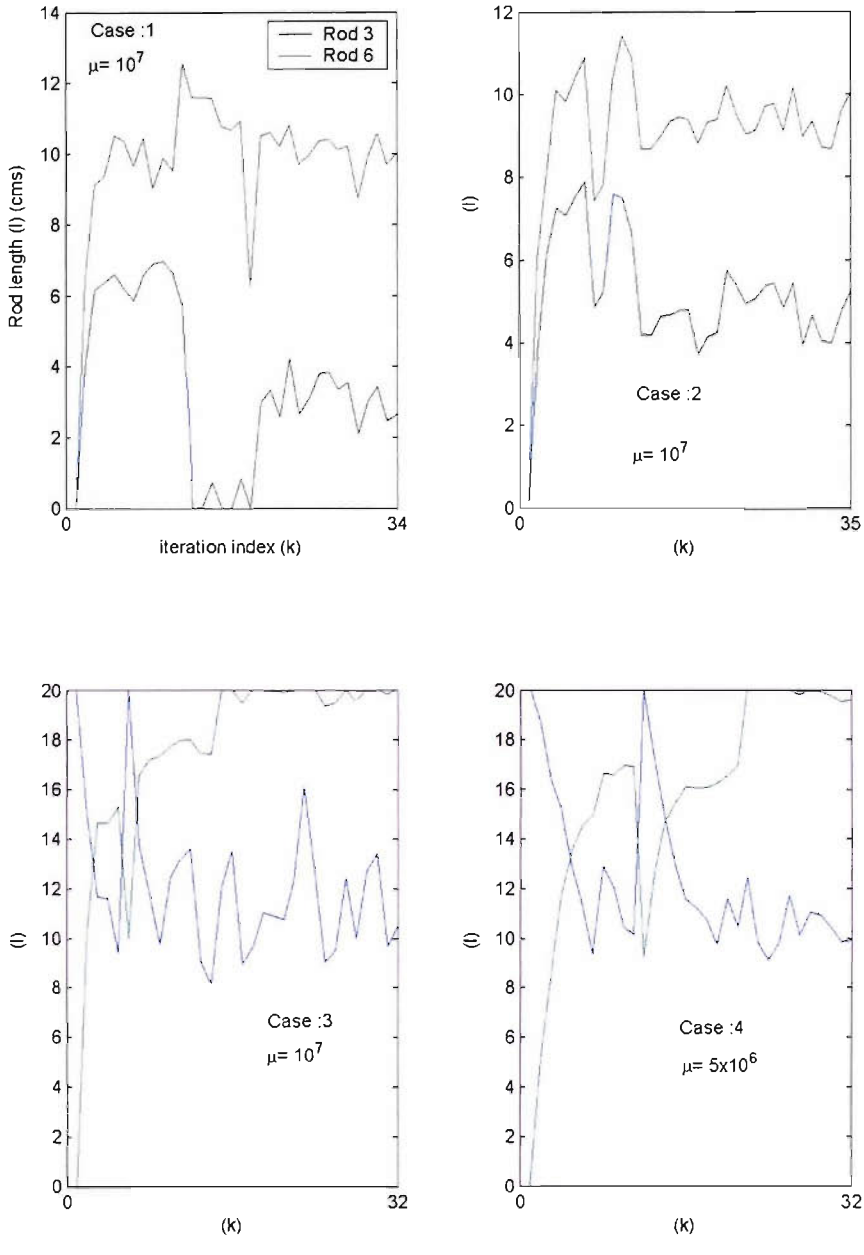

Figure 5.37 Length convergences for control experiments in cases (1-4).

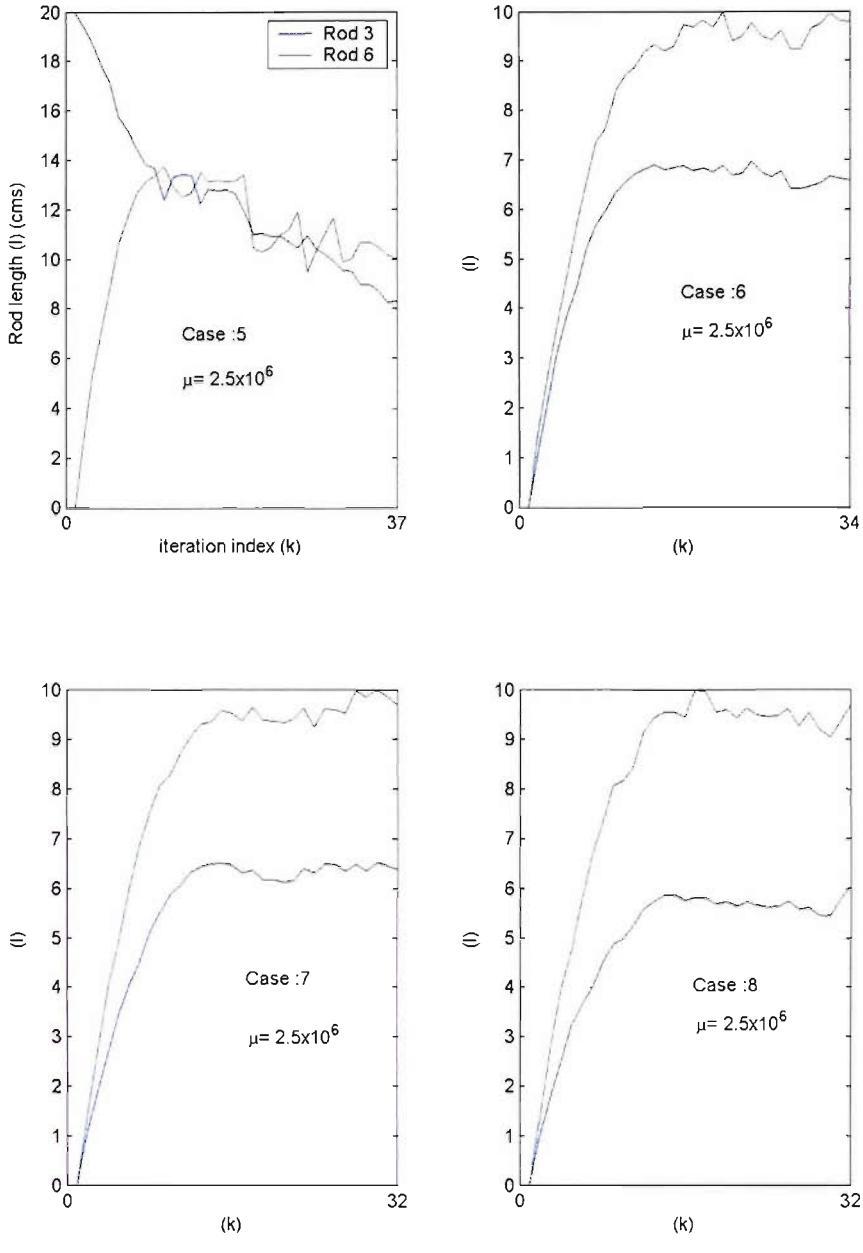

Figure 5.38 Length convergences for control experiments in cases (5-8).

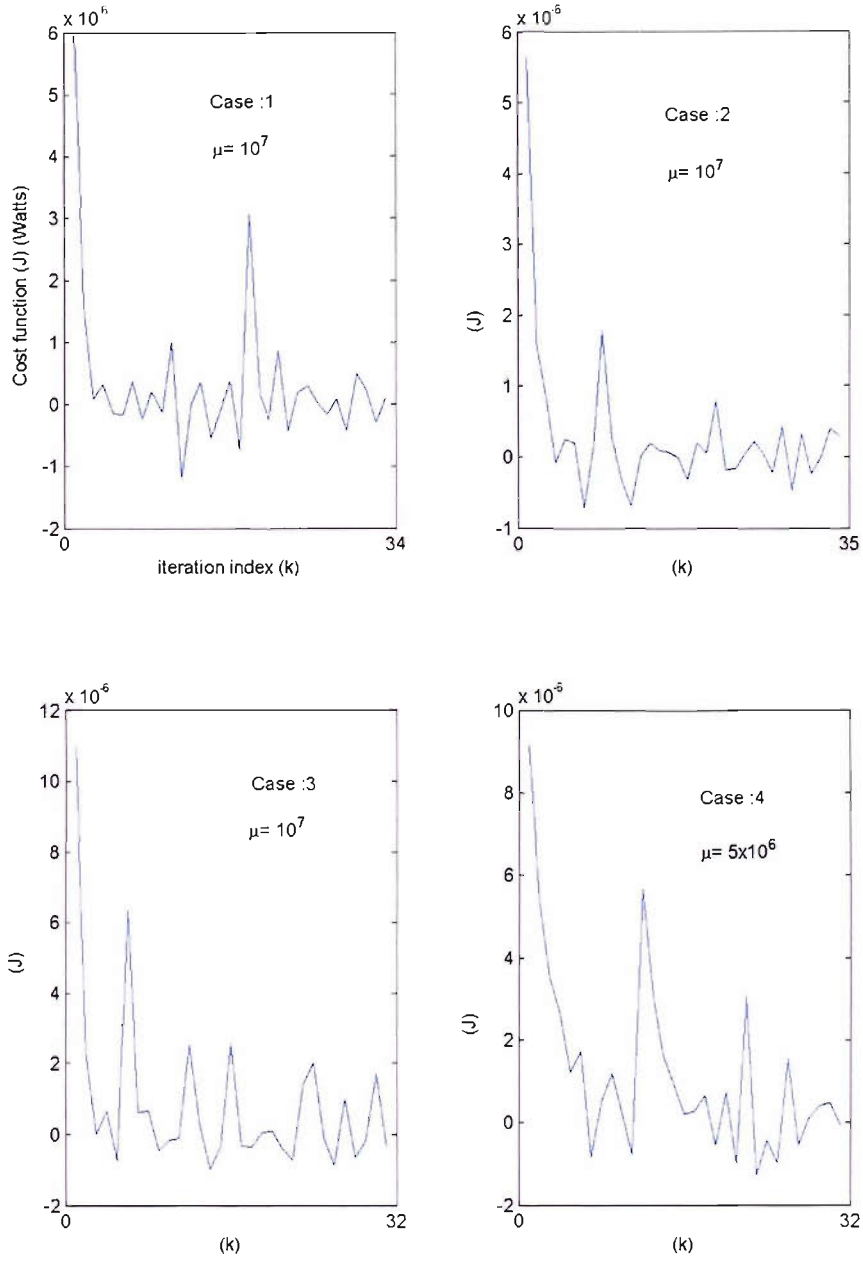

Figure 5.39 Cost function (Watts) convergences for control experiments in cases (1-4).

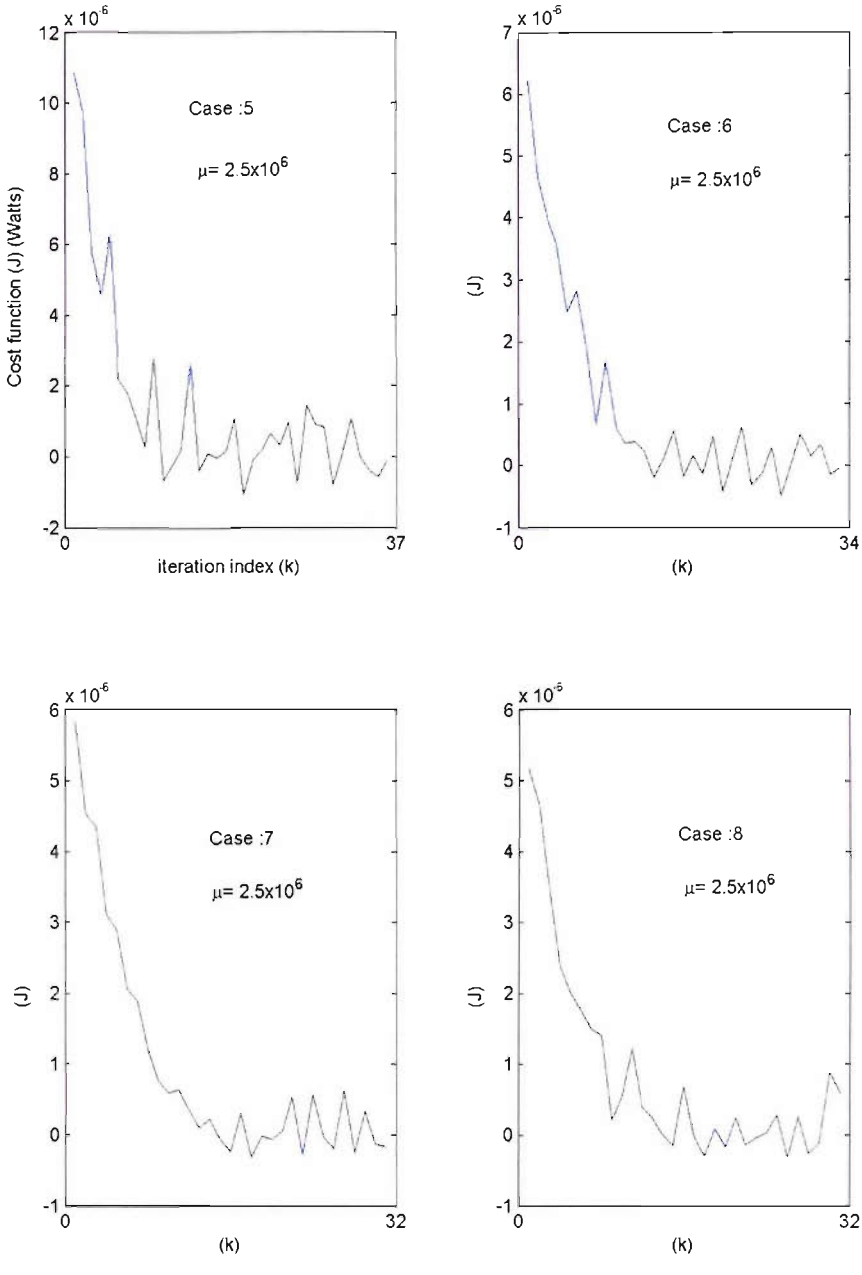

Figure 5.40 Cost function (Watts) convergences for control experiments in cases (5-8).

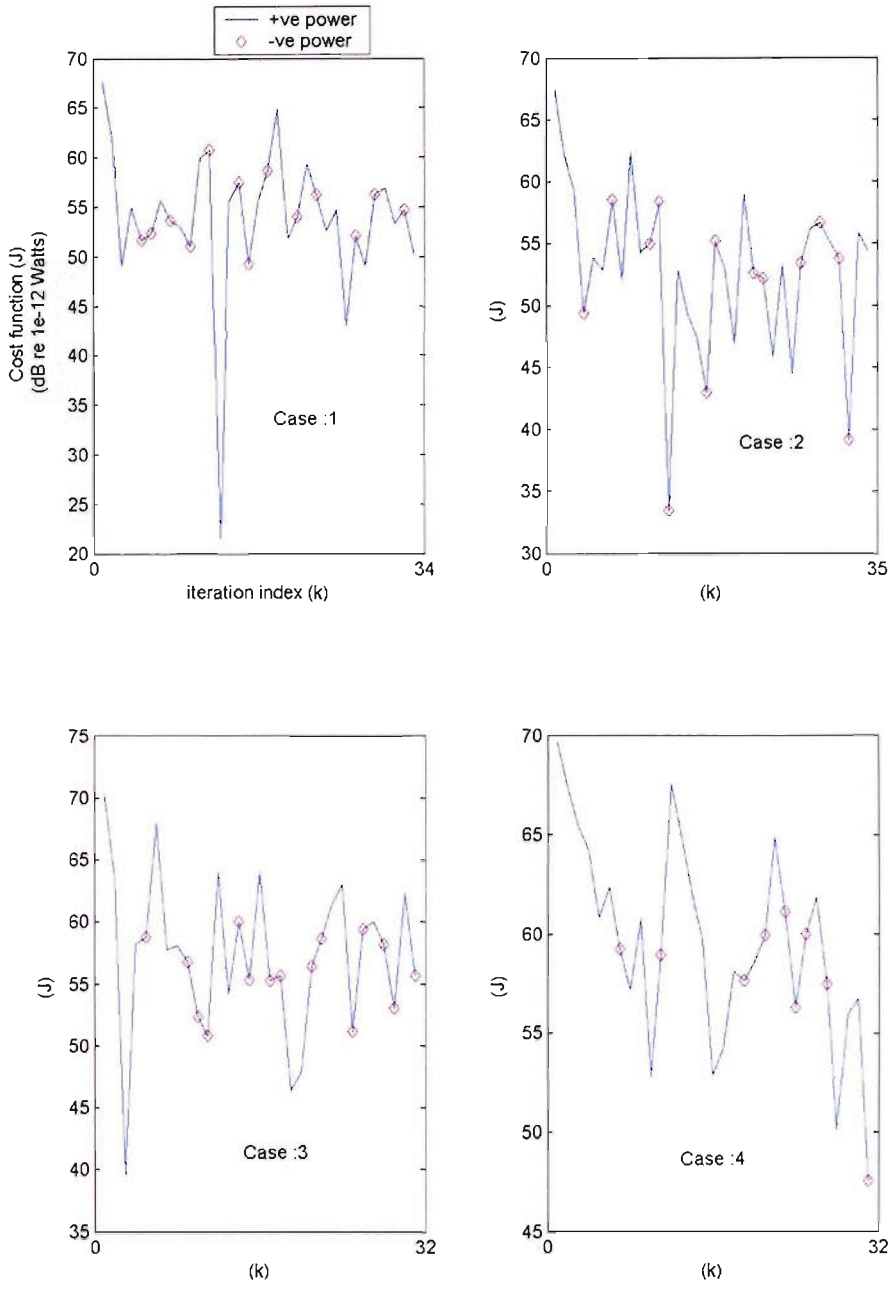

Figure 5.41 Cost function (dB) convergences for control experiments in cases (1-4).

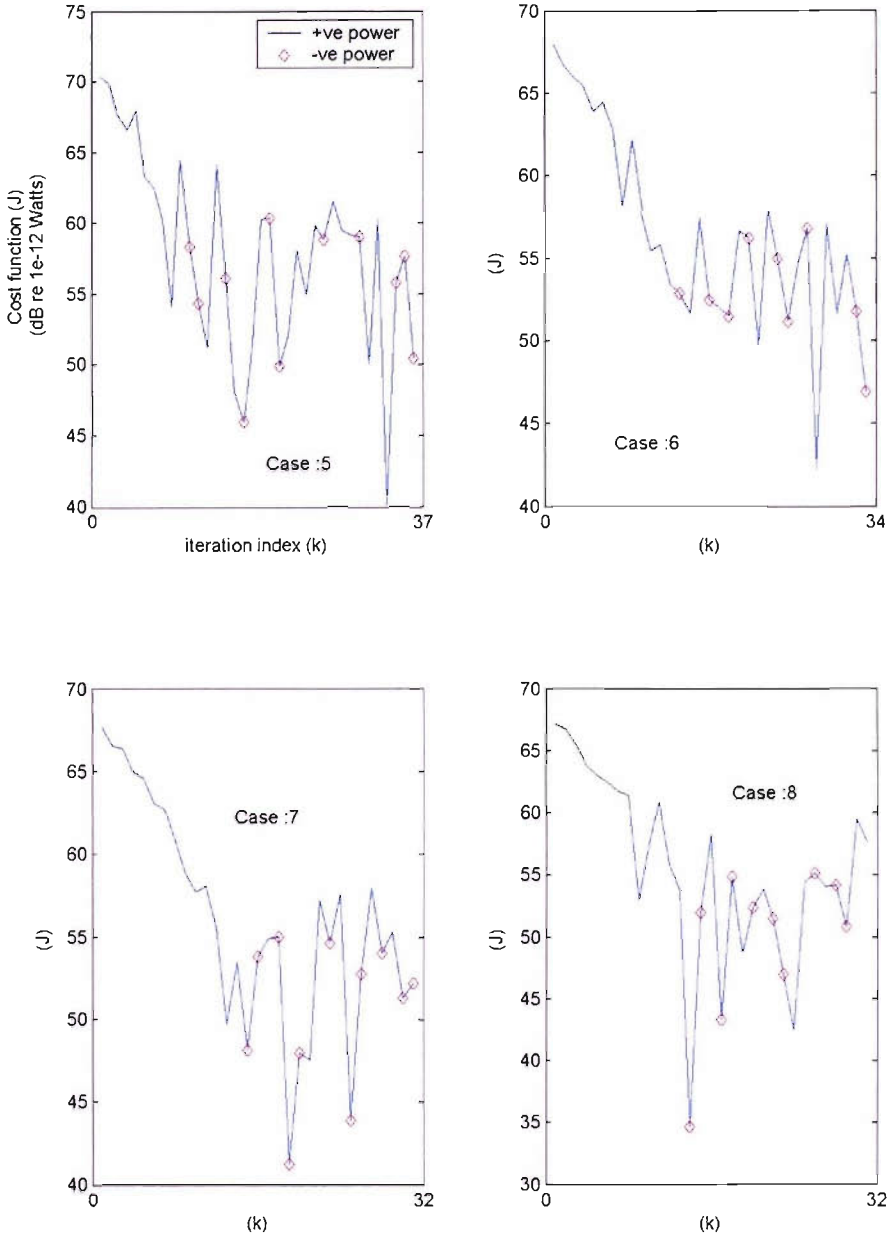

Figure 5.42 Cost function (dB) convergences for control experiments in cases (5-8).

The far-field sound pressure level (at the BPF of 262 Hz) measured from the B&K microphone is given only for cases (2-8) in Figure 5.43-Figure 5.44 as the capturing of the far-field measurements in the algorithm were begun to be included from case 2 onwards.

The above far field sound pressure level (SPL) variation is given for the BPF and its two harmonics in Figure 5.45 only for case 8. The first harmonic reduces from 91 dB to 85 dB. The second harmonic reduces from 87 dB to 79 dB. The third harmonic increases from 77 dB to 82 dB.

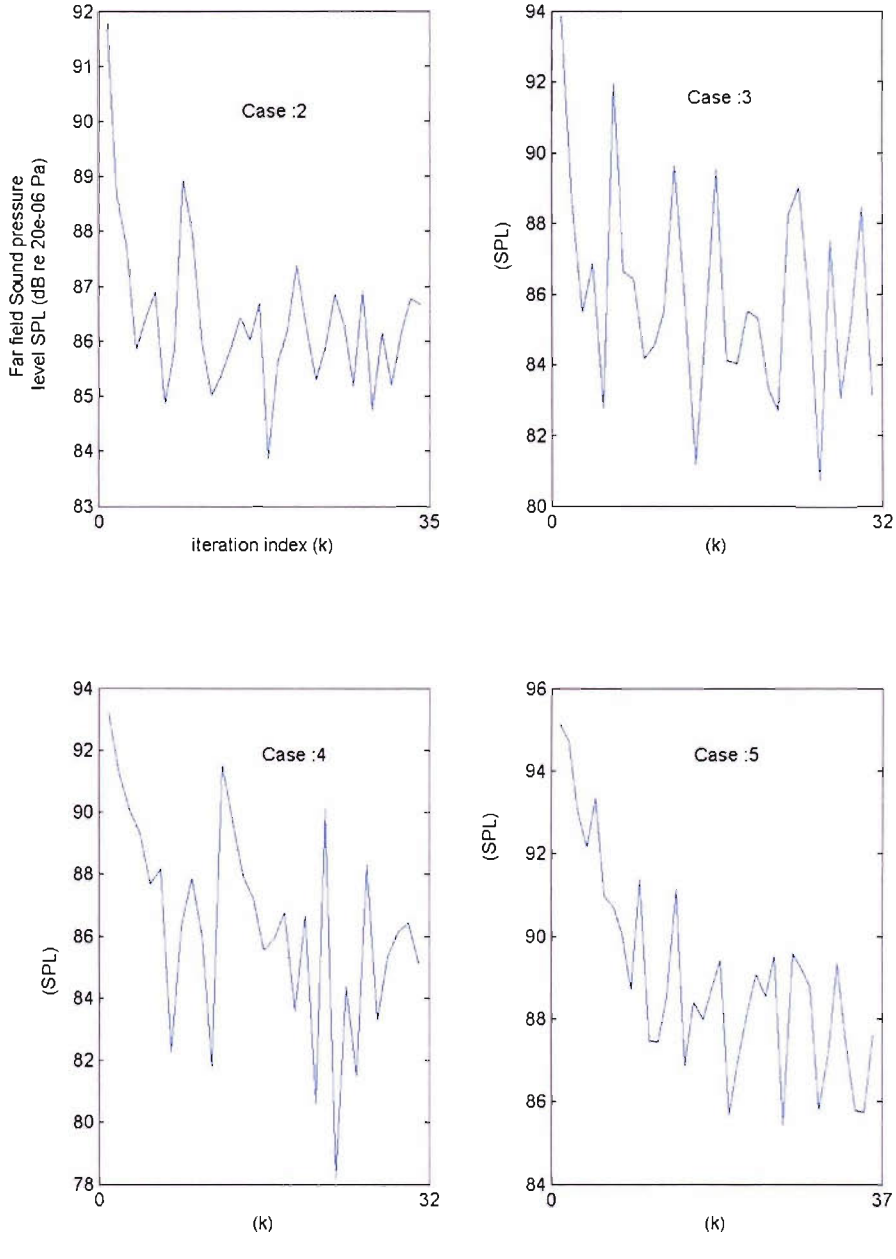

Figure 5.43 Far-field sound pressure level (dB) variations for control experiments in cases (2-5).

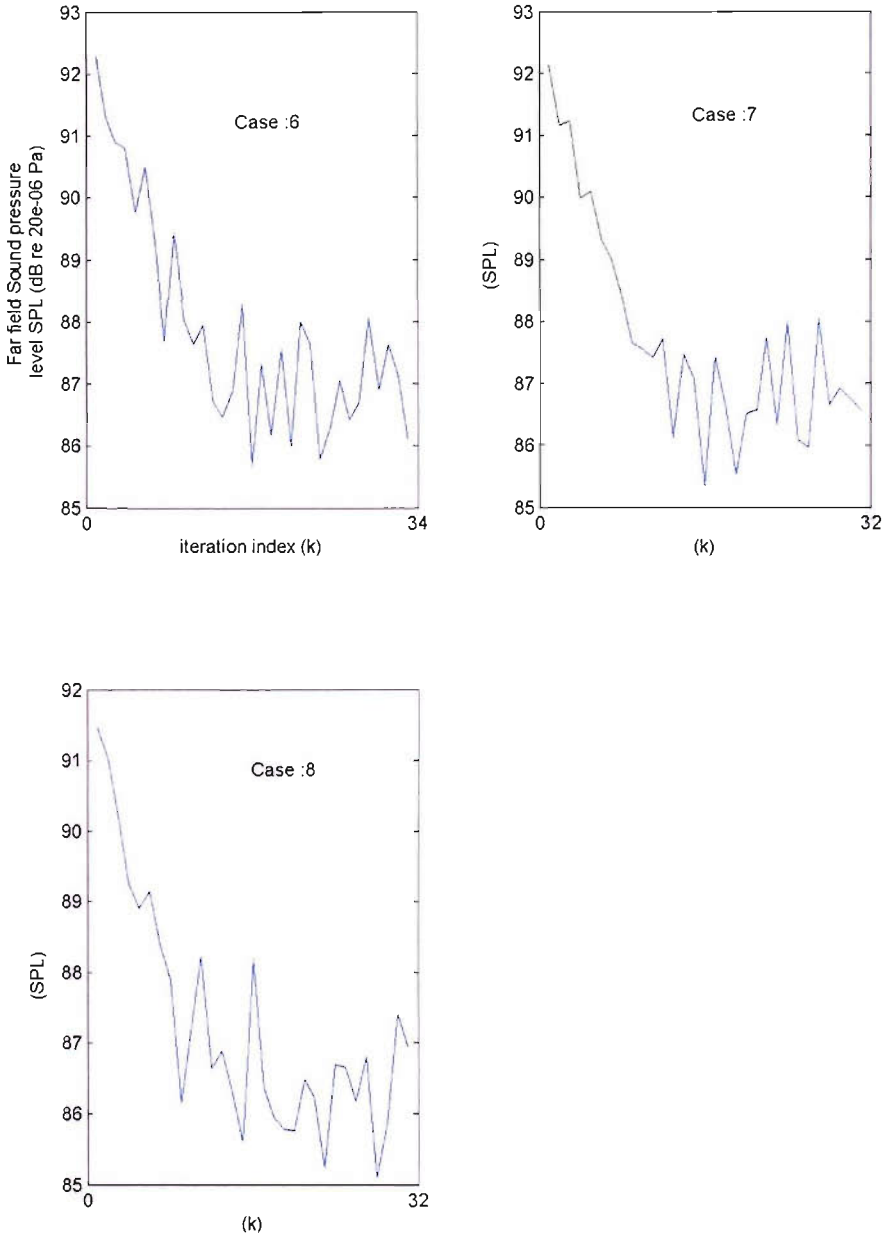

Figure 5.44 Far-field sound pressure level (dB) variations for control experiments in cases (6-8).

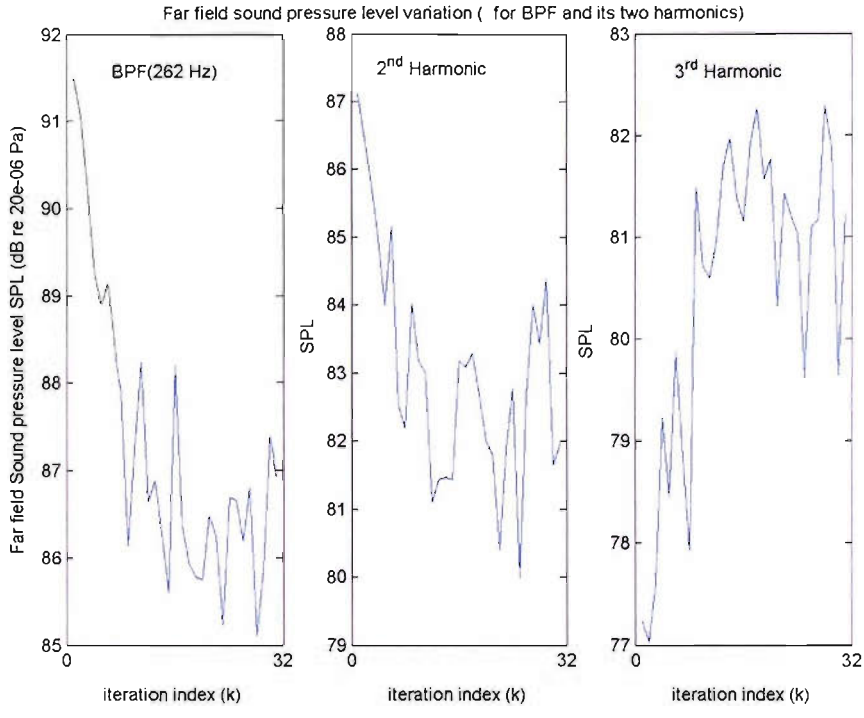

Figure 5.45 Far-field sound pressure level (dB) variation (BPF and its 2 harmonics) for control experiment in case 8.

Finally the convergence superposed on the error surface contour J for cases 1-8 are given in Figure 5.46-Figure 5.47. As already seen from the table listing the experiments cases (1-2) have the same initial condition and convergence coefficient and follow a jittery trace on the error surface. Similar jittery trace is obtained with the same convergence coefficient and a different initial condition in case 3. The convergence coefficient in case 3 is fine tuned gradually for cases 4 and 5. With the fine tuning the trace gets smoother in case 5. The fine tuned convergence coefficient is then used in case 6 for the previous initial condition and is repeated through 7 and 8 obtaining a smoother convergence each time.

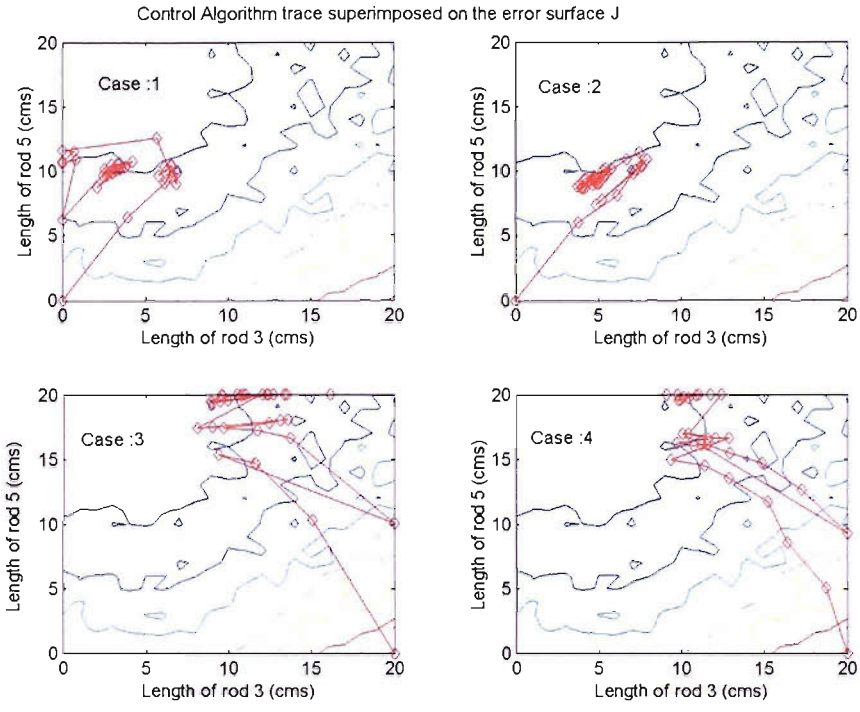

Figure 5.46 Convergence superposed on the error surface contour *J* for cases 1-4

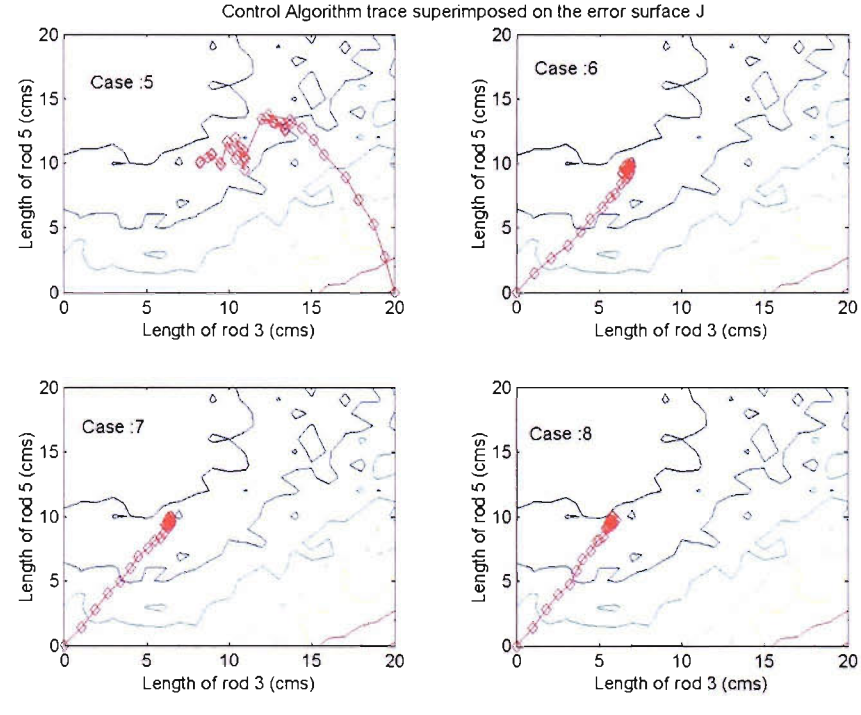

Figure 5.47 Convergence superposed on the error surface contour *J* for cases 5-8

The far-field noise spectra for case 7 with and without control are shown in Figure 5.48.

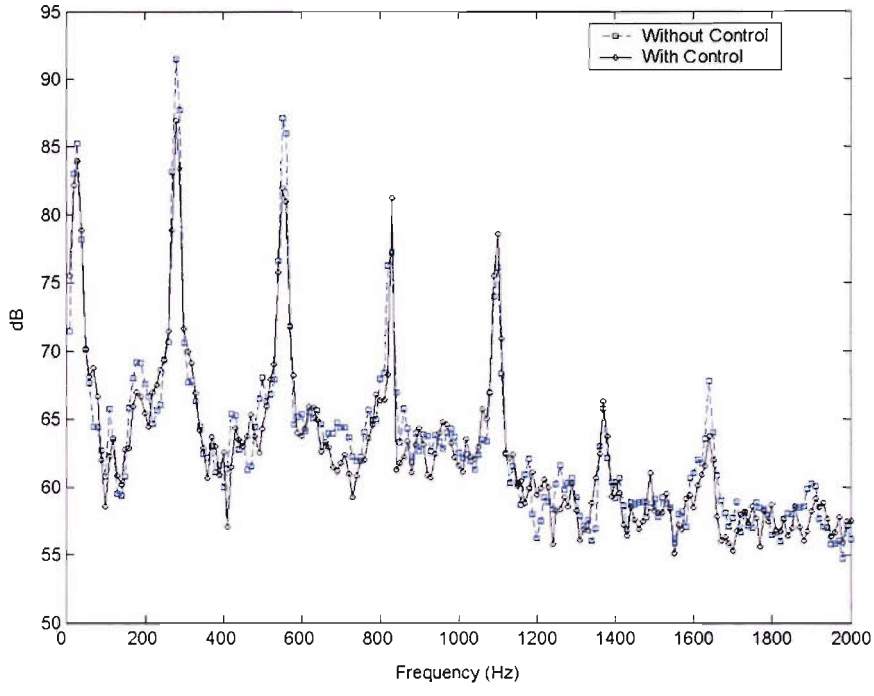

Figure 5.48 Far-field noise spectra with and without control.

5.3.2.7. Active control experiments at high speed

The list of experiments summarised in the following table were performed in the high speed case where there were three modes cut-on. Under each experiment the number of rods used for the source, and those used as the controllers and the number of iterations (k) taken for convergence, the convergence coefficients (μ) used and the initial conditions used for the controllers are all listed therein.

Experiment description	BPF of the fan (Hz)	Source rod	Source rod length (mm)	Controller rods	Initial condition: Controller rod lengths(mm)	(k)	(μ)
Control (Case1)	441	None		1 2 3 4 5 6 7	All set to 0	38	10^5
(Case2)	441	None		1 2 3 4 5 6 7	All set to 0	37	10^4
(Case3)	441	1	200	2 3 4 5 6 7	All set to 0	27	10^5
(Case4)	441	1 2	[200 200]	3 4 5 6 7	All set to 0	29	10^5

(Case5)	441	1 2	[200 200]	3 4 5 6 7	All set to 0	73	10^5

Table 5.4 List of Control experiments conducted at high speed. (*Refer to Table 5.1 for the rod identifications.)

The results of the control experiments for Case(1-5) are given below. The convergence of lengths in these cases is given in Figure 5.49. The convergence of cost function (in-duct power in dB) in these cases is given in Figure 5.50. The cost function oscillates in cases 1 and 2 and reduces only in cases 3-5. For Case 3 the reduction is from 80.5 to 78.4 dB. It is 83.3 to 81.6 for case 4 and 83.6 to 81.5 for case 5. Thus the reduction of the in-duct noise power at BPF is around 2 dB in the last three cases. The individual modal coupling coefficient variations for these cases are given in Figure 5.51 -Figure 5.53. Of the three modes only modes m=(-1,0) seem to be exhibiting a variation in cases 3-5 that is consistent with the overall sound power level variation. This should be expected because the rods themselves are used as sources in these cases and this is also consistent with the explanation given in Sub-section 4.3.3 which tells us that mode m=1 cannot be controlled using the rods on the array when some of these rods are used as sources due to the in-phase contribution of each rod to this mode.

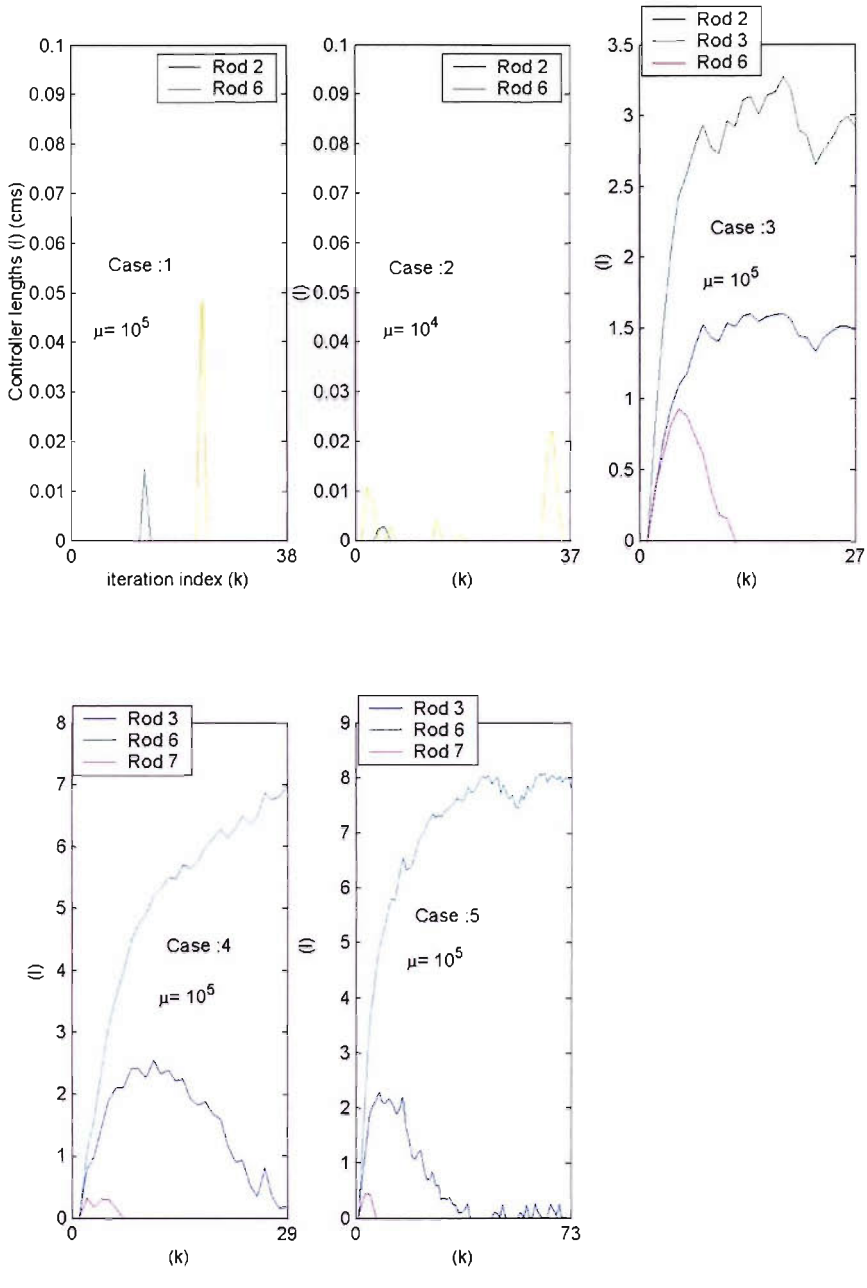

Figure 5.49 Length convergences for control experiments in cases (1-5) at high speed.

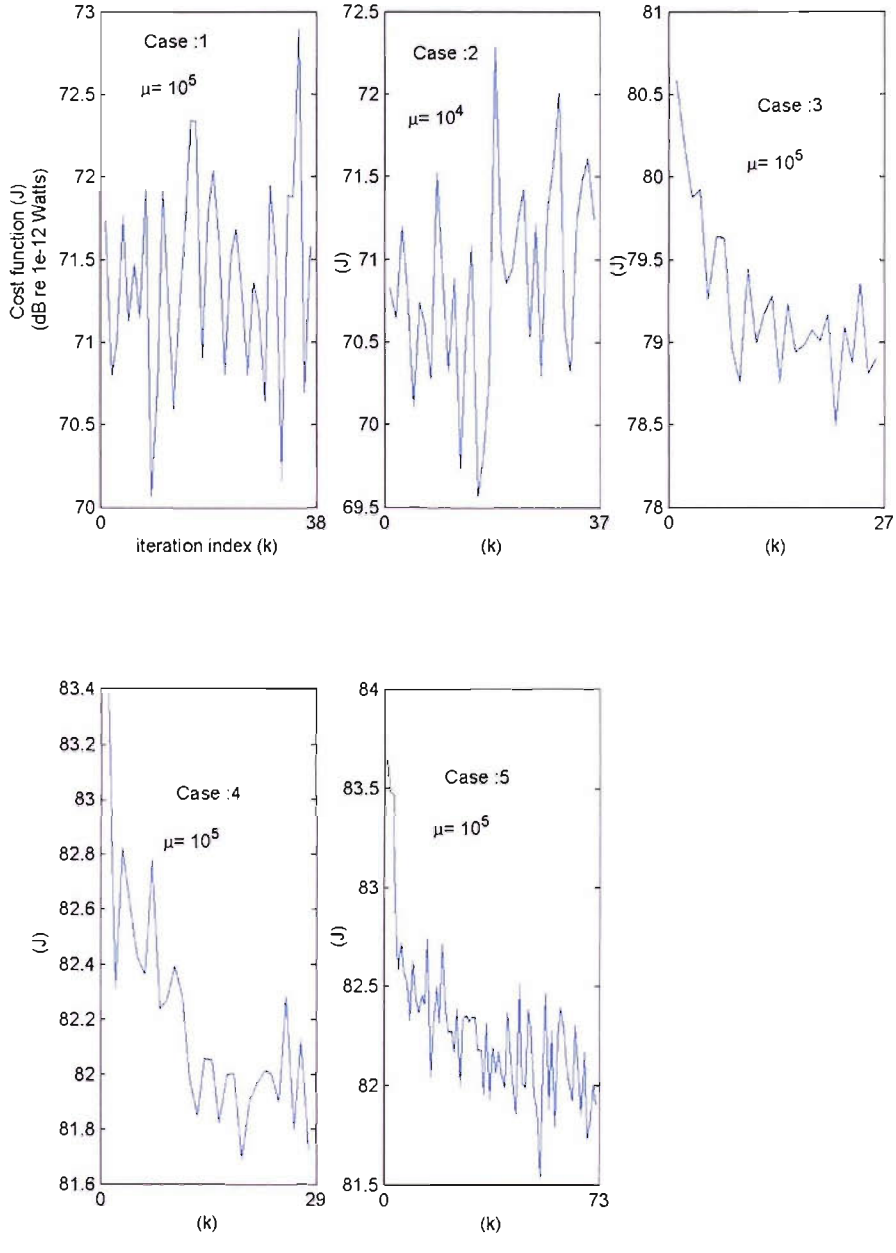

Figure 5.50 Cost function (dB) convergences for control experiments in cases (1-5)

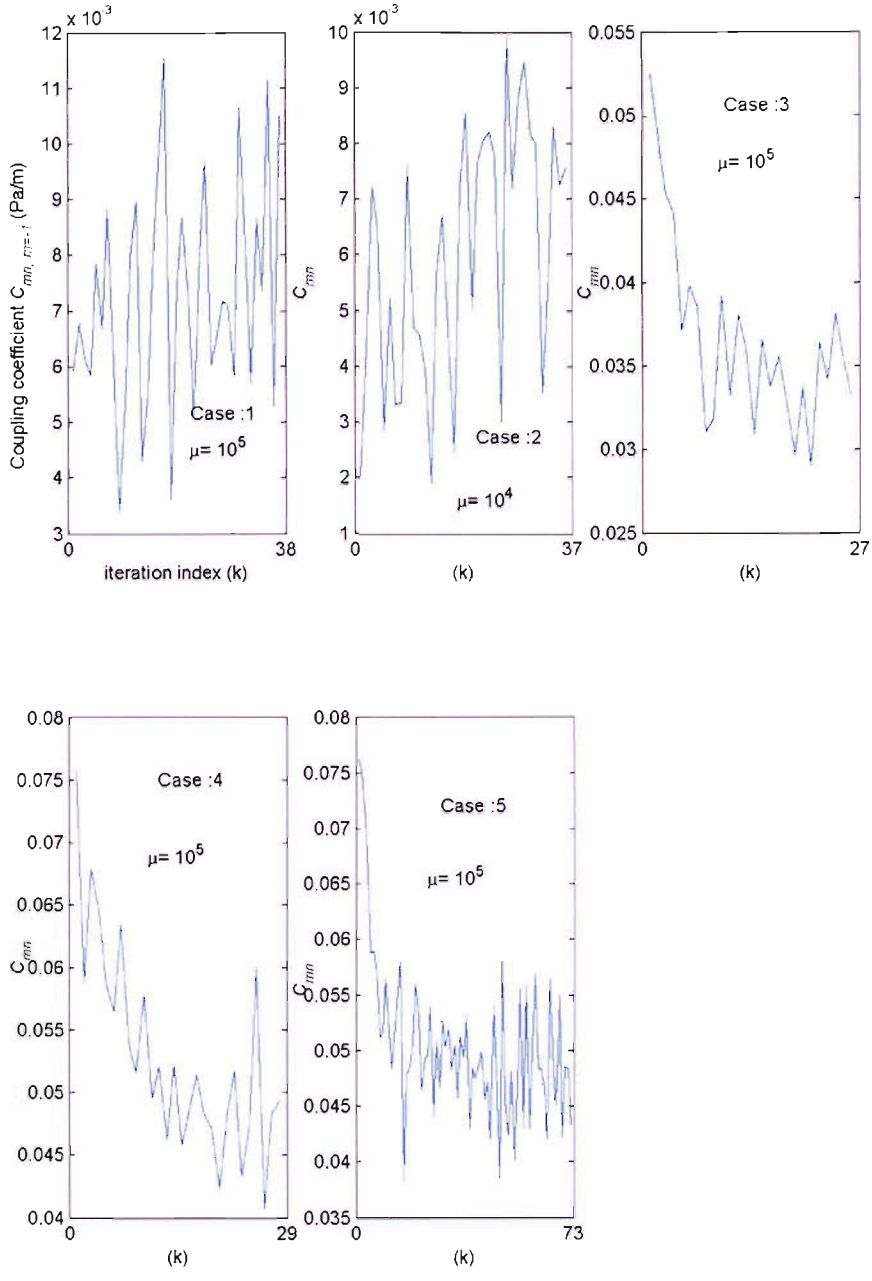

Figure 5.51 Coupling coefficient variation for mode *m* =-1 in cases (1-5)

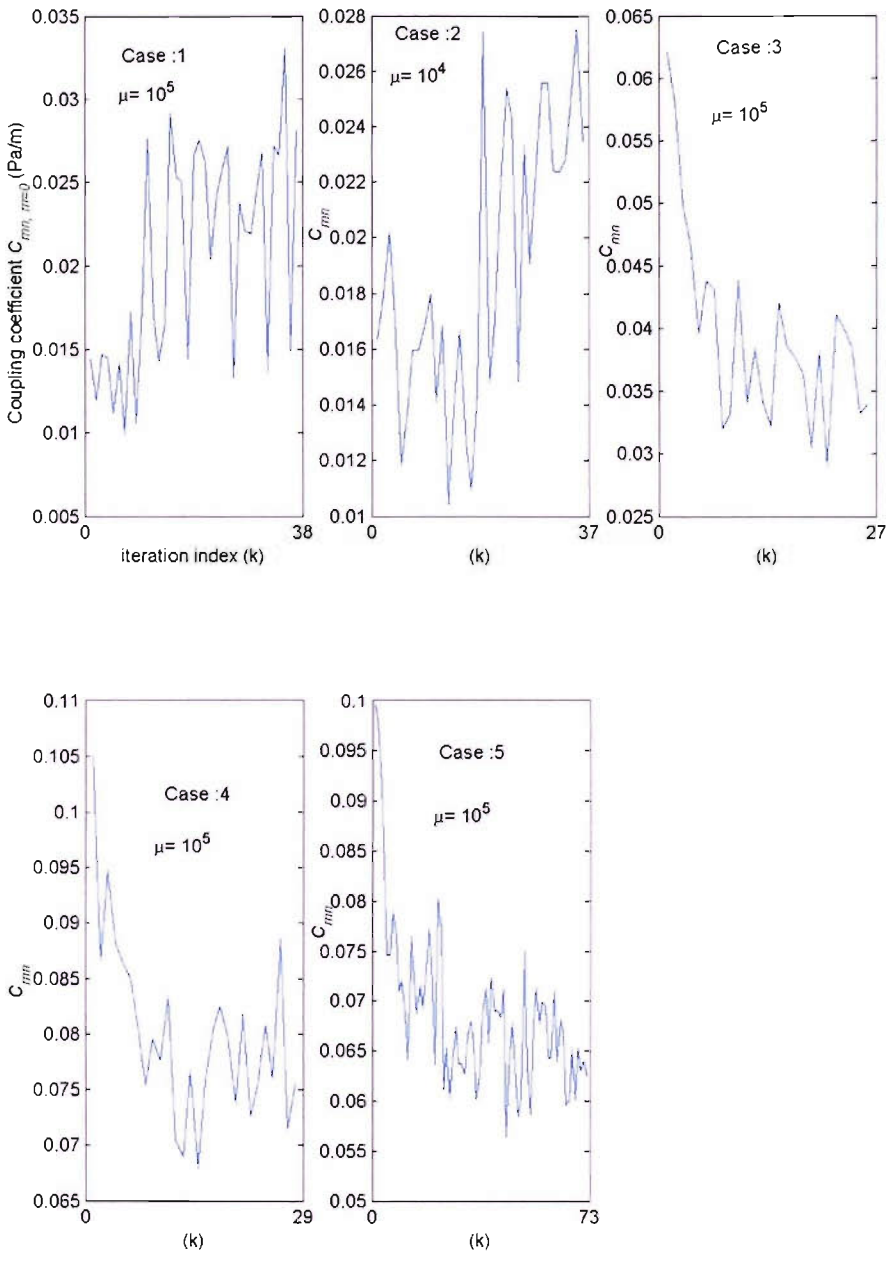

Figure 5.52 Coupling coefficient variation for mode *m* =0 in cases (1-5)

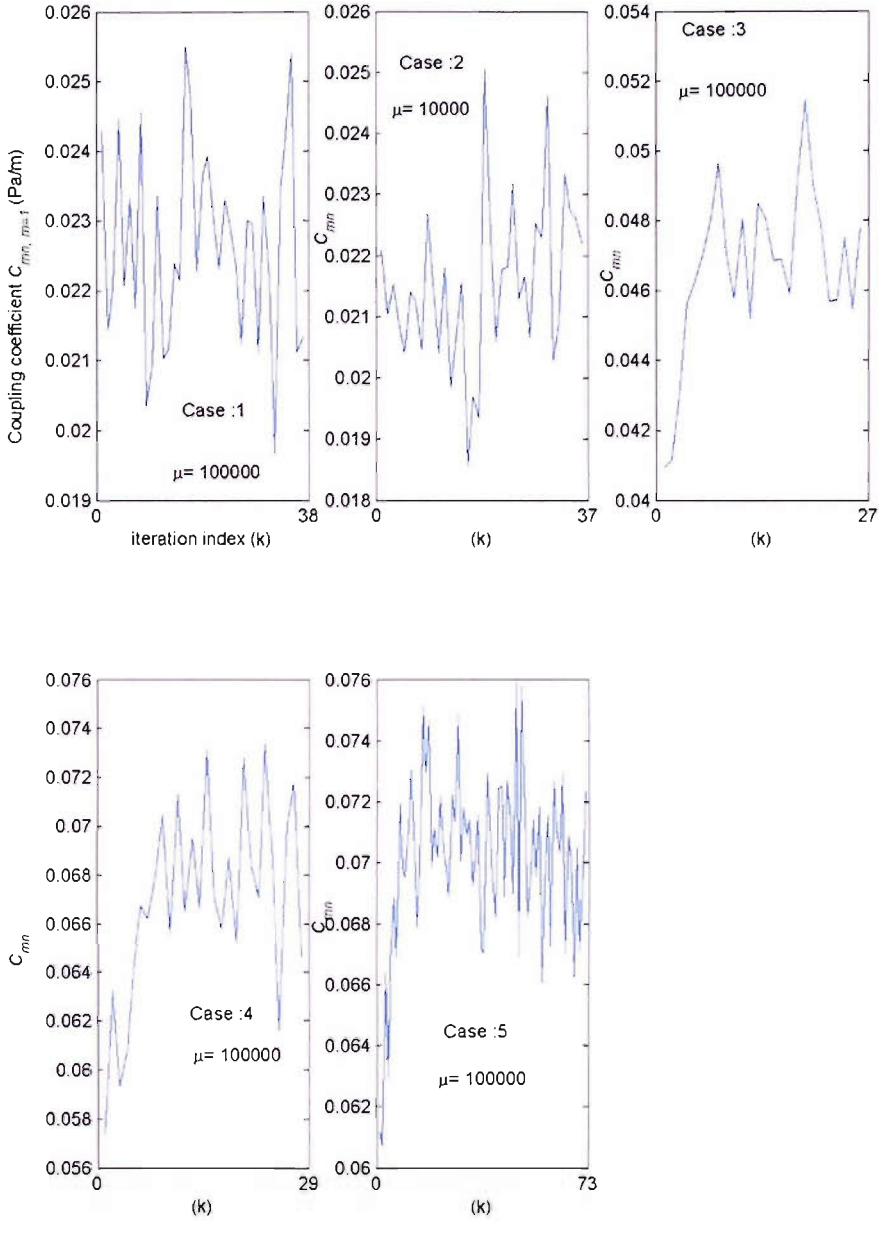

Figure 5.53 Coupling coefficient variation for mode *m* =1 in cases (1-5)

The far field sound pressure level variation (in dB) in these cases is given in Figure 5.54-Figure 5.56 for three harmonics. The first harmonic shows a consistent variation for cases 4 and 5 exhibiting a reduction from 107.5 to 105.5 dB. While the second one reduces from 91 to 86 dB for case 3, the third harmonic

reduces for cases 3-5: from 75 to 70 dB for case 3, from 95 to 88 dB for case 4 and 95 to 86 dB for case 5.

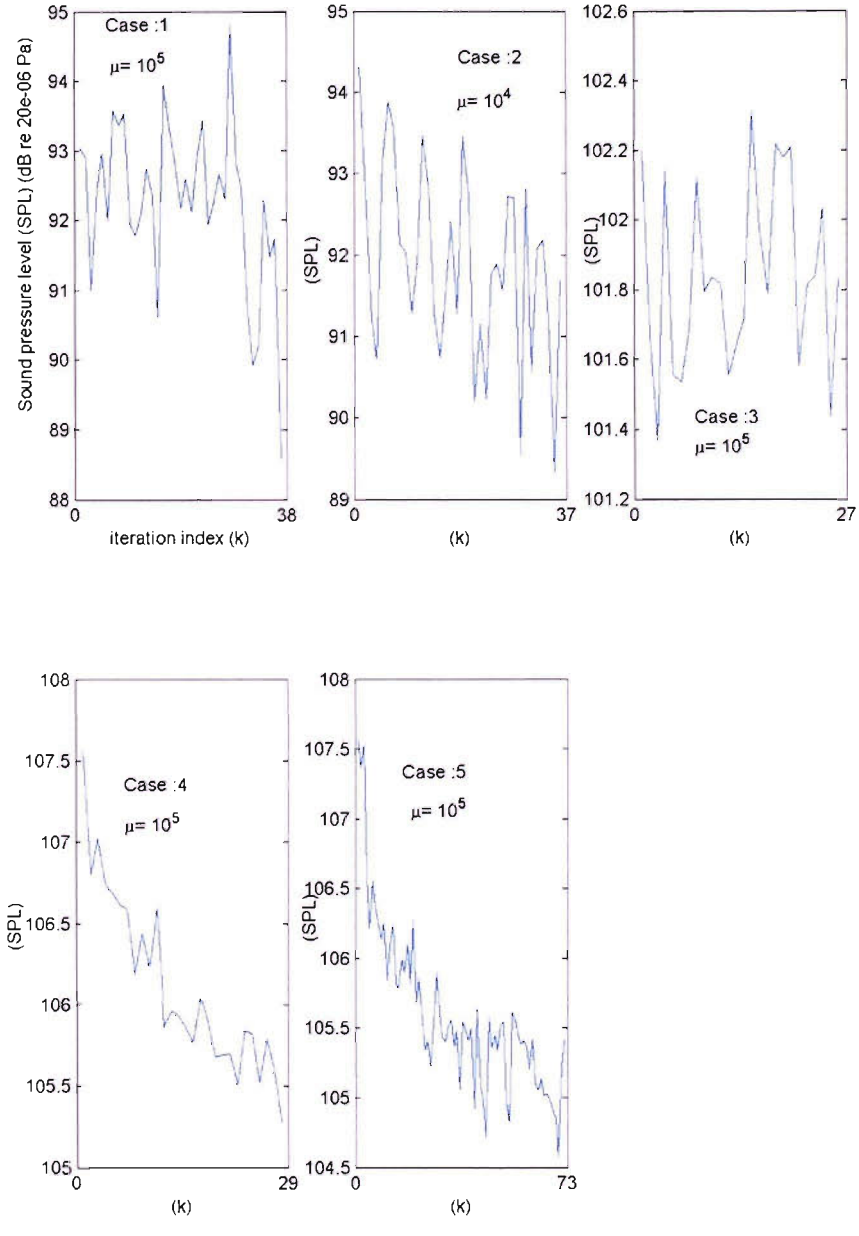

Figure 5.54 Far-field sound pressure level (1st harmonic, in dB) variations for control experiments in cases (1-5)

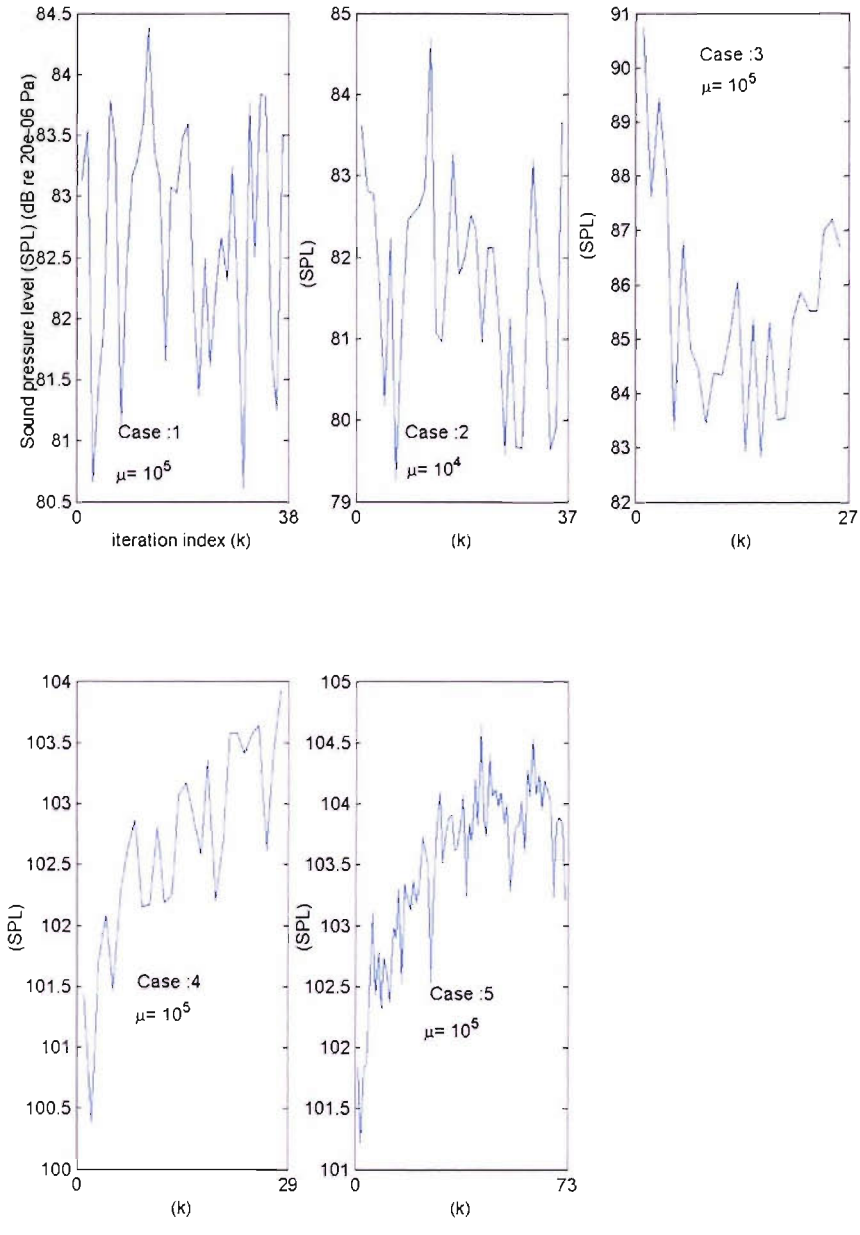

Figure 5.55 Far-field sound pressure level (2nd harmonic, in dB) variations for control experiments in cases (1-5)

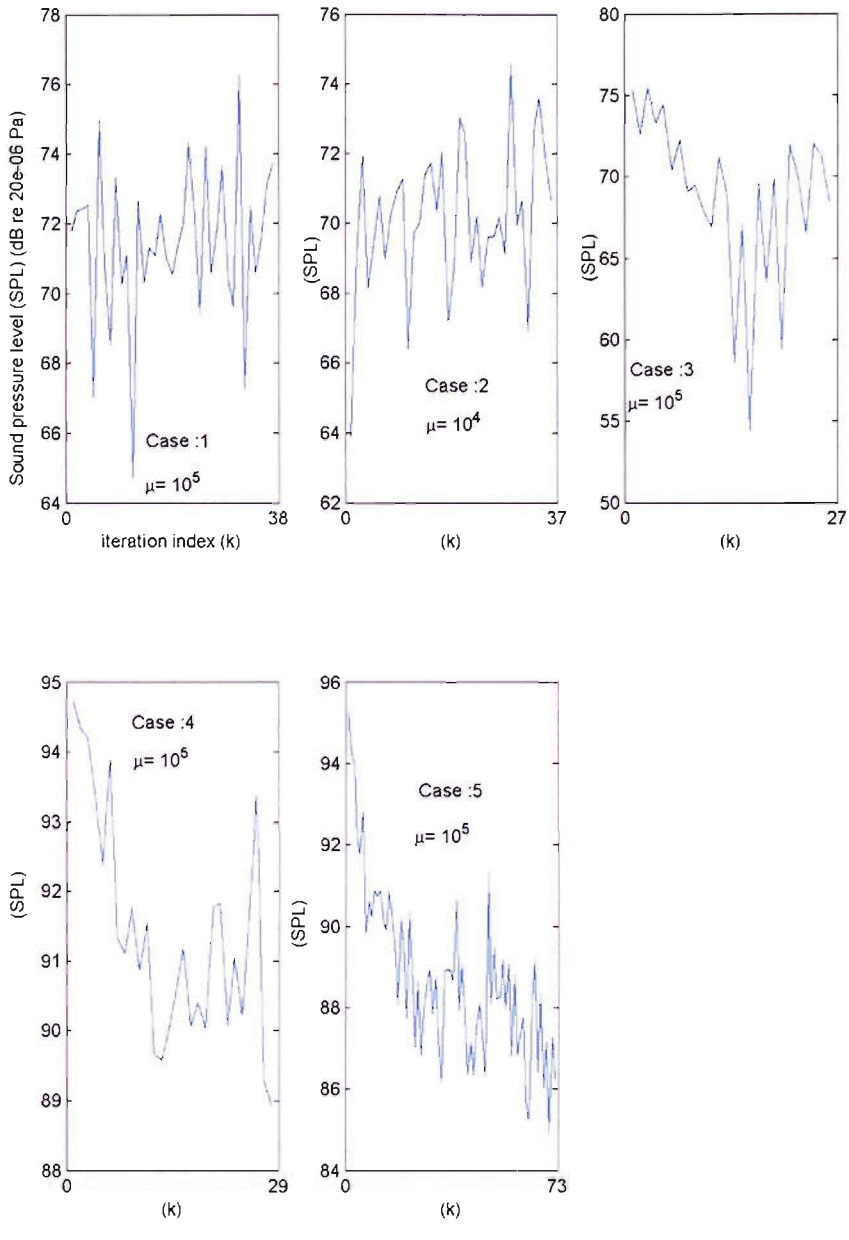

Figure 5.56 Far-field sound pressure level (3rd harmonic, in dB) variations for control experiments in cases (1-5)

The far-field noise spectra for the case 3 and 5 with and without control are shown in Figure 5.57-Figure 5.58.

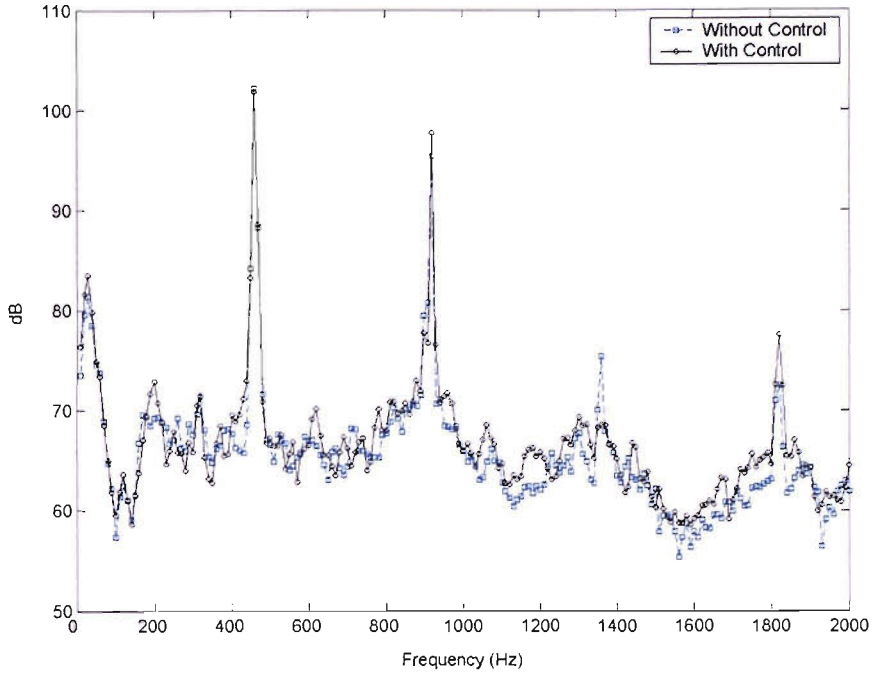

Figure 5.57 Far-field noise spectra with and without control (Case 3).

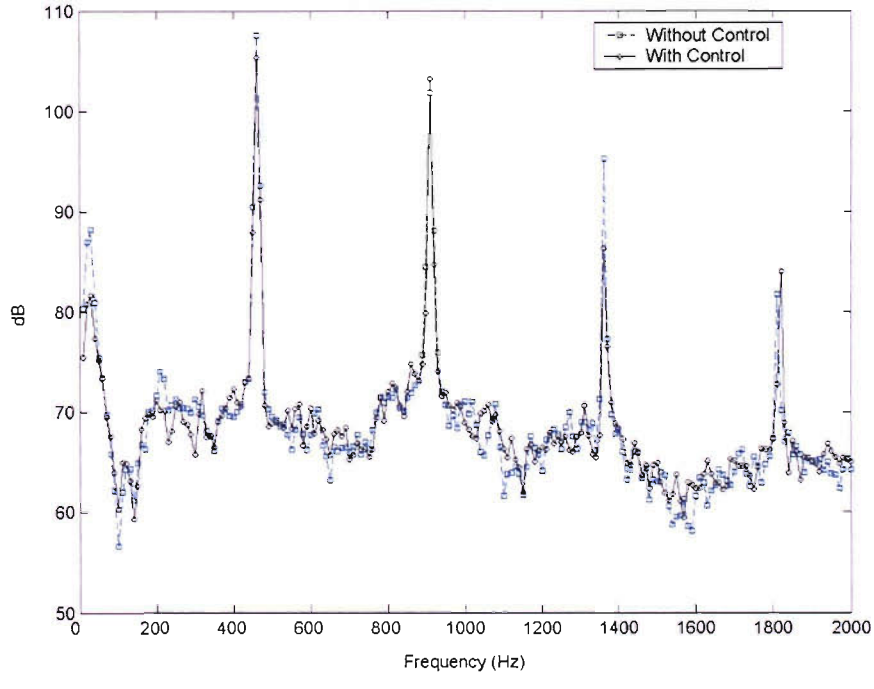

Figure 5.58 Far-field noise spectra with and without control (Case 5).

The times (in hours) taken for completion of Case 8 at the low speed and cases 3-5 at the high speed are given below with the corresponding time for the algorithm to reach the reduction of the cost functions mentioned previously.

Case	Completion time (hrs)	Time to attain reduction(hrs)
Low speed (Case 8)	0.9865	0.8009
High speed (Case 3)	1.5852	1.3407
High speed (Case 4)	1.5602	1.1335
High speed (Case 5)	3.826	2.8882

Table 5.5 Performance statistics for the control algorithm.

Since the presence of rods in the duct can cause the production of wakes in the duct, a test was also conducted to assess the loss of pressure rise across the fan by measuring the fan inlet and exit pressures. The measured pressure rise across the fan corresponded to 31 mm at the low speed and 88 mm at the high speed. The tests showed that there is no loss of pressure at the two fan speeds mentioned here when the rods are introduced into the duct.

5.4. Summary

The noise control concept introduced in Chapter 1 was implemented in this Chapter on a test fan rig and an 8-rod controller array using the instrumentation described in the initial sections of the chapter. The controller rod response was determined at the BPF for the two fan speeds. Using this response the control algorithm based on steepest gradient descent was tested at the BPF of the two speeds. At the low fan speed the BPF tone was unsteady and had very low amplitude. Hence one of the rods on the array was used as the source to generate the plane wave mode and two others rods on the array were used as controllers. Upon running the algorithm the in-duct noise power at the BPF in the duct reduced from 67 to 42 dB. Far-field spectra also showed reduction in the Sound Pressure Level at the BPF from 91 to 85 dB. The SPL at the 2^{nd} harmonic reduced from 87 to 79 dB and at the 3^{rd} harmonic it increased from 77 to 82 dB. The error surface was measured in the control rod vector space for this case and the control trajectory was superimposed on it and it showed that the convergence of the rod lengths was sensitive to the choice of the descent step. At the high fan speed a

case that was run with all the rods on the array turned on as controllers did not show any reduction in the duct noise power or far-field pressure levels. Cases where one or two of the rods were made to act as sources and the rest as controllers did show that the controller rod length variations exhibit smooth convergence. But these did not result in any significant reduction in the duct noise power which was around 2dB. The individual modal coupling coefficient variations showed that this is due to the difficulty in controlling multiple cut-on modes at this speed which was explained theoretically in Chapter 4. Thus the method of the thesis could be used to achieve useful noise reductions by controlling a single dominant mode.

Chapter 6 Concluding Remarks

The purpose of this thesis was to demonstrate the possibility of adaptive control of flow disturbance induced tonal noise from fans using a cylindrical rod array. The first task in this study was to look at an analytical model that describes the relationship between a flow disturbance induced by cylindrical rods and the noise radiated from their interaction with the fan blades. The second task was to study numerically the problem of optimising the noise power when multiple acoustic modes are controlled using multiple control rods. The final task was to implement this on a model fan rig.

In Chapter 1 the concept of control of noise using flow disturbances was introduced. Although the study of the problem of control of tonal noise using flow disturbances has been taken up recently by a few investigators they focussed on the passive control of a single mode which required the manipulation of the rod lengths using trial and error. Since it is known that the focussing of control on a single mode could lead to the increase in the amplitudes of the other modes, the current study involved focussing on the optimal control of multiple modes.

The present thesis considered the study of wake generator based control both numerically and experimentally using Goldstein's analytical model that gives the relationship between the rod length and the generated acoustic response through interaction with the fan blades. The presence of rods in the fan duct results in the generation of wakes and these wakes interact with the fan blades to produce unsteady blade forces which then radiate the acoustic field in the duct. An expression was derived in Chapter 2 for the acoustic pressure field associated with the interaction of the fan with a flow disturbance. This expression was given by Goldstein for the case of a fan situated in an infinite duct and this was extended to the finite duct case by Pitelet (2000) and the present thesis considered the extension of the finite duct expressions to the semi-infinite duct case to take into account the configuration of the anechoic termination at the exit of the fan during implementation. The expression for the acoustic pressure also pointed out that a term in it called the modal coupling coefficient directly representing the blade response in terms of the unsteady forces experienced by it could be extracted for each acoustic mode generated by the interacting flow disturbance. It is this term

that is useful in terms of formulating the acoustic response of a rod for control purposes. Thus by knowing the profile of the flow disturbance the resulting acoustic pressure field in the duct can be estimated from the acoustic pressure expression developed in that chapter.

The expression derived in Chapter 2 was used in the control problem formulated in Chapter 3 which consisted of (i) the determination of the acoustic pressure field resulting from the wake generated by the presence of a cylindrical rod in the duct upstream of the fan rotor, and (ii) the problem of optimising the noise power when several such rods are used for control. The controller response in the form of the modal coupling coefficients was numerically determined using analytical expressions for the flow disturbances generated by the control rods and a simple case of the problem of cancellation of noise was numerically simulated and studied by using a source rod and a controller rod. It was deduced that cancellation is possible through translations and rotations of the control rod. It was later shown that the presence of the control rod can cause the production of modes other than the mode that is being considered for control and this subsequently led to formulation of the problem of noise optimisation. The optimisation problem consisted of minimising a cost function representing the noise power in the duct which is equal to the weighted sum of the squares of the amplitudes of the modes. The cost function is in turn a function of the rod lengths on the controller and hence the minimisation of it would lead to finding these lengths. The algorithm that was proposed for the minimisation is the steepest descent algorithm which upon running would iteratively determine the controller lengths using the gradient of the cost function with respect to the controller lengths. The simple case for the problem of noise cancellation was repeated numerically using an algorithm based on the noise optimisation theory developed in that chapter. Thus the optimisation algorithm was tested using the case of the noise cancellation problem. The simulation of the optimisation problem presented in that chapter revealed the importance of the approximation of the controller response and also of constraining the control vector. In particular the polynomial approximation led to less error in the residual power estimates than the linear response, and constraining the algorithm caused the rod lengths to be positive.

Chapter 4 focussed on the numerical simulation of optimal control of multiple modes using multiple control rods as the previous chapter indicated that

focussing the control on a single mode might lead to the increase in the amplitudes of the other modes. The study involved selection of two disturbances to test the control of multiple modes. The first disturbance was a spatially harmonic flow disturbance and the second was a randomly distributed flow disturbance. In both situations error surfaces were plotted for selected cases and it was shown that the choice of initial condition could lead the convergence to a local minimum which is a feature of the steepest descent algorithm. While with the spatially harmonic disturbance increasing the number of controllers led to increased reduction in the noise power, the randomly distributed disturbance showed that increasing the number of controllers for the control of multiple modes is not effective. Although increasing the number of equispaced controllers in the random disturbance case showed increased reduction, not all of the controllers used in the array were being utilised by the algorithm. This had later led to the attempt of controlling this disturbance using non-equispaced rod arrays. Both types of rod arrays showed that the circumferential orientation of the controller rod array has a significant influence on the control. Later the same algorithm was used to test the cancellation problem involving cancelling N modes with 2N controllers. Testing this hypothesis with different rod spacings did not yield cancellation in these cases as we know that steepest descent algorithm could lead convergence to local minimum. An alternative means of cancelling multiple modes with a combination of multiple equispaced rod arrays was found to be promising. Since the rod array circumferential orientation was also found to be an important control variable, the problem of control with its inclusion in the control vector was also attempted for two cases, one in each of the two flow disturbances chosen in this chapter. This was performed to check if its inclusion in the control vector would lead to convergence to that orientation which was found to be the best when it was manually varied. For a control case in the spatially harmonic flow disturbance, the inclusion of the rod array circumferential orientation in the control vector led the convergence of the control algorithm directly to the point which corresponded to best orientation found through manual variation. When the same problem of controlling the array orientation was attempted with a case in the randomly distributed flow disturbance the control showed that it is very sensitive to the choice of the convergence coefficient.

The noise control concept thus introduced in Chapter 1 was finally implemented in Chapter 5 on a test fan rig and an 8-rod controller array using the pressure signals acquired from duct microphones. The simulations discussed in Chapter 3 and Chapter 4 required the rod responses to be determined from the flow disturbance profile. In the experimental situation the response estimation involved the measurement of the pressure signals from the microphones. These were phase locked with a trigger signal consisting of one pulse per fan-pass and Fast Fourier Transformed to extract tones which were later decomposed into duct modes and then into modal coupling coefficients. The controller rod response in the form of the modal coupling coefficients was thus determined experimentally at the BPF for the two fan speeds. Using this response the control algorithm based on steepest gradient descent was tested at the BPF of the two speeds. At the low speed the BPF tone was unsteady and had very low amplitude. Hence one of the rods on the array was used as the source to generate the plane wave mode and two other rods on the array were used as controllers. Upon running the algorithm the in-duct noise power at the BPF in the duct reduced from 67 to 42 dB. Far-field spectra also showed reduction in the Sound Pressure Level at the BPF from 91 to 85 dB. The SPL at the 2^{nd} harmonic reduced from 87 to 79 dB and at the 3^{rd} harmonic it increased from 77 to 82 dB. The error surface was measured in the control rod vector space for this case and the control trajectory was superimposed on it and it showed that the convergence of the rod lengths was sensitive to the choice of the descent step. At the high fan speed a case that was run with all the rods on the array turned on as controllers did not show any reduction in the duct noise power or far-field pressure levels. Cases where one or two of the rods were made to act as sources and the rest as controllers did show that the controller rod length variations exhibit smooth convergence. But these did not result in any significant reduction in the in-duct noise power which was around 2dB. The individual modal coupling coefficient variations showed that this is due to the difficulty in controlling multiple cut-on modes at this speed which was explained theoretically in Chapter 4. Thus the method of the thesis could be used to achieve useful noise reductions by controlling a single dominant mode.

The current thesis has thus achieved the objective of a successful demonstration of the implementation of the concept of adaptively controlling fan tonal noise using wake generators by employing the theoretical relationship

between the flow disturbances and resulting noise through interaction with the blades. Though the current study of the control system has focussed on its applicability to aircraft engines, factors like performance and safety have to be evaluated before considering implementation. Otherwise the system discussed is readily suited for implementation in a situation where noise studies are conducted on models objects in wind tunnels where some form of masking the background noise of the wind tunnel fan is necessary in order that the noise characteristics of the model are not contaminated (Allen 2002).

Since the optimisation exercise performed here with the steepest descent algorithm showed that the convergence to local minima is more probable, future studies should consider attempting the study using global optimisation techniques like Genetic Algorithms.

Appendix 2.1 Reduction of the convected wave equation to the modified Helmholtz equation

The convected wave equation is

$$\left[\nabla^2 - \frac{1}{c_0^2}\left(\frac{\partial}{\partial t} + \mathbf{U}.\nabla\right)^2\right] p(\mathbf{x},t) = 0\,,$$

(A.2.1.1)

where

$$\nabla^2 \equiv \frac{\partial^2}{\partial z^2} + \left(\frac{\partial^2}{\partial r^2} + \frac{1}{r}\frac{\partial}{\partial r} + \frac{1}{r^2}\frac{\partial^2}{\partial \theta^2}\right) \equiv \frac{\partial^2}{\partial z^2} + \nabla_\perp^2 \quad \text{and}$$

$$\nabla \equiv \frac{\partial}{\partial z} + \left(\frac{\partial}{\partial r} + \frac{1}{r}\frac{\partial}{\partial r} + \frac{1}{r}\frac{\partial}{\partial \theta}\right) \equiv \frac{\partial}{\partial z} + \nabla_\perp .$$

(A.2.1.2)

If $p(\mathbf{x},t) = \mathrm{Re}\{p(\mathbf{x})e^{j\omega t}\}$ is substituted in equation (A.2.1.1) then since the operator ∇ is linear with respect to the operation of taking the real part (Re{}), the wave equation can be written as

$$\mathrm{Re}\left\{\left[\nabla^2 - \frac{1}{c_0^2}\left(\frac{\partial}{\partial t} + \mathbf{U}.\nabla\right)^2\right] p(\mathbf{x})e^{j\omega t}\right\} = 0\,.$$

(A.2.1.3)

Carrying out the differentiation with respect to the time variable t we have

$$\mathrm{Re}\left\{\left[\nabla^2 + \left(\frac{\omega}{c_0}\right)^2\left(1 - \frac{j}{\omega}\,\mathbf{U}.\nabla\right)^2\right] p(\mathbf{x})e^{j\omega t}\right\} = 0\,.$$

(A.2.1.4)

The above must hold for all values of time t. Since $e^{j\omega t} \neq 0$, for arbitrary t we must have

$$\left[\nabla^2 + \left(\frac{\omega}{c_0}\right)^2 \left(1 - \frac{j}{\omega}\,\mathbf{U}.\nabla\right)^2\right] p(\mathbf{x}) = 0\,,$$

(A.2.1.5)

as given in Equation (2.3.5).

Denoting the operator on the left hand side of the above equation as L we have

$$L[p(\mathbf{x})] = 0$$

(A.2.1.6)

Appendix 2.2 Expression for k_{mn}

The modified Helmholtz equation is

$$\left[\nabla^2+\left(\frac{\omega}{c_0}\right)^2\left(1-\frac{j}{\omega}\,\mathbf{U}.\nabla\right)^2\right]p(\mathbf{x})=0\,.$$

(A.2.2.1)

The operator ∇^2 can be written in terms of its axial component and an operator $\nabla_\perp^2$ acting over the duct cross-section. For example in cylindrical co-ordinates

$$\nabla^2\equiv\frac{\partial^2}{\partial z^2}+\left(\frac{\partial^2}{\partial r^2}+\frac{1}{r}\frac{\partial}{\partial r}+\frac{1}{r^2}\frac{\partial^2}{\partial\theta^2}\right)\equiv\frac{\partial^2}{\partial z^2}+\nabla_\perp^2\,.$$

(A.2.2.2)

Also since the mean flow in the duct is in the axial direction only we have

$$\left(1-\frac{j}{\omega}\,\mathbf{U}.\nabla\right)^2=\left(1-\frac{j}{\omega}U_z\frac{\partial}{\partial z}\right)^2=1-\frac{c_0^2}{\omega^2}M^2\frac{\partial^2}{\partial z^2}-2j\frac{c_0}{\omega}M\frac{\partial}{\partial z},$$

(A.2.2.3)

where the Mach number $M=U_z/c_0$ has been used. We can therefore write the operator L as

$$L\equiv\frac{\partial^2}{\partial z^2}+\nabla_\perp^2+k_0^2\left(1-\frac{c_0^2}{\omega^2}M^2\frac{\partial^2}{\partial z^2}-2j\frac{c_0}{\omega}M\frac{\partial}{\partial z}\right),$$

(A.2.2.4)

which reduces to

$$L\equiv\nabla_\perp^2+k_0^2+\beta^2\frac{\partial^2}{\partial z^2}-2jk_0M\frac{\partial}{\partial z}\,.$$

(A.2.2.5)

If we now consider eq. A.2.2.1 individually for each mode we have

$$\left[\nabla_{\perp}^{2}+k_{0}^{2}+\beta^{2}\frac{\partial^{2}}{\partial z^{2}}-2jk_{0}M\frac{\partial}{\partial z}\right]\left\{A_{mn}\,e^{-jk_{mn}^{z}.z}.\Psi_{mn}(r,\theta)\right\}=0\,.$$

(A.2.2.6)

Note that the operator $\nabla_{\perp}^{2}$ only applies to the cross-section component $\Psi_{mn}(r,\theta)$, and also that $\Psi_{mn}(r,\theta)$ satisfies

$$\left(\nabla_{\perp}^{2}+\kappa_{mn}^{2}\right)\Psi_{mn}(r,\theta)=0\,.$$

(A.2.2.7)

Therefore equation (A.2.2.6) reduces to

$$\left[k_{0}^{2}-\kappa_{mn}^{2}+\beta^{2}\frac{\partial^{2}}{\partial z^{2}}-2jk_{0}M\frac{\partial}{\partial z}\right]\left\{A_{mn}\,e^{-jk_{mn}^{z}z}\,\Psi_{mn}(r,\theta)\right\}=0\,.$$

(A.2.2.8)

Defining an operator L_{mn} that is different for each mode:

$$L_{mn}\equiv k_{0}^{2}-\kappa_{mn}^{2}+\beta^{2}\frac{\partial^{2}}{\partial z^{2}}-2jk_{0}M\frac{\partial}{\partial z}\,,$$

(A.2.2.9)

and carrying out the differentiation in equation (A.2.2.8) leads to

$$\left(k_{0}^{2}-\kappa_{mn}^{2}-\beta^{2}k_{mn}^{z\;2}-2k_{0}Mk_{mn}^{z}\right)A_{mn}\,e^{-jk_{mn}^{z}z}\,\Psi_{mn}(r,\theta)=0$$

(A.2.2.10)

or

$$\beta^{2}k_{mn}^{z\;2}+2k_{0}M\,k_{mn}^{z}+\kappa_{mn}^{2}-k_{0}^{2}=0\,,$$

(A.2.2.11)

which is a polynomial of the 2nd order in k_{mn}^{z}.

The solution of this equation is

$$k_{mn}^{z} = \frac{-k_0 M \pm \sqrt{k_0^2 M^2 - \beta^2 \left(\kappa_{mn}^2 - k_0^2\right)}}{\beta^2}$$

(A.2.2.12)

which can be written in the form of equation (2.3.7)

$$k_{mn}^{z} = \frac{\pm \sqrt{k_0^2 - \beta^2 \kappa_{mn}^2} - M k_0}{\beta^2}.$$

(A.2.2.13)

Appendix 2.3 Expression for $\eta^{\pm}_{mn}(z)$

Axial wave number $k_{mn}^{z^{\pm}}$ (from the previous section) is

$$k_{mn}^{z^{\pm}} = \frac{\pm\sqrt{k_0^2 - \beta^2\kappa_{mn}^2} - Mk_0}{\beta^2} = \frac{\pm k_{mn} - Mk_0}{\beta^2}.$$

(A.2.3.1)

Using the definition for the reflection coefficient given by equation (2.3.16), the expression for this quantity at any axial location z can be given as

$$\frac{B_{mn}^{\pm}}{A_{mn}^{\pm}}\frac{e^{-jk_{mn}^{z-}z}}{e^{-jk_{mn}^{z+}z}} = e^{2j\eta_{mn}^{0\pm}} \times e^{2j\frac{k_{mn}}{\beta^2}z}.$$

(A.2.3.2)

Expressing the quantity on the right as $e^{2j\eta_{mn}^{\pm}(z)}$ we have

$$\eta_{mn}^{\pm}(z) = \eta_{mn}^{0\pm} + \frac{k_{mn}}{\beta^2}z.$$

(A.2.3.3)

Appendix 2.4 Expression for $b_{mn}(z)$

Equation 2.3.14 is repeated here

$$G(\mathbf{x}|\mathbf{y}) = \sum_{m=-\infty}^{+\infty} \sum_{n=1}^{+\infty} b_{mn}(z)\Psi_{mn}(r,\theta),$$

(A.2.4.1)

where the term $b_{mn}(z)$ is given as follows.

$$b_{mn}(z) = A_{mn}\, e^{-jk_{mn}^{z+}z} + B_{mn}\, e^{-jk_{mn}^{z-}z}.$$

(A.2.4.2)

A_{mn} and B_{mn} can be obtained by substituting the above general solution in Equation (2.3.13) and then integrating over the cross section S after multiplying each side of the equation by the conjugate of the mode shape function $\Psi_{ql}(r,\theta)$ to utilize the mode orthogonality/orthonormality relationship.

$$\int_S L\left[\sum_{mn} b_{mn}(z)\Psi_{mn}(r,\theta)\right]\Psi_{ql}^{*}(r,\theta)\,\mathrm{d}S = -\int_S \delta(\mathbf{x}-\mathbf{y})\Psi_{ql}^{*}(r,\theta)\,\mathrm{d}S.$$

(A.2.4.3)

Taking the integral inside the summation we have

$$\sum_{mn}\int_S \Psi_{ql}^{*}(r,\theta)L[b_{mn}(z)\Psi_{mn}(r,\theta)]\,\mathrm{d}S = -\int_S \delta(\mathbf{x}-\mathbf{y})\Psi_{ql}^{*}(r,\theta)\,\mathrm{d}S.$$

(A.2.4.4)

The operator L can be written independently for each mode since the solution is a linear sum of modes

$$L_{mn} = k_0^2 - \kappa_{mn}^2 + \beta^2\frac{\partial^2}{\partial z^2} - 2jk_0M\frac{\partial}{\partial z}.$$

(A.2.4.5)

This results in

$$\sum_{mn} L_{mn}\left\{b_{mn}(z)\int_S \Psi_{ql}^*(r,\theta)\Psi_{mn}(r,\theta)\,\mathrm{d}S\right\} = -\int_S \delta(\mathbf{x}-\mathbf{y})\Psi_{ql}^*(r,\theta)\,\mathrm{d}S\,,$$

(A.2.4.6)

and

$$\left\{k_0^2 - \kappa_{mn}^2 + \beta^2\frac{\partial^2}{\partial z^2} - 2jk_0M\frac{\partial}{\partial z}\right\}b_{mn}(z) = -\delta(z-z_s)\Psi_{mn}^*(r_s,\theta_s).$$

(A.2.4.7)

Integrating the above equation over an axial distance $[z_s-\varepsilon, z_s+\varepsilon]$ containing the source and taking the limit $\varepsilon \to 0$

$$\left(k_0^2 - \kappa_{mn}^2\right)\int_{z_s-\varepsilon}^{z_s+\varepsilon} b_{mn}(z)\,\mathrm{d}z + \left[\left\{\beta^2\frac{\partial}{\partial z} - 2jk_0M\right\}b_{mn}(z)\right]_{z_s-\varepsilon}^{z_s+\varepsilon} = -\Psi_{mn}^*(r_s,\theta_s) \times \int_{z_s-\varepsilon}^{z_s+\varepsilon}\delta(z-z_s)\,\mathrm{d}z.$$

(A.2.4.8)

Since $b_{mn}(z)$ is continuous across the interval

$$\int_{z_s-\varepsilon}^{z_s+\varepsilon} b_{mn}(z)\,\mathrm{d}z = 0 \qquad \text{and} \qquad \left[b_{mn}(z)\right]_{z_s-\varepsilon}^{z_s+\varepsilon} = 0\,, \text{ and}$$

(A.2.4.9)

$$\left[\frac{\partial b_{mn}(z)}{\partial z}\right]_{z_s-\varepsilon}^{z_s+\varepsilon} = -\frac{\Psi_{mn}^*(r_s,\theta_s)}{\beta^2}\,.$$

(A.2.4.10)

The Equations (2.3.16) for the reflection coefficients are given here again.

$$R_{mn}^{+} = \frac{B_{mn}^{+}}{A_{mn}^{+}} = e^{2j\eta_{mn}^{0+}}$$

$$\frac{1}{R_{mn}^{-}} = \frac{B_{mn}^{-}}{A_{mn}^{-}} = e^{2j\eta_{mn}^{0-}}.$$

(A.2.4.11)

In Equation (A.2.4.2) B_{mn} is expressed in terms of A_{mn} via the reflection coefficient phase $\eta_{mn}^{0\pm}$. Each of the regions z_s^{+} and z_s^{-} of the duct have to be considered separately as the above three quantities will have different values on each side of the source:

$$B_{mn}^{+} = A_{mn}^{+} e^{2j\eta_{mn}^{0+}}$$

$$B_{mn}^{-} = A_{mn}^{-} e^{2j\eta_{mn}^{0-}}.$$

(A.2.4.12)

We can write b_{mn} in the form

$$b_{mn}^{\pm}(z) = A_{mn}^{\pm}\left(e^{-jk_{mn}^{z+}z} + e^{2j\eta_{mn}^{0\pm}} e^{-jk_{mn}^{z-}z}\right),$$

(A.2.4.13)

or

$$b_{mn}^{\pm}(z) = A_{mn}^{\pm}\, e^{j\eta_{mn}^{0\pm}}\left(e^{-j\eta_{mn}^{0\pm}}\, e^{-j\left(\frac{k_{mn}-Mk_0}{\beta^2}\right)z} + e^{j\eta_{mn}^{0\pm}}\, e^{-j\left(\frac{-k_{mn}-Mk_0}{\beta^2}\right)z}\right),$$

(A.2.4.14)

where $k_{mn}^{z\pm} = \dfrac{\pm k_{mn} - Mk_0}{\beta^2}$.

It follows that

$$b_{mn}^{\pm}(z) = A_{mn}^{\pm}\, e^{j\left(\eta_{mn}^{0\pm}+\frac{Mk_0}{\beta^2}z\right)}\left(e^{-j\left(\eta_{mn}^{0\pm}+\frac{k_{mn}}{\beta^2}z\right)} + e^{j\left(\eta_{mn}^{0\pm}+\frac{k_{mn}}{\beta^2}z\right)}\right).$$

(A.2.4.15)

We now use the notation defined in Equation (A.2.3.3) which results in the following expression for b_{mn}

$$b_{mn}^{\pm}(z) = 2A_{mn}^{\pm} e^{j\left(\eta_{mn}^{0\pm} + \frac{Mk_0}{\beta^2} z\right)} \cos\left(\eta_{mn}^{\pm}(z)\right).$$

(A.2.4.16)

Expressing the equation for b_{mn} in terms of the forward propagating amplitude A_{mn} we get

$$b_{mn}^{\pm}(z) = 2A_{mn}^{\pm} e^{j\left(\eta_{mn}^{0\pm} + \frac{Mk_0}{\beta^2} z\right)} \cos\left(\eta_{mn}^{\pm}(z)\right).$$

(A.2.4.17)

Thus

$$\frac{\partial\, b_{mn}^{\pm}(z)}{\partial z} = b_{mn}^{\pm}(z)\left(j\frac{Mk_0}{\beta^2} - \frac{k_{mn}}{\beta^2}\tan\left(\eta_{mn}^{\pm}(z)\right)\right).$$

(A.2.4.18)

Substituting $z = z_s$ in equation (A.2.4.10) and (A.2.4.18) and letting $\varepsilon \to 0$ we have

$$b_{mn}^{+}(z_s)\left(j\frac{Mk_0}{\beta^2} - \frac{k_{mn}}{\beta^2}\tan\left(\eta_{mn}^{+}(z_s)\right)\right) - b_{mn}^{-}(z_s)\left(j\frac{Mk_0}{\beta^2} - \frac{k_{mn}}{\beta^2}\tan\left(\eta_{mn}^{-}(z_s)\right)\right)$$
$$= -\frac{\Psi_{mn}^{*}(r_s,\theta_s)}{\beta^2}.$$

(A.2.4.19)

Since b_{mn} is continuous at $z = z_s$ we can factorise the above equation by $b_{mn}(z_s)$ and get

$$b_{mn}(z_s) = \frac{\Psi_{mn}^{*}(r_s,\theta_s)}{k_{mn}\left[\tan\left(\eta_{mn}^{+}(z_s)\right) - \tan\left(\eta_{mn}^{-}(z_s)\right)\right]}.$$

(A.2.4.20)

The value of b_{mn} at any axial position z can be expressed in terms of that at z_s as follows:

$$\frac{b_{mn}^{\pm}(z)}{b_{mn}^{\pm}(z_s)} = e^{j(z-z_s)\frac{Mk_0}{\beta^2}} \frac{\cos\left(\eta_{mn}^{\pm}(z)\right)}{\cos\left(\eta_{mn}^{\pm}(z_s)\right)}$$

(A.2.4.21)

or

$$b_{mn}^{\pm}(z) = \frac{\Psi_{mn}^{*}(r_s,\theta_s)e^{j(z-z_s)\frac{Mk_0}{\beta^2}}}{k_{mn}\left[\tan\left(\eta_{mn}^{+}(z_s)\right)-\tan\left(\eta_{mn}^{-}(z_s)\right)\right]} \frac{\cos\left(\eta_{mn}^{\pm}(z)\right)}{\cos\left(\eta_{mn}^{\pm}(z_s)\right)}.$$

(A.2.4.22)

Appendix 2.5 Spatial derivatives of the Green function

The Green's function is

$$G^{\pm}(\mathbf{x}|\mathbf{y}) = \sum_{m=-\infty}^{m=+\infty}\sum_{n=1}^{+\infty} \frac{J_m(\kappa_{mn} r)e^{-jm\theta}\, J_m(\kappa_{mn} r_s)e^{jm\theta_s}}{N_{mn}^2\, k_{mn} \sin(\eta_{mn}^{0+} - \eta_{mn}^{0-})} e^{j(z-z_s)\frac{Mk_0}{\beta^2}} \times \cos(\eta_{mn}^{\pm}(z))\cos(\eta_{mn}^{\mp}(z_s))$$

(A.2.5.1)

The differentiation with respect to θ_s is straightforward and results in

$$\frac{\partial G^{\pm}}{\partial \theta_s} = \sum_m \sum_n jm G_{mn}^{\pm}(\mathbf{x}|\mathbf{y}).$$

(A.2.5.2)

The differentiation with respect to z_s gives for a single mode

$$\frac{\partial G_{mn}^{\pm}}{\partial z_s} = -j\frac{Mk_0}{\beta^2} G_{mn}^{\pm}(\mathbf{x}|\mathbf{y}) - \left\{ \begin{array}{l} \dfrac{\partial \eta_{mn}^{\mp}(z_s)}{\partial z_s} \sin(\eta_{mn}^{\mp}(z_s)) \dfrac{J_m(\kappa_{mn} r)e^{-jm\theta}\, J_m(\kappa_{mn} r_s)e^{jm\theta_s}}{N_{mn}^2\, k_{mn} \sin(\eta_{mn}^{0+} - \eta_{mn}^{0-})} \\ \times e^{j(z-z_s)\frac{Mk_0}{\beta^2}} \cos(\eta_{mn}^{\pm}(z)) \end{array} \right\}.$$

(A.2.5.3)

Since $\eta_{mn}^{\mp}(z_s) = \eta_{mn}^{0\mp} + \dfrac{k_{mn}}{\beta^2} z_s$ and using the identity $\sin x = \tan x \cos x$ we have

$$\frac{\partial G_{mn}^{\pm}}{\partial z_s} = j\left(j\frac{k_{mn}}{\beta^2} \tan(\eta_{mn}^{\mp}(z_s)) - \frac{Mk_0}{\beta^2} \right) G_{mn}^{\pm}(\mathbf{x}|\mathbf{y}).$$

(A.2.5.4)

Therefore

$$\frac{\partial G^{\pm}}{\partial z_s} = \sum_m \sum_n j\left(j\frac{k_{mn}}{\beta^2} \tan(\eta_{mn}^{\mp}(z_s)) - \frac{Mk_0}{\beta^2} \right) G_{mn}^{\pm}(\mathbf{x}|\mathbf{y}).$$

(A.2.5.5)

Defining the term

$$\gamma_{mn}^{\pm}(z_s) = j\frac{k_{mn}}{\beta^2}\tan\left(\eta_{mn}^{\mp}(z_s)\right) - \frac{Mk_0}{\beta^2},$$

(A.2.5.6)

we have

$$\frac{\partial G^{\pm}}{\partial z_s} = \sum_m \sum_n j\gamma_{mn}^{\pm}(z_s) G_{mn}^{\pm}(\mathbf{x}|\mathbf{y}).$$

(A.2.5.7)

Appendix 2.6 Force fluctuation distribution on a fan rotor with identical B blades

Starting with the first step in Equation (2.3.43) which is repeated here the intervening steps that lead to the final expression are detailed below. A change of variable from $(\theta_s' - 2\pi(s-1)/B)$ to θ_s' is made to arrive at the final result.

$$
\begin{aligned}
\widetilde{T}^{\pm}_{mn,p} &= \int_A J_m(\kappa_{mn} r_s)\cos\left(\eta^{\mp}_{mn,s}(z_s^c)\right) e^{-j\left(\frac{Ms\Omega}{c_0\beta^2} z_s^c - m\theta_s'\right)} F_p^T \gamma^{\pm}_{mn,s}(z_s^c)\, r_s \, \mathrm{d}r_s \, \mathrm{d}\theta_s' \\
&= \sum_{s=1}^{B} e^{j2\pi p(s-1)/B} \int_{A_0} J_m(\kappa_{mn} r_s)\cos\left(\eta^{\mp}_{mn,s}(z_s^c)\right) e^{-j\left(\frac{Ms\Omega}{c_0\beta^2} z_s^c - m\theta_s'\right)} \\
&\qquad \times F^0_{\alpha,p}(r_s, \theta_s' - 2\pi(s-1)/B)\gamma^{\pm}_{mn,s}(z_s^c)\, r_s \, \mathrm{d}r_s \, \mathrm{d}\theta_s' \\
&= \sum_{s=1}^{B} e^{j2\pi p(s-1)/B} e^{j2\pi m(s-1)/B} \int_{A_0} J_m(\kappa_{mn} r_s)\cos\left(\eta^{\mp}_{mn,s}(z_s^c)\right) e^{-j\left(\frac{Ms\Omega}{c_0\beta^2} z_s^c - m\theta_s'\right)} \\
&\qquad \times F^0_{\alpha,p}(r_s, \theta_s')\gamma^{\pm}_{mn,s}(z_s^c)\, r_s \, \mathrm{d}r_s \, \mathrm{d}\theta_s' \\
&= \sum_{s=1}^{B} e^{j2\pi (p+m)(s-1)/B} e^{j2\pi m(s-1)/B} \int_{A_0} J_m(\kappa_{mn} r_s)\cos\left(\eta^{\mp}_{mn,s}(z_s^c)\right) e^{-j\left(\frac{Ms\Omega}{c_0\beta^2} z_s^c - m\theta_s'\right)} \\
&\qquad \times F^0_{\alpha,p}(r_s, \theta_s')\gamma^{\pm}_{mn,s}(z_s^c)\, r_s \, \mathrm{d}r_s \, \mathrm{d}\theta_s' \\
&= B \int_{A_0} J_m(\kappa_{mn} r_s)\cos\left(\eta^{\mp}_{mn,s}(z_s^c)\right) e^{-j\left(\frac{Ms\Omega}{c_0\beta^2} z_s^c - m\theta_s'\right)} \\
&\qquad \times F^0_{\alpha,p}(r_s, \theta_s')\gamma^{\pm}_{mn,s}(z_s^c)\, r_s \, \mathrm{d}r_s \, \mathrm{d}\theta_s' \\
&= \begin{cases} BT^{\pm}_{mn,p} & \text{for } (m+n) = sB \\ 0 & \text{for } (m+n) \neq sB. \end{cases}
\end{aligned}
$$

(A2.6.1)

Appendix 2.7 Expressions for the Sears function

Goldstein (1976) gives the following expressions for the Sears function and its subsequent generalisations:

The ordinary Sears function S, given by Sears (1941) is given by the following expression. This is the expression for the fluctuating lift due to a frozen sinusoidal gust impinging on a fixed airfoil in an incompressible flow.

$$S(x) = \frac{1}{-jx\left[K_0(-jx) + K_1(-jx)\right]},$$

(A2.7.1)

where K_0 and K_1 are the modified Bessel functions.

The two-dimensional compressible Sears function S_c, given by Landahl (1961) for an oblique gust incident on an airfoil of infinite span is

$$S_c(\sigma_p, M_r) = \frac{e^{-j\sigma_p}}{\sigma_p \pi}\sqrt{\frac{j2}{M_r}}F\left(\sqrt{\frac{4\sigma_p M_r}{\pi(1+Mr)}}\right),$$

(A.2.7.2)

where $F(x) = \int_0^x e^{j(\pi/2)\xi^2} d\xi$ is the Fresnel integral. The above expression for the Sears function is for the high reduced frequency of the incident flow gust defined as $\sigma_p = \frac{p\Omega c}{2U_r}$ in which p refers to the circumferential harmonic of the gust, Ω the rotational frequency, c the chord of the blade, and U_r the relative flow velocity of the fluid. These terms were already illustrated in Figure 2.5.

For low frequency, the reference cited above gives the following expression which is due to Amiet (1974).

$$S_c(\sigma_p, M_r) = \frac{S\left(\sigma_p/\beta_r^2\right)}{\beta_r}\left[J_0\left(M_r^2\sigma_p/\beta_r^2\right) + jJ_1\left(M_r^2\sigma_p/\beta_r^2\right)\right]e^{-j\sigma_p f(M_r)/\beta_r^2},$$

(A.2.7.3)

where S denotes the ordinary Sears function, $\beta_r = \sqrt{1 - M_r^2}$, $f(M_r) = (1 - \beta_r)\ln M_r + \beta_r \ln(1 + \beta_r) - \ln 2$.

Appendix 3.1 Derivation of an expression for the transmitted sound power at any harmonic for the semi-infinite duct case

The expression for the pressure field with the semi-infinite duct approximation can be obtained by substituting $\eta_{mn}^{0+} = +j\infty$ in it to set the downstream reflection coefficient to zero:

$$
\begin{aligned}
p_{sB}(x) = B \sum_{p=-\infty}^{\infty} \sum_{n=1}^{\infty} & \frac{J_m(\kappa_{mn} r) e^{j\frac{MsB\Omega}{c_o\beta^2}z} e^{-jm\theta}}{N_{mn}^2 k_{mn,sB}} e^{-j\eta_{mn}^{0-}} \cos\left(\eta_{mn,sB}^{-}(z)\right) \\
& \times (m\hat{D}_{mn,p} + \gamma_{mn,sB}^{-} \hat{T}_{mn,p}) \\
= B \sum_{p=-\infty}^{\infty} \sum_{n=1}^{\infty} & \frac{J_m(\kappa_{mn} r) e^{-jm\theta}}{N_{mn}^2 k_{mn,sB}} e^{-j\eta_{mn}^{0-}} (m\hat{D}_{mn,p} + \gamma_{mn,sB}^{-} \hat{T}_{mn,p}) e^{j\frac{MsB\Omega}{c_o\beta^2}z} \\
& \times \cos\left(\eta_{mn,sB}^{-}(z)\right) \\
= B \sum_{p=-\infty}^{\infty} \sum_{n=1}^{\infty} & \frac{J_m(\kappa_{mn} r) e^{-jm\theta}}{N_{mn}^2 k_{mn,sB}} e^{-j\eta_{mn}^{0-}} (m\hat{D}_{mn,p} + \gamma_{mn,sB}^{-} \hat{T}_{mn,p})(1/2) \\
& \times \left(e^{j\left(\frac{MsB\Omega}{c_o\beta^2}z + \eta_{mn,sB}^{-}(z)\right)} + e^{j\left(\frac{MsB\Omega}{c_o\beta^2}z - \eta_{mn,sB}^{-}(z)\right)} \right),
\end{aligned}
$$

(A.3.1.1)

where

$$
\gamma_{mn,sB}^{-} = -\frac{k_{mn,sB}}{\beta^2} - \frac{MsB\Omega}{c_o\beta^2}.
$$

(A.3.1.2)

The axial component of the acoustic particle velocity can be obtained by considering the conservation equation for momentum (Goldstein 1976).

$$\rho_o c_o \left[jk_o + M \frac{\partial}{\partial x} \right] U_{sB}(z) = -\frac{\partial p_{sB}(x)}{\partial z}$$

(A.3.1.3)

and

$$U_{sB}(z) = -(1/\rho_o c_o M) e^{-j(k_o/M)z} \int \frac{\partial p_{sB}(x)}{\partial z} e^{j(k_o/M)z} dz \,.$$

(A.3.1.4)

The axial derivative of the pressure field is

$$\frac{\partial p_{sB}(x)}{\partial z}$$
$$= B \sum_{p=-\infty}^{\infty} \sum_{n=1}^{\infty} \frac{J_m(\kappa_{mn} r) e^{-jm\theta}}{N_{mn}^2 k_{mn,sB}} e^{-j\eta_{mn}^{0-}} (m \hat{D}_{mn,p} + \gamma_{mn,sB}^{-} \hat{T}_{mn,p}) (\frac{1}{2}) \cdot$$
$$\times \left(\begin{array}{l} e^{j\left(\frac{MsB\Omega}{c_o\beta^2} z + \eta_{mn,sB}^{-}(z)\right)} j(\frac{MsB\Omega}{c_o\beta^2} + \frac{k_{mn,sB}}{\beta^2}) \\ + e^{j\left(\frac{MsB\Omega}{c_o\beta^2} z - \eta_{mn,sB}^{-}(z)\right)} j(\frac{MsB\Omega}{c_o\beta^2} - \frac{k_{mn,sB}}{\beta^2}) \end{array} \right).$$

(A.3.1.5)

The axial component of the velocity field can be expressed in terms of the pressure field as follows:

$$
\begin{aligned}
U_{sB}(z) &= -(1/\rho_o c_o M) e^{-j(k_o/M)z} \int \frac{\partial p_{sB}(x)}{\partial z} e^{j(k_o/M)z} dz \\
&= -(1/\rho_o c_o M) \\
&\quad \times B \sum_{p=-\infty}^{\infty} \sum_{n=1}^{\infty} \frac{J_m(\kappa_{mn} r) e^{-jm\theta}}{N_{mn}^2 k_{mn,sB}} e^{-j\eta_{mn}^{0-}} (m \hat{D}_{mn,p} + \gamma_{mn,sB}^{-} \hat{T}_{mn,p})(\frac{1}{2}) \\
&\quad \times \left(\begin{array}{l} \dfrac{e^{j\left(\frac{MsB\Omega}{c_o\beta^2} z + \eta_{mn,sB}^{-}(z)\right)}}{j(\frac{MsB\Omega}{c_o\beta^2} + \frac{k_{mn,sB}}{\beta^2} + \frac{k_o}{M})} j(\frac{MsB\Omega}{c_o\beta^2} + \frac{k_{mn,sB}}{\beta^2}) \\ + \dfrac{e^{j\left(\frac{MsB\Omega}{c_o\beta^2} z - \eta_{mn,sB}^{-}(z)\right)}}{j(\frac{MsB\Omega}{c_o\beta^2} - \frac{k_{mn,sB}}{\beta^2} + \frac{k_o}{M})} j(\frac{MsB\Omega}{c_o\beta^2} - \frac{k_{mn,sB}}{\beta^2}) \end{array} \right) \\
&= -(1/\rho_o c_o M) p_{sB}(x) \left(\begin{array}{l} \dfrac{e^{j\eta_{mn,sB}^{-}(z)} (\frac{MsB\Omega}{c_o\beta^2} + \frac{k_{mn,sB}}{\beta^2})}{(\frac{MsB\Omega}{c_o\beta^2} + \frac{k_{mn,sB}}{\beta^2} + \frac{k_o}{M})} \\ + \dfrac{e^{-j\eta_{mn,sB}^{-}(z)} (\frac{MsB\Omega}{c_o\beta^2} - \frac{k_{mn,sB}}{\beta^2})}{(\frac{MsB\Omega}{c_o\beta^2} - \frac{k_{mn,sB}}{\beta^2} + \frac{k_o}{M})} \end{array} \right) \frac{1}{2\cos(\eta_{mn,sB}^{-}(z))}.
\end{aligned}
$$

(A.3.1.6)

Intensity and hence power transmitted through the duct for any cut-on mode are given by the following expressions which are mentioned in Goldstein (1976),

$$
I_{sB,m,n} = (1+M^2) p_{sB,m,n} U_{sB,m,n}^{*} + (M/\rho_o c_o) \left| p_{sB,m,n} \right|^2 + \rho_o c_o M \left| U_{sB,m,n} \right|^2,
$$

(A.3.1.7)

and

$$
P_{sB,m,n} = 2 \int_S I_{sB,m,n} dS .
$$

(A.3.1.8)

Considering the modal admittance as defined by $B_{sB,m,n} = \rho_o c_o p_{sB,m,n} / U_{sB,m,n}$, the expression for intensity as given in Morfey (1971) is as follows:

$$I_{sB,m,n} = (1/\rho_o c_o)\left\{(1+M^2)\,\mathrm{Re}(\mathrm{B}_{sB,m,n}) + M(1+\left|\mathrm{B}_{sB,m,n}\right|^2)\right\}\left|p_{sB,m,n}\right|^2 .$$

(A.3.1.9)

Using the expressions for velocity and pressure, the modal admittance can be written as follows

$$\begin{aligned}\mathrm{B}_{sB,m,n} &= -(1/M)\left(\frac{e^{j\bar{\eta}_{mn,sB}(z)}\left(\frac{MsB\Omega}{c_o\beta^2}+\frac{k_{mn,sB}}{\beta^2}\right)}{\left(\frac{MsB\Omega}{c_o\beta^2}+\frac{k_{mn,sB}}{\beta^2}+\frac{k_o}{M}\right)} + \frac{e^{-j\bar{\eta}_{mn,sB}(z)}\left(\frac{MsB\Omega}{c_o\beta^2}-\frac{k_{mn,sB}}{\beta^2}\right)}{\left(\frac{MsB\Omega}{c_o\beta^2}-\frac{k_{mn,sB}}{\beta^2}+\frac{k_o}{M}\right)}\right) \\ &\quad \times \frac{1}{2\cos\left(\bar{\eta}_{mn,sB}(z)\right)} \\ &= -\left(\frac{M(1-\alpha_{mn,sB}^2)+j\alpha_{mn,sB}\beta^2\tan(\bar{\eta}_{mn,sB}(z))}{1-\alpha_{mn,sB}^2 M^2}\right),\end{aligned}$$

(A.3.1.10)

where $\alpha_{mn,sB} = k_{mn,sB} / k_o$.

The modal admittance as expressed above is complex valued and it varies axially along the duct. The axial dependence is due to the term $\tan(\bar{\eta}_{mn,sB}(z))$ which is also complex valued. Further simplifications in the expression for modal admittance can be obtained by resolving the complex valued reflection coefficient.

$$\eta^{-}_{mn,sB}(z) = \eta^{0-}_{mn,sB} + \frac{k_{mn,sB}}{\beta^2} z = \xi^{0-}_{mn,sB} + j\phi^{0-}_{mn,sB} + \frac{k_{mn,sB}}{\beta^2} z = \xi^{-}_{mn,sB}(z) + j\phi^{0-}_{mn,sB},$$

(A.3.1.11)

$$\mathrm{B}_{sB,m,n} = -\left(\frac{\begin{array}{l} M(1-\alpha^2_{mn,sB})(\cosh 2\phi^{0-}_{mn,sB} + \cos 2\xi^{-}_{mn,sB}(z)) \\ +\alpha_{mn,sB}\beta^2 (j\sin 2\xi^{-}_{mn,sB}(z) - \sinh 2\phi^{0-}_{mn,sB}) \end{array}}{(1-\alpha^2_{mn,sB}M^2)(\cosh 2\phi^{0-}_{mn,sB} + \cos 2\xi^{-}_{mn,sB}(z))} \right).$$

(A.3.1.12)

Having expressed the modal admittance as above, the sound intensity for any harmonic can be obtained as follows:

$$\mathrm{Re}(\mathrm{B}_{sB,m,n}) = \left(\frac{-M(1-\alpha^2_{mn,sB})(\cosh 2\phi^{0-}_{mn,sB} + \cos 2\xi^{-}_{mn,sB}(z)) + \alpha_{mn,sB}\beta^2 \sinh 2\phi^{0-}_{mn,sB}}{(1-\alpha^2_{mn,sB}M^2)(\cosh 2\phi^{0-}_{mn,sB} + \cos 2\xi^{-}_{mn,sB}(z))} \right),$$

(A.3.1.13)

$$\left|\mathrm{B}_{sB,m,n}\right|^2 = \left(\frac{\begin{array}{l} \left(\alpha_{mn,sB}\beta^2 \sinh 2\phi^{0-}_{mn,sB} - M(1-\alpha^2_{mn,sB})(\cosh 2\phi^{0-}_{mn,sB} + \cos 2\xi^{-}_{mn,sB}(z))\right)^2 \\ +\left(\alpha_{mn,sB}\beta^2 \sin 2\xi^{-}_{mn,sB}(z)\right)^2 \end{array}}{(1-\alpha^2_{mn,sB}M^2)^2(\cosh 2\phi^{0-}_{mn,sB} + \cos 2\xi^{-}_{mn,sB}(z))^2} \right),$$

(A.3.1.14)

$$\begin{aligned} &(1+M^2)\mathrm{Re}(\mathrm{B}_{sB,m,n}) + M(1+\left|\mathrm{B}_{sB,m,n}\right|^2) \\ &\quad = \left(\frac{2M\alpha^2_{mn,sB}\beta^4 \cosh 2\phi^{0-}_{mn,sB} + \alpha_{mn,sB}\beta^4(1+\alpha^2_{mn,sB}M^2)\sinh 2\phi^{0-}_{mn,sB}}{(1-\alpha^2_{mn,sB}M^2)^2(\cosh 2\phi^{0-}_{mn,sB} + \cos 2\xi^{-}_{mn,sB}(z))} \right), \end{aligned}$$

(A.3.1.15)

$$(1+M^2)\mathrm{Re}(\mathrm{B}_{sB,m,n})+M(1+\left|\mathrm{B}_{sB,m,n}\right|^2)$$
$$=\left(\frac{2M\alpha_{mn,sB}^2\beta^4\cosh 2\phi_{mn,sB}^{0-}+\alpha_{mn,sB}\beta^4(1+\alpha_{mn,sB}^2M^2)\sinh 2\phi_{mn,sB}^{0-}}{(1-\alpha_{mn,sB}^2M^2)^2(\cosh 2\phi_{mn,sB}^{0-}+\cos 2\xi_{mn,sB}^{-}(z))}\right),$$

(A.3.1.16)

$$I_{sB,m,n}=(1/\rho_o c_o)\left(\frac{2M\alpha_{mn,sB}^2\beta^4\cosh 2\phi_{mn,sB}^{0-}+\alpha_{mn,sB}\beta^4(1+\alpha_{mn,sB}^2M^2)\sinh 2\phi_{mn,sB}^{0-}}{(1-\alpha_{mn,sB}^2M^2)^2(\cosh 2\phi_{mn,sB}^{0-}+\cos 2\xi_{mn,sB}^{-}(z))}\right)\left|p_{sB,m,n}\right|^2,$$

(A.3.1.17)

where the squared amplitude of pressure in any harmonic is the sum of the squares of the amplitudes of the cut-on modes.

$$\left|p_{sB}\right|^2=B^2\sum_{p=-\infty}^{\infty}\sum_{n=1}^{\infty}\frac{J_m^2(\kappa_{mn}r)}{N_{mn}^4k_{mn,sB}^2}e^{2\phi_{mn,sB}^{0-}}\left|(m\hat{D}_{mn,p}+\gamma_{mn,sB}^{-}\hat{T}_{mn,p})\right|^2\left|\cos(\eta_{mn,sB}^{-}(z))\right|^2$$
$$=B^2\sum_{p=-\infty}^{\infty}\sum_{n=1}^{\infty}\frac{J_m^2(\kappa_{mn}r)}{N_{mn}^4k_{mn,sB}^2}e^{2\phi_{mn,sB}^{0-}}\left|(m\hat{D}_{mn,p}+\gamma_{mn,sB}^{-}\hat{T}_{mn,p})\right|^2$$
$$\times\frac{(\cosh 2\phi_{mn,sB}^{0-}+\cos 2\xi_{mn,sB}^{-}(z))}{2}.$$

(A.3.1.18)

Power in any harmonic is

$$
\begin{aligned}
P_{sB} &= 2\int_S I_{sB}\, dS \\
&= B^2(1/\rho_o c_o)\sum_{p=-\infty}^{\infty}\sum_{n=1}^{\infty}\frac{1}{N_{mn}^2 k_{mn,sB}^2}\, e^{2\phi_{mn,sB}^{0-}} \\
&\qquad \times\left(\begin{array}{l} 2M\alpha_{mn,sB}^2\beta^4\cosh 2\phi_{mn,sB}^{0-} \\ +\alpha_{mn,sB}\beta^4(1+\alpha_{mn,sB}^2 M^2)\sinh 2\phi_{mn,sB}^{0-} \end{array}\right) \\
&\qquad \times\left|(m\hat{D}_{mn,p}+\gamma_{mn,sB}^{-}\hat{T}_{mn,p})\right|^2 \\
&= B^2(1/\rho_o c_o)\sum_{p=-\infty}^{\infty}\sum_{n=1}^{\infty}\frac{1}{N_{mn}^2 k_{mn,sB}^2}\frac{\alpha_{mn,sB}\beta^4}{(1-\alpha_{mn,sB}^2 M^2)^2}\, e^{2\phi_{mn,sB}^{0-}} \\
&\qquad \times\left(\begin{array}{l} \dfrac{e^{2\phi_{mn,sB}^{0-}}}{2}(1+\alpha_{mn,sB}M)^2 \\ -\dfrac{e^{-2\phi_{mn,sB}^{0-}}}{2}(1-\alpha_{mn,sB}M)^2 \end{array}\right)\left|(m\hat{D}_{mn,p}+\gamma_{mn,sB}^{-}\hat{T}_{mn,p})\right|^2
\end{aligned}
$$

.

(A.3.1.19)

The sound power thus obtained is independent of the axial location, indicating that the acoustic energy conservation is satisfied, as any variation in it has to be accompanied by the presence of acoustic sources or sinks. The expression also takes into account only the cut-on modes as the resolution of the complex reflection coefficient into amplitude and phase for cut-off modes would yield a different dependence on the axial coordinate. Letting $\varphi_{mn,sB}^{0-} \to -\infty$ (to account for zero upstream reflection) results in the intensity expression applicable for the infinite duct case.

$$P_{sB} = B^2(1/\rho_o c_o)\sum_{p=-\infty}^{\infty}\sum_{n=1}^{\infty}\frac{1}{N_{mn}^2 k_{mn,sB}^2}\frac{\alpha_{mn,sB}\beta^4}{(1-\alpha_{mn,sB}^2 M^2)^2}\left(-\frac{1}{2}(1-\alpha_{mn,sB}M)^2\right)$$
$$\times\left|(m\hat{D}_{mn,p}+\gamma^{-}_{mn,sB}\hat{T}_{mn,p})\right|^2$$
$$= -B^2(1/2\rho_o c_o)\sum_{p=-\infty}^{\infty}\sum_{n=1}^{\infty}\frac{1}{N_{mn}^2 k_{mn,sB}^2}\frac{\alpha_{mn,sB}\beta^4}{(1+\alpha_{mn,sB}M)^2}\left|(m\hat{D}_{mn,p}+\gamma^{-}_{mn,sB}\hat{T}_{mn,p})\right|^2 .$$

(A.3.1.20)

This expression agrees with that given in Goldstein (1976) for the infinite-duct approximation.

Appendix 5.1 Unsteadiness analysis

A.5.1.1 Introduction

As mentioned in Chapter 5 material is presented here relating to the unsteadiness analysis for the following quantities in the table below against the speeds indicated. This table tells us that the unsteadiness in the far-field measurements is quantified by analysing the tonal amplitudes and pressure levels from the far-field B&K microphone. Similarly the unsteadiness in the upstream in-duct measurements is quantified by analysing the tonal amplitudes registered on the upstream in-duct microphones and the amplitudes of the modes which were obtained through decomposition of the tones and the sound power resulting from the summation of the squares of the modal amplitudes. The unsteadiness in the downstream in-duct measurements is given by analysing the tonal amplitudes registered on the downstream in-duct microphones. Graphs illustrating the effect of successive (incremental) and moving averages variations are presented for the cases of the 30 s data capture on the microphones. Both types of averaging were explained in Chapter 5. The incremental average variation was already presented in Figure 5.14 and Figure 5.15 for the tonal amplitude measured from the upstream in-duct microphone for the two speeds of the fan for the case without the rod inserted into the duct.

Position along the fan duct (with BPF corresponding to the two fan speeds)	Quantity
Far field (for BPF=262 and 441 Hz) Data capture made through far-field microphone.	Tonal amplitude and phase (for the first three harmonics)
	Sound pressure level (first three harmonics)
In-duct Upstream (BPF=262 and 441 hz) Data capture made through in-duct upstream microphone.	Tone on the first microphone (first three harmonics)
	Incident and reflected modal amplitudes (B_{mn} and A_{mn})

	Modal coupling coefficients (C_{mn})
	Modal reflection coefficients (R_{mn})
	In-duct sound power level (P)
In-duct Downstream (Only BPF=262hz) Data capture made through in-duct downstream microphone.	Tone on the first microphone (first three harmonics)
	Incident and reflected modal amplitudes (B_{mn} and A_{mn})
	Modal reflection coefficients (R_{mn})

Table A.5.1.1 Quantities presented for the unsteadiness analysis.

As mentioned in Chapter 5 the fan was run at two speeds at which the experiments described were all conducted. The two speeds as measured from the counts of the trigger pulses turned out 1767 and 2934 rpm which correspond to 29.4 and 48.9 rev/s. Since each revolution of the fan rotor will have one instrumented blade pass, a 30 s microphone signal has around 1500 blocks of instrumented blade passes at the high speed and around 900 blocks at the low speed. Only 1400 blocks at the high speed and 800 blocks at low speed in the 30 s data capture were used for the successive averaging which translates to 28 s at high speed and 26.66 s at the low speed. For moving averaging each average spanned 800 blocks at high speed and 400 at the low speed. As mentioned in Chapter 5 successive averaging illustrates how many blocks are to be chosen for averaging during subsequent experiments. With these many blocks the moving average should illustrate and quantify any residual unsteadiness in the averaged estimates. Using the variations obtained from the moving averaging the residual unsteadiness is given in terms of the mean and standard deviations for the in-duct sound power and far-field pressure levels at the end of this appendix.

A.5.1.2 Far field quantities:

In this section unsteadiness variations in quantities pertaining to the measurements of the far field microphone are given for the two fan speeds.

Far field tonal amplitude and phase (262 hz BPF):

As said previously the 30s signal from the far-field microphone at the low fan speed had around 800 blocks of instrumented blade passes. Each block corresponding to a single instrumented blade pass was Fast Fourier Transformed and the complex tonal amplitudes of the three harmonics were obtained and these amplitudes were incrementally averaged as the number of blocks was increased from 1 to 800. The effect of this incremental averaging on the amplitude and the phase of the three harmonics can be seen in graphs (i-vi) of Figure A.5.1.1. The variation indicated in blue is for the case when there is no rod inside the duct and that in red is when a single rod of 200 mm length is inserted into the duct. For example the first harmonic amplitude is shown for the cases with and without the rod in the graph (i) in Figure A.5.1.1. As in the rest of the rest graphs (ii-iii) the tonal amplitude is higher with the rod inside the duct than that without the rod. As the averaging proceeds from 1 to 800 blocks the initial unsteadiness during the first few averages should die out. This seems to happen for all the three tonal amplitudes and phases for the case with the rod inside the duct. It can be seen that the tonal phase exhibits unsteadiness in the first two harmonics for the case without the rod inside the duct as seen in graphs (iv-v). Though the unsteadiness in the amplitudes for the case without the rod in the duct is not obvious in these graphs, they will be made obvious in the graphs presented later in this section for the sound pressure level.

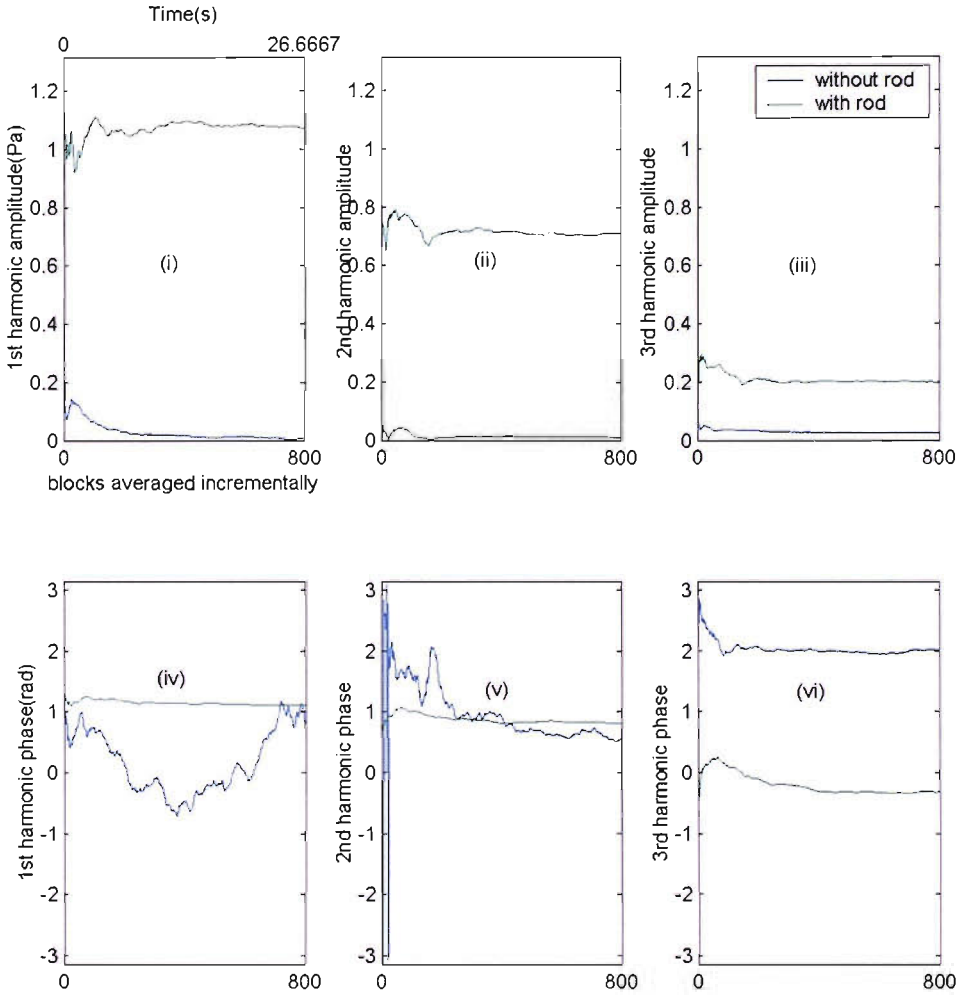

Figure A.5.1.1 Effect of incremental averaging on far-field BPF tone (262 hz) and its harmonics: (i-iii) tonal amplitudes (iv-vi) tonal phases.

The averaging was also performed using the moving averaging method described in Chapter 5. The averaging was performed over 400 instrumented blade passes commencing from the start of the first instrumented blade pass in the 30 s signal and the averaging was repeated for every set of 400 instrumented blade passes commencing from each subsequent instrumented blade pass. Since there are around 800 instrumented blade passes in the 30 s signal the averaging described can be repeated only 400 times. These 400 averages are represented in the variation shown in graphs (i-vi) of Figure A.5.1.2 for the tonal amplitudes and phases. It can be seen that the estimates of the amplitudes and phases have the same values as were seen for the incremental averaging in Figure A.5.1.2. It can

be seen that the phase unsteadiness in the first two harmonics for the case without rod in graphs (iv-v) of Figure A.5.1.1 is carried over to the moving averaged variation also. This unsteadiness in the phase is due to a wide variation of the phase of the tones across the individual instrumented blade passes. This should also cause the corresponding averaged tonal amplitudes to show similar unsteadiness. It is not obvious from the variations shown here. This unsteadiness as mentioned previously will be obvious in the sound pressure level estimates shown subsequently. As mentioned in the beginning of this appendix the residual unsteadiness in these variations is described at the end of this Appendix in terms of the mean and standard deviation for these tonal amplitudes and the quantities listed in Table A.5.1.1.

Similar incremental and moving average variations are given for the above quantity at the higher fan speed and also for the rest of the quantities at the two fan speeds presented subsequently in this and the later sections of this appendix. Important consequences of the unsteadiness are described wherever necessary.

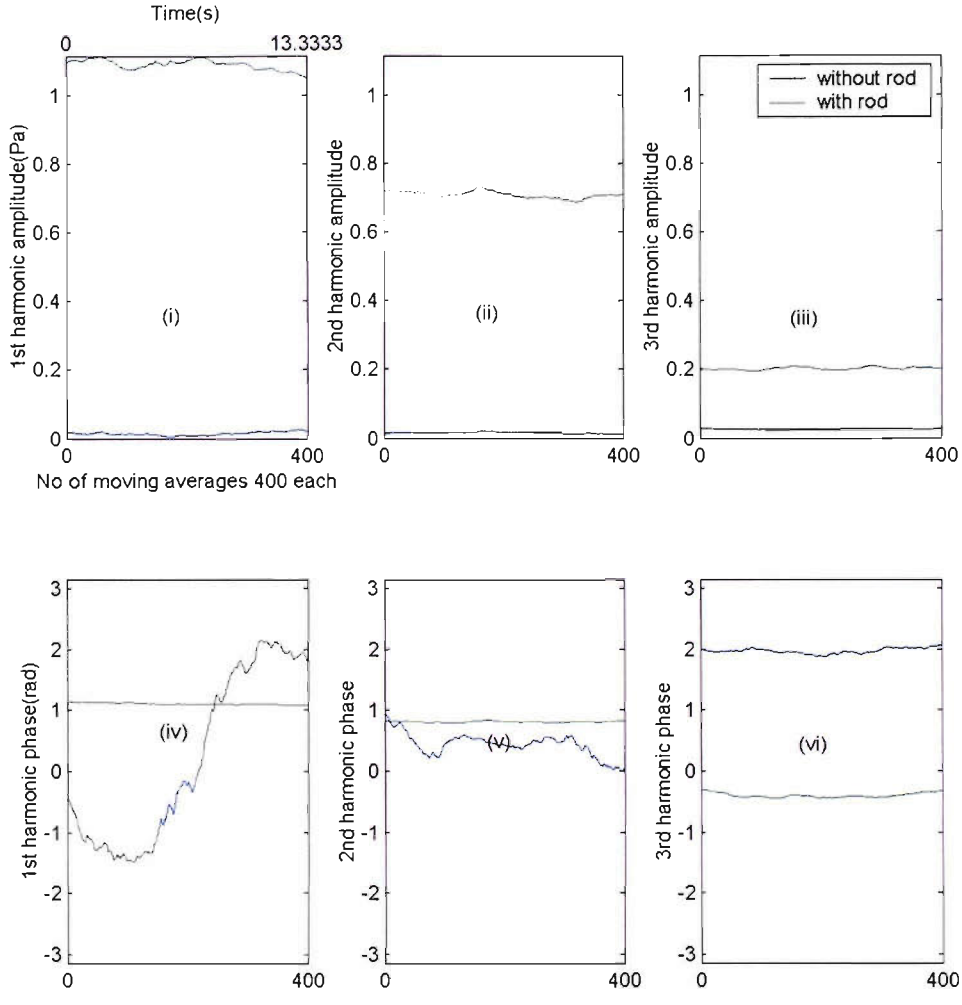

Figure A.5.1.2 Effect of moving averaging on far-field BPF tone (262 hz) and its harmonics: (i-iii) tonal amplitudes (iv-vi) tonal phases.

Far field tonal amplitude and phase (441 hz BPF):

The effect of incremental averaging on the amplitude and the phase of the three far-field harmonics for the high speed case can be seen in graphs (i-vi) of Figure A.5.1.3. Corresponding moving average variations are given in graphs (i-vi) of Figure A.5.1.4. At this speed the phase of the third harmonic without the rod exhibits more unsteadiness.

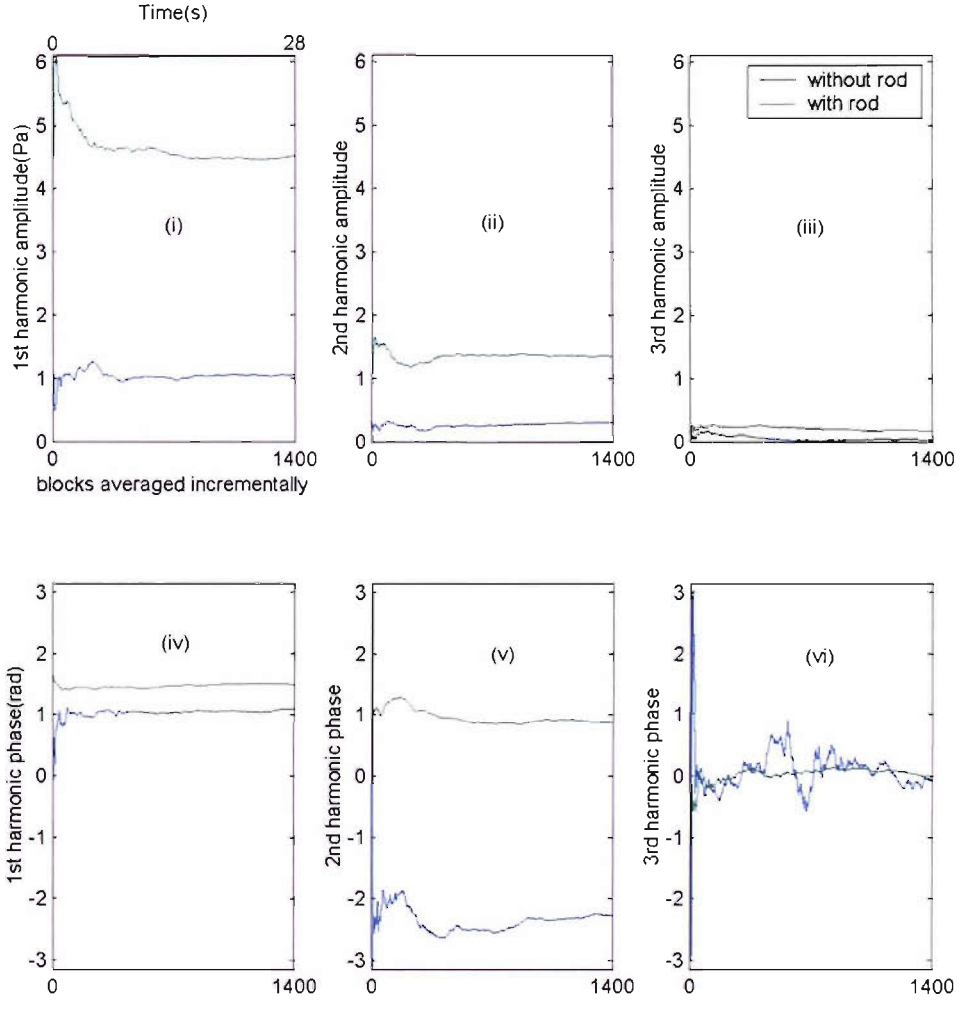

Figure A.5.1.3 Effect of incremental averaging on far-field BPF tone (441 hz) and its harmonics: (i-iii) tonal amplitudes (iv-vi) tonal phases.

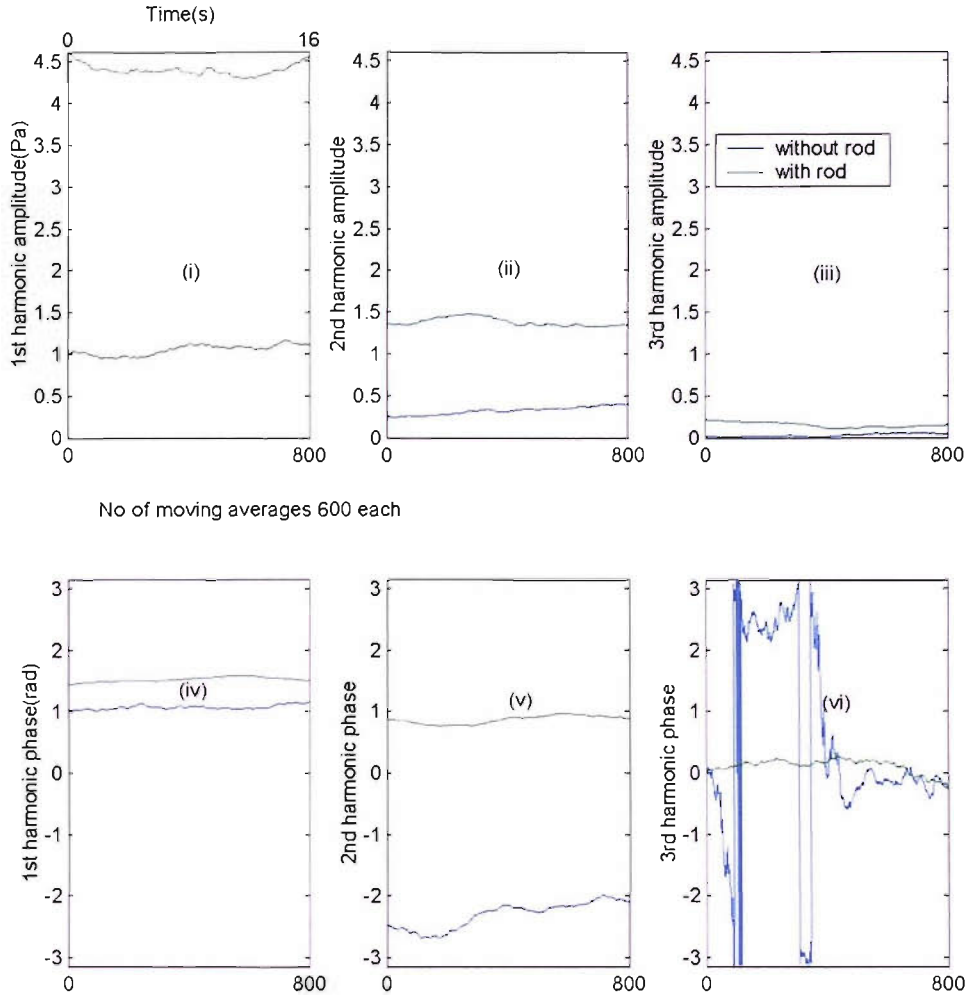

Figure A.5.1.4 Effect of moving averaging on far-field BPF tone (441 hz) and its harmonics: (i-iii) tonal amplitudes (iv-vi) tonal phases.

Far field Sound pressure level (262 and 441 hz BPF):

Previously in this section the unsteadiness variations in the tonal pressures were presented in Figures A.5.1.1 – A.5.1.4 for the two speeds and the sound pressure level variations estimated from the tonal amplitudes are described here. The incrementally averaged variations for the far-field sound pressure level at the two speeds are shown in graphs (i-vi) of Figure A.5.1.5. Graphs (i-iii) correspond to the low fan speed and (iv-vi) correspond to the high speed. The undulations in the amplitude of the tones described previously are now very obvious in the sound pressure level variations for the first and second harmonics at the low speed and the third harmonic at the high speed for the cases without the rod. The corresponding moving averaged variations in the sound pressure level for the two speeds are shown in the graphs (i-vi) of Figure A.5.1.6.

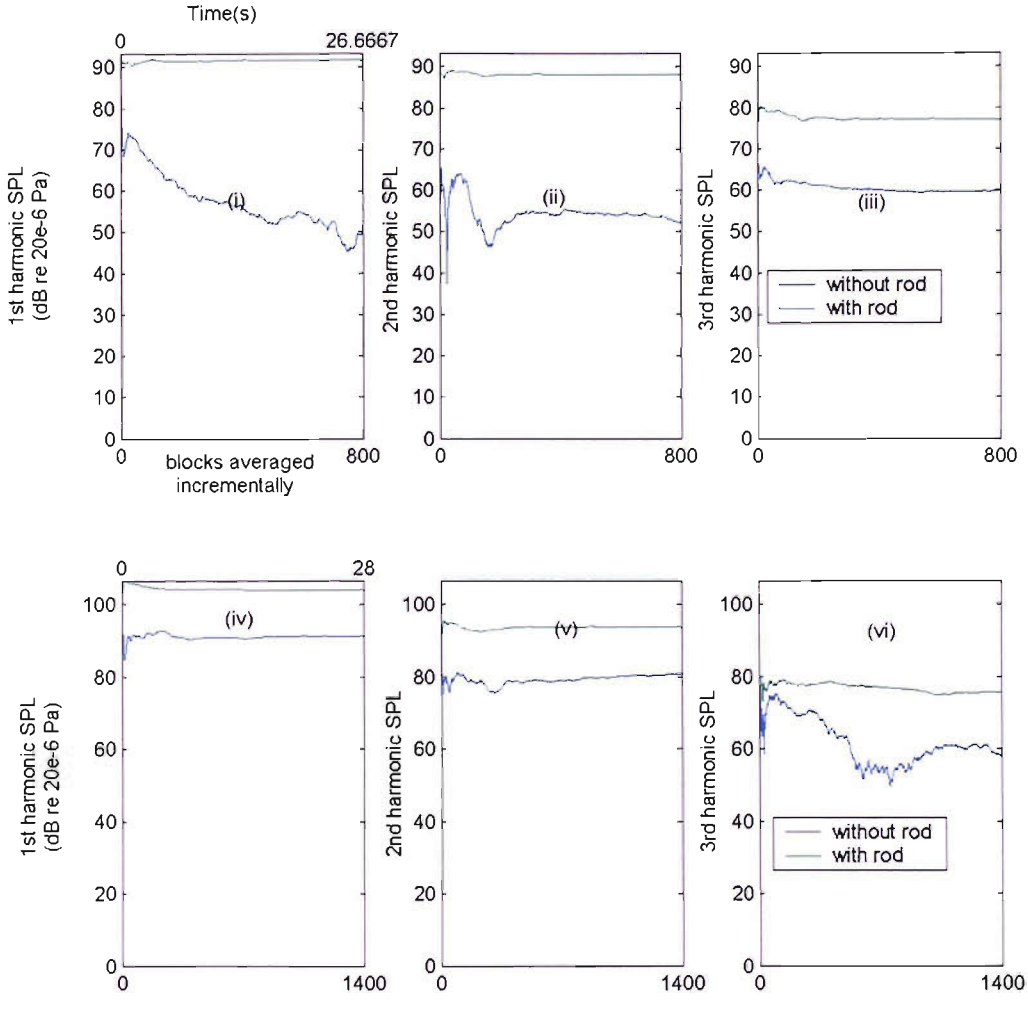

Figure A.5.1.5 Effect of incremental averaging on far-field sound pressure level of the BPF tone (262 hz) and its harmonics : (i-iii); Effect of incremental averaging on far-field sound pressure level of the BPF tone (441 hz) and its harmonics : (iv-vi).

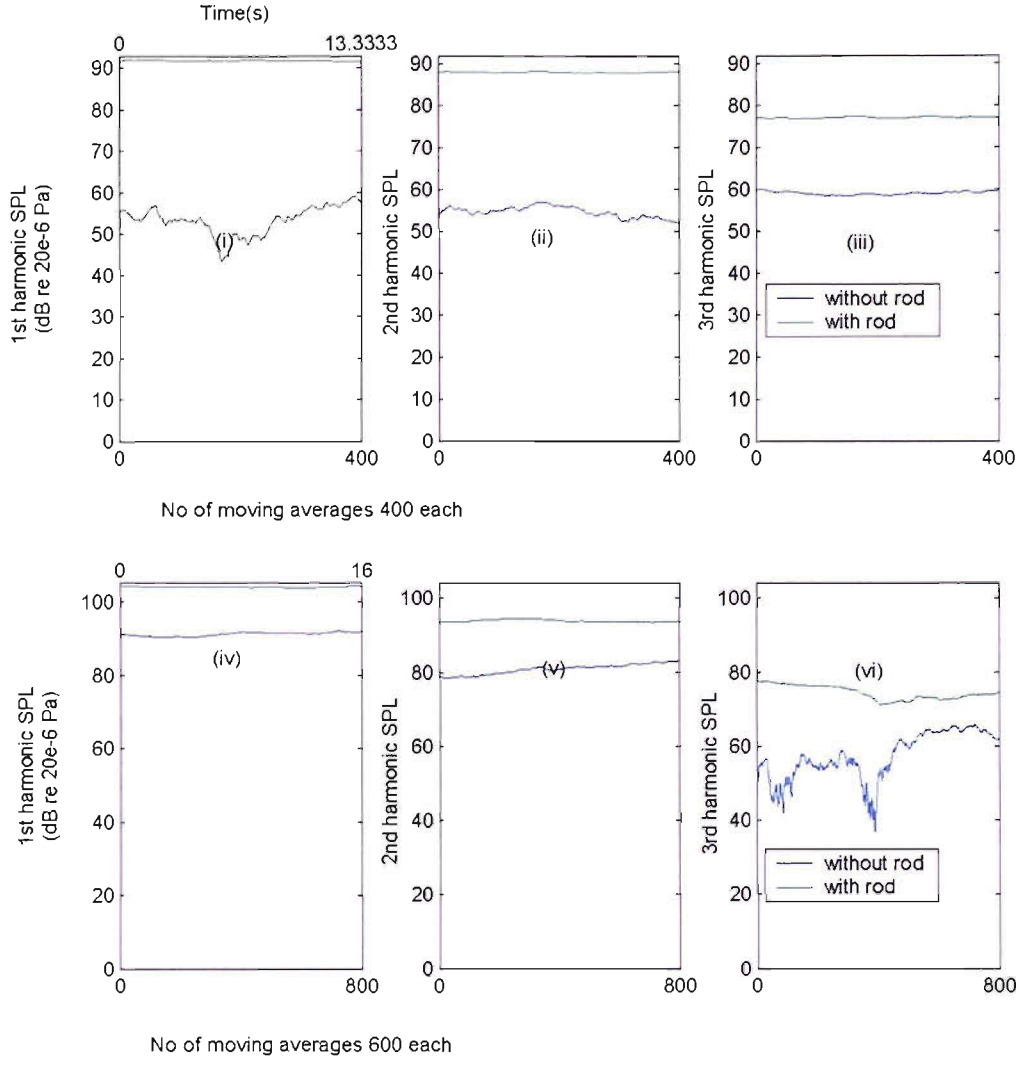

Figure A.5.1.6 Effect of moving averaging on far-field sound pressure level of the BPF tone (262 hz) and its harmonics : (i-iii); Effect of moving averaging on far-field sound pressure level of the BPF tone (441 hz) and its harmonics : (iv-vi).

A.5.1.3 In-duct Upstream quantities:

In the previous section the description of the unsteadiness focussed on the far-field quantities. In this section unsteadiness variations in quantities pertaining to the measurements of the first upstream in-duct microphone are given for both the fan speeds.

Tonal amplitude and phase (262 hz BPF):

Incrementally averaged variations are given for the estimates of the low speed tonal pressures here in the graphs (i-vi) of Figure A.5.1.7. As seen in graph (iv) the fluctuation in the phase of the first harmonic without the rod is very high. This is because the tone at the BPF for the case without the rod doesn't exhibit phase coherence across the instrumented blade passing segments in the trace of the acquired signal from in-duct microphone. This was also the case with the far-field measurements as mentioned previously. The phase fluctuation in the first harmonic can also be seen from the moving averaged variations which are given in graphs (i-vi) of Figure A.5.1.8. Hence the amplitude of the tone for this case is also very low and very small compared to other harmonics and is also unsteady.

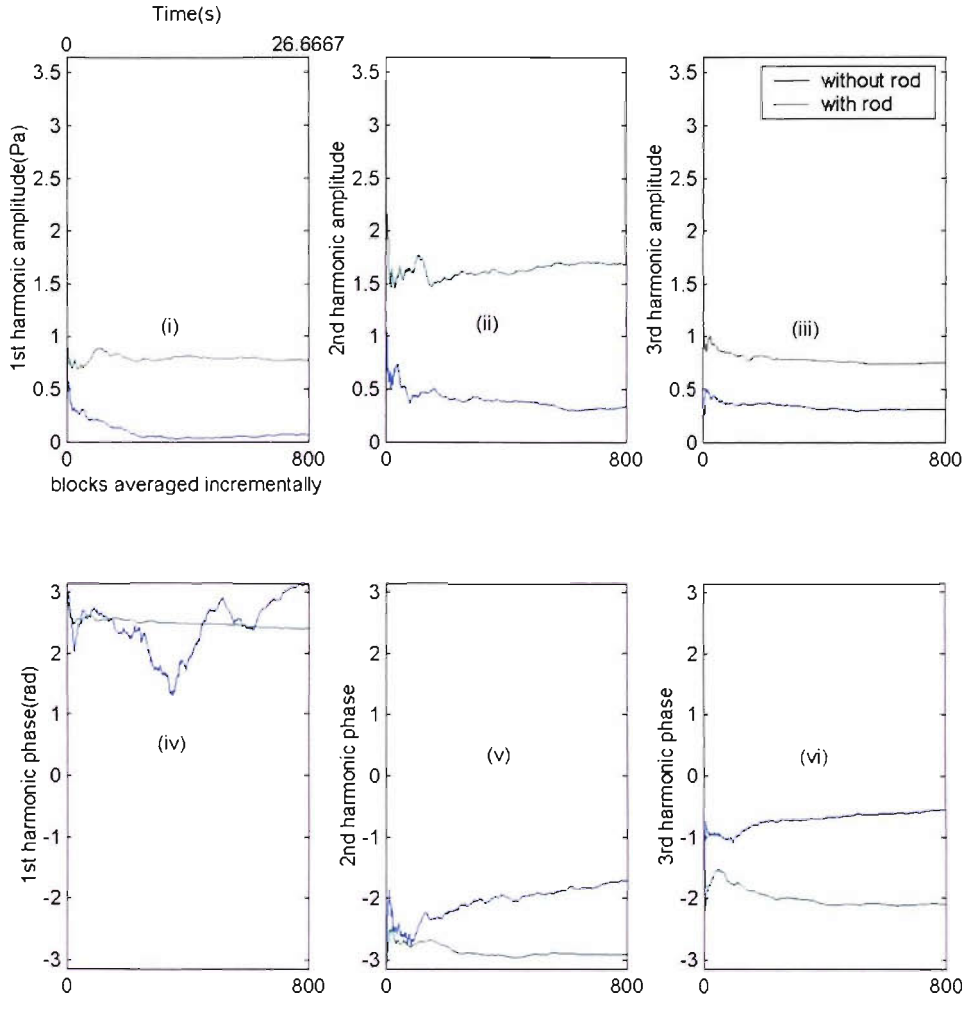

Figure A.5.1.7 Effect of incremental averaging on the BPF tone (262 hz) and its harmonics measured on the in-duct upstream microphone: (i-iii) tonal amplitudes, (iv-vi) tonal phases.

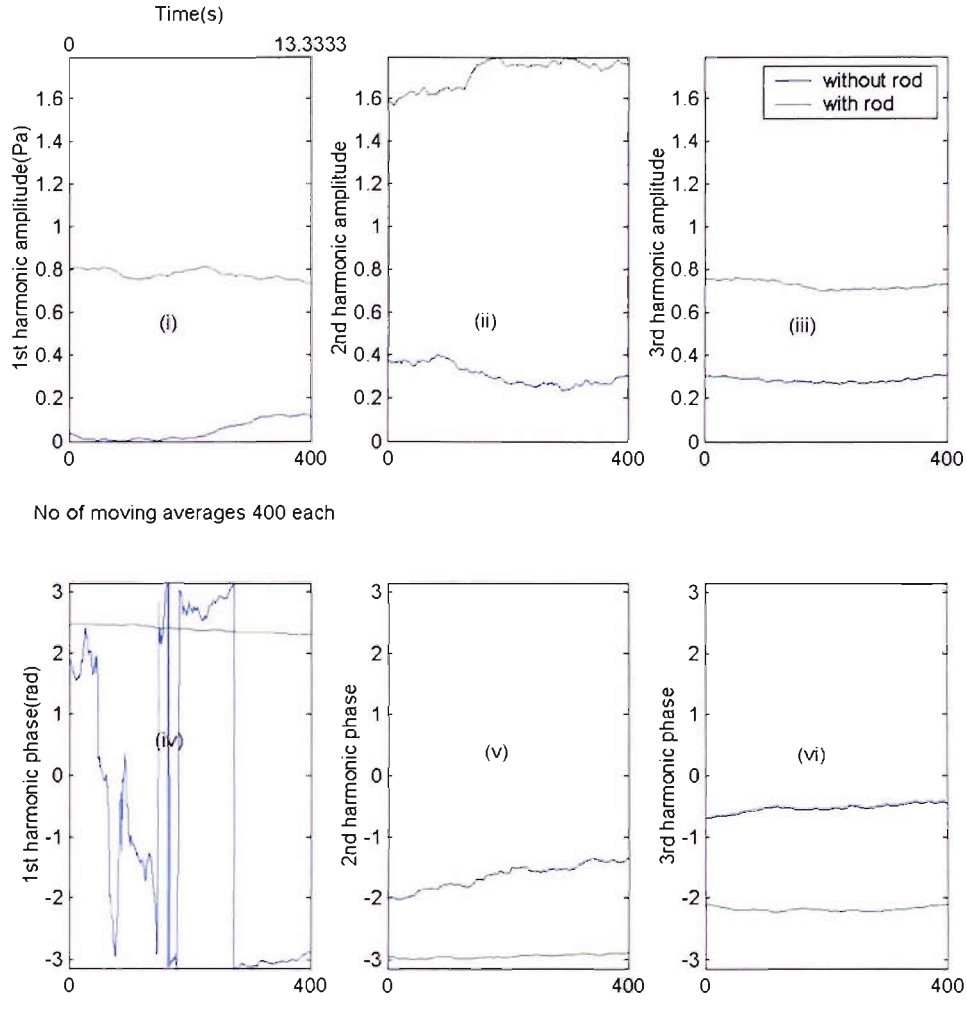

Figure A.5.1.8 Effect of moving averaging on the BPF tone (262 hz) and its harmonics measured on the in-duct upstream microphone: (i-iii) tonal amplitudes, (iv-vi) tonal phases.

Tonal amplitude and phase (441 hz BPF):

Incrementally average variations are given for the estimates of the high speed tonal pressures here in the graphs (i-vi) of Figure A.5.1.9. Graphs (i-vi) of Figure A.5.1.10 give the corresponding moving average variations.

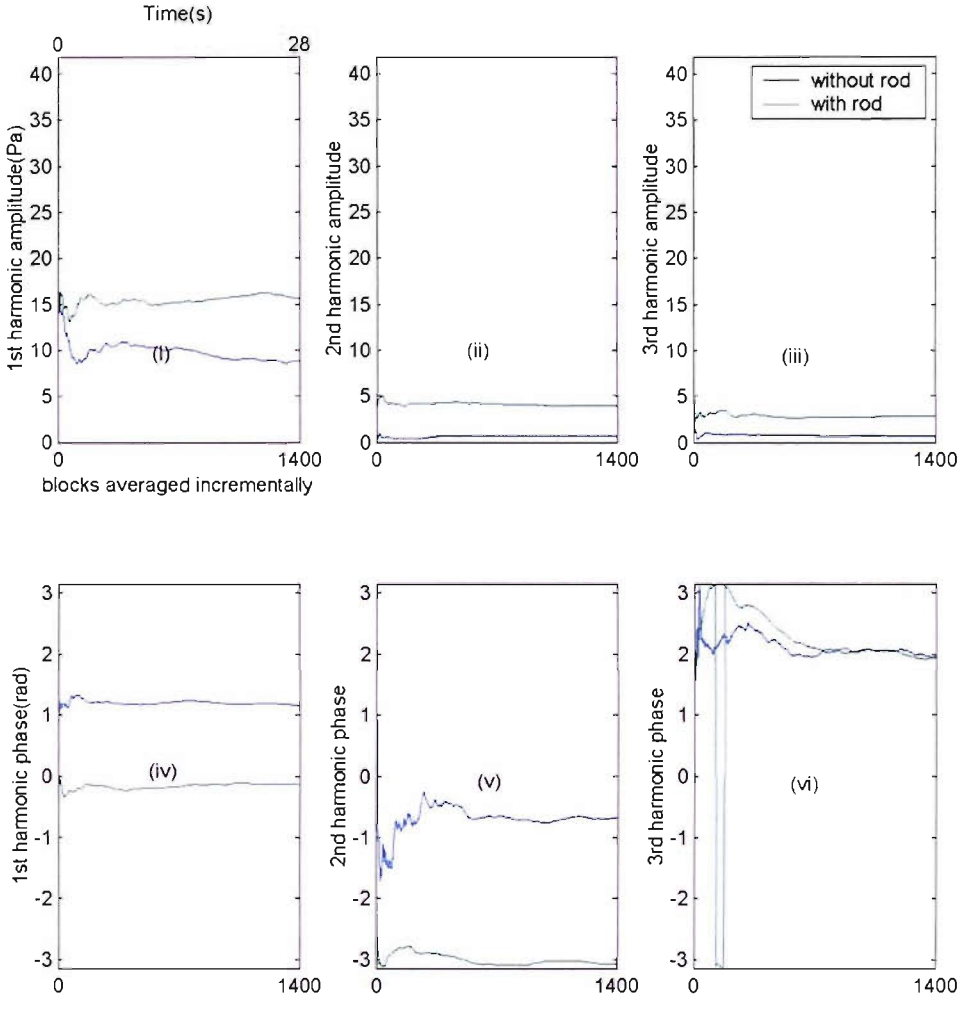

Figure A.5.1.9 Effect of incremental averaging on the BPF tone (441 hz) and its harmonics measured on the in-duct upstream microphone: (i-iii) tonal amplitudes, (iv-vi) tonal phases.

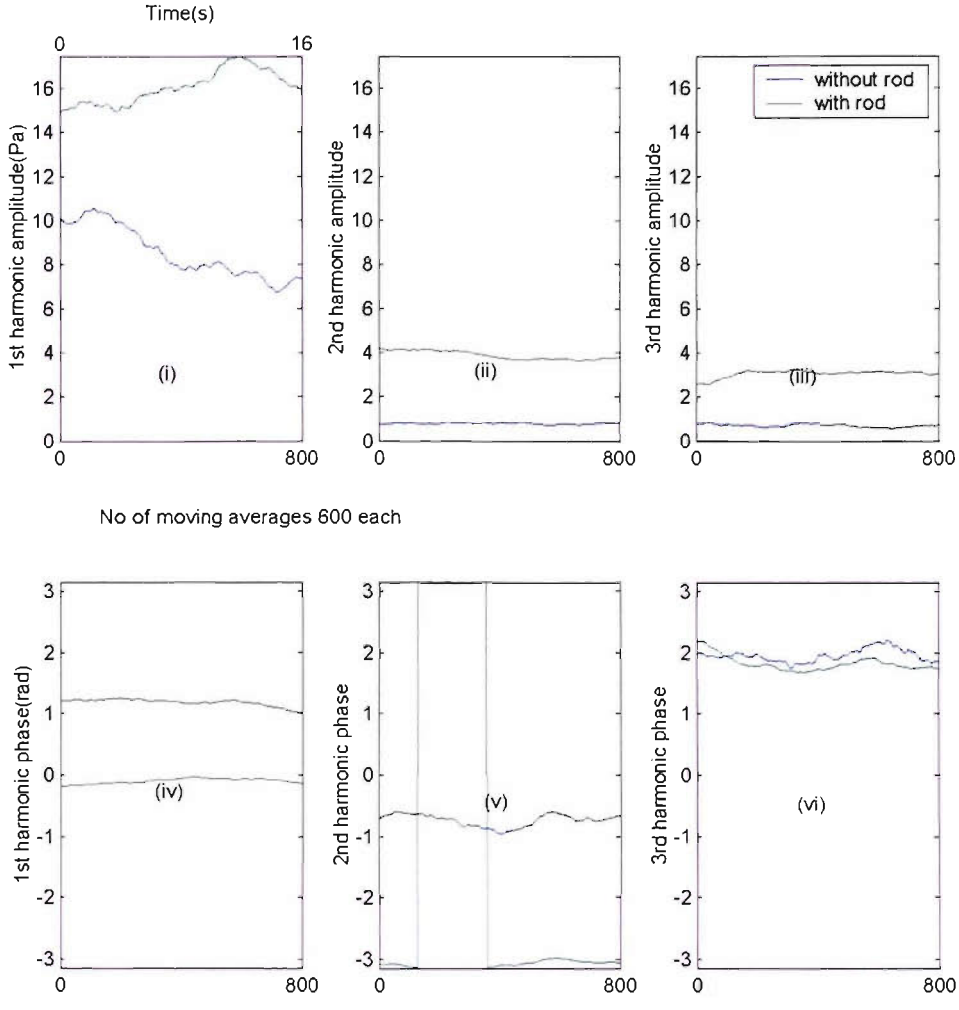

Figure A.5.1.10 Effect of moving averaging on the BPF tone (441 hz) and its harmonics measured on the in-duct upstream microphone: (i-iii) tonal amplitudes, (iv-vi) tonal phases.

Upstream incident and reflected modal amplitudes and phases (262 hz BPF, m=0): Effect of averaging on tonal unsteadiness from the first upstream in-duct microphone measurements at the two speeds was described in Figures A.5.1.7 – A.5.1.10. The incremental average variation of the incident and reflected modes resulting from the decomposition of the low speed first harmonic duct tones measured on all the 14 in-duct microphones are given here in graphs (i-iv) of Figure A.5.1.11. The BPF at the low speed has only the plane wave mode (m=0) that is cut-on. Since the tone at the BPF for the case without the rod was small and exhibited significant unsteadiness the resulting incident and reflected modes also show this variation. Their amplitudes are small compared to the case with the rod inserted in the duct. Corresponding moving average variations are shown in graphs (i-iv) of Figure A.5.1.12.

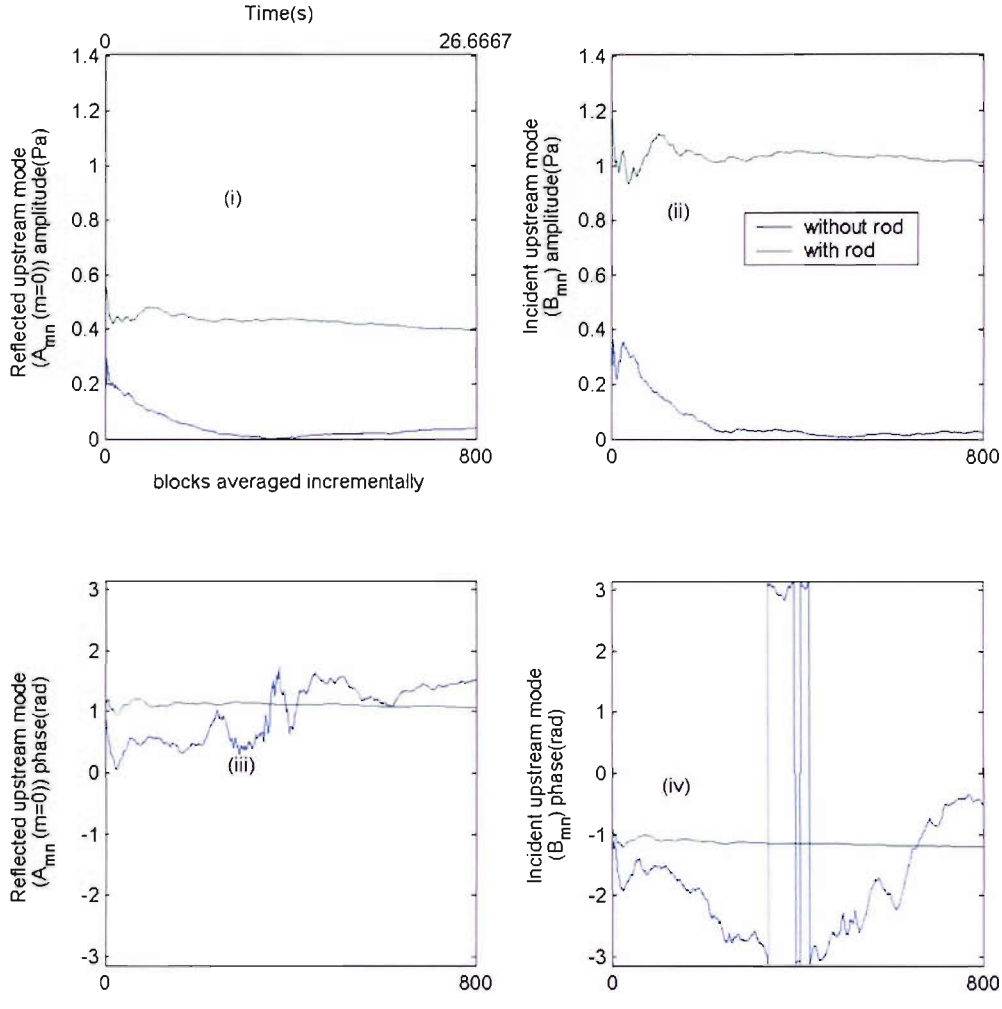

Figure A.5.1.11 Effect of incremental averaging on upstream incident and reflected mode (m=0, 262 hz BPF): (i-ii) amplitudes, (iii-iv) phases.

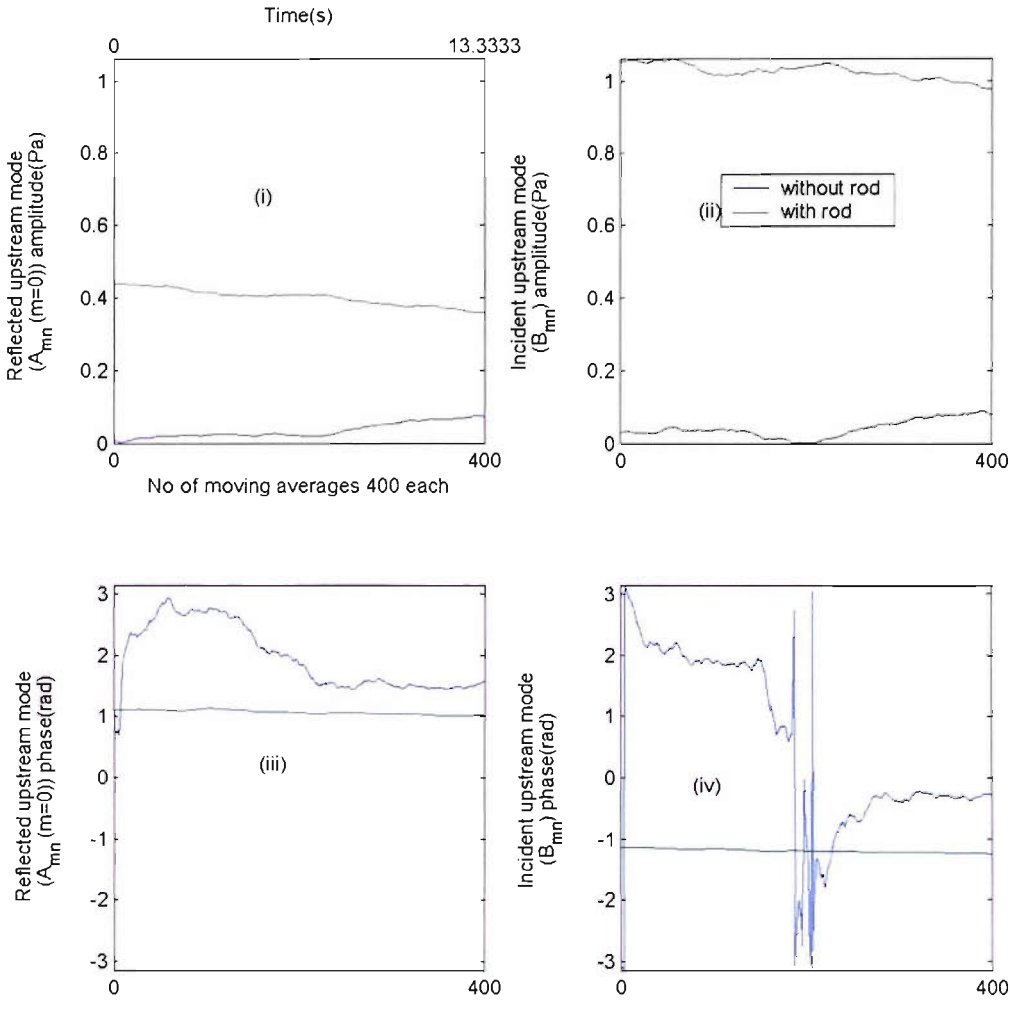

Figure A.5.1.12 Effect of moving averaging on upstream incident and reflected mode (m=0, 262 hz BPF): (i-ii) amplitudes, (iii-iv) phases.

Upstream incident and reflected modal amplitudes and phases (441 hz BPF, m=(-1, 0 1)):

The first harmonic at the high speed has three cut-on duct modes (m=(-1,0,1)). As in the low speed case the high speed first harmonic tonal pressures measured on the in-duct upstream microphone array is decomposed into these three modes. The effect of incremental and moving averaging on the variation of the incident and reflected amplitudes of these modes are given in graphs (i-iv) in each of the Figures A.5.1.13 – A.5.1.18.

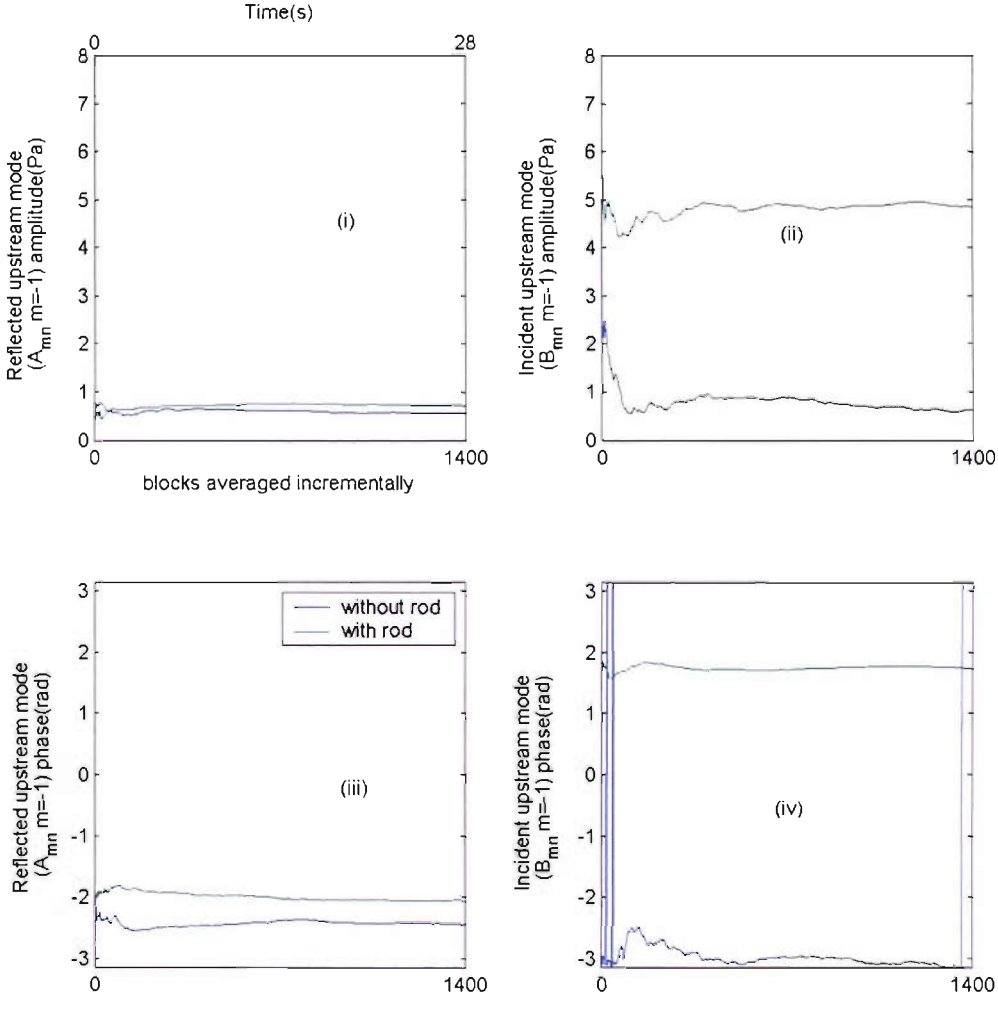

Figure A.5.1.13 Effect of incremental averaging on upstream incident and reflected mode (m=-1, 441 hz BPF): (i-ii) amplitudes, (iii-iv) phases.

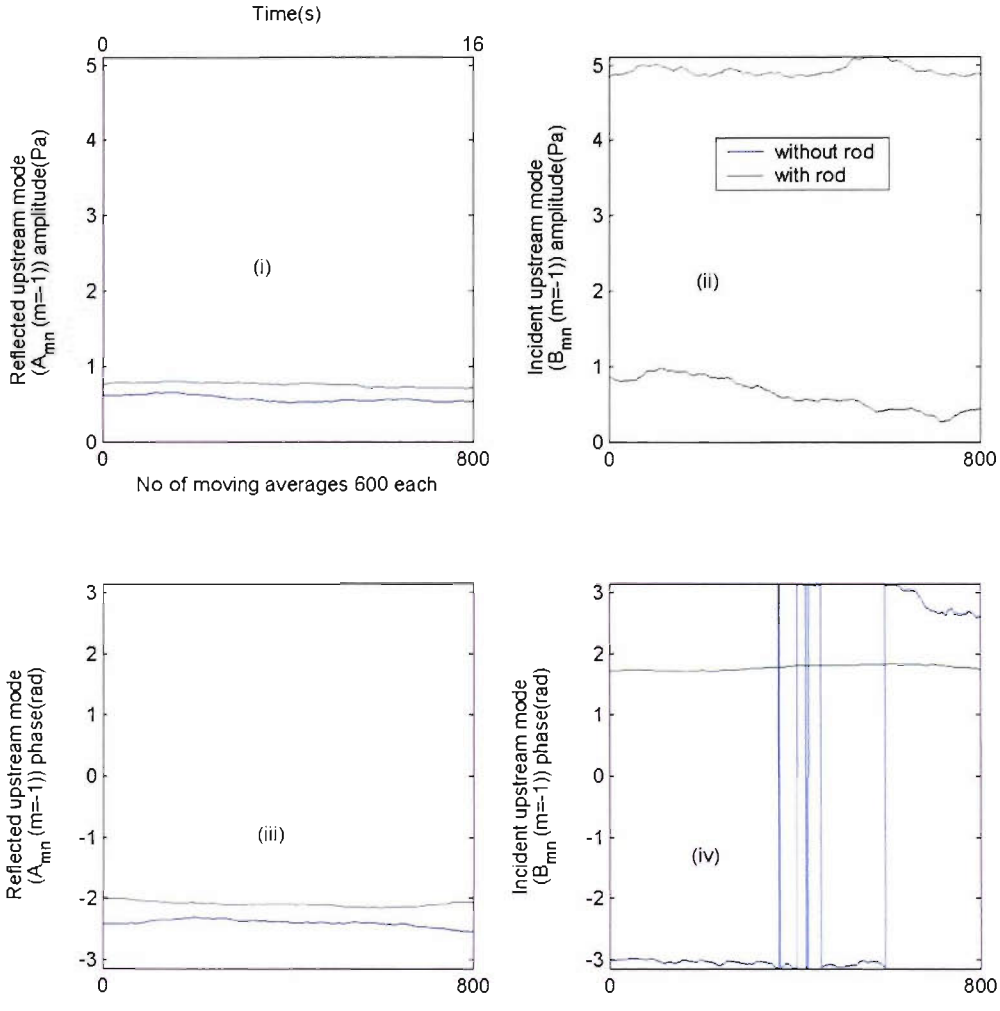

Figure A.5.1.14 Effect of moving averaging on upstream incident and reflected mode (*m*=-1, 441 hz BPF): (i-ii) amplitudes, (iii-iv) phases.

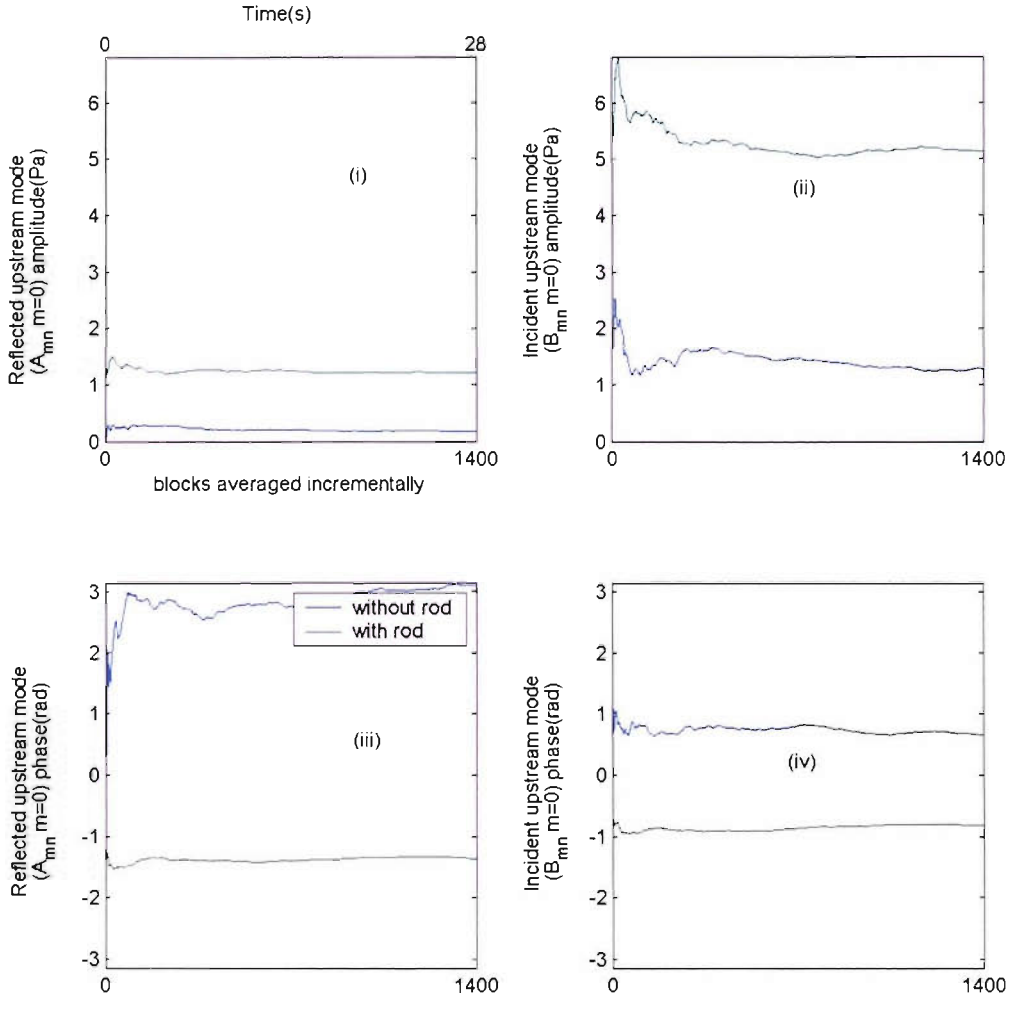

Figure A.5.1.15 Effect of incremental averaging on upstream incident and reflected mode (m=0, 441 hz BPF): (i-ii) amplitudes, (iii-iv) phases.

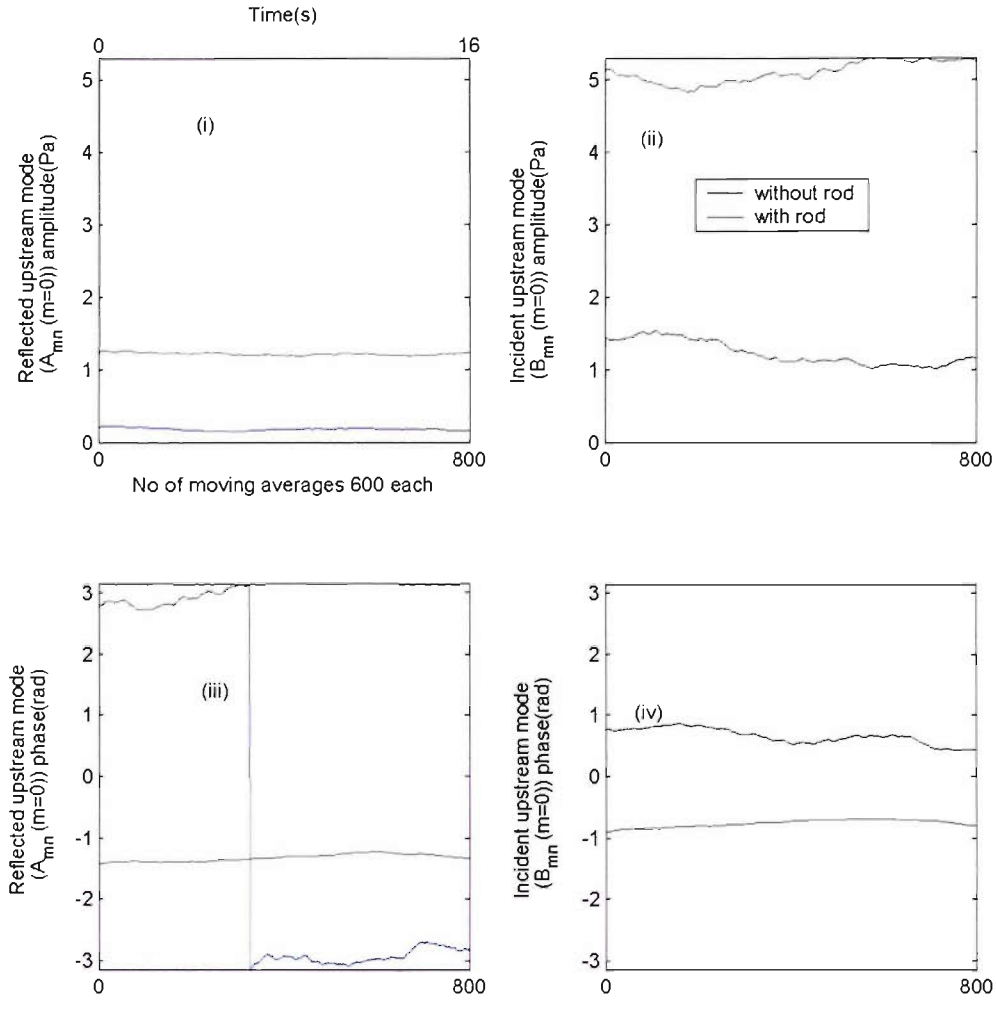

Figure A.5.1.16 Effect of moving averaging on upstream incident and reflected mode (m=0, 441 hz BPF): (i-ii) amplitudes, (iii-iv) phases.

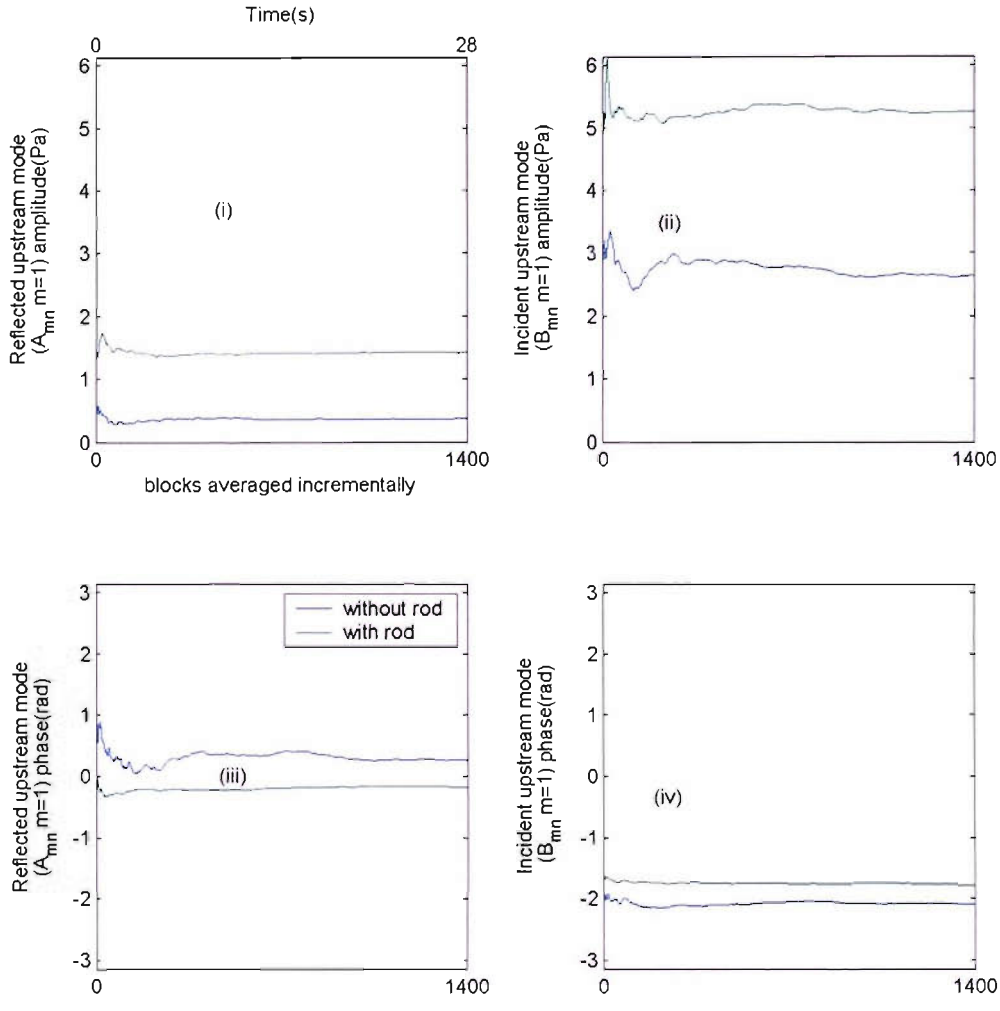

Figure A.5.1.17 Effect of incremental averaging on upstream incident and reflected mode (m=1, 441 hz BPF): (i-ii) amplitudes, (iii-iv) phases.

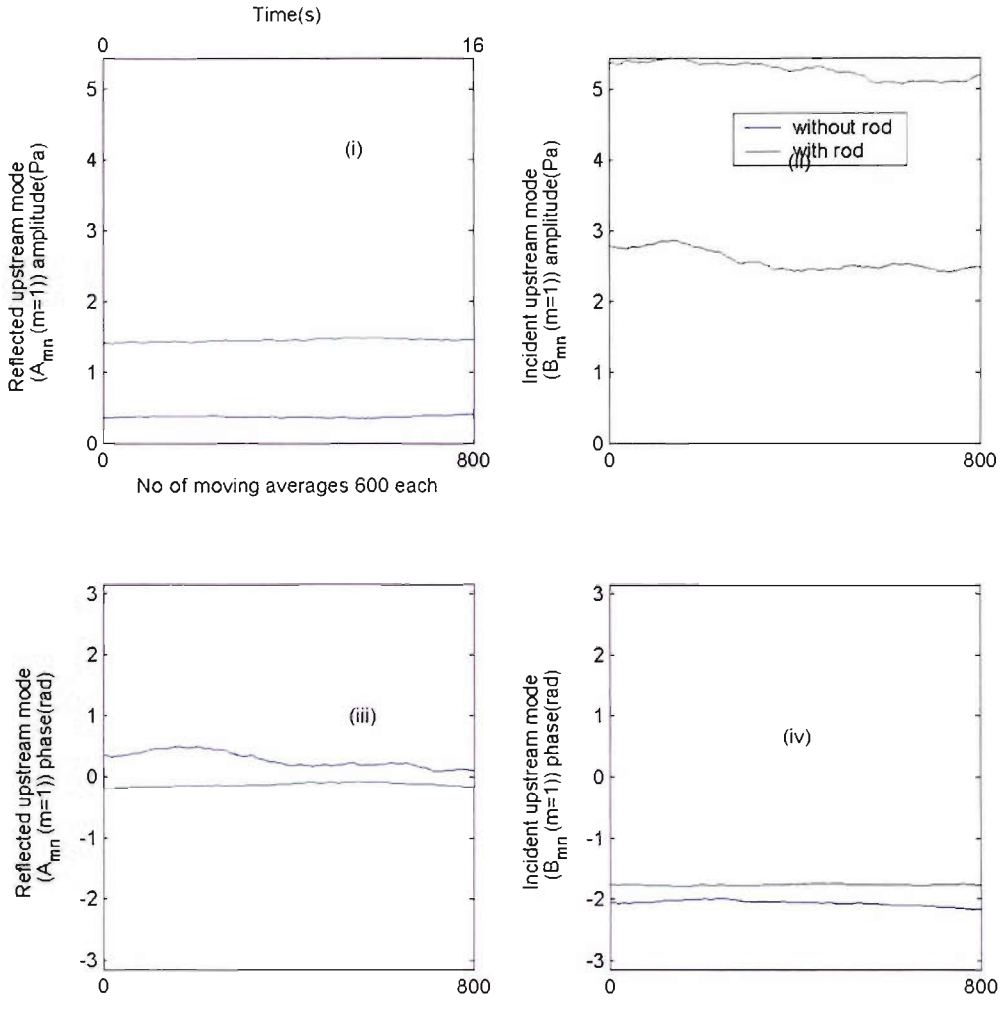

Figure A.5.1.18 Effect of moving averaging on upstream incident and reflected mode (m=1, 441 hz BPF): (i-ii) amplitudes, (iii-iv) phases.

Upstream modal coupling coefficient amplitudes and phases (262 hz BPF, m=0): From the modal amplitudes the coupling coefficients were determined and the effect of incremental and moving averaging on the low speed plane wave modal coupling coefficient is given in Figure A.5.1.19. The same variation sensed in the modal amplitudes of Figures A.5.1.11 –A.5.1.12 is also seen here.

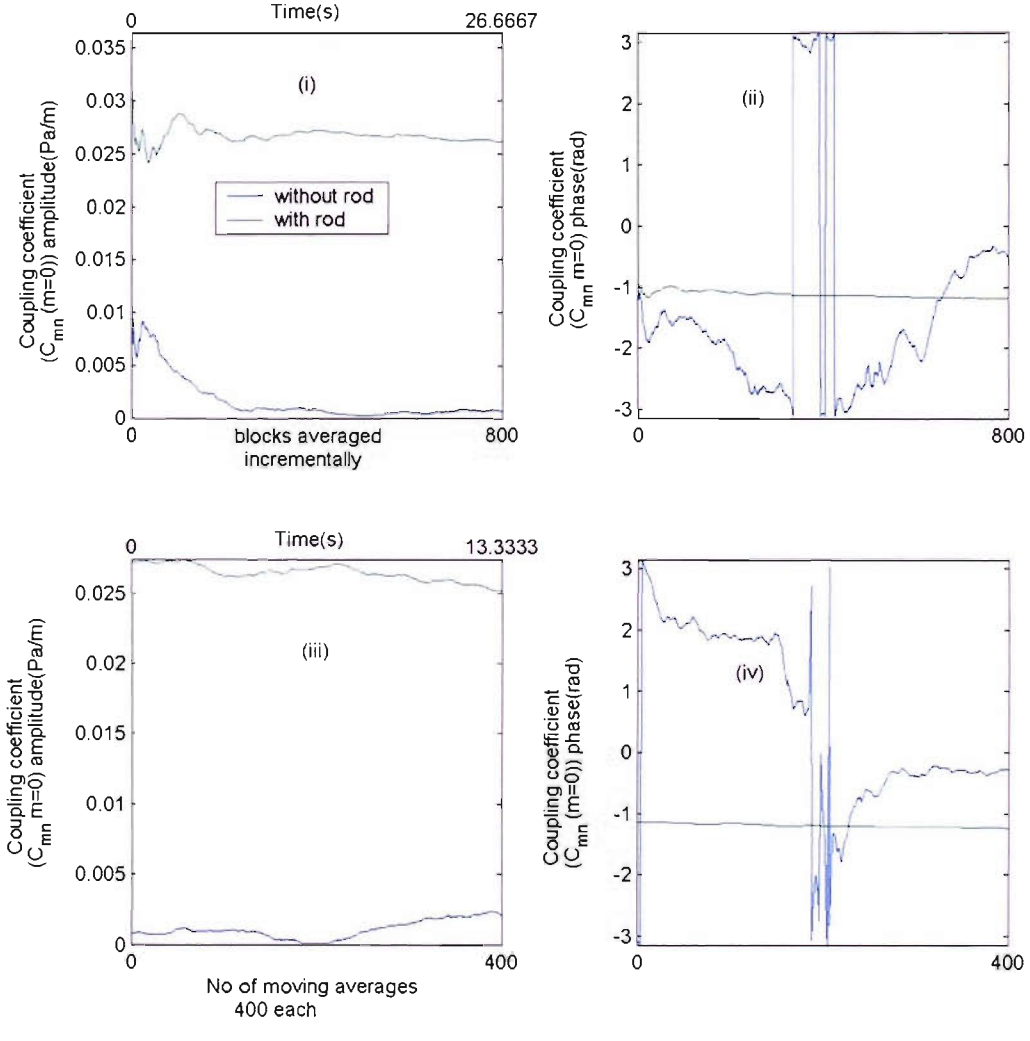

Figure A.5.1.19 Effect of incremental averaging on upstream modal coupling coefficient (m=0, 262 hz BPF): (i-ii) amplitude and phase; Effect of moving averaging on upstream modal coupling coefficient (m=0, 262 hz BPF): (iii-iv) amplitude and phase.

Upstream modal coupling coefficient amplitudes and phases (441 hz BPF, m=(-1,0,1)):

The effect of incremental and moving averaging on the high speed modal coupling coefficients are given for the three modes in Figure A.5.1.20 – A.5.1.21. The same variation sensed in the modal amplitudes of Figures A.5.1.13 –A.5.1.18 is also seen here.

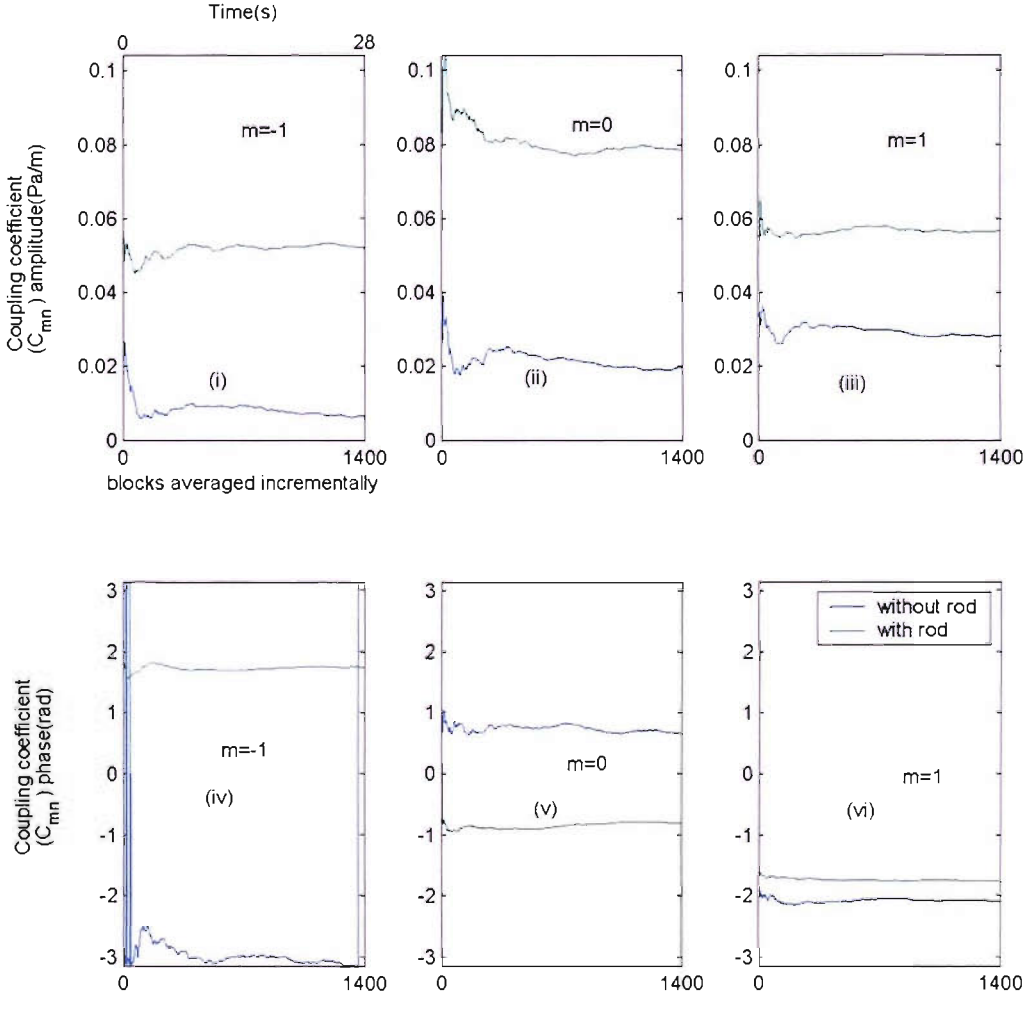

Figure A.5.1.20 Effect of incremental averaging on upstream modal coupling coefficients (m=-1,0,1; 441 hz BPF): (i-iii) amplitudes (iv-vi) phases.

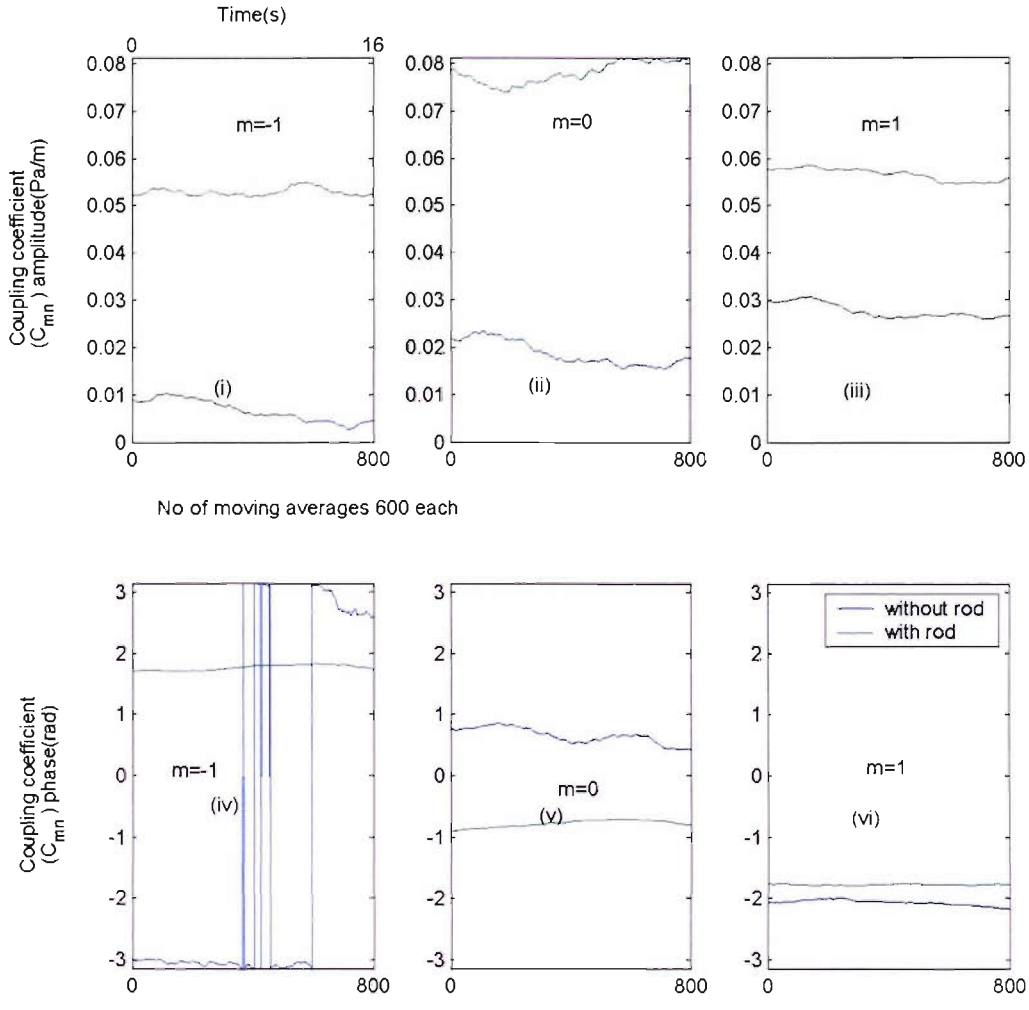

Figure A.5.1.21 Effect of moving averaging on upstream modal coupling coefficients (*m*=-1,0,1; 441 hz BPF): (i-iii) amplitudes (iv-vi) phases.

Upstream modal reflection coefficient amplitudes (262 hz BPF, m=0):

The reflection coefficient was estimated for the low speed plane wave mode from the variations given in Figures A.5.1.11 –A.5.1.12. The effect of averaging on the plane wave mode reflection coefficient is given in Figure A.5.1.22. The low amplitude and high unsteadiness in the tone at the BPF for the low speed case without the rod which also caused similar levels of unsteadiness in the incident and reflected modal amplitudes also causes the reflection coefficients to exhibit large fluctuations. The reflection coefficient is seen to fluctuate above and below 1 for this case in contrast to the case with the rod. This is because the first harmonic amplitude for the low speed case without the rod inside the duct was found to be very low due to the phase incoherence of the tone across the individual blade pass segments in the microphone signal. The low amplitude tone combined with the unsteadiness caused the estimate of the upstream duct reflection coefficient to fluctuate widely above and below 1. For the case where the rod is inserted into the duct this coefficient is steady.

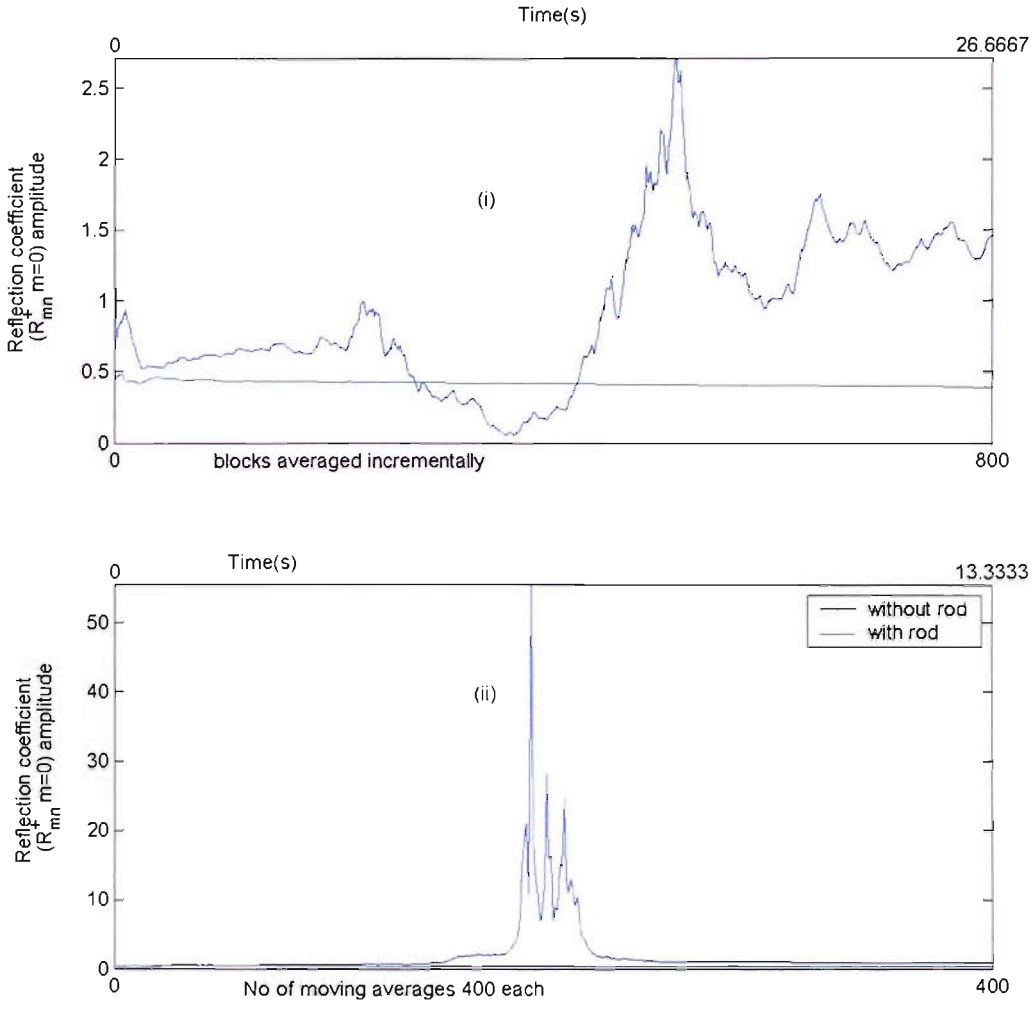

Figure A.5.1.22 Effect of averaging on upstream modal reflection coefficient (m=0, 262 hz BPF): (i) incremental (ii) moving.

Upstream modal reflection coefficient amplitudes (441 hz BPF, m=(-1,0,1)):

The reflection coefficient was estimated for the three high speed cut-on modes from the variations given in Figures A.5.1.13 –A.5.1.18. The effect of averaging on the three cut-on modal reflection coefficients is given in Figure A.5.1.23.

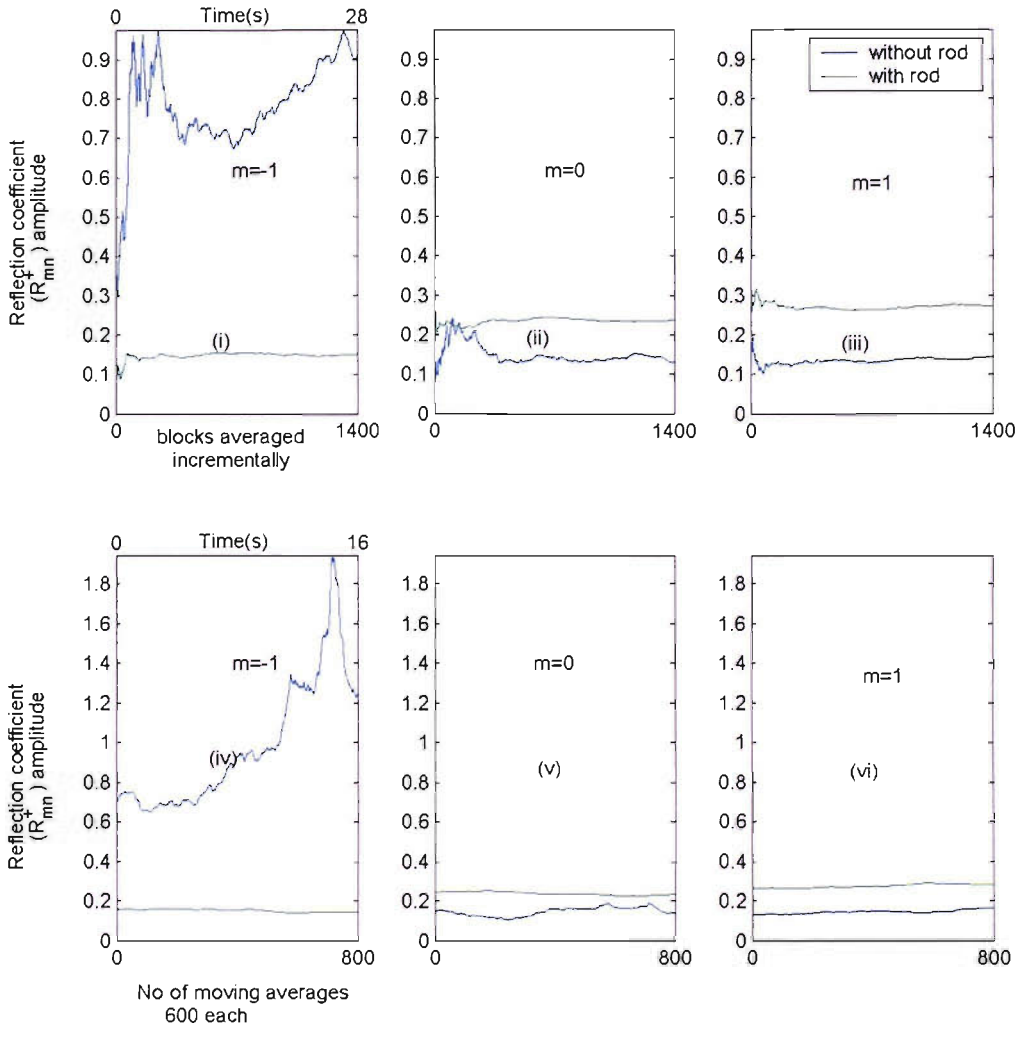

Figure A.5.1.23 Effect of averaging on upstream modal reflection coefficients (*m*=-1,0,1; 441 hz BPF): (i-iii) incremental (iv-vi) moving.

Upstream in-duct sound power level (262 Hz BPF):

The effect of averaging on the low speed in-duct sound power level is given in Figure A.5.1.24. We know that the estimation of in-duct sound power can be performed by using the duct modal amplitudes and reflection coefficients. Note that the power measured in Watts is negative during some of the averages for the case without the rod. In the illustration below the absolute of the power is plotted in decibels and wherever the power in watts has gone negative it is indicated appropriately by a marker which switches between '0' and '1' when the sound power changes from positive to negative. The negative power situation arises only at the low speed with no rod projecting inside the duct. This is because the

estimate of the reflection coefficient at these instances is greater than 1 as described previously in Figure A.5.1.22 in this Appendix. When the estimate of the reflection coefficient alternates between values above and below 1, the transmitted sound intensity vector is undergoing a reversal in the sign. The transmitted sound power becomes negative when the reflected intensity is greater than the incident intensity in magnitude and hence the absolute value is shown at these instances.

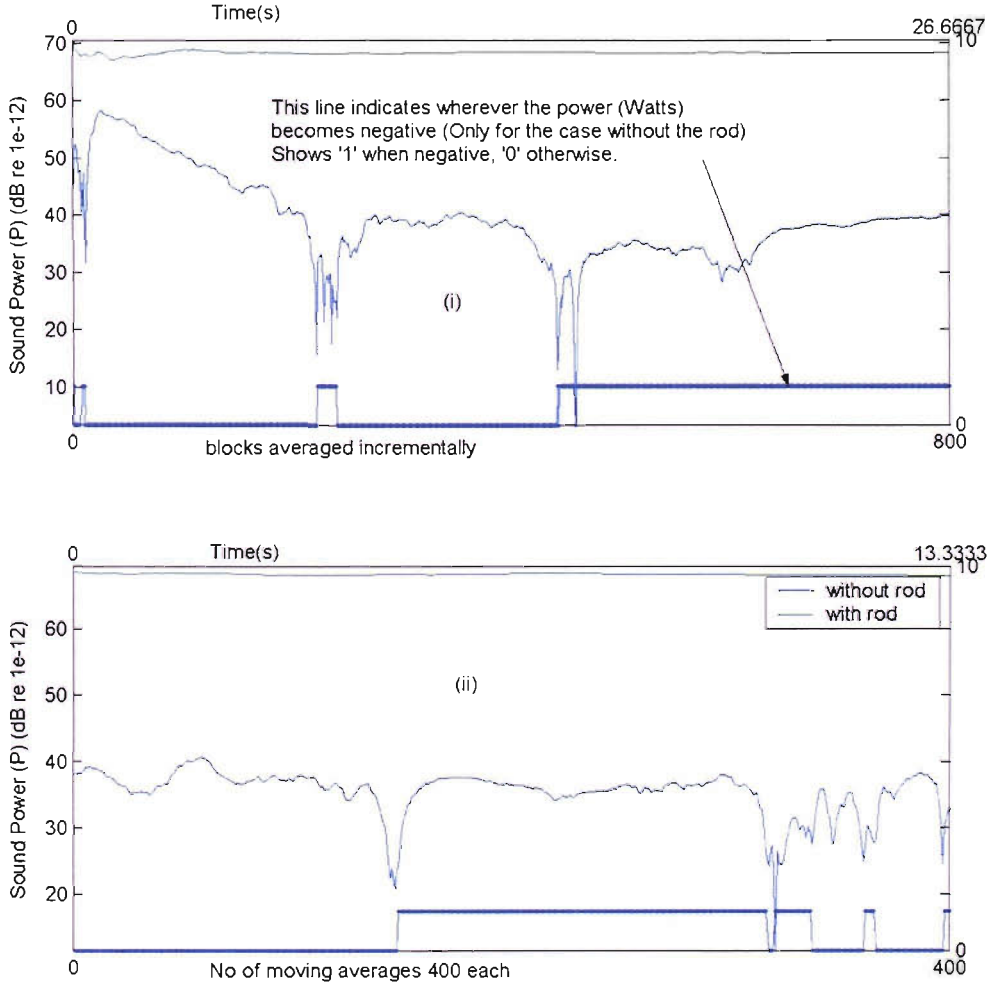

Figure A.5.1.24 Effect of averaging on in-duct upstream sound power level (262 hz BPF): (i) incremental (ii) moving.

Upstream in-duct sound power level (441 hz BPF):

The effect of averaging on the high speed in-duct sound power level is given in Figure A.5.1.25.

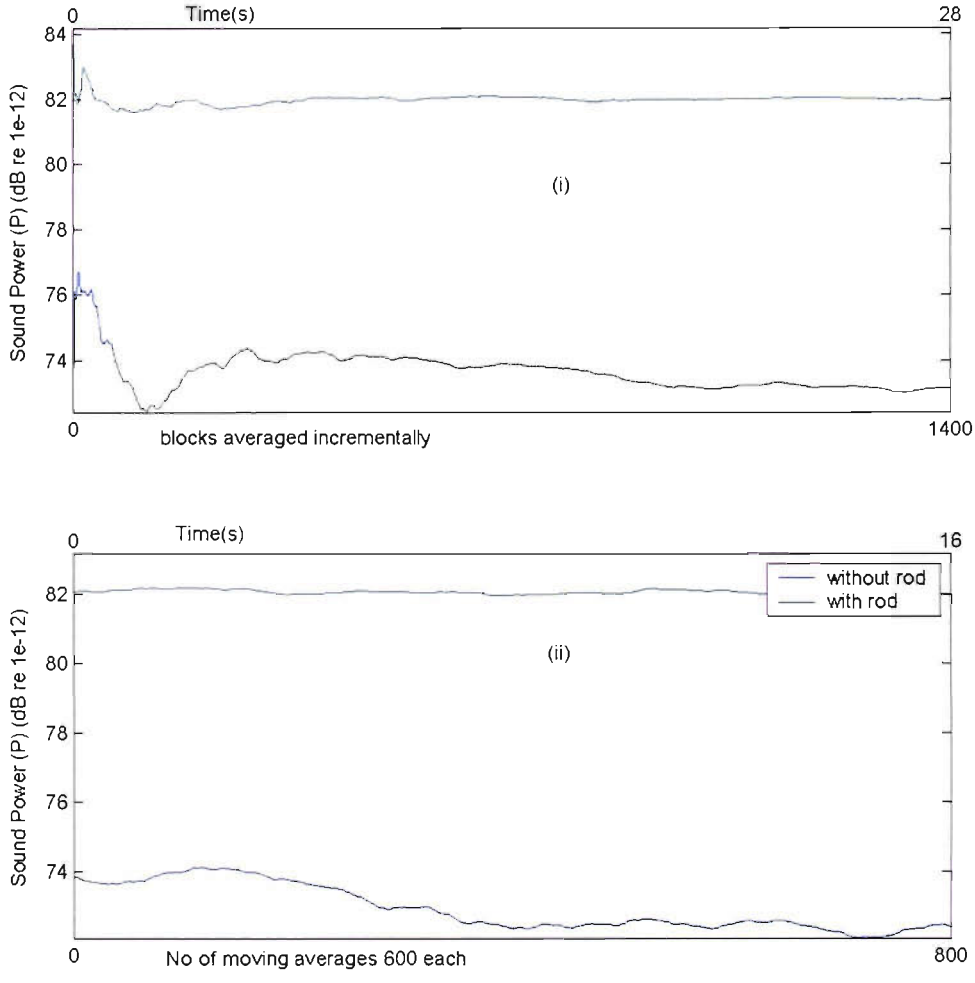

Figure A.5.1.25 Effect of averaging on in-duct upstream sound power level (441 hz BPF): (i) incremental (ii) moving.

A.5.1.4 Induct Downstream quantities:

In the previous two sections the effect of averaging on the unsteadiness in the far-field and in-duct upstream quantities were thoroughly dealt with. In this section unsteadiness variations in quantities pertaining to the measurements of the downstream in-duct microphone are given. These measurements were made only at the low speed as there is only an axial microphone array in the downstream which cannot be used to decompose the radial modes in the high speed harmonics.

Downstream tonal amplitude and phase (262 hz BPF):

The effect of incremental and moving averaging on the three tones measured on the first downstream microphone at the low speed are given in Figures A.5.1.26 – A.5.1.27. It can be seen that the unsteadiness is lesser that what was observed on the upstream measured tonal amplitudes which were given in Figures A.5.1.7 – A.5.1.8 of Section A.5.3.

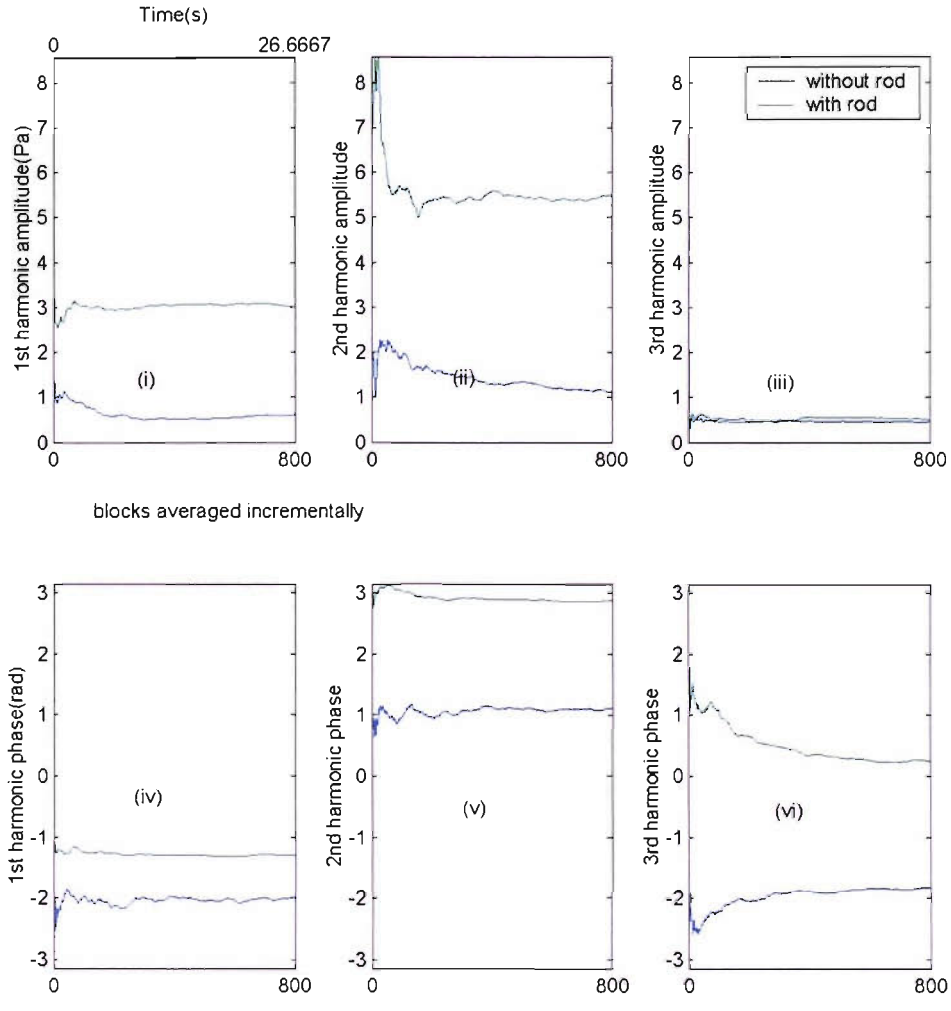

Figure A.5.1.26 Effect of incremental averaging on the BPF tone (262 hz) and its harmonics measured on the in-duct downstream microphone: (i-iii) tonal amplitudes, (iv-vi) tonal phases.

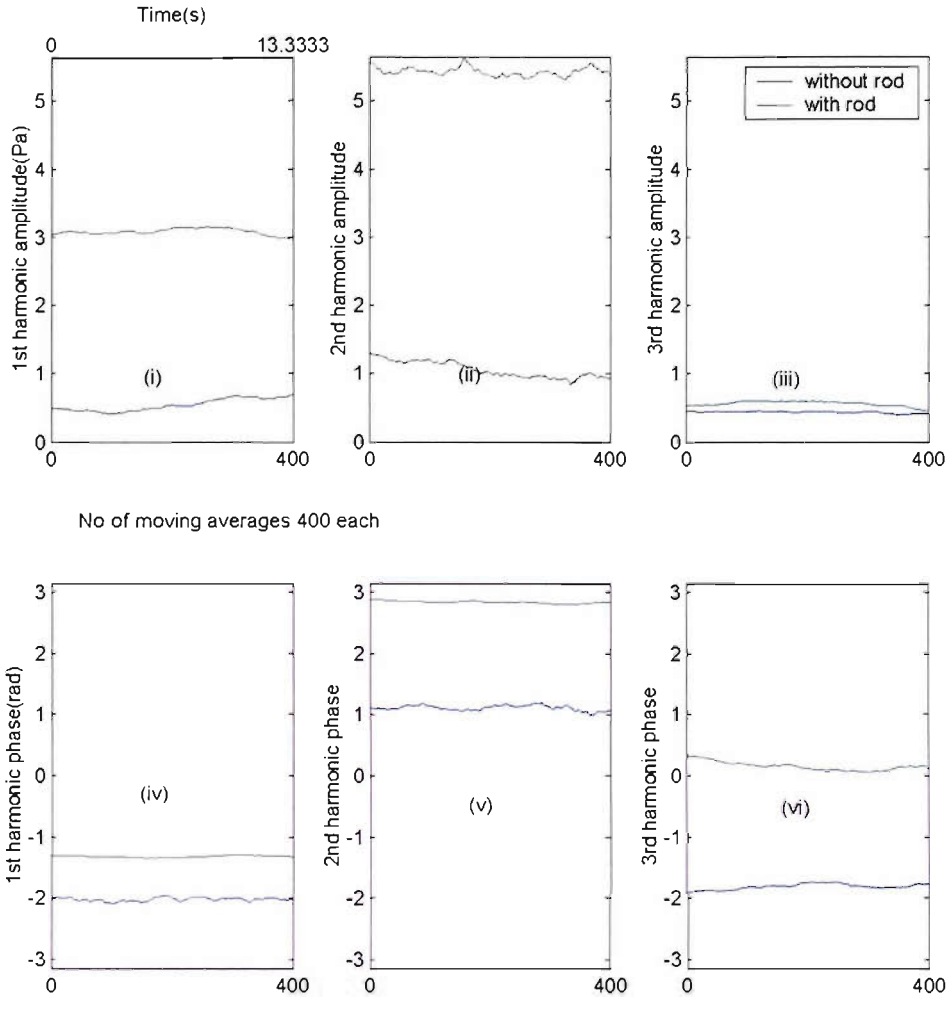

Figure A.5.1.27 Effect of moving averaging on the BPF tone (262 hz) and its harmonics measured on the in-duct downstream microphone: (i-iii) tonal amplitudes, (iv-vi) tonal phases.

Downstream incident and reflected modal amplitudes and phases (262 hz BPF): The downstream first harmonics described in Figures A.5.1.26 – A.5.1.27 were used along with those measured on the rest of the downstream microphones in the decomposition of downstream incident and reflected plane wave mode. The effect of averaging on the amplitudes of these are given in Figures A.5.1.28 – A.5.1.29.

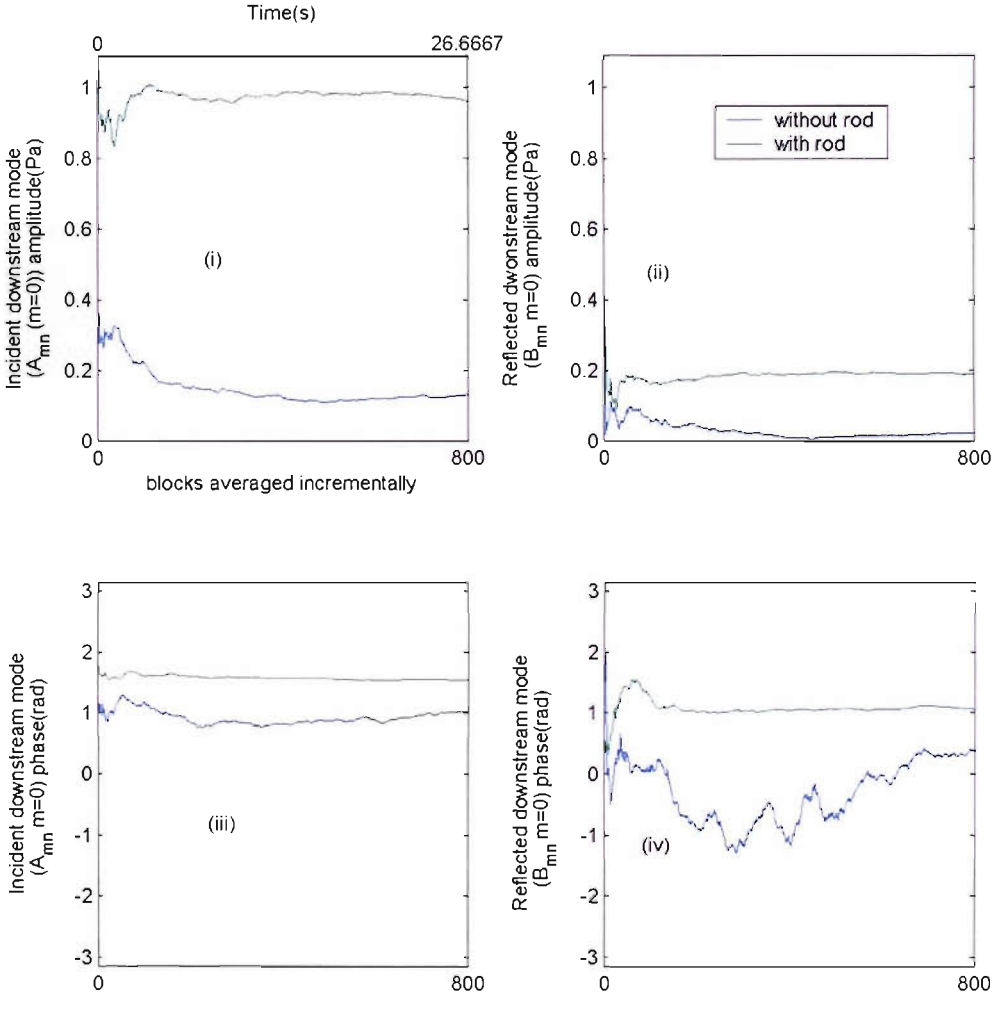

Figure A.5.1.28 Effect of incremental averaging on downstream incident and reflected mode (m=0, 262 hz BPF): (i-ii) amplitudes, (iii-iv) phases.

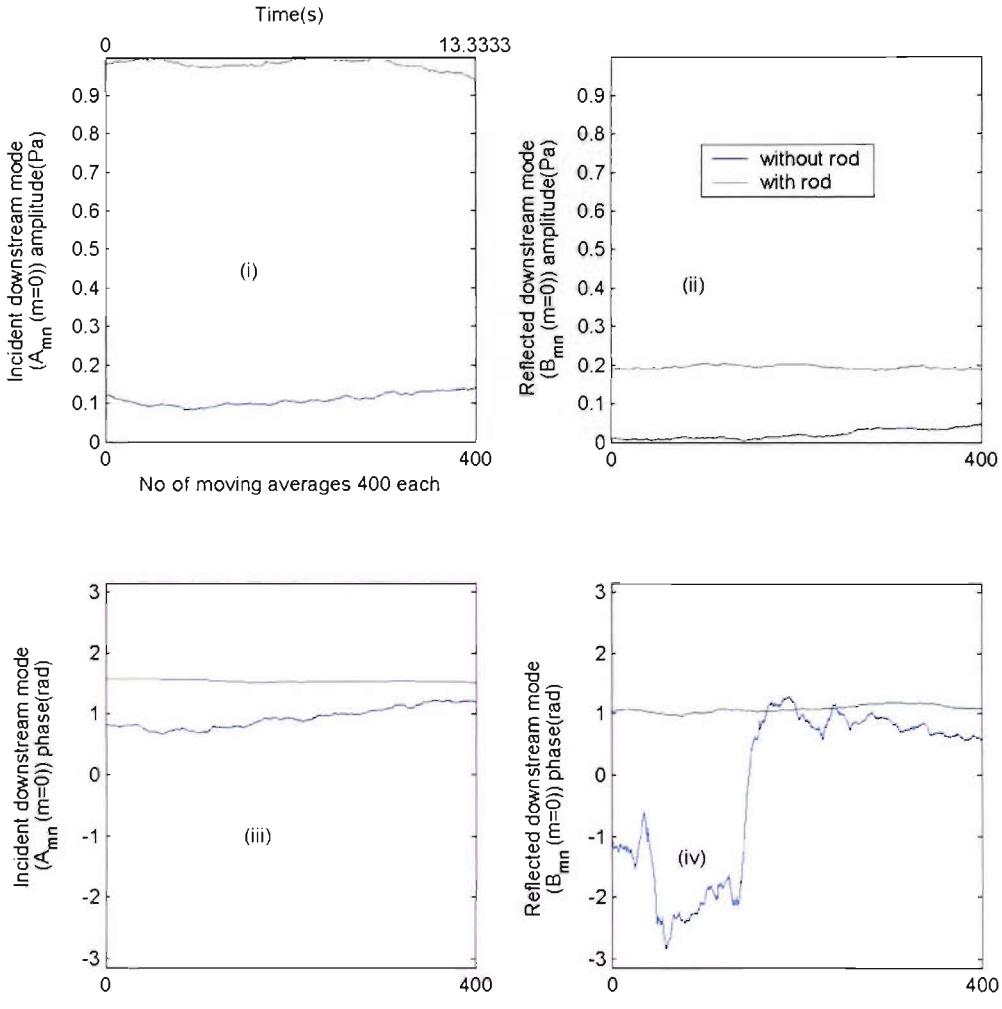

Figure A.5.1.29 Effect of moving averaging on downstream incident and reflected mode (m=0, 262 hz BPF): (i-ii) amplitudes, (iii-iv) phases.

Downstream modal reflection coefficients (262 hz BPF):

Finally the effect of averaging on the downstream plane wave reflection coefficient is given in Figure A.5.130. Though there is fluctuation in this coefficient in the case without the rod in the duct, this quantity doesn't exceed 1 as opposed to the upstream mode mentioned previously.

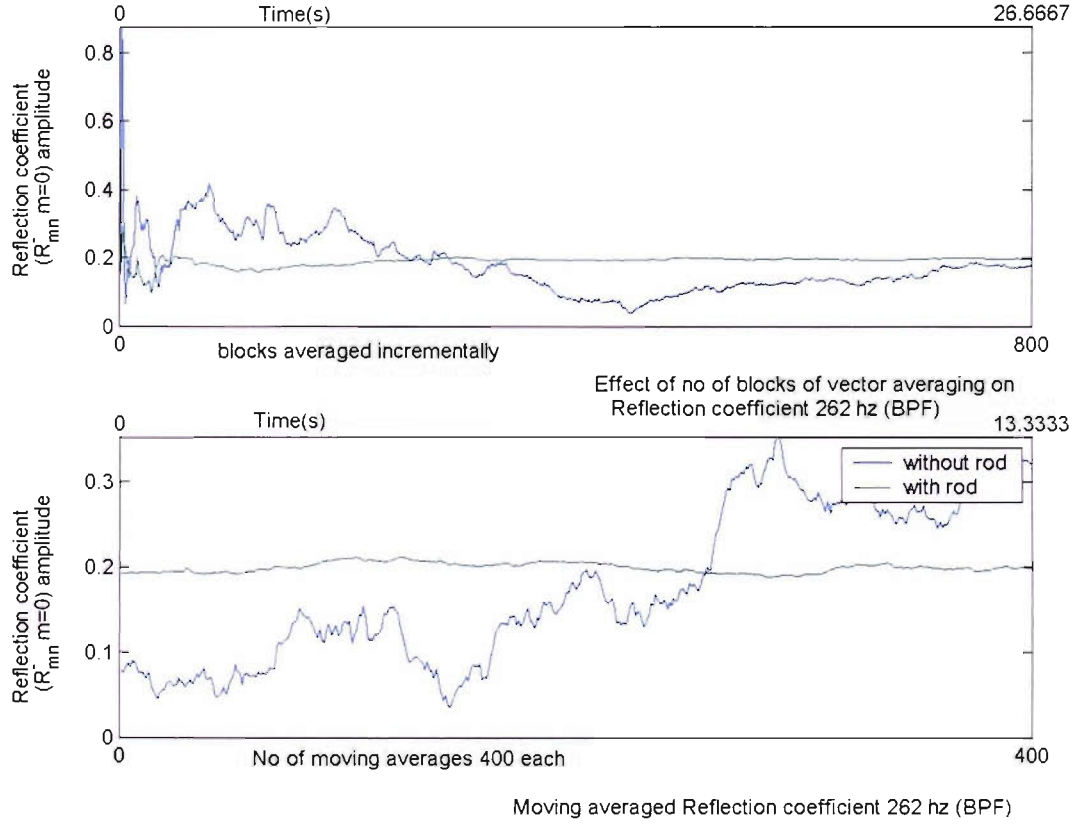

Figure A.5.1.30 Effect of averaging on downstream modal reflection coefficient (*m*=0, 262 hz BPF): (i) incremental (ii) moving.

A.5.1.5 Summary:

In general it could be seen that the tonal fluctuation was observed in the far-field quantities only for some harmonics in the cases without the rod inside the duct. In the in-duct measurements the first harmonic amplitude for the low speed case without the rod inside the duct was found to be very low due to the phase incoherence of the tone across the individual blade pass segments in the microphone signal. The low amplitude tone combined with the unsteadiness caused the estimate of the upstream duct reflection coefficient to fluctuate widely above and below 1. This caused the power to change from positive to negative values due to the reversal of the sign of the transmitted sound intensity. Table A.5.1.2 lists the mean and standard deviations in the far field sound pressure level and the in-duct power level from the moving average illustrations shown before. The estimates are not shown for the in-duct power for the low speed case without rod as the power fluctuates through negative and positive values. Based on the effect of averaging on the unsteadiness of the various quantities described in this appendix, it was decided that microphone signal acquisition during subsequent experiments should be long enough to perform 400 averages at the high speed and 600 averages at the high speed. This means that in all end-results like the far-field sound pressure and in-duct sound power levels the error involved is given by the standard deviation listed in the table below. Whilst selection of the number of averages for subsequent experiments was the reason to perform incremental averaging, the reason to perform moving averaging and illustrate its effect on the various quantities throughout this appendix was to determine the standard deviations in all those quantities after the choice of the number of averages is made.

	Low speed		High speed		Low speed		High speed	
Quantity	mean		mean		Standard deviation		Standard deviation	
	Without rod	With Rod	Without rod	With Rod	Without rod	With Rod	Without rod	With Rod
Sound pressure level (dB) (1st harmonic)	53.3481	91.7103	91.362	103.8379	3.452	0.115	0.5013	0.1236
(2nd harmonic)	54.7748	87.9751	80.9671	93.7363	1.2995	0.1135	1.3111	0.3018
(3rd harmonic)	59.0014	77.0681	57.2851	74.3186	0.3942	0.1429	6.3519	1.8808
In-duct power (dB)		68.2789	72.9171	82.0149		0.1247	0.6450	0.0779

Table A.5.1.2 Unsteadiness estimates from measurements.

Appendix 5.2 The phenomenon of mode scattering and its effect on controller acoustic response

In the experiment to determine the controller response, a single rod is placed upstream of the fan at the azimuthal zero reference and the wake produced from it is allowed to interact with the fan and this causes the production of the acoustic modes. These modes propagate in both directions along the duct. The circumferential order of these modes determine whether they spin or cause a piston-like reciprocating action as they propagate. Modes with a circumferential order other than zero spin in the circumferential direction. The spinning rate or the rotational speed of these modes differs for each mode. Section 3.2 described the contribution of these spinning modes to the production of harmonics of blade passing frequency in the case of interacting flow disturbances with the moving fan blades. Since spinning acoustic modes also represent a form of disturbance in the flow the interaction of these with the stationary rod is examined in this section. This phenomenon of interaction acoustic modes with rotating blades is also responsible for the production of sum and difference tones (Cumpsty 1974, Groeneweg 1991). In the recent times, Holste and Neise (1997) have reported the presence of these modes in the results of the experiments conducted on a propfan consisting of two contra-rotating rotors and a downstream array of seven struts. Their experimental results have shown the presence of modes whose order cannot be explained using the strut-rotor or the rotor-rotor interaction. They attributed these modes to the modes from the above mentioned interaction which propagate and impinge on the struts and transform from an interaction with it. They have even shown from their results that these modes can have amplitudes as high or even higher than the primary modes. Considering the propagating primary modes akin to rotor wakes, the order of the scattered mode can be explained using the rotor-stator interaction theory. In the present problem of the controller response determination the discussion of this phenomenon is made in order to offer an explanation for the variation in the amplitude response for the plane wave mode across the controllers spaced out in the azimuthal direction as is the case with the 8 rod equispaced controller array used in the current rig.

In the experiment where the fan was run at a speed that gave a blade passing frequency of 441 Hz there were three cut-on modes present in the system

with their circumferential orders being m = -1, 0 ,1. They are generated from the interaction of the fan blades (B=9) with the flow modes of order p = 10, 9 ,8. The speeds at which the modes m = -1 ,1 rotate (since the plane wave mode doesn't spin) are given in the Table A.5.2.1 below. The order of the modes is determined using the relationship $m=sB-p$.

No. of fan blades B	Flow mode order p	Acoustic Mode order m ($m=sB-p$, where s=1)	Speed of the fan blades Ω (rad/s)	Speed of the spinning acoustic mode $B\Omega/m$ (rad/s), where $m\neq 0$
9	10	-1	Ω	9Ω ($=BPF$)
9	8	1	Ω	-9Ω($=BPF$)

Table A.5.2.1 Spinning modes generated at the fan origin.

It can be seen that the modes spin at a speed corresponding to the BPF. These modes propagate upstream and interact with the rod and produce modes of a different order. This transformation is termed as the mode scattering phenomenon. The order of the modes produced from the interaction can be known by considering the relationship for the rotor-stator interactions. $m=sB+kV$ gives the order of the modes issuing out of the interaction of the rotor wakes of order sB of a B bladed rotor with a stator of V vanes, where k is an integer. In the case of the acoustic mode-rod interaction this relationship can be used with term sB replaced by the order of the spinning mode m and the term kV retained to represent the rod order. Representing the order of the scattered mode as m_s we have $m_s=m+kV$ for the acoustic mode-rod interaction.

The Table A.5.2.2 below illustrates the determination of the order of the modes resulting from the acoustic mode-rod interaction case.

No. of rods V	Interacting acoustic mode order m	Scattering acoustic mode order m_s	Speed of the interacting acoustic mode	Excitation of the scattered mode (rad/s)

		(m_s=m+kV)	(rad/s)	
1	-1	0 (k=1)	9Ω	9Ω (=BPF)
1	1	0 (k=-1)	9Ω	9Ω (=BPF)

Table A.5.2.2 Scatter modes produced through interaction of spinning modes with the controller array rod.

As explained in the above table, the two spinning modes present at the BPF mentioned before interact with the rod and scatter into the plane wave mode. The excitation of the scattered plane wave mode is also at the BPF since the interacting modes spin at this frequency. Other modes can also result from scattering if one were to substitute different integral values for k. Only the plane wave mode is considered here for explaining the variation of the amplitude response along the circumferential direction of the 8 rod equispaced controller array used in the current rig. Thus the effective amplitude of the plane wave mode is the resultant of the original plane wave mode from the fan-flow disturbance case and the case of scattering. The original plane wave mode has its origin at the fan and the scattered mode has its origin at the rod. Both these combine at the rod plane and the resultant amplitude can have a variation with the circumferential orientation of the rod as explained below. This is explained in a two-step process. The first step to account for the above variation is the phase change of the original modes at the fan origin due to the change in the rod's angular disposition. This is understood from the relationship $e^{-jp\theta}$, where θ is the angle of the rod's disposition from the circumference and p is the order of the flow mode that induces the corresponding acoustic mode of order m. The phase of the plane wave mode is to be reckoned with respect to the axial coordinate of the fan origin and the phases of the spinning modes with the circumferential coordinate of the same. Assuming all modes have zero phase at the fan origin due to the interaction with the flow disturbance issuing out from a rod placed at the vertical reference, the phase change suffered by the three modes when the rod's azimuthal position is stepped through 45^0 increments are given below in Table A.5.2.3. The phase change from each mode is given by ($-p\theta$). According to the information in this table the spinning mode m=1 doesn't suffer any phase change at the fan origin. The phase change in mode m=-1 corresponds to an amount which is 2 times the

rotation of the rod and with the mode m=0 it is equal to one times the same quantity.

Rod position, $\theta = n\times45$ (deg), where n=0,7	Phase change of mode (m=-1, p=10), $-p\theta = -10n\times45 = -n\times90$ (deg)	Phase change of mode (m=0, p=9), $-p\theta = -9n\times45 = -n\times45$ (deg)	Phase change of mode (m=1, p=8), $-p\theta = -8n\times45 = 0$ (deg)
0	0	0	0
45	-90	-45	0
90	-180	-90	0
135	-270	-135	0
180	0	-180	0
225	-90	-225	0
270	-180	-270	0
315	-270	-315	0

Table A.5.2.3 Phase change of the modes at the fan origin due to rod rotation.

The second step examines the phase of the scatter mode m_s=0 resulting from the interaction of the acoustic modes m = -1, 1 which happens only after they travel towards and reach the rod. The modes travel towards the rod and let's assume they arrive at the same phase which they started with from the fan origin. Then at the rod plane it can be seen from the above table that the rod moves away relative to the mode m = -1 by ($-n\pi/4 - n\pi/2$) radians and by $-n\pi/4$ radians relative to mode m = 1. The unsteady forces generated on the rod and hence the radiated scatter modes due to the impingement of the two modes m = -1, 1 on the rod also undergo the same phase change. For mode m=1 let's say the scattered m_s=0 has a phase ϕ_1 when the mode m=1 impinges on the rod at 0^0, the phases of the scattered mode for the rest of the rod positions are given by $\phi_1 - n\pi/4$, and the same scattered mode resulting from the impingement of the m=-1 mode on the rod will

have a phase given by ϕ_2-$n\pi/4$- $n\pi/2$, if ϕ_2 is assumed as the phase when the impingement happens at the rod angle of 0^0.

Assuming the amplitude of the original plane wave mode to be *a*, its variation with the rod rotation as given in Table A.5.2.2 is $ae^{-jn\pi/4}$. Similarly if the amplitudes of the scatter modes resulting from the interaction of the modes *m* = -1, 1 with the rod at 0^0 are assumed to be *b* and *c*, their variation with the rod position is given by $be^{-j3n\pi/4}$ and $ce^{-jn\pi/4}$. Then the variation of the resultant amplitude of the plane wave mode with the circumferential orientation of rod is the sum of the variations of the original plane wave mode and the scatter modes with the rod position, i.e., $ae^{-jn\pi/4}+be^{-j3n\pi/4}+ce^{-jn\pi/4}$. Factoring out $e^{-jn\pi/4}$ from this expression we see that the magnitude of the resultant plane wave mode amplitude varies with the circumferential orientation of the rod array. This is made evident in the graphical illustrations in Figures A.5.2.1 – A.5.2.5. Assuming zero phase and unit amplitude for the vector *a*, the variation of $ae^{-jn\pi/4}$ for the original plane wave mode *m=0* is shown plotted in the polar plot of Figure A.5.2.1 for the various rotated rod positions. Similarly the scatter mode variations $ce^{-jn\pi/4}$ and $be^{-j3n\pi/4}$ are shown in Figures A.5.2.2 and Figure A.5.2.3. Vectors *c* and *b* are assumed to be of unit amplitude and with 0^0 and 22.5^0 phase respectively. The sum, $ae^{-jn\pi/4}+ce^{-jn\pi/4}$, representing the sum of the individual plane wave and the scatter mode resulting from impingement of mode *m* = 1 is shown in Figure A.5.2.4. Finally the sum, $ae^{-jn\pi/4}+be^{-j3n\pi/4}+ce^{-jn\pi/4}$, representing the variation in the magnitude of the resultant plane wave mode is shown in Figure A.5.2.5.

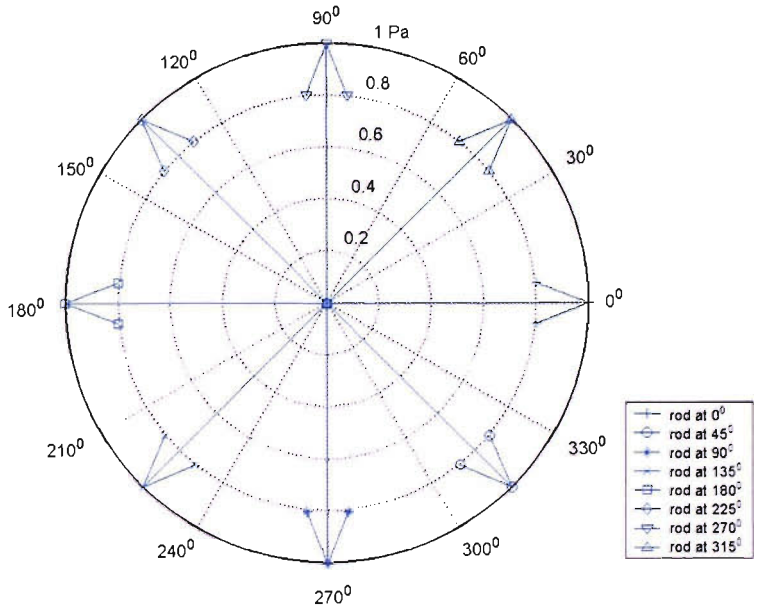

Figure A.5.2.1. Polar plot showing the phase change of the plane wave mode due to the rod rotation.

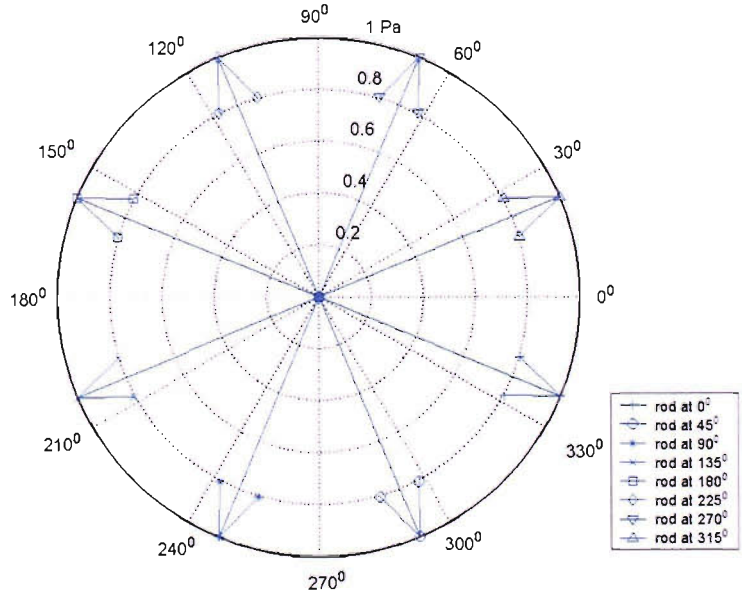

Figure A.5.2.2. Polar plot showing the phase change of the scattered plane wave mode $m_{s,l}$=0 with the rod rotation as the mode m=1 impinges on it.

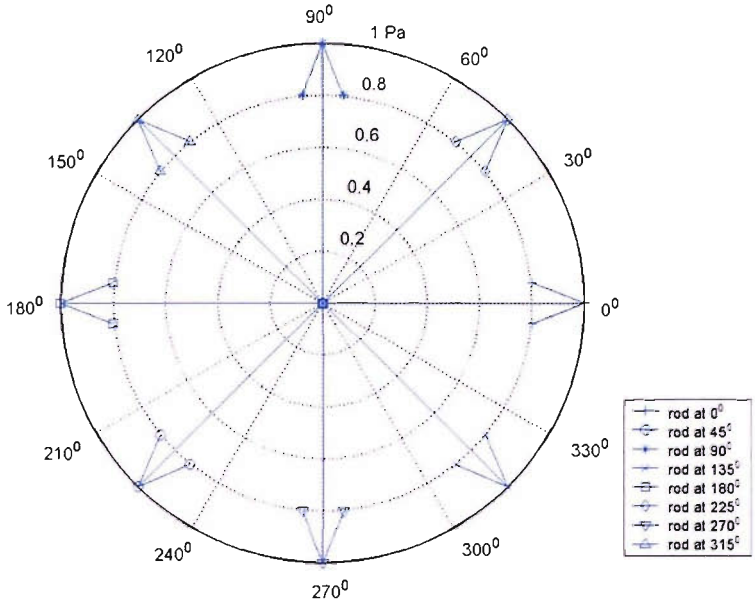

Figure A.5.2.3. Polar plot showing the phase change of the scattered plane wave mode $m_{s,-1}$=0 with the rod rotation as the mode m=-1 impinges on it.

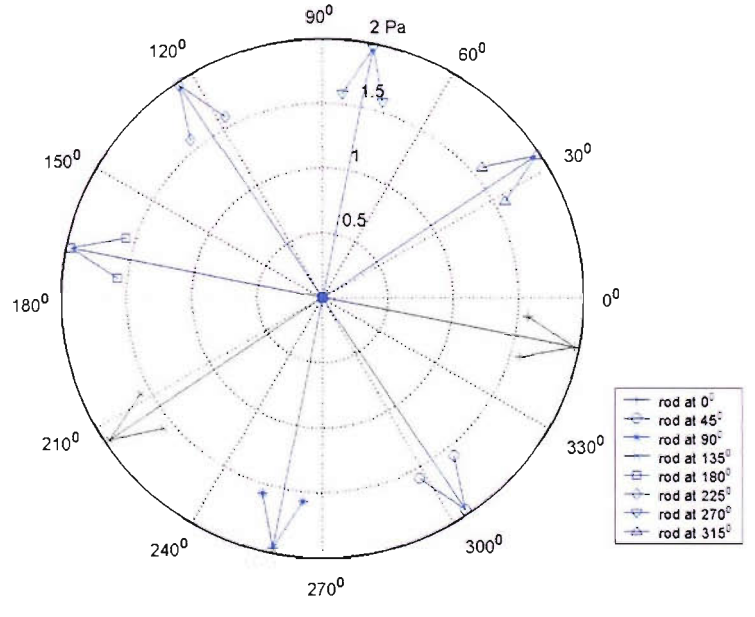

Figure A.5.2.4. Polar plot showing the phase change with rod rotation of the resultant of plane wave mode m=0 from fan-flow interaction and the scattered plane wave mode $m_{s,1}$=0.

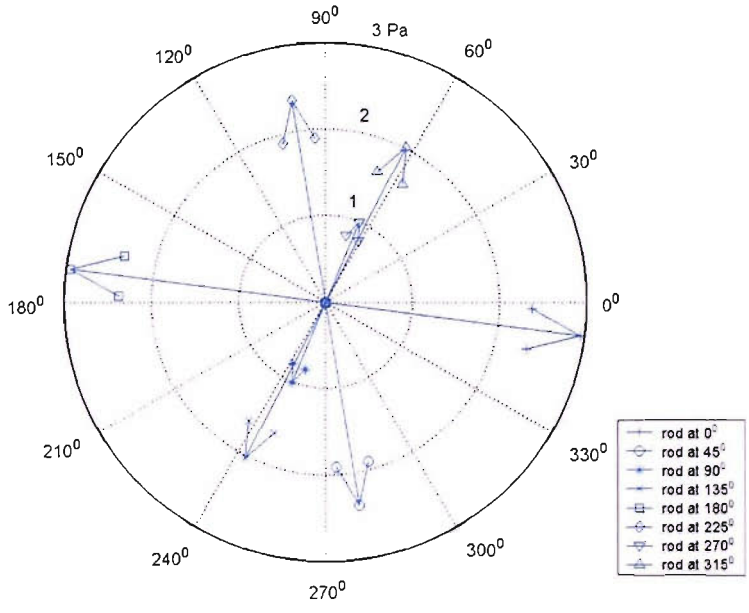

Figure A.5.2.5. Polar plot showing the phase change with rod rotation of the resultant of plane wave mode m=0 from fan-flow interaction and the scattered plane wave modes $m_{s,1}$=0 and $m_{s,-1}$=0.

References

Airbus Industries, "Airbus global market forecast," 1999.

Allen, C.S., Blake, W.K., Dougherty, R.P., Lynch, D., Soderman, P.T. and Underbrink, J.R., "*Aeroacoustic Measurements*," Edited by T.J. Mueller, Springer-Verlag, 2002.

Amiet, Roy K., "Compressibilty effects in unsteady thin-airfoil theory," *AIAA Journal*, Vol. 12, No. 2, pp.252-255, Feb. 1974.

Cumpsty, N.A., "Sum and difference tones from turbomachines," *Journal of Sound and Vibration*, Vol. 32, No. 3, pp. 383-386, Feb. 1974.

Envia, E., "Fan noise reduction: An overview," *Intl. Journal of Aeroacoustics*, Vol. 1, No. 1, pp. 43-44, 2002.

Ganz, U., Glegg, S.A.L. and Joppa, P., "Measurement and prediction of broadband fan noise," *AIAA* Paper 98-2316, 1998.

Goldstein, M. E., "*Aeroacoustics*," McGraw-Hill Book Co., 1976.

Goldstein, M. E. and Atassi, H., "A complete second-order theory for the unsteady flow about an airfoil due to a periodic gust," *Journal of Fluid Mechanics*, Vol. 74, pt. 4, Apr. 22, pp. 741-765, 1976.

Graham, J. M. R., "Similarity rules for thin air for thin air foils in non stationary flows," *Journal of Fluid Mechanics*, Vol. 43, pt. 4, Oct.2, pp. 753-766, 1970.

Groeneweg, J. F., Sofrin, T. G., Rice, E. J. and Gliebe, P. R., "Turbomachinery noise. Aeroacoustics of flight vehicles: Theory and practice, Vol. 1: Noise sources," Edited by H. Hubard, *NASA* RP-1258, pp.151-204, 1991.

Holste, F. and Neise, W., "Noise source identification in a propfan model by means of acoustical near field measurements," *Journal of Sound and Vibration*, Vol. 203, pp. 641-665, 1997.

Huff, D. L., "Fan noise prediction: Status and needs," *AIAA* Paper 98-0177, 1998.

Kousen, A.K. and Verdon, J.M., "Active control of wake/blade-row interaction noise," *AIAA Journal*, Vol. 32, No. 10, pp. 1953-1960, 1994.

Landahl, M., "*Unsteady transonic flow*," Pergamon Press, pp. 27-29, 1961.

Moore, C. J., "Reduction of fan noise by annulus boundary layer removal," *Journal of Sound and Vibration*, 43, pp 671-681, 1975.

Namba, M., "Three-dimensioanl analysis of blade force and sound generation for an annular cascade in distorted flows," *Journal of Sound and Vibration*, Vol. 50, No. 4, Feb. 22, pp. 479-508, 1977.

Nelson, P.A., "Active techniques and their potential for application in aeroacoustics," keynote lecture, *6th CEAS/AIAA Aeroacoustics Conf.*, Lahaina, Hawaï, June 2000.

Nuehas, L., Schulz, J., Neise, W. and Moser, M., "Active control of aerodynamic performance and tonal noise of axial turbomachines," *5th Euro Conference on Turbomachinery Fluid Dynamics and Thermodynamics*, Praha, Czech Republic, March 2003.

Owens, R.E., "Energy efficient engine propulsion system – Aircraft engine evaluation," *NASA* CR-159488, 1979.

Pitelet, C., "Flow control for fan noise reduction," M.Sc. Thesis, ISVR, University of Southampton, 2000.

Polacsek, C., "Reduction of fan rotor-stator interacting modes using a novel design: an experimental study," *6th International Congress on Sound and Vibration*, Copenhagen, Denmark, 5-8 July 1999.

Polacsek, C. and Desbois-Lavergne, F., "Fan interaction noise reduction using a wake generator: experiments and computational aero-acoustics," *Journal of Sound and Vibration*, Vol. 265, No. 4, Aug 22, pp. 725-743, 2003.

Quinlan, D.A. and Bent, P.H., "High frequency noise generation in small axial flow fans," *Journal of Sound and Vibration*, Vol. 218, No. 2, pp. 177-204, 1998.

Rangwalla, A.A. and Rai, M. M., "A numerical analysis of tonal acoustics in rotor-stator interactions," *Journal of Fluids and Structures*, Vol. 7, pp. 611-637, 1993.

Sawyer, S. and Fleeter, S., "Active control of discrete-frequency noise generated by rotor-stator interactions," *Journal of Propulsion and Power*, Vol. 18, No. 1, pp. 100-106, 2002.

Schlichting, H., "*Boundary layer theory*," McGraw-Hill Book Co., 1960.

Sears, W.R., "Some aspects of non-stationary airfoil theory and its practical application," *Journal of the Aeronautical Society*, Vol. 8, No. 3, pp. 104-108, Jan. 1941.

Sutliff, D.L., Bridges, J. and Envia, E., "Comparison of predicted low speed fan rotor/stator interaction modes to be measured," *AIAA* Paper 97-1609, May 1997.

Sutliff, D. L., Tweedt, D. L., Fite, E. B. and Envia, E., "Low-speed fan noise reduction with trailing edge blowing," *Intl. Journal of Aeroacoustics*, Vol. 1, No. 3, pp. 275-305, 2002.

Thomas, R.H., Chaudhari, M.M. and Joslin, R.D., "Flow and noise control: Review and assessment of future directions," *NASA* TM 2002-211631, 2002.

Topol, D. A., "Rotor wake/stator interaction noise: Prediction vs. data," *Journal of Aircraft*, Vol.30, No. 5, pp. 728-735, 1993.

Tyler, J.M. and Sofrin, T.G., "Axial flow compressor noise studies," *SAE Aeronautic Meeting*, 345D, 1961.

Waitz, I. A., Brookfield, J. M., Sell, J. and Hayden, B., "Preliminary assessment of wake management strategies for reduction of turbomachinery fan noise," *Journal of Propulsion and Power*, Vol.12, No. 5, pp.958-966,1996.

Widrow, B. and Stearns, S.D., "*Adaptive signal processing*," Prentice Hall, 1985.